Imperial College London

Department of Materials

Phase Evolution and Properties of a Porcelain Body Fabricated Using Different Rapid Firing Techniques

A thesis submitted in partial fulfilment of the requirements for the degree of Doctor of Philosophy of Imperial College London

Wirat Lerdprom

London, March 2019

“ If you're not prepared to be wrong, you'll never come up with anything original ”

— Sir Ken Robinson —

Declaration of Originality

I hereby declare that this thesis is my original work. Other contributions, which are not my own, have been properly referenced and acknowledged.

Wirat Lerdprom

March 2019

Staines-upon-Thames

Preface

This thesis summarises the research carried out by the author in the Department of Materials at Imperial College London during the period November 2014 to November 2017, under the supervision of Dr Doni D. Jayaseelan and Prof William E. Lee. No part of this work has been submitted for any other qualification in this college or elsewhere. Some of the results presented in this thesis have been published and presented in various journals and conferences.

Publications

1. **Lerdprom, W.,** Chinnam, R.K., Jayaseelan, D.D., and Lee, W.E., *Porcelain production by direct sintering.* Journal of the European Ceramic Society, 2016. 36(16): p. 4319-4325.

2. **Lerdprom, W.,** Li, C., Jayaseelan, D.D., Skinner, S.J., and Lee, W.E., *Temperature dependence of electrical conductivity of a green porcelain mixture.* Journal of the European Ceramic Society, 2017. 37.(1): p. 343-349.

3. **Lerdprom, W.,** Grasso, S., Jayaseelan, D.D., Reece, M.J., and Lee, W.E., *Densification behaviour and physicomechanical properties of porcelains prepared using spark plasma sintering.* Advances in Applied Ceramics: Structural, Functional and Bioceramics, 2017. 116 (6): p. 307-315.

4. **Lerdprom, W.,** Zapata-Solvas, E., Jayaseelan, D.D., Borrell, A., Salvador, M.D., and Lee, W.E., *Impact of microwave processing on porcelain microstructure.* Ceramics International, 2017.43 (16): p. 13765-13771.

5. **Lerdprom, W.,** Bhowmik, A., Grasso, S., Zapata-Solvas, E., Jayaseelan, D.D., Reece, M.J., and Lee, W.E., *Impact of spark plasma sintering (SPS) on mullite formation in porcelains.* Journal of the American Ceramic Society, 2018. 101 (2): p. 525-535.

6. **Lerdprom, W.,** *Ceramic technology for cleaner water in Africa: When academia meets imagination.* Bulletin of the American Ceramic Society, 2017. 96 (5): p. 9.

7. **Lerdprom, W.,** *Current challenges for whitewares industry.* Bulletin of the American Ceramic Society, 2018. 97 (8): p. 48.

8. **Lerdprom, W.,** Ji, W., Zapata-Solvas, E., Jayaseelan, D.D., Todd, R.I., and Lee, W.E., *Preliminary study of flash sintering and electric field-induced mullitization in porcelains.* (manuscript in preparation)

9. **Lerdprom, W.,** Jayaseelan, D.D., and Lee, W.E., *Impact of Field Assisted Sintering on porcelain microstructure*. (manuscript in preparation)

Conference contributions

1. **Lerdprom, W.,** Chinnam, R.K., Jayaseelan, D.D., and Lee, W.E., *Feasibility study of porcelain production by direct sintering.* Poster presentation at Reduce-Replace-Recycle: Effective Material Resource Management in Ceramics. 14 April 2015, Stoke on Trent, UK.

2. **Lerdprom, W.,** Chinnam, R.K., Jayaseelan, D.D., and Lee, W.E., *Feasibility study of porcelain production by a direct sintering technique.* Oral presentation at International Conference of Traditional and Advanced Ceramics. 9-11 September 2015, Bangkok, Thailand.

3. **Lerdprom, W.,** Chinnam, R.K., Jayaseelan, D.D., and Lee, W.E., *Porcelain production by direct sintering.* Oral presentation at Materials Science & Technology 2015. 14-18 October 2015, Columbus, OH, USA.

4. **Lerdprom, W.,** Jayaseelan, D.D., and Lee, W.E., *Fabrication of a vitreous porcelain by conventional sintering and spark plasma sintering*. Oral presentation at Electric Field Assisted Sintering and Related Phenomena far from Equilibrium. 6-11 March 2016, Tomar, Portugal.

5. **Lerdprom, W.,** Jayaseelan, D.D., and Lee, W.E., *Fabrication of a vitreous porcelain by conventional sintering and spark plasma sintering.* Poster

presentation at PG Research Day, Imperial College London. 21 March 2016, London, UK.

6. **Lerdprom, W.,** *Advanced rapid sintering of whitewares.* Oral presentation at 2nd year PhD presentation, Imperial College London. 21 April 2016, London, UK.

7. **Lerdprom, W.,** Zapatas-Solvas, E., Jayaseelan, D.D., and Lee, W.E., *Phase evolution, microstructure, and properties of porcelains using field enhanced sintering.* Oral presentation at Materials Science & Technology 2016. 23-27 October 2016, Salt Lake City, UT, USA.

8. **Lerdprom, W.,** Zapatas-Solvas, E., Jayaseelan, D.D., and Lee, W.E., *Phase evolution, microstructural and properties of porcelains using field enhanced sintering.* Oral presentation at 1-Day Research Meeting on Advanced Ceramics (1DRAC) meeting. 5 December 2016, Kingston, UK.

9. **Lerdprom, W.,** *Advanced rapid sintering of whitewares.* Oral presentation at PG Research Day, Imperial College London. 20 March 2017, London, UK.

10. **Lerdprom, W.,** Zapatas-Solvas, E., Jayaseelan, D.D., and Lee, W.E., *Impact of Field Assisted Sintering on porcelains microstructure*. Oral presentation at the 15th Conference & Exhibition of the European Ceramic Society (ECerS 2017). 9-13 July 2017, Budapest, Hungary.

11. **Lerdprom, W.,** Zapatas-Solvas, E., Jayaseelan, D.D., and Lee, W.E., *Observations on the effect of electric field on mullite formation in porcelains.* Oral presentation at Materials Science & Technology 2017. 8-12 October 2017, Pittsburgh, PA, USA.

12. **Lerdprom, W.,** and Lee, W.E., *Advanced rapid sintering of whitewares—microstructure evolution, energy consumption and industrial application opportunity*. Oral presentation at CASC Industry Day 2018, Imperial College London. 12 January 2018, London, UK.

13. **Lerdprom, W.,** *SPS, Microwave, Flash sintering; do they really work for porcelains?* Oral presentation at UK Ceramics Talent, Queen Mary University London. 10 October 2018, London, UK.

Awards

1. Travel grant to attend MS&T2016—awarded by the Armourers & Brasiers Gauntlet Trust (October 2016).
2. Travel grant to Uganda for a charity project: Ceramic water filter—awarded by the internal funding of Prof Bill Lee (January 2017).
3. General funds—awarded by the Imperial College London Trust (September 2017).
4. Travel grant to attend PCSA annual meeting and MS&T2017—awarded by the President's Council of Student Advisors (PCSA), the American Ceramic Society (October 2017).
5. Sapphire award in the Graduate Excellence in Materials Science Awards –awarded by the Basic Science Division of the American Ceramic Society (October 2017).
6. UK Outstanding Ceramic Students—awarded by The UK Chapter, the American Ceramic Society (October 2018).
7. Outstanding Journal Reviewer—awarded by the American Ceramic Society (December 2018).

Academic service

1. Editorial member-Journal Council of China Ceramics Industry (2016-2019).
2. Reviewer for Journal of Non-Crystalline Solids.
3. Reviewer for International Journal of Applied Ceramic Technology.
4. Reviewer for Journal of the American Ceramic Society.

Abstract

A porcelain powder was sintered using different rapid sintering techniques including direct sintering (DS), spark plasma sintering (SPS), microwave sintering (MWS), and flash sintering (FS). Densification, phase evolution, and physicomechanical properties of the fully sintered porcelain samples were investigated to improve understanding of the role of particular process parameters.

Densification of the porcelains was controlled by liquid phase formation. Study of the DS revealed that formation of liquid glass is rapid even at 780 °C/min heating rate, and the porcelain was fully densified within 15 min dwelling at 1175 °C. SPS enhanced densification rate about 10 times greater over that of conventional sintering, starting at 920 °C. The dwelling step was negligible due to the rapid flow of the liquid glass filling the pores, assisted by the applied pressure. On using microwave energy, the sintering temperature of the porcelain was reduced by ~75 °C and dwell time from 15 min to 5 min compared to conventional sintering. Formation of the liquid phase was observed at 900-1000 °C and it was the key for the rapid densification because it promoted microwave absorbability. Densification in FS was difficult to resolve, but it could be deduced that by applying an electric potential of 1.5 kV/cm for 30 seconds, large amounts of glassy phase were produced.

Various microstructures were observed as a result of the different processing routes. DS and MWS produced a typical porcelain microstructure which is dense but has numbers of residual pores embedded in the glassy phase. SPS produced a highly dense microstructure with a few residual pores assisted by applied pressure. FS, in contrast, produced a nonuniform microstructure containing under-sintered, well-sintered, and over-sintered regions due to localised melting. Etched microstructures revealed special mullite morphologies. The applied pressure in SPS caused mullite orients perpendicular to the direction of the applied load. SPS also induced mullite dissolution at 1200 °C. Microwave produced fibre-like mullite via a vapour-liquid-solid mechanism having Fe(l) as a catalyst. Flash sintered samples contained dendritic mullite and some mullite needles were formed via a screw dislocation mechanism. However, mullite

crystallite sizes calculated by the Scherrer equation revealed that in fully dense samples from each processing route, mullite crystallite sizes were in a narrow range of 25-40 nm.

Physicomechanical of the porcelains produced using the different processing routes were similar; for example, apparent bulk density ranged 2.35-2.46 g/cm^3 (MWS<DS<SPS), water absorption <0-0.5 wt.% (MWS>DS>SPS), hardness varied 5-7 GPa (MWS<SPS<DS) while fracture toughness varied from 3-6 MPa · m$^{1/2}$ (MWS<DS<SPS).

A comparison of energy consumption during the various sintering routes for this porcelain composition showed that DS consumed ~11 MJ/kg, MWS ~18 MJ/kg, FS ~3060 MJ/kg and SPS ~1612 MJ/Kg. While, the energy consumption listed here must be viewed with caution, the values are useful for comparison of the amounts of energy required for the different rapid sintering processes.

Abbreviations

ABD	Apparent Bulk Density
AC	Alternate Current
AP	Apparent Porosity
BF	Bright Field Image
BFP	Back Focal Plane
BSE	Backscattered Electrons
CS	Conventional Sintering
DC	Direct Current
DCS	Diametral Compressive Strength
DTS	Diametral Tensile Strength
DF	Dark Field Image
DP	Diffraction Pattern
DSC	Differential Scanning Calorimetry
DTA	Differential Thermal Analysis
EDS	Energy Dispersive Spectroscopy
EPAC	Electric Pulse Assisted Consolidation
EU	European Union
FAS	Field Assisted Sintering
FAST	Field Assisted Sintering Techniques
FDA	Finite Difference Approximation
FF	Fast Firing
FS	Flash Sintering
HIP	Hot Isostatic Pressing
HP	Hot Press
HUP	Hot Uniaxial Pressing
H_V	Vickers Hardness
ICDD	International Centre for Diffraction Data
IS	Impedance Spectroscopy
JCPDS	Joint Committee on Powder Diffraction Standards
K_{IC}	Fracture Toughness
LFA	Laser Flash Apparatus

LPS	Liquid Phase Sintering
MWS	Microwave Sintering
PAS	Plasma Activated Sintering
PDF	Powder Diffraction File
PECS	Pulsed Electric Current Sintering
PM	Primary Mullite
SAD	Selected Area Diffraction
SE	Secondary Electrons
SEM	Scanning Electron Microscopy
SM	Secondary Mullite
SPS	Spark Plasma Sintering
SSS	Solid State Sintering
TEM	Transmission Electron Microscopy
VCS	Viscous Composite Sintering
VGS	Viscous Glass Sintering
WA	Water Absorption

Acknowledgements

I will not be standing at this point without these people;

To Prof Bill Lee who is everything during my 1460 days in the UK, without his guidance, patience, and encouragement, this work could not be possible. He always cheers me up when I am confused. It is not just about the academic stuff that he advised, he also indirectly showed how to be effective and a better person. I am honoured to be his no.66 PhD student.

To Dr Doni Daniel Jayaseelan of Kingston University London who countlessly helps me during experiments, writing, publications, and fruitful discussion. He also opened me a door to explore the coating technology.

To Dr Eugenio Zapatas-Solvas who truly deserves my gratitude for introducing me to the collaborators and being a very good mentor.

To Prof Dr Salvatore Grasso, and Prof Mike Reece of Queen Mary University of London who stepped in and supported the SPS experiments and gave valuable recommendations, discussion, and feedback.

To Dr Amparo Borrell, and Prof Maria Salvador of University Polytechnic of Valencia who hosted me the microwave processing and long-term collaboration.

To Prof Richard Todd of University of Oxford, and Dr Wei Ji of Wuhan University of Technology who took a risk on the flash sintering experiments.

To Prof Saiz and Dr Cohen who help to improve the structure of the thesis and having an intellectually stimulating conversation during the viva.

Dr Mahmoud Ardakani, Dr Ecaterina Ware, Mr Garry Stakalls and Mr Richard Sweeney and Mr Benjamin Chan for their kind help with experiments.

To Dr Dan Glymond, Tom Hopkin, Pin Juthapakdeeprasert who helped to read chapters.

To all colleagues at CASC for their help, all their constructive discussions and having those words of support in the good and the bad days.

To Miss Aumaporn Chareonsak who believed and gave a big chance by supporting me with a Cementhai Ceramics Co., Ltd funding. You opened a door for me pursuing a deep understanding of ceramics.

Thanks to my dearest sister, Rodchasa for her endless support and taking care of our parents during my time in London.

To Worraya, Rachata and Rachita Lerdprom for leaving the sweet home in Thailand and travelling with me on this adventurous journey. Thanks for your patience during this 4-year roller—coaster and giving me unconditioned love. This work is also yours.

วิรัช เลิศพรม

March 2019
Staines upon Thames, Surrey, UK

Table of Contents

List of Figures

List of Tables

Chapter 1

Introduction and objective of the research

1.1 Introduction

Sintering is the final process in producing ceramics and has a great impact on the properties of the final products. Sintering requires a high temperature to densify a loose powder compact to a dense ceramic article. Densification needs a high temperature which may also cause grain growth, which may have an undesirable effect on the properties of the ceramics such as lower strength and toughness. Commercial benefit may result from producing ceramics in a more competitive way using lower sintering temperature and so reducing grain growth.

There has been continuous technological development in the sintering of ceramics over the past century. New technologies have been recently introduced with lower energy consumption as well as reduce of grain growth. Researchers have reported that rapid sintering techniques, including direct sintering (DS), spark plasma sintering (SPS), microwave sintering (MWS) and flash sintering (FS) are all beneficial by providing faster heating and cooling rates, lower sintering temperatures, shorter sintering times and smaller grain growth compared with conventional sintering (CS). These new approaches have made a significant contribution in terms of energy reduction as well as reduction of processing time.

Japan, for instance, leads in implementing SPS in the production of ceramics, metallic, and composite components in very short processing times (a few minutes) compared to hours and days using conventional processes [1]. For example, it is reported that SPS reduces power consumption during production of

functionally graded materials (FGMs) i.e. WC-Co by 1/5 to 1/3 of conventional sintering techniques such as pressureless sintering, hot pressing, and hot isostatic pressing [2]. In addition, it is reported that SPS can save significant energy (60 to 70% of total energy) when used to sinter copper-diamond, Cu-W, W, and WC [3].

Comparative study by Rajeswari showed that yttria stabilized zirconia (8YSZ) powder was fully sintered (99% theoretical density) after 2 h dwell at 1550 °C in a conventional sintering process but was fully sintered in SPS at 1250 °C after only 5 min and in 15 mins by MWS at 1525-1550 °C [4].

1.2 Objective of the research

Rapid sintering techniques have been successfully applied to many oxide and non-oxide ceramics, to great benefit such as reduced energy consumption, and processing time. However, there is a lack of research attempting to sinter porcelains using these rapid sintering techniques, therefore this study the effect of DS, SPS, MWS, and FS on sintering of porcelains aims to address this gap. The results obtained by such techniques will be compared with the well-established CS process by means of processing time and temperature, as well as the phase and microstructural development. In addition, this study aims to explain and improve the understanding of densification and phase evolution of a porcelain body under such processes. The results and knowledge gained will have an impact on both academic and industry in terms of reduced energy consumption in porcelain production.

Chapter 2 of this thesis presents research challenges for the whitewares industry. A literature review in Chapter 3 outlines the fundamentals of sintering from solid state sintering to vitrification as well as porcelains including their raw materials, chemical reactions, and phase evolution under a conventional sintering process are addressed. The working principles of the new rapid sintering techniques (SPS, MWS, and FS) and some published research results on porcelains are also reviewed. Chapter 4 summarises experimental methods used in this work and basic knowledge of working principles for each instrument used.

Chapter 5 summaries the porcelain sample properties as a function of temperature (up to 1200 °C). Chapter 6 examines the effect of rapid heating rate (DS) on densification, microstructural evolution and physicomechanical properties

of the porcelain. Chapter 7 gives results of densification, physicomechanical properties and mullite formation under the SPS setup. Densification and mullite formation during MWS are examined in Chapter 8 while the effect of the FS on porcelain is studied in Chapter 9. Chapter 10 further discusses and compares densification, physicomechanical properties, mullite formation, and energy used in each technique. Finally, Chapter 11 gives overall conclusions of this work and suggestions for future work.

Chapter 2

Current challenges for the whitewares industry

Whitewares, which are eathernware, stoneware, porcelain and china, have a rich history of impact on human civilisation, and are widely used from simple household appliances, such as tableware, cookware, and building materials—wall/floor/roof tiles, sanitaryware, to scientific and engineering applications such as laboratory-wares and electrical insulators. From an economical perspective, in 2016 the EU-28 (the major ceramic producing countries, Italy, Germany, Spain, France, the UK, Poland, Portugal and Austria) accounted for 25% of global ceramics production, which was worth €28 billion of which whitewares shared about 66% [5]. On a global scale, whitewares were produced in massive quantities, for instance, 13,056 million m^2 of ceramic tiles (including wall and floor tiles) were produced worldwide. Global production of sanitaryware reached 137.60 million pieces or 2.9 million tons in 2016 and the global demand is still growing [6,7].

There are several significant current developments in the whitewares industry such as changing from wet to dry processing, extrusion to dry pressing, double firing to single firing, pressureless casting to high pressure casting and screen printing to digital ink-jet printing decoration. Whitewares research still mainly focuses on the processing, raw materials, microstructural evolution, and properties to improve understanding of the forming operations, defect elimination, microstructure control, and mechanical properties. Recently, the whitewares research field has been extended to the area of additive manufacturing [8], functional glazes such as self-cleaning, anti-bacterial [9-11], thermochromic whitewares [12], extra-large, thin and light weight porcelain stoneware tiles [13].

Additive manufacturing or 3D-printing of whitewares has been successfully demonstrated by a number of research groups such as those at Alfred University and Bowling Green State University (USA) [14], and the University of the West of England (UK) [14]. Moreover, 3D printing machines are commercially available for producing whiteware products such as the WASP clay extruder (Italy), 3D Potter Bot (USA), LUTUM 3D Clay printer (Netherlands) [8]. 3D-printing technology of whitewares allows artists, designers, and consumers to produce whiteware objects with ease and freedom of shape complexity. However, the whiteware body needs to be reformulated since the clay negatively affects the printing process because clays need time to set causing an unstable printed structure and shift during printing. Thus, replacing clays with non-plastic materials, adding organic binders and a well-controlled particle distribution of the mixture, are key to making 3D printing of whitewares possible [8].

Due to a better understanding of nanotechnology, the addition of a photocatalytic material, i.e. TiO_2 into the outer surface of whitewares, by means of coating, allows these surfaces to have more functionality, such as water and air purification, self-cleaning, anti-bacterial behaviour, decomposing atmospheric pollution, and self-sterilization. The coatings also provide a good aesthetic appearance because they are transparent thanks to the incorporation of nano-size particles [9-11].

Light weight and thin porcelain tiles are beneficial for both production and application. Light weight and thin (3.5 mm thick) porcelain tiles are easy to install and 1/3 of the weight of traditional tiles, but they can be as large as 1x3 m^2. For the production side, thin tiles require less raw materials to be used, less energy consumption, and lower CO_2 emission [13].

These examples reflect the final application of whitewares by adding functionality on their surface and making them more aesthetically pleasing. Nevertheless, the driving factor for making the whitewares industry more competitive, is to reduce energy consumption. The energy cost of a range of ceramic products reported by the British Ceramic Confederation such as bricks, roof tiles and drainage pipes, tableware, giftware, sanitaryware, wall and floor tiles, refractories, technical ceramics (sensors, filtration, prosthetics, armour, wear

components, and abrasives is 30 % of the total cost (firing temperatures between 900 and 2750 °C) [15]. In Spain, in addition, the energy cost during tile manufacture is about 15-20% of the total manufacturing cost [16-18] and the firing cost in tile manufacturing covers about 55% of this total energy cost [16].

Therefore, a vital area of research within the whitewares industry is the firing process. Most recently, researchers have attempted to shorten firing cycles and reduce firing temperatures by adopting Field Assisted Sintering (FAS). Lucideon Co., Ltd, Stoke-on-Trent, UK reported that they successfully developed a commercial FAS kiln, which has the potential to revolutionise the firing of whitewares [19].

Chapter 3

Literature review

3.1 Chapter review

This chapter reviews current understanding of the sintering of ceramics including solid state sintering, liquid phase sintering, and vitrification. It also introduces field assisted sintering techniques (FAST)—spark plasma sintering (SPS), microwave sintering (MS), and flash sintering (FS). Porcelains, including their raw materials, and phase evolution on conventional sintering, are also addressed. Examples of densification behaviour and physical properties of porcelains sintered by different FAST techniques are also reviewed to establish a background for this research. Many of the results presented in the following chapters are developed from this current understanding.

3.2 Sintering of ceramics

Sintering is a key process in ceramic manufacture because the properties of the finished products depend on an interplay of raw materials and sintering conditions (time, temperature, pressure, and atmosphere). Different types of ceramic products require different sintering conditions to obtain the desired properties. The thermal energy required to convert porous compacted powder (initial state of high free energy) to the consolidated dense body (the final state of lower free energy) varies for different ceramics. Different ceramics use different mass transport mechanisms to complete their densification including e.g. vapour phase, liquid phase, volume diffusion through a crystal, or viscous flow of a glass [20]. Fig. 3.1 illustrates different types of ceramic products and their sintering temperatures. Silicate ceramics or traditional ceramics, for example, are in the

range of 800-1500 °C (via liquid phase sintering, vitrification) while advanced ceramics (oxide and non-oxide ceramics) require higher sintering temperatures of 1200-2000 °C (predominantly via solid state sintering)[21].

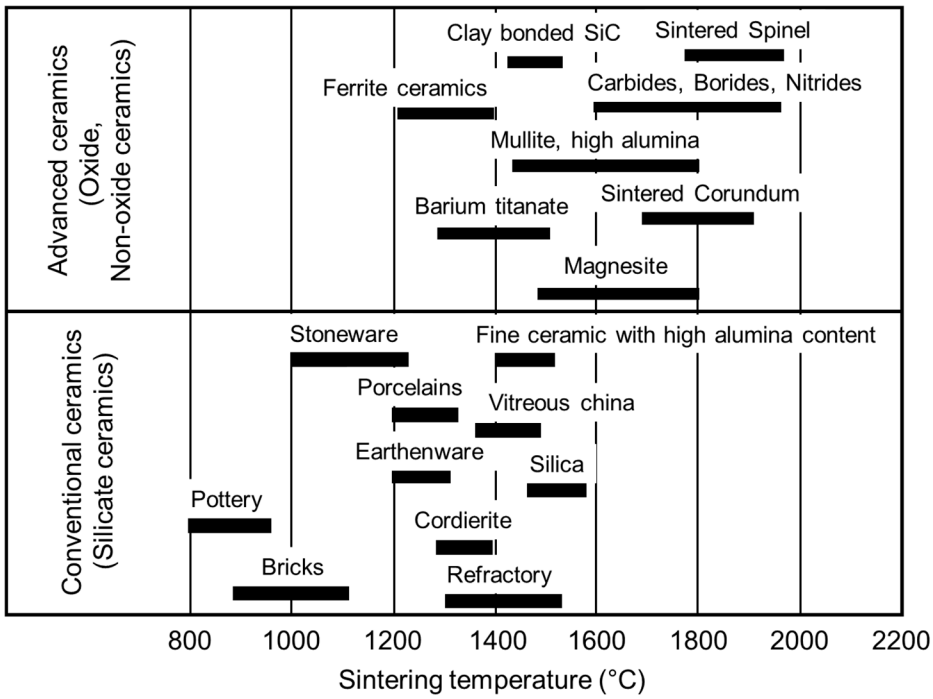

Figure 3.1: Ceramic products and their sintering temperatures [adapted from Ref. 21].

3.3 Fundamentals of sintering

Sintering is defined as a process of elimination of pores located between particles in powder compacted. It involves the shrinkage of the component and grain growth. From the thermodynamic point of view, sintering is a process of surface free energy reduction, from porous compacted powder to the consolidated dense body. There are different types of sintering depending on the relationship between the three components (solid particles, liquid phase, and porosity), including (*(1) solid state sintering (SSS), (2) liquid phase sintering (LPS), (3) viscous glass sintering (VGS), and (4) viscous composite sintering (VCS)* [22].

In summary, solid state sintering involves only solid and pores, e.g. sintering of alumina while liquid phase sintering involves solid, liquid (<20 vol.%) and pores. An example of liquid phase sintering is the sintering of Si_3N_4 with 5-10 wt.% of Y_2O_3, SiO_2 and Al_2O_3 added. The sintering type involving only liquid and pores is the viscous glass sintering which can be seen in glazing and

enamelling. Viscous composite sintering is similar to the liquid phase sintering, but a greater liquid content (>20 vol.%) is used to densify the samples, this is seen in whitewares production [22].

3.3.1 Solid state sintering

Solid state sintering of single phase ceramics provides the foundation of our understanding of sintering. Consider a compacted porous powder of a single phase ceramic is heated; the porous powder becomes a dense and strong compact. The driving force for sintering is the reduction of surface area by densification and grain growth. Densification reduces the surface area of the loose powder compact by reducing the solid-vapour (pore) surfaces with increased solid-solid grain boundary. Grain growth reduces the number of grain boundaries (grain boundary area) to lower the energy of the system.

In the global (macro) scale, sintering is monitored using densification (development of sample's density) or shrinkage of the sample as a function of temperature (Fig. 3.2). The plot of sample's density against firing temperature is a common plot to study the sintering process. From the plot in Fig. 3.2, the sintering can be distinguished into three stages: initial, intermediate and final.

Fig. 3.3 schematically presents the three stages of solid state sintering. *The initial stage* of solid state sintering (Fig. 3.3b) involves the rearrangement of particles at a global scale and neck formation at a local scale. Particle rearrangement is the movement and/or rotation of particles increasing the numbers of contact points leading to neck formation. During the initial stage, densification is relatively small compared to the other two stages as there is no significant mass transport. *The intermediate stage* (Fig. 3.3c) involves increasing neck area, from sharply concave to moderate concave, and formation of interconnected pores. At the intermediate stage, significant densification is observed as presented in Fig. 3.2. Densification occurs by shrinking the pores as well as by grain growth. Since the necks and grains continue to grow, the pores become isolated indicating the *final stage of sintering* (Fig. 3.3d).

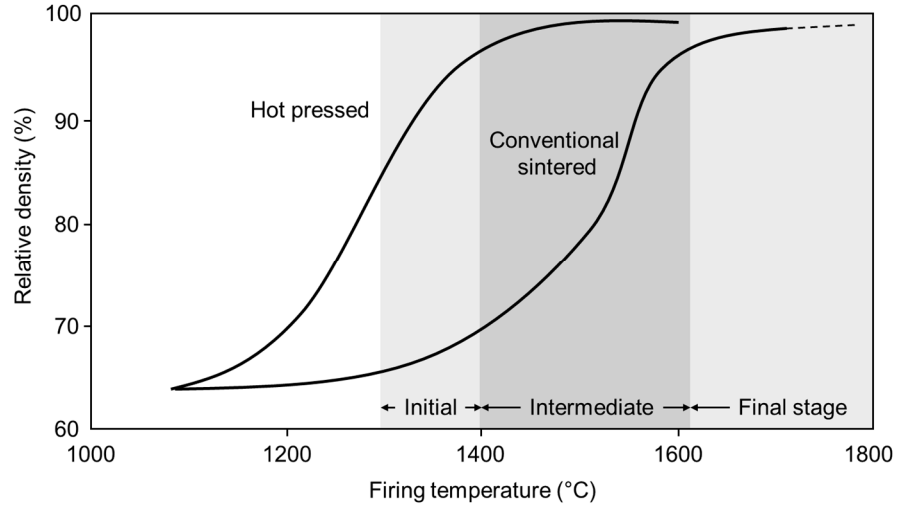

Figure 3.2: Sample density against firing temperature is commonly used to study the sintering process [22].

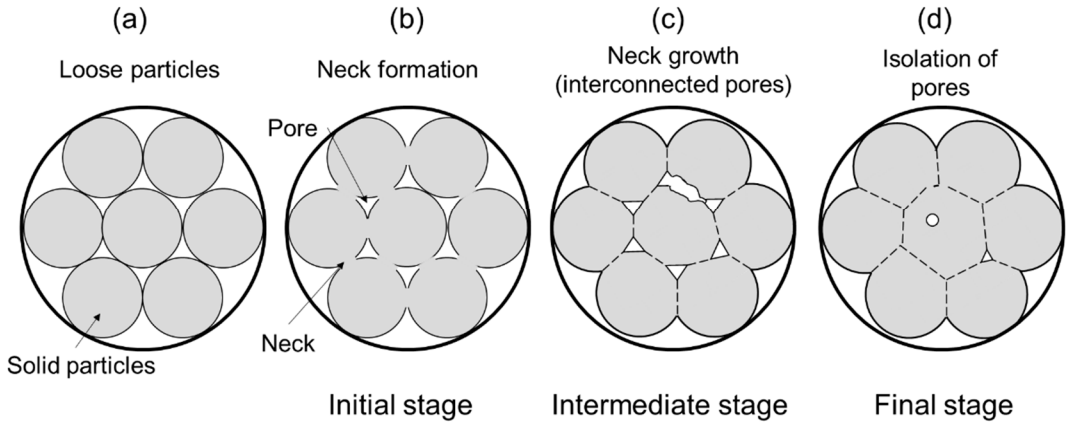

Figure 3.3: Development of the sample microstructure during sintering shows the sintering stages [author's figure].

At the local scale (Fig. 3.4), consider two spherical particles in two dimensions connecting each other, the minimum surface free energy of the system is obtained when the contact angle between the two particles or dihedral angle (φ_e) is in equilibrium which is mathematically expressed by Eq. 3.1

$$\frac{\gamma_{ss}}{\gamma_{sv}} = 2\,cos(\frac{\varphi_e}{2}) \tag{3.1}$$

where γ_{ss} is the specific grain boundary energy (solid-solid), γ_{sv} is the specific surface energy of solid particle and vapour phase (solid-vapour) [23-25]. The dihedral angle is solely defined by the interfacial energies and it is independent of

the pressures in the phases. In other words, the dihedral angle is constant, regardless of the pressure of vapour phase [23].

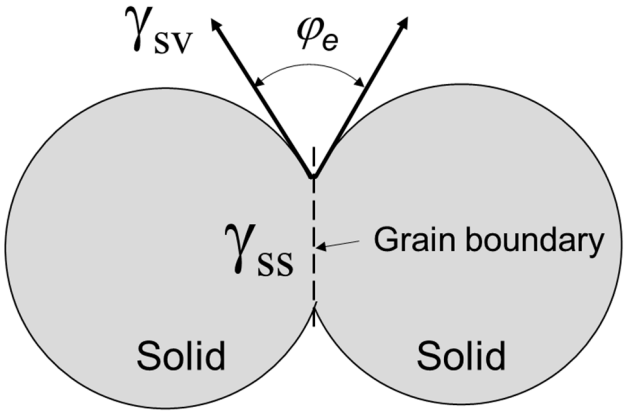

Figure 3.4: Two-dimensional schematic diagram of the solid particles represents dihedral angle [adapted from Ref. 23].

3.3.1.1 Mass transport mechanisms

The driving mechanism for sintering process is provided by mass transport. The two main mass transport mechanisms are *surface transport and volume transport*, each of which differently contributes to the sintering. Surface transport including surface diffusion and vapour transport (evaporation-condensation) occur at the particle surfaces generating neck growth but contribute little to densification while bulk transport including volume diffusion, grain boundary diffusion, and transport via dislocations result in shrinkage of the sample because the mass flow is within the interior. Fig. 3.5 illustrates the driving mechanism provided by the different mass transport processes on sintering. Mass comes from different paths—surface or interior—but always sinks at the neck because of the effect of different surface curvatures.

The surface curvature plays an important role in reduction of surface free energy because the different curvatures provide different vapour pressure and chemical potentials, these chemical potentials drive atomic diffusion. Consider the numbers of atoms and vacancies on the curvatures; the convex (positive curvature) (Fig. 3.5a) has higher chemical potential compared to a flat surface (a reference surface), and when the two particles join, they create a neck which is concave

(negative curvature) (Fig. 3.5b). The diffusion of atoms then moves from convex site to the concave site and the vacancies move in the opposite direction.

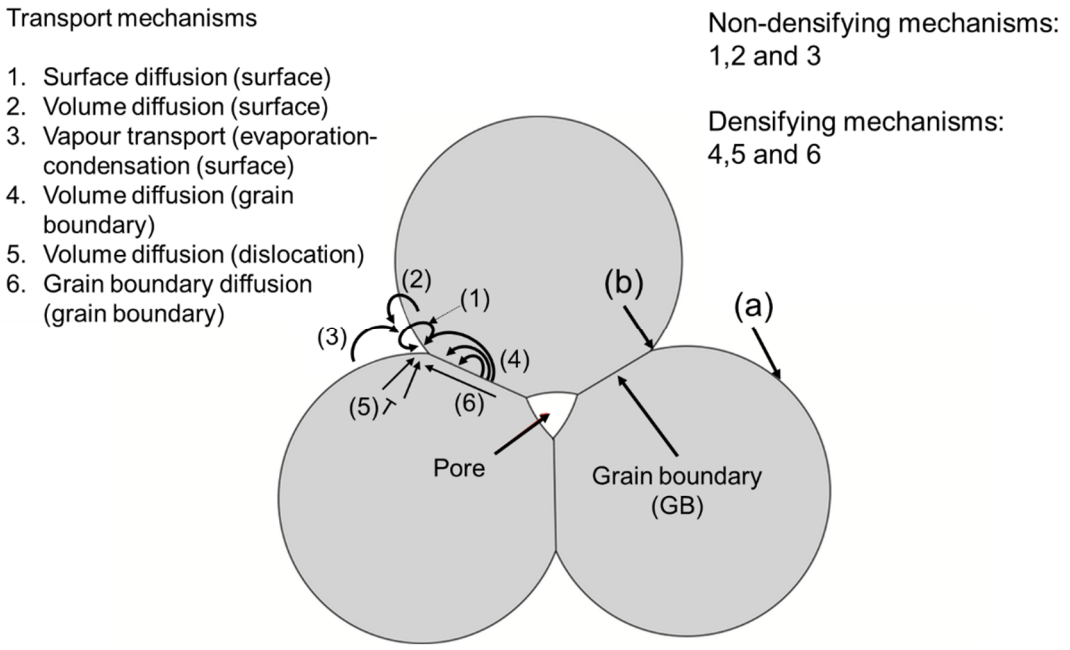

Figure 3.5: Schematic representation of mass transport mechanisms in polycrystalline ceramics [22].

3.3.1.2 Grain growth

As previously mentioned, sintering involves shrinkage and grain growth. Grains with curved surface always either shrink or grow depending on the curvature types and their number of surrounding grains. A two-dimensional model in Fig.3.6 shows that grain boundaries always move towards their concave of the curvature so the grains with concave curvature (considered from their centres) tend to shrink but the convex grains tend to grow (Fig.3.6a). In the case of number of surrounding grains (Fig. 3.6b), grains having more than 6 surrounding grains are convex (labelled as no. 10 and 50) and grains with less than 6 surrounding grains are concave (labelled as no.3 and 4). Thus, the grains with more than 6 surrounding grains tend to grow and vice versa. The grain labelled as no.6 is the ideal case which has six boundaries and no boundary curvatures making the grains stable.

The grain labelled as no. 50 in Fig. 3.6b can also represent abnormal grain growth. In general, abnormal grain growth occurs when most boundaries of a grain

are immobilised while one boundary is not constrained making this boundary free to move. However, the abnormal grain growth can be inhibited by the presence of pores, second phase or inclusions at the grain boundary. As the grain boundary moves (to reduce the free energy), the free energy is decreased when it reaches the pore, inclusion or the second phase. In other words, the grain boundary drags these obstacles and becomes less mobile. In addition, second phases can inhibit grain growth because mass transport (diffusion) from the grain boundary to the second phase is more favoured than diffusion to move the grain boundary.

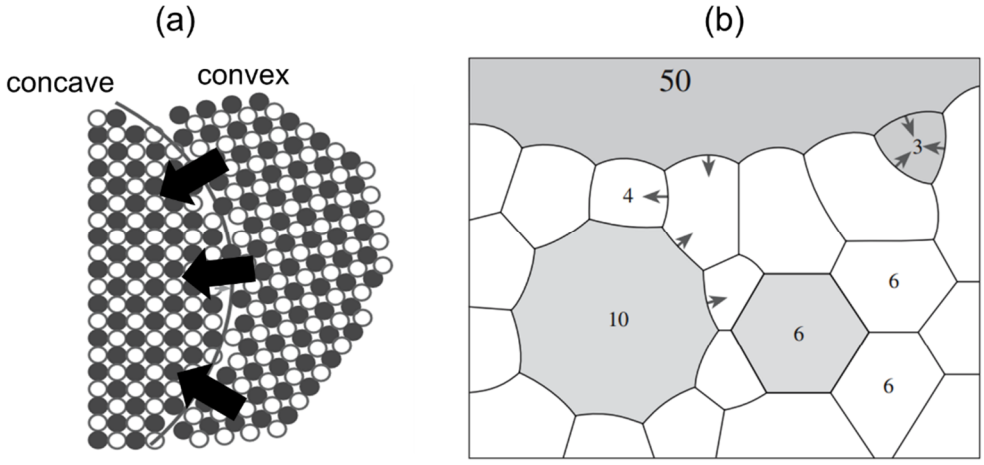

Figure 3.6: (a) Schematic diagram shows grain boundary moving towards concave curvature, and (b) different grain boundary curvatures produced by surrounding grains [22].

3.3.2 Liquid phase sintering

Most commercial ceramics are produced by liquid phase sintering because the presence of liquid phase during sintering process can densify ceramics at lower temperature compared to solid state sintering. The liquid phase provides a high diffusivity path and causes capillary forces that pull the solid particles together, enhancing densification. However, to achieve an effective liquid phase sintering, the liquid must spread over the solid particles, which is explained by the wetting behaviour.

Fig. 3.7 presents the interactions between solid particles and liquid phase showing wetting behaviours. The wetting behaviour can be explained using the contact angle between a solid surface and the tangent of liquid surface, expressed by Eq. 3.2.

$$\gamma_{sv} = \gamma_{sl} + \gamma_{lv}cos\theta \tag{3.2}$$

The wetting behaviour of the solid-liquid is represented by their interfacial energy (γ_{sl}). The liquid phase wets a solid particle when the contact angle is <90°. In the ideal case, which the contact angle is 0, the liquid phase completely wets the solid particles as presented in Fig. 3.7a. If the solid-liquid interfacial energy is high, the liquid does not spread over the solid particles producing poor wetting behaviour (Fig. 3.7c).

In contrast, if the solid-vapour interfacial energy (γ_{sv}) is high, the liquid tends to spread over the solid particles to lower the solid-vapour interfacial energy (Fig. 3.7b). In other words, the driving force for liquid phase sintering is the reduction of solid-vapour interfacial energy by the solid-liquid interfacial.

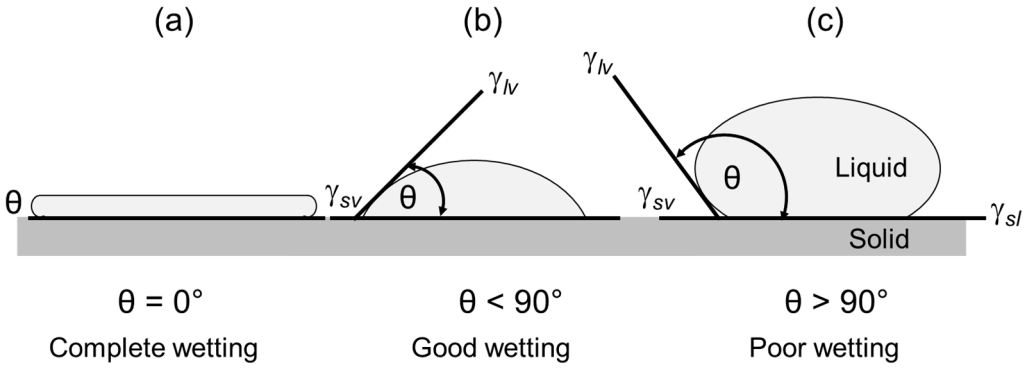

Figure 3.7: Wetting behaviours of the liquid phase in solid surface [adapted from Ref. 20].

During sintering, the liquid phase also interacts with the solid particles changing the chemistry of the liquid which may change its wetting behaviour. Thus, transient liquid phase sintering is often observed because the liquid phase can disappear by incorporating into the solid particles or it de-wets the solid particles (chemistry changed) and stays at either grain boundaries or grain junctions.

The stages in liquid phase sintering are different from the stages of solid state sintering. Starting with the loose particles compacts (Fig. 3.8a). *The first stage* involves *rearrangement* of the solid particles (Fig. 3.8b). This rearrangement of the solid particles is rapid (compared to the same stage of solid state sintering)

when the liquid phase forms because the solid particle can easily rotate and slip over other particles. *The second stage* is called *solution-precipitation,* which involves dissolution of the solid particles into the liquid phase. Grains can grow by two ways including Oswald ripening and/or reprecipitation (Fig. 3.8c).

Oswald ripening occurs when smaller particles dissolve in the liquid phase and redeposit on the larger particles because the smaller particles have high surface energy and they need to reduce the high surface energy by reprecipitation onto the larger one. If the solid particles dissolve in the liquid phase, solute reprecipitation takes place if this is thermodynamically possible leading to grain growth.

The *final stage* of liquid phase sintering is *coalescence,* elimination of closed porosity (Fig. 3.8d). In this stage, densification is slow and eventually stopped because grain growth (from the second stage) produces a dense solid bulk, and only closed pores are present. Closed pores can be eliminated by buoyancy driven pore migration. However, bloating can occur if closed pores remain in the liquid phase and the internal pressure of the gas in the pore increases.

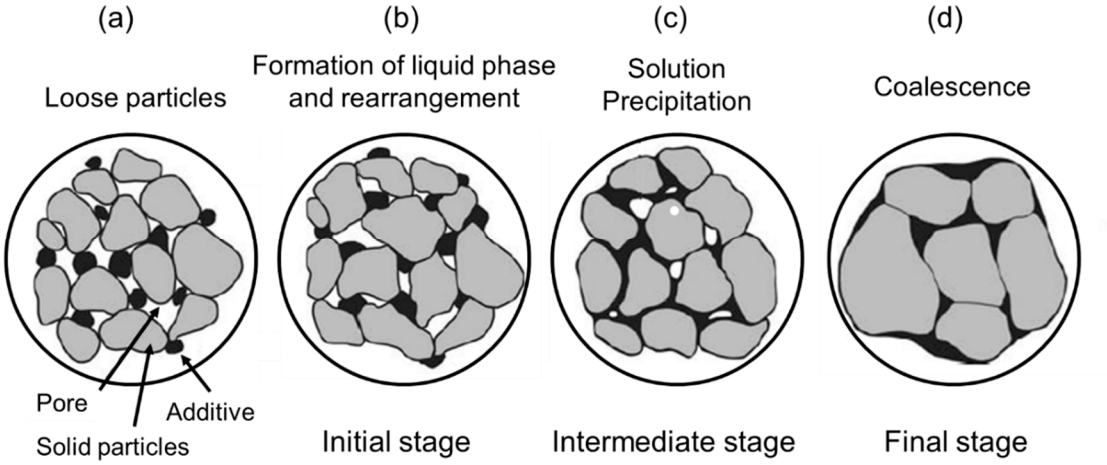

Figure 3.8: Development of the sample microstructure during liquid phase sintering shows the sintering stages [22].

3.3.3 Vitrification

Vitrification is the typical method to produce whiteware products. Vitrification is similar to liquid phase sintering, but the liquid content is larger (>20 vol. %. liquid compared to ~5 vol.%. in liquid phase sintering). Vitrification

enhances densification not only by producing the capillary force but also by flow of the large amount of liquid and filling of pores between the solid particles (viscous flow).

The flow of liquid phase during vitrification is governed by the three factors including surface tension of the liquid phase (γ), viscosity of the liquid phase (η), and pore size (a). Surface tension affects wetting behaviour as previously described in liquid phase sintering. However, the effect of surface tension of the liquid phase can be negligible since it does not significantly change with the chemistry over the firing temperature range of whitewares (1200-1400 °C). In contrast, the viscosity of the liquid phase changes with the chemistry and temperature. The densification rate (ρ) during vitrification can be predicted by Eq. 3.3.

$$\rho \sim \frac{\gamma}{\eta a} \tag{3.3}$$

Since there is a large volume of liquid phase involved, significant dissolution and crystallization of new phases are also possible. For example, quartz dissolution and mullite formation are commonly found in whitewares. However, the presence of large volumes of liquid during vitrification may lead to deformation of the products by so-called pyroplastic deformation [20].

3.3.4 Pressure assisted sintering

To sinter a ceramic compact powder with an externally applied pressure is called *pressure assisted sintering*. The applied pressure enhances densification by providing additional force as well as increasing the rate of particle rearrangement, plastic deformation, and viscous flow. There are three types of pressure assisted sintering including hot uniaxial pressing (HUP), hot isostatic pressing (HIP), and sinter forging (SF). In brief, hot uniaxial pressing applies uniaxial pressure to the powder in a die while sinter forging uses uniaxial pressure but no die. In hot isostatic pressing, isostatic pressure is applied to the sample in all directions via pressurized inert fluid (gas or liquid).

3.4 Development of rapid sintering techniques

New sintering techniques have been successfully applied to sinter 'hard-to-sinter' materials including fast firing (FF), hot press (HP), spark plasma sintering (SPS), microwave sintering (MWS) and flash sintering (FS) all of which have been beneficial by providing faster heating and cooling rates, lower sintering temperatures, shorter sintering times, and smaller grain growth, compared with conventional sintering (CS) [20,26-30]. These new approaches have made a significant contribution in terms of energy reduction. Fig. 3.9 presents development of sintering process in terms of time and temperature. The processing time can be reduced to minutes or even seconds instead of hours in conventional sintering process.

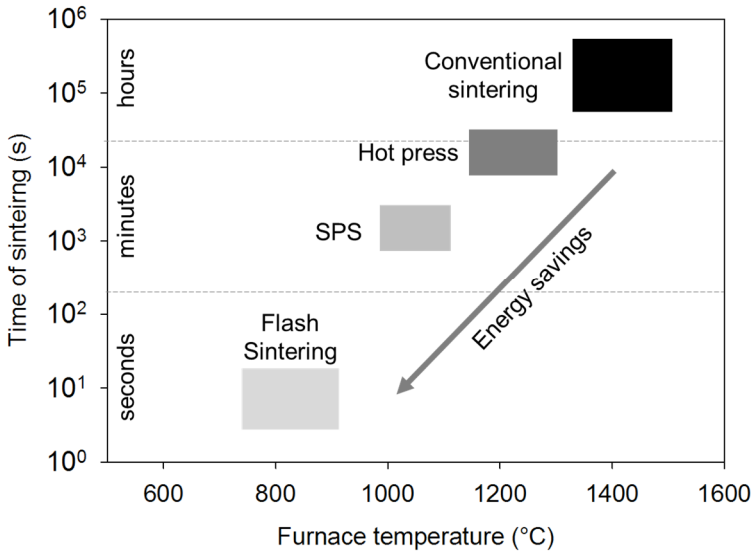

Figure 3.9: Development of advanced sintering techniques in terms of time, furnace temperature and energy consumption [adapted from Ref. 31].

3.5 Fast firing (FF)

The term 'fast firing' in ceramic manufacture was introduced in 1965 with the concept of optimum firing cycle [28]. Fast firing is used to sinter various ceramic materials such as lead zirconate titanate (PZT) [28,32-34], alumina [35, 36], clay bricks [37], tiles [38], and red clay products [39]. It has been reported that the final properties of fast-fired products are comparable with the conventionally fired products [38,39]. In modern porcelain manufacturing, for instance, the fastest sintering cycle times are 35 minutes for mosaic tiles, 40 minutes for wall

tiles, 60 minutes for porcelaneous-stoneware floor tiles, 7 hours for sanitaryware, and 2 hours for dinnerware (Fig. 3.10) [28].

The fast firing process has been used to produce porcelain tiles for more than 30 years. It is applied extensively in the porcelain industry because it substantially reduces production cost by consuming energy more efficiently [40, 41]. Development of the porcelain fast firing process required knowledge of raw materials used, chemical reactions and microstructure development during the firing process [42]. In addition, several factors are involved in the fast firing development including work piece thickness, thermal expansion, sintering rate, the kiln furniture used, kiln design, microstructure development, carbon and organic substances burnout, and shape of work piece [40].

Fig. 3.10a illustrates a typical roller kiln with 90 m long used to produces porcelain tiles. It presents an example of temperature profile and processing time (Fig. 3.10b). This kiln uses energy efficiently because fuel is only used in the firing zone, the preheated zone uses hot air flow from the firing zone via flue gas.

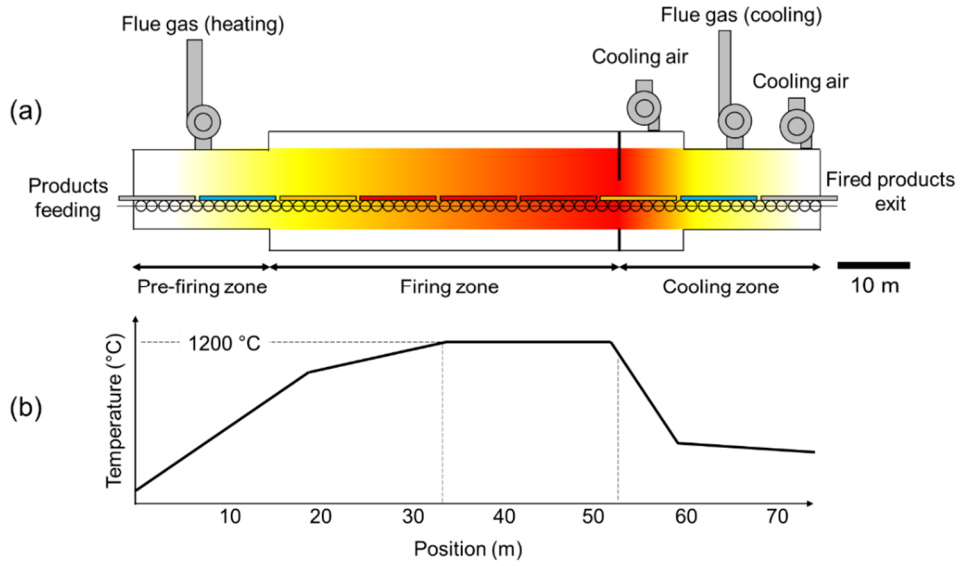

Figure 3.10: (a) Schematic diagram of a roller kiln for a fast firing process, and (b) an example of temperature profile in a roller kiln [16].

3.6 Spark plasma sintering (SPS)

Field Assisted Sintering Technology (FAST), Pulsed Electric Current Sintering (PECS), Electric Pulse Assisted Consolidation (EPAC), and Plasma Activated Sintering (PAS) are alternative names for Spark Plasma Sintering

(SPS) [43]. SPS is defined as a consolidation process of powder utilising a low voltage of pulsed (on-off) direct current (DC), and externally applied pressure. SPS is similar to a hot uniaxial pressing (HUP) process; both techniques employ uniaxial pressure, and graphite dies to improve the sinterability of powder, but the heat supply source is different. In SPS, powder is loaded in a set of conductive dies—normally made of graphite. Pulsed DC current is applied to the graphite die, then heat is generated by resistive heating or 'Joule heating' in the die and then heat transfers to the sample. Unlike SPS, powder in a graphite die in hot pressing is sintered by conventionally radiative heat. The advantages of SPS over HUP are (i) rapid heating and cooling rates (500 °C/min or faster depending upon the sample size) by volumetric heating (in case of conductive materials), (ii) shorter and lower temperature in sintering process resulting from applied pressure and Joule heating, and (iii) smaller grain size is obtained due to lower activation energy of consolidation process [27,44-46]. Many materials are successfully sintered using SPS, for instance, metal alloys, pure metals, ceramics, composites, functionally graded materials, semiconductors, and thermoelectric materials.

Since graphite is required in the SPS process, graphite contamination must be considered. Graphite is considered to be chemically inert and it can be used at high temperature up to 2200 °C under inert or vacuum atmosphere [47] but it can be oxidized if exposed to oxidising atmosphere above 1200 °C [20]. Graphite can also react with metal oxides to form carbides at certain temperatures such as with SiO_2 at 1250 °C, Al_2O_3 at 1350 °C and Fe_2O_3 at 485 °C. However, these reactions occur when metal oxide powder and graphite are mixed together in stoichiometric proportion [47].

Graphite contamination can also be found at the sample surface because during sintering carbon can diffuse into the sample over short distances (~10 μm) e.g. for SmCo based magnets produced by SPS using 100 °C/min heating rate, 1100 °C sintering temperature, 5 min holding time and a maximum pressure of 51 MPa [49]. Carbon uptake by the sintered samples during SPS becomes more significant at high sintering temperatures (>1550 °C) [27]. At lower temperature (<1550 °C), the carbon-contaminated layer either did not form or was so thin, which can be removed easily from the sample's surface [27]. It has been reported

that at the fast heating rate used by SPS, the interaction between the sintering samples and graphite tools can also be reduced due to the short time for carbon diffusion [27]. Carbon contamination can also be addressed by placing Ta foil between the graphite die and sample to prevent carbon diffusion into the samples [50]. A practical approach used to get rid of carbon contamination is to polish the surface of the sample with diamond paper [27].

A problem of the use of graphite, in addition, is the reactivity of graphite towards the ceramic sample leading to sticking at the contact of the die and sample surface. However, this problem can be resolved by coating the inside die wall with boron nitride but not above 1350 °C because at this temperature boron nitride can react with the graphite foil used as a liner to prolong the life of the die [48].

3.6.1 Working principle

A mechanical loading system—uniaxial pressing is simultaneously applied with low voltage pulsed DC current (typical below 10V applied constantly to the whole set-up) produce high currents (typical from 1 to 10 kA) leading to 'Joule heating' in the graphite die. It is believed that this process generates spark discharge at the particle contact points, and the local temperature at particle contacts can be several thousand degrees Celsius.

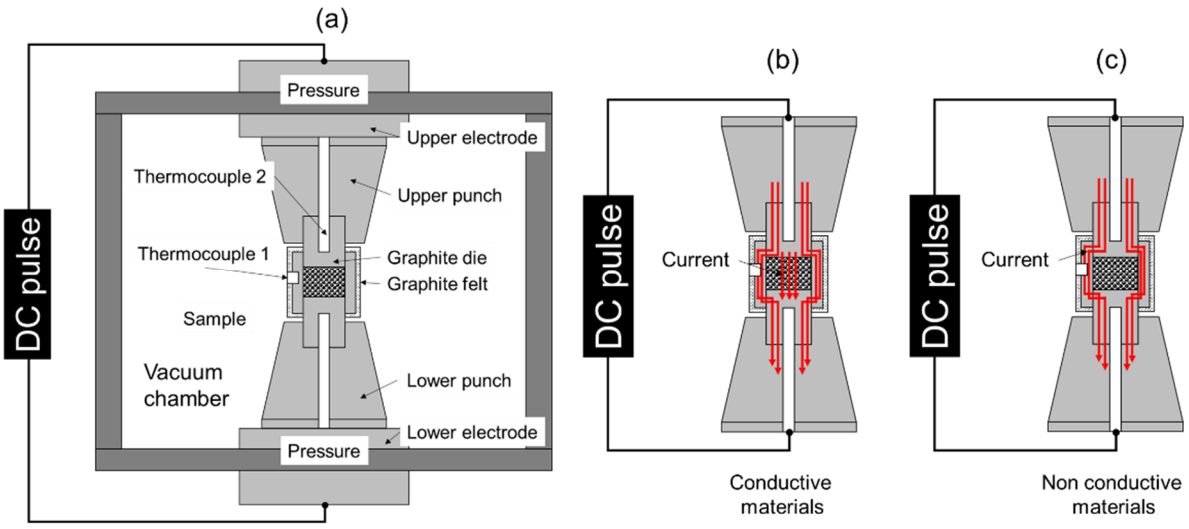

Figure 3.11: (a) Schematic diagram of a typical SPS apparatus, (b) current passes through a conductive sample, and (c) current does not pass through a non-conductive sample [author's figure].

Fig. 3.11a shows a typical SPS unit. SPS can reduce sintering temperature by 200-500 °C compared with conventional sintering process. In the case of conductive materials, Joule heating also takes places volumetrically in the sample bulk because current passes through the sample body (Fig. 3.11b). However, in the case of non-conductive materials, heat transfers quickly and efficiently from graphite die to sample body and no current passes through the sample (Fig. 3.11c).

3.6.2 Process parameters

Effect of pressure—when a compact powder is heated under applied pressure, higher consolidation rate can be achieved compared with the same sintering parameters when pressureless sintering [15]. Typical pressures used in SPS are less than 200 MPa because of strength the limit of the die materials such as graphite (70 MPa), zirconia (100 MPa), and SiC (280 MPa). The uniaxial pressure has a mechanical effect on the particle re-arrangement, destruction of agglomerates, and collapse of large pores [41]. The presence of an externally applied pressure can increase densification rate as presented in Eq. 3.4 [20].

$$\frac{d\rho}{(1-\rho)dt} = B(g\frac{\gamma}{d_p} + P) \tag{3.4}$$

where ρ is the density, t is time, B represents the term of diffusion coefficient and temperature, g is geometric constant, γ is surface energy, d_p is particle size parameter, and P is applied pressure. The applied pressure also influences the temperature distribution across the punch/die/sample assembly because it introduces significant changes in bulk electric and thermal fields, including Joule heating. For example, increasing applied pressure can reduce the temperature difference in the die as well as in the sample [51].

Effect of electrical field—the effect of electrical field (voltage) influences mass transport, grain boundary migration and related defect formation [52,53]. However, since SPS employs a low voltage the particular effects can be difficult to observe [27]. However, this effect can be significant in high-dielectric materials [54].

Effect of electric current—when electric current flows through a conductive material, Joule heating occurs, and it is speculated that this current induces plasma at the interfaces between the particles. Experiments on SPS were conducted by Zhang et al., [55], Omori [43], and Groza et al., [56] to understand the SPS mechanisms. Based on the results of the direct visual observations and sample microstructure analysis, they believed that spark discharge does indeed occur during the SPS process. The high-temperature spark plasma could be generated in the microgaps due to the discharge effect [43,55,56]. Fast and efficient sintering can be achieved under the combined action of spark discharge, Joule heating, electrical diffusion and plastic deformation effect in the SPS process [55]. Plasma subsequently cleans the particle surfaces resulting in the enhancement of consolidation via vaporisation. However, some have proposed that when the powder in the die is uniaxially pressed, the contact between particles is large and as a result the plasma discharge becomes small [46]. Thus, in this case, there is still no strong evidence of plasma generation in SPS.

Effect of pulsing—the pulse cycle plays an important role in the sintering process, and final properties of the products. For instance, by changing the DC pulse on–off patterns during SPS of ZrB_2, the density, and fracture toughness of ZrB_2 sample changes. Chakraborty et al., reported that that maximum relative density (98.65%) and fracture toughness (4.69 MPa·$m^{1/2}$) of ZrB_2 samples is achieved with 50 ms pulse on and 5 ms pulse off time conditions [57]. In addition, changing the pulse pattern modifies the current peak intensities, and influences the microstructure of alumina-hematite powder. The SPS sintered sample is composed of a Fe-Al_2O_3 composite layer at the outer surfaces (top, bottom and radial), a biphasic core ($FeAl_2O_4$ and Al_2O_3) and a depletion layer without Fe or $FeAl_2O_4$ near the cathode [58]. However, others report that there is no effect of pulsing pattern on the physical properties of SPS-fired material e.g. the growth rate of $MoSi_2$ (using Si and Mo under SPS with different pulse patterns at three temperatures in the range 1070-1270 °C) showed no dependence on the pulse pattern. The reason was that the effect of pulsed current on mass transport across particle–particle interfaces in a powder compact is the same as in the case of a multilayer system [59]. In addition, Al powder was sintered using SPS with

different pulse frequency. Xie et al., concluded that the effects of pulse frequency on densification, deformation and microstructure of the Al compacts sintered by SPS were not significant because the change of activation energy of densification at different pulse frequency was insignificant for the pulse frequencies ranged from 0 Hz to 40 kHz [60]. However, it is evident that even though pulse patterns are different, the amplitude of the pulse (the voltage) either increases or decreases to compensate the power requirements under the particular temperature. In other words, the root mean square of the current is independent of the changing pulse pattern [59].

3.7 Flash sintering (FS)

Flash sintering is an active research topic in ceramics since it was introduced by Cologna et al., [61] and it has been extensively studied and developed by many researchers [62]. A great benefit of the flash sintering process is that highly dense ceramics can be produced within a few seconds. It is hoped to replace the existing sintering processes of ceramics with significant reduction in energy consumption and produces a unique microstructure to improve material technological properties [62-66].

Yu et al., [62] provide an overview of the flash sintering technique stating that "Flash sintering (FS) is an energy efficient sintering technique involving electrical Joule heating, which allows very rapid densification (<60 s) of particulate materials". They also highlighted that many ceramics (i.e. 3YSZ and its composites, 8YSZ and its composites, yttria, and alumina and its composites) were successfully sintered by flash sintering techniques with much shorter processing time compared to conventionally pressureless sintering processes. Yu et al., [62] also mentioned that a large flash sintering furnace (25 m long) has been developed to process conventional floor tiles, which can be operated 300 °C below the conventional sintering furnace. Gonzalez-Julian and Guillon [63] showed that densification rate of alumina sintered via liquid phase using calcium-aluminium-silicate glass was enhanced under an AC electric field because current flowed through the liquid phase at high temperature, enhancing densification by Joule heating and athermal response pf the liquid phase under the applied electric field.

Zapata-Solvas et al., [64] concluded that a novel technique called flash spark plasma sintering (FSPS, use of an SPS machine to perform FS experiments) using an electrically insulated graphite die allowed $MoSi_2$ and ZrB_2/20 vol. % $MoSi_2$ to be sintered in less than 60s at heating rates of 2000 °C/min and consumed much lower energy compared to conventional SPS.

Zapata-Solvas et al., [65] also concluded that SiC with Al_2O_3 and Y_2O_3 as sintering aids can be sintered using flash sintering with low energy consumption at furnace temperatures as low as 1170 °C, 100 V/cm with flash sintering times of 150 s. Cubic nano-SiC can be sintered using SPS at 1700 °C under an applied pressure of 40 MPa. Additive-free-SiC was sintered using SPS at 2200 °C under an applied pressure of 150 MPa. In addition, by using Al_2O_3 and Y_2O_3 as sintering aids, reduces sintering temperatures of SiC to ~1900 °C. Thus, the low furnace temperature and rapid sintering times confirm the commercial advantage of flash sintering SiC with suitable sintering aids and thermal management.

In addition, Cologna et al., [66] presented that flash sintering had an effect on the microstructure of alumina. They found that conventionally sintered alumina specimens had an average grain size of 1.9 μm, while the flash-sintered specimens had a smaller grain size of 0.8 μm.

Heat produced in the sample during flash sintering comes from Joule heating. However it has been also reported that the Joule heating might not be responsible for rapid densification process because the temperature generated by the Joule heating is not high enough to densify a ceramic body [67] but instead the densification of ceramics is due to thermal runaway [68]. Due to the complex interplay between material chemistry, furnace temperature, and applied electric field, various mechanisms during flash sintering including local melting at grain boundaries, pore migration, Frenkel-pair, defect generation, electroluminescence and photoemissions have been proposed [52,69-74].

Flash sintering process involves an externally applied electric field to the sample whereby the mechanisms behind flash sintering are different from a conventional sintering process. It has been reported that Joule heating and dielectric breakdown are possible mechanisms of the rapid sintering rates [75-77].

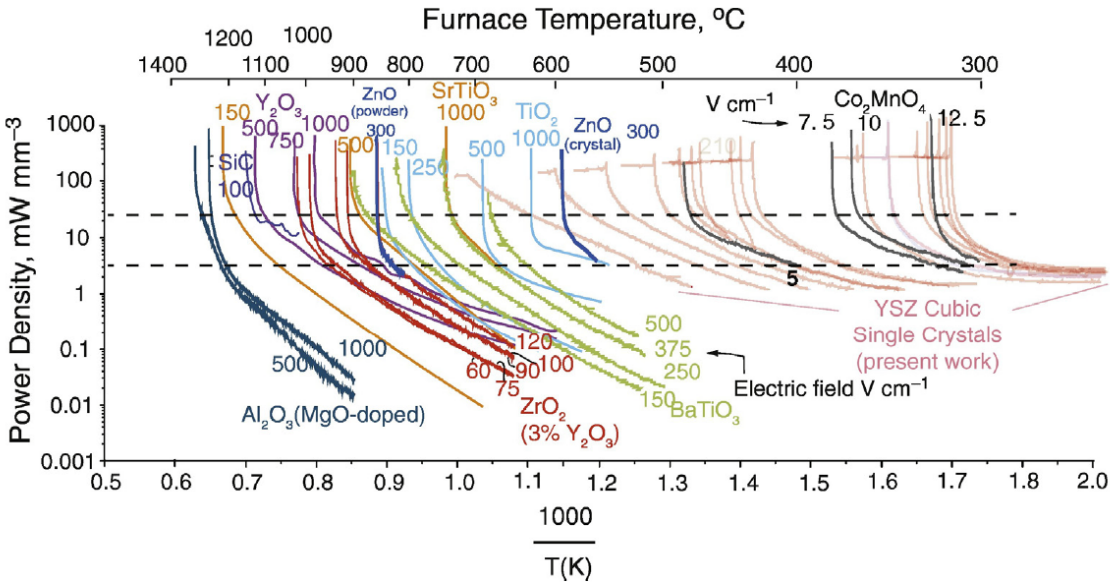

Figure 3.12: Various types of ceramics sintered by flash sintering showing power density and furnace temperature required to trigger flash sintering [78].

Various types of ceramics (ionic conductors, ferroelectrics or semiconductors) have been successfully flash sintered, such as YSZ (3YSZ, 8YSZ) [79-81], Co_2MnO_4 [82], $BaTiO_3$ [83], $SrTiO_3$ [84], TiO_2 [85], ZnO [86], and SiC [65] as shown in Fig. 3.12. Even different parameters and experimental setups were used for different samples, the power required for triggering flash sintering is in a similar range of 10-50 mW/mm^3 as shown in Fig. 3.12 [78].

Composite materials, which contains different volume fraction of phases such as alumina-titania composite [77], alumina doped zirconia [87], SiC whisker reinforced ZrO_2 composites [88], Al_2O_3-$Y_3Al_5O_{12}$-ZrO_2 [89], 90 wt.% alumina-10 wt.% calcium–aluminium–silicate glass [62] and 90 wt.% alumina containing 10 wt.% magnesia silicate glass [90] were successfully flash sintered. However, the secondary phases present in these composites were small (<10 wt.%), hence the mechanism behind the flash sintering of composite materials containing large volume of foreign phases (>10 wt.%) might be different compared with that which occurs in monolithic materials and it is still an open question.

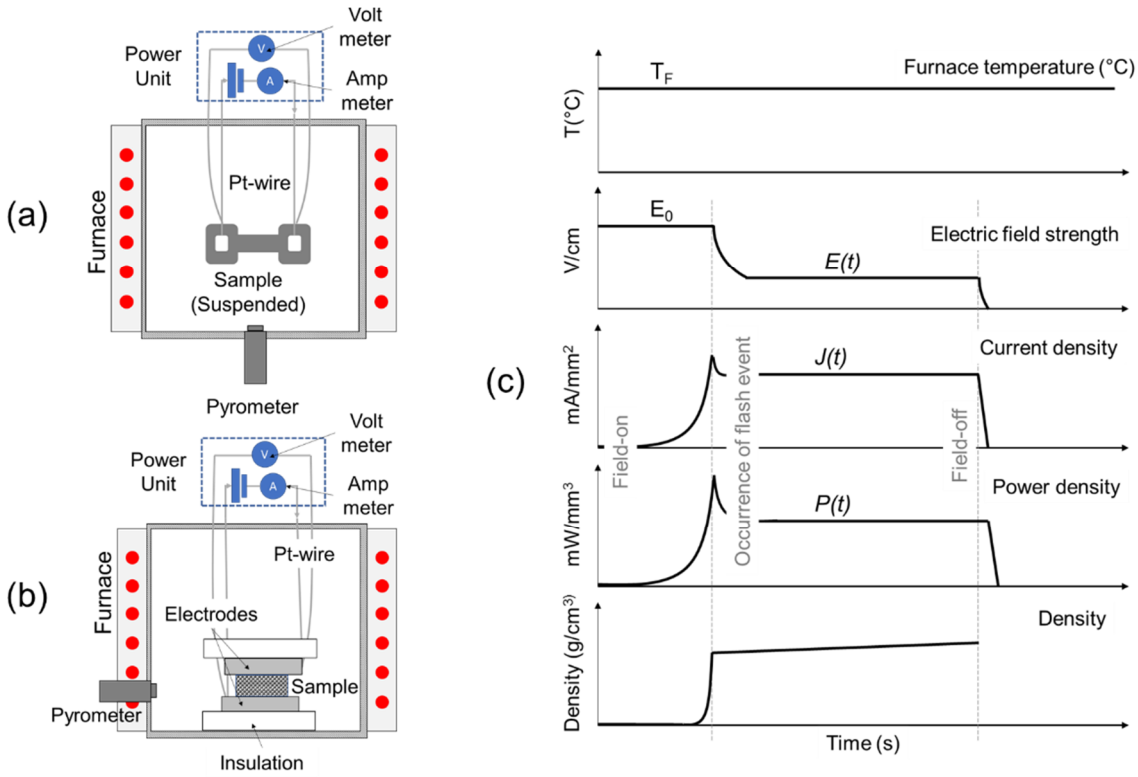

Figure 3.13: (a) A schematic diagram of a flash sintering setup using a dog-bone shape sample, (b) pellet sample, and (c) a typical result of a flash sintering process at a constant furnace temperature [author's figure].

Fig. 3.13a presents a schematic of the flash sintering process (to be discussed in section 3.7.1) and its process parameters (Fig. 3.13b) shows a change of the applied electric field, current density, power density and density of the sample before and after the flash events. Fig. 3.13c represents the typical data acquired from a flash sintering process including furnace temperature, electric field, current density, power density, and sample density. In flash sintering, firstly the furnace temperature is kept constant at T_F, and the electric field (E_0) is then applied before flash event occurs, which is indicated by the rapid increases of current density $(E_{(t)})$ and power density $(J_{(t)})$. The electric field strength decreases after the flash event to maintain the current and power density at the current limit.

3.7.1 Working principle

A green sample either in dog-bone or pellet shape is sandwiched between two metal electrodes to make electrical contact so current flows through the

sample body (Fig. 3.13a-b). At laboratory scale, sample surfaces are coated by conductive paste, usually Pt paste and electrically connected through Pt conductive wires. In the case of pellets, a minimal pressure of ~1 MPa may be uniaxially applied to ensure that both surfaces are properly contacted to the power source. The process control of flash sintering is critical because the material's conductivity changes with temperature resulting in changing power dissipation in the sample.

The furnace temperature can be ramped up (Fig. 3.14a) or kept constant (Fig. 3.14b) while an electric field *(E)* is applied to the sample. Once the applied electric potential and furnace temperature reach an onset point, the flash sintering event occurs indicating a sudden increase of the electric current. The flow of electric current *(J)* must be controlled closely since it can lead to thermal runaway. Generally, a voltage control is used in the first step then switched to a current control when the flash event takes place [77,91].

A constant voltage, which is called 'voltage control step' (labelled as (1) in Fig.3.14c), is applied to the sample being heated under simultaneous increase of furnace temperature (Fig. 3.14a). Once, the furnace temperature reaches an onset value (depending on material characteristics) an abrupt increase of current flow (J) and power dissipation (W) occurs and the process switches to 'current control step' (labelled as (2) in Fig. 3.14c) in order to control power dissipation. The power dissipation during flash sintering expressed by Ohm's law can be divided into two regimes. The first regime, labelled as (3) in Fig. 3.14c is the power dissipation which depends on the magnitude of the electric field, while the power dissipation of the second regime (labelled as (4) in Fig. 3.14c) depends on the current as presented by Eq. 3.5 and 3.6.

$$W = V^2/R \tag{3.5}$$

$$W = I^2R \tag{3.6}$$

where V is the applied electric field, I is electric current, and R is the electrical resistance of the sample.

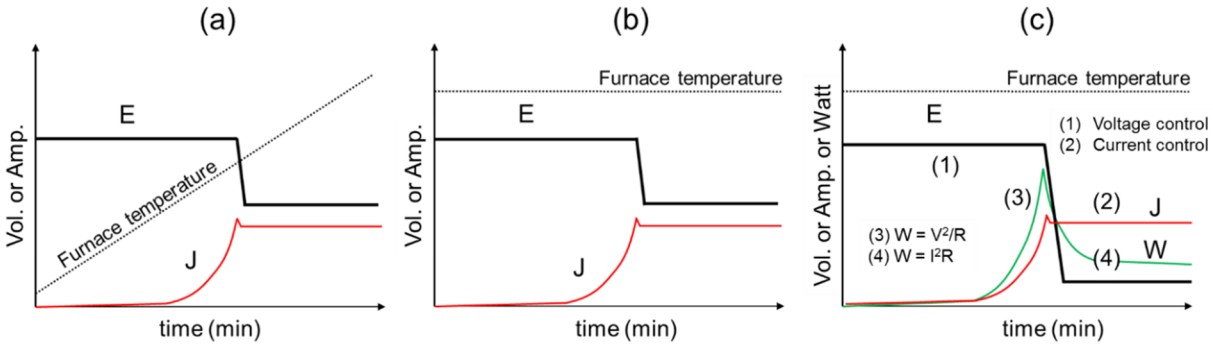

Figure 3.14: (a) Ramping up furnace temperature, (b) constant furnace temperature, and (c) the flow of electric current (J) in the voltage (1) and current control (2), the power dissipation according to the control modes (3), and (4) [author's figure].

3.7.2 Process parameters

Effect of voltage—studies on electric field effect of flash sintering demonstrates that flash sintering of TiO_2 occurs at lower furnace temperature (1150 °C) with increasing electric field. The greater the electric field applied the lower the furnace temperature needed for flash sintering to occur. It can be concluded that there is some combination of furnace temperature and electrical field applied which can activate the flash sintering [92].

Effect of electrical conductivity—conductivity is the key for making flash sintering possible. The electrical conductivity of materials is affected by electronic structure, chemical bonding, defects, grain size, density, crystallinity, and impurities. It also can be controlled by other external parameters such as temperature, pressure, and magnetic fields [62]. In general, electrical conductivity of ceramics is temperature dependence. With increasing temperature, the electrical conductivity of most ceramics increases. The charge carriers in ceramics are mainly ions but as temperature increases ceramics can become electronically conductive. For example, when α-alumina (high purity >99.99%) is heated, it can be an ionic conductor at temperatures below 873 °C, but when temperature is higher than 1323 °C, α-alumina becomes an electronic conductor and its electrical behaviour changes. In the case of flash sintering, good understanding of electrical conductivity of the samples is important because it also changes the powder dissipation as temperature increases affecting Joule heating of the sample.

Joule heating (during flash sintering)— is defined as the heat generation in a material body via power dissipation of electric current. The sample temperature increases as a function of power dissipation as previously mentioned. However, temperature of the sample generated via Joule heating cannot be directly measured because a thermocouple cannot be inserted to the sample body. The sample temperature can be indirectly measured using a calculation of the power dissipation (W_v) and the black body radiation model as expressed by Eq. 3.7 [78, 93].

$$\frac{T_s}{T_0} = \left[1 + \frac{1000 W_v}{\sigma T_0^4}\left(\frac{V}{A}\right)\right]^{1/4} \tag{3.7}$$

where T_s is the specimen temperature (K), T_0 is the furnace temperature (K), W_v is the power dissipation per unit volume (mW/mm^3), σ is the black body radiation constant (5.67×10^{-8} W·m^{-2} K^{-4}), and V/A is the volume per unit surface area (mm).

3.8 Microwave sintering (MWS)

Microwave sintering (MWS) is a field assisted sintering technique but is different from those already described. Microwave sintering exploits an ability of materials to absorb and transform electromagnetic energy to heat. Heat is internally generated in the material bulk by the interaction of microwaves with atoms, ions, and molecules. However, interactions of microwave radiation and materials vary and are divided, by dielectric loss factor, into three groups including opaque (reflector, conductor), transparent and absorber (Fig. 3.15) [94-96].

Opaque materials or conductors such as metals possess infinite dielectric loss factor. When an opaque material is subjected to microwave radiation, microwaves are reflected from the material surfaces; thus, it will not be absorbed and there is no heat generation in the material bulk. However, heat can be generated at the material's surface by the Ohmic heating mechanism where electrons are free to move under microwave field resulting in production of electric current and heat. Plasma or arcing can also be produced because free electrons are excited by microwave energy to jump and collide with air molecules.

Transparent materials such as insulators exhibit low dielectric loss factor, in contrast to conductive materials, electrons in insulators do not move under an electromagnetic field. So, microwaves can pass through insulators without any absorption.

Absorbers have high dielectric loss factor and can be polarized under microwave radiation. When a dielectric material is subjected to microwaves, electric charges do not flow through the material, but only slightly shift from their average equilibrium positions causing dielectric polarization which creates induced dipoles. When dipoles are oriented by microwaves, they collide with one another; thus, dissipating energy. In this context, only the absorbers will be used to explain the microwave sintering process.

Fig. 3.15 presents the microwave absorption of some materials as a function of loss factor and penetration depth. For example, alumina and quartz are transparent to microwaves so all the microwave radiation passes through the material bulk. Because there is no absorption, the penetration depth is large. In contrast, microwaves cannot pass through the bulk of the opaque materials where the penetration depth approaches zero. Thus, all microwave radiation reflects. In the case of absorbers some microwaves are absorbed to a certain penetration depth. So, a good microwave absorber should have a great penetration depth allowing microwaves to range throughout the sample bulk.

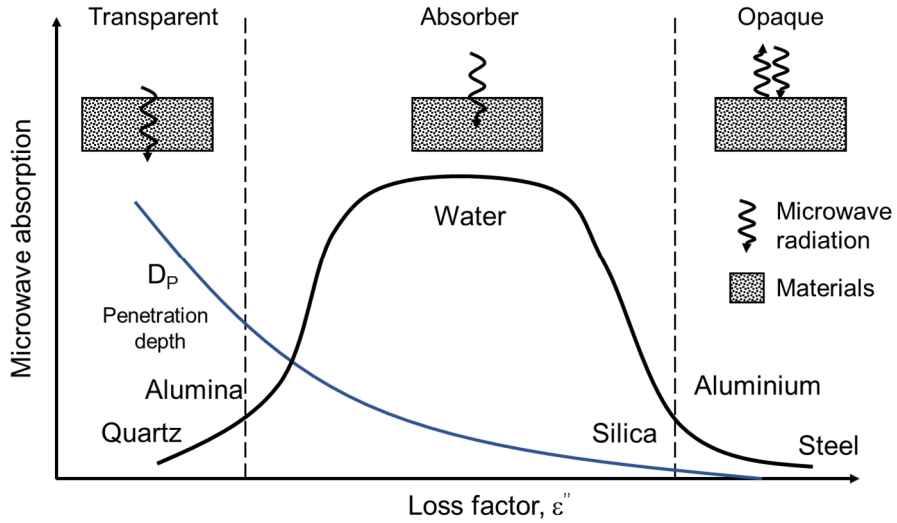

Figure 3.15: Relationship between the dielectric loss factor and microwave power absorption of some common materials at 2.45 GHz [97].

3.8.1 Working Principle

Most ceramic materials (dielectrics or insulators) are transparent to microwave radiation at room temperature but they can absorb microwaves when heated above a critical temperature depending on their dielectric characteristics. To describe microwave absorption mechanisms quantitatively, a complex dielectric constant (ε*) is used as presented in Eq. 3.8 [98].

$$\varepsilon^* = \varepsilon' - j\varepsilon''_{eff} \tag{3.8}$$

$$\varepsilon''_{eff} = \varepsilon''_c + \varepsilon''_S + \varepsilon''_d + \varepsilon''_i + \varepsilon''_e \tag{3.9}$$

where ε' is the real part of the complex dielectric constant (or relative permittivity; $\varepsilon' = \varepsilon/\varepsilon_0$), $j\varepsilon''_{eff}$ is the imaginary part of the complex dielectric constant also known as 'loss factor' indicating ability of the material to dissipate energy. ε_0 is the permittivity of vacuum (8.854x10^{-12} F/m), and ε''_{eff} is the effective dielectric loss under an electromagnetic radiation. The ε''_{eff} is the summation of $\varepsilon''_c, \varepsilon''_S, \varepsilon''_d, \varepsilon''_i$ and ε''_e which are loss by conduction, loss by interfacial polarisation, loss by dipolar polarisation, loss by ionic polarisation, and loss by electronic polarisation, respectively. However, at the microwave frequency, the major loss mechanisms of ceramics (non-magnetic materials) are dipolar polarisation loss and conduction loss. Dipolar loss is the energy dissipation resulting from re-alignment of the polarisation direction under oscillating electromagnetic radiation while conduction loss results from long-range charge flow through the material.

Another equation used to explain losses in dielectric materials under microwave radiation is 'loss tangent' ($tan\ \delta$) which is simply calculated by a ratio of $\varepsilon''$and ε' or calculated using ionic conduction as presented in Eq. 3.10.

$$tan\ \delta = \frac{\varepsilon''_{eff}}{\varepsilon'} = \frac{\sigma}{2\pi f \varepsilon_0 \varepsilon'} \tag{3.10}$$

where σ is the total effective conductivity (S/m) caused by ionic conduction, and f is the frequency (Hz). The loss tangent is temperature, and frequency dependent.

An explanation of temperature dependence of loss tangent is that kinetic energy of the dipole increases as a function of temperature making it easier to couple with the microwaves. In other words, ε' decreases by increasing temperature which results from poor alignment under the electromagnetic field (an effect of thermal motion) [94,95].

3.8.2 Process parameters

Power dissipation—microwaves interact with ceramics via ionic conduction and dipolar polarization. Total power dissipation per unit volume, W_{total} is expressed by the sum of the two mechanisms [99]. Eq. 3.11 presents the power dissipation caused by ionic conduction.

$$W_i = E_i^2 qnu \tag{3.11}$$

where W_i is the power dissipation resulting from ionic conduction, E_i^2 is internal electric field, q is amount of electrical charge of each of ion, n is the number of ions per unit volume, and u is permitted level of ion mobility.

The power dissipation per unit volume of dipolar rotation, W_d is expressed by

$$W_d = \omega \varepsilon_0 \varepsilon''_{eff} E_i^2 \tag{3.12}$$

where ω is angular frequency which is $2\pi f$ (f is frequency of the applied microwave), ε_0 is permittivity of free space ($8.85\text{x}10^{-12}$, V/m^3), ε''_{eff} is the effective dielectric loss, E_i^2 is internal electric field intensity (V/m).

However, ionic conduction decreases with increasing frequency, but it is negligible at microwave frequencies. Therefore, the total energy dissipation in a ceramic material resulting from microwave radiation is;

$$W_{total} = 2\pi f \varepsilon_0 \varepsilon''_{eff} E_i^2 \tag{3.13}$$

The total power dissipation results in increased sample temperature (ΔT) which is expressed by Eq. 3.14 [99].

$$\frac{\Delta T}{\Delta t} = \frac{\omega \varepsilon_0 \varepsilon''_{eff} E_i^2}{\rho C_p} \tag{3.14}$$

where ρ is bulk density of the material (kg/m^3) and C_p is the heat capacity of the material at constant pressure (J/g·K).

Penetration depth—power dissipation is strongly restricted by an attenuation factor of microwaves within the material bulk. The *penetration* (D_p) is used to define the distance which allows microwaves to travel. D_p value is a calculated distance from the material surface toward the bulk which is expressed by Eq. 3.15 [99].

$$D_p = \frac{C \varepsilon_0}{2\pi f \varepsilon''_{eff}} \tag{3.15}$$

where C is the speed of light. For a given microwave frequency, microwave absorption depends on effective dielectric loss (ε''_{eff}) and magnitude of the internal electric field (E_i^2) (Eq. 3.13). In other words, the higher these values, the greater power can dissipate. In contrast, the microwaves are converted to heat limited by D_p as in Eq. 3.15. For instance, in a highly effective dielectric loss material, microwave heating occurs at the material's surface because it has small penetration depth. In addition, as the effective dielectric loss increases, the D_p approaches zero. This phenomenon acts similarly to conventional heating so that the bulk is not heated uniformly resulting in a temperature gradient.

A microwave frequency of 2.45 GHz, this frequency is used for material processing. By considering this frequency, most ceramics are transparent to the microwaves because they exhibit a low ε''_{eff} (<0.08) at room temperature, but when temperature is greater than 400 °C, the ε''_{eff} is high enough (ε''_{eff} >1) to couple with the microwave. Therefore, microwave heating for ceramics is possible [99]. In addition, microwave heating is developed to process ceramics by employing

a *'susceptor'*, which has high ε''_{eff}. The susceptor couples with microwaves at room temperature, and acts as a heat source to raise the ceramics temperature. Once, the ceramic sample reaches high enough temperature, the ceramic sample starts to absorb microwaves and heats by itself [96].

Since microwave heating is volumetric heating, the temperature profile in the sample bulk is inverse due to thermal heat loss at the sample surface (inside is hotter than surface); thus, a potential drawback of microwave heating, in samples with low thermal conductivity, is the 'thermal runaway' (an uncontrolled temperature rises inside the sample). Thermal runaway may lead to a non-uniform microstructure or localised melting [100,101] but it can be minimised by using the heating associated with conventional firing so called hybrid microwave heating [102-104].

Fig. 3.16 compares of the sintering techniques in terms of process setups and process parameter profiles including temperature, applied pressure (in SPS), and power density (in FS).

Figure 3.16: Schematic diagram of sintering techniques and their sintering profiles [author's figure].

3.9 Porcelains

Porcelains are defined as a fired silicate ceramic product, which have fine and dense microstructure. They are used in many household, scientific and engineering applications. High mechanical strength, low water absorption, translucence and durability are key technological advantages of porcelains [42,105]. Porcelains are commonly glazed, but sometimes unglazed depending on the application [105]. A porcelain body is typically made of clays, feldspars, and quartz along with other constituents (e.g. alumina to increase toughness) to promote desired characteristics [42,105,106].

Compositions for the various types of industrial porcelains and their firing temperatures are presented graphically in the clays, feldspars, and quartz phase diagram as presented in Fig. 3.17.

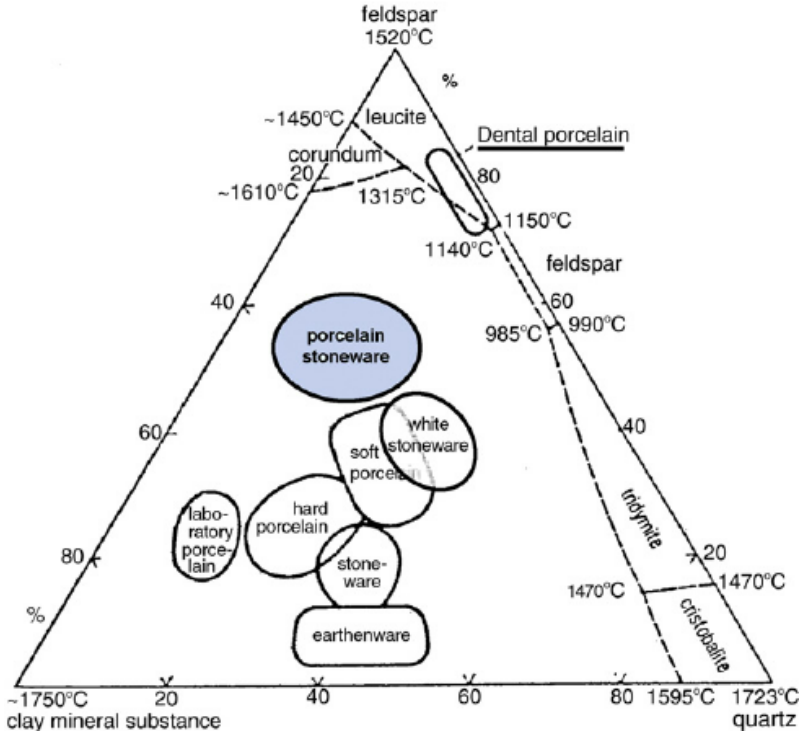

Figure 3.17: Formulation range of porcelains in the clay–quartz-feldspars ternary diagram (wt.%) [107].

Porcelain microstructures are complex because of the interplay between raw materials, reactions on firing, precipitation of mullite, and slow dissolution of quartz into the glass phase. Fig. 3.18 presents a typical porcelain microstructure (50 wt.% clays, 25 wt.% feldspars, and 25 wt.% quartz) produced in a conventional

sintering process. Fig. 3.18a shows the polished surface of the porcelain having residual pores. Glass is the most abundant phase in the porcelain microstructure shown in Fig. 3.18b. Fig. 3.18c reveals the etched microstructure (using 5% HF with 10s) containing primary mullite (PM), secondary mullite (SM), and quartz (Q) embedded in the glassy phase. Porcelains, moreover, have been extensively studied and well understood in several aspects including effect of starting compositions, phase evolution, process parameters, and firing conditions on their technological properties [106,108-111].

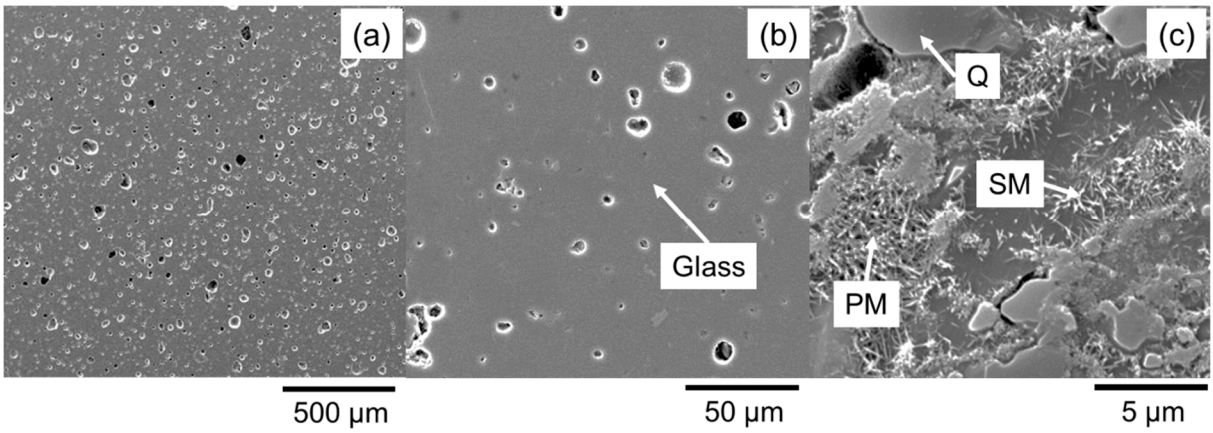

Figure 3.18: SEM images of porcelain microstructures fired at 1200 °C, 30 °C/min, and 15 min dwell, (a) represents a low magnification of a polished microstructure, (b) represents a high magnification of the polished microstructure showing glassy phase, the major phase in porcelain, and (c) reveals three constituents; PM is primary mullite, SM is secondary mullite, Q is Quartz [author's figure].

3.9.1 A brief description of porcelain raw materials

A typical porcelain composition is 50 wt.% clays, 25 wt.% feldspars, and 25 wt.% quartz. Clays provide plasticity and green strength to the mixture in the forming process. Feldspars are fluxing agents which reduce sintering temperature and promote glass formation by reacting with other constituents to form a melt. Quartz controls the porcelain characteristics both in green and fired stages. In the green stage, quartz prevents cracking during drying process and disperses in the fired body as a skeletal network, but the large residual quartz grain can reduce mechanical strength of the final porcelain.

3.9.1.1 Kaolinitic clays

Kaolinite is a 1:1 sheet silicate clay mineral composed of a $[Si_2O_5]^{-2}$ layer and $[Al(OH)_4]^{+2}$ layers. The chemical formula is $Al_2O_3 \cdot 2SiO_2 \cdot 2H_2O$ (39.8% Al_2O_3, 46.38% SiO_2, and 13.9% H_2O by wt.%). Kaolinite is also called as china clay or ball clay, which are distinguished by their origin. Kaolinite is a primary clay which is formed by the decomposition of feldspathic rocks and it deposits at the origin, thus it contains fewer impurities, coarse particles and low plasticity. Ball clay is the secondary clay which is transported away from its origin hence it contains more impurities (both chemical and organic matter), finer particles, but it provides better plasticity. From the chemistry point of view, kaolinite and ball clay exhibit similar chemical composition but ball clay may have more impurities such as iron oxide, titania and quartz [42,112,113]. When kaolinite is heated, several thermal events take place, which will be discussed in section 3.9.2.

3.9.1.2 Feldspars

Feldspars are aluminosilicate minerals originated from crystallization of granitic melts. They contain different alkaline or alkaline-earth minerals. Microcline and orthoclase are potash feldspars ($K_2O \cdot Al_2O_3 \cdot 6SiO_2$), albite is sodium feldspar ($Na_2O \cdot Al_2O_3 \cdot 6SiO_2$), and anorthite is calcium feldspar ($CaO \cdot Al_2O_3 \cdot 2SiO_2$). During heating of feldspars at about 700-1000 °C, they form a solid solution of sanidine ($3K_2O \cdot Na_2O \cdot 4Al_2O_3 \cdot 24SiO_2$) before melting to form liquid glass at ~1100 °C. A major function of feldspar in porcelains is to form liquid glass phase at low temperature to promote vitrification.

Mixed feldspars lower the glass formation temperature compared with pure feldspar. For instance, pure potash feldspar begins to melt at ~1150 °C, pure soda feldspar melts at ~1118 °C but when potash and soda feldspar are mixed together, they melt at ~1050 °C.

Moreover, feldspars in a triaxial blend react with other constituents such as liberated amorphous silica (from kaolinite decomposition) to form liquid glass at eutectic points. A eutectic melt of potash feldspar in a $K_2O \cdot Al_2O_3 \cdot SiO_2$ phase diagram appears at ~990 °C while a eutectic temperature of soda feldspar is at ~1050 °C, in the $Na_2O \cdot Al_2O_3 \cdot SiO_2$ ternary phase diagram [42,114].

3.9.1.3 Quartz

Quartz and flint are sources of silica used in porcelain bodies. Their crystal structure is built up from continuous frameworks of SiO_4 tetrahedra. The SiO_4 tetrahedra share their oxygen atoms giving an overall formula SiO_2. Quartz transforms from an original alpha polymorph to beta when it is heated at 573 °C which changes in structure, density, and thermal properties. Upon further heating, beta quartz transforms to tridymite at 870 °C before the third transformation to cristobalite occurs at 1470 °C. Since, the melting point of quartz is ~1700 °C, the quartz present in the porcelain body only partially melts when it is fired at 1200 °C and leaves residual quartz in the fired products. Residual quartz particles remaining in porcelains after firing decrease the mechanical strength by initiating microcracks in the microstructure. In addition, alumina is used as a filler to increase elastic modulus and thereby reduces the weakening of the quartz inversion [42,115,116].

3.9.2 Chemical reactions

3.9.2.1 General chemical reactions

Several chemical reactions occur when a porcelain body is being fired. Fig. 3.19 presents a series of common reactions and phase transformations of a typical porcelain body during firing.

To begin with, a drying process occurs at about 100-150 °C during which the physically absorbed water evaporates. Some organic compounds (raw material impurities) and additives are burnt out in the temperature range of 250-650 °C, depending on their types and content. Dehydroxylation of clay minerals occurs at ~450-700 °C resulting in metakaolin ($Al_2O_3 \cdot 2SiO_2$).

A displacive transformation of quartz theoretically occurs at 573 °C. It has been believed that it is the most critical point during firing, and cooling processes because the volumetric change during this transformation is approximately 1.6 vol.% [117]. However, alpha to beta quartz transformation generates no defects during firing because of a great flexibility of the green body [42]. Sanidine formation—a mixed alkalis of both potash and soda feldspars—occurs at above 700 to 1000 °C which depends on the ratio of sodium to potash in the composition [42, 118].

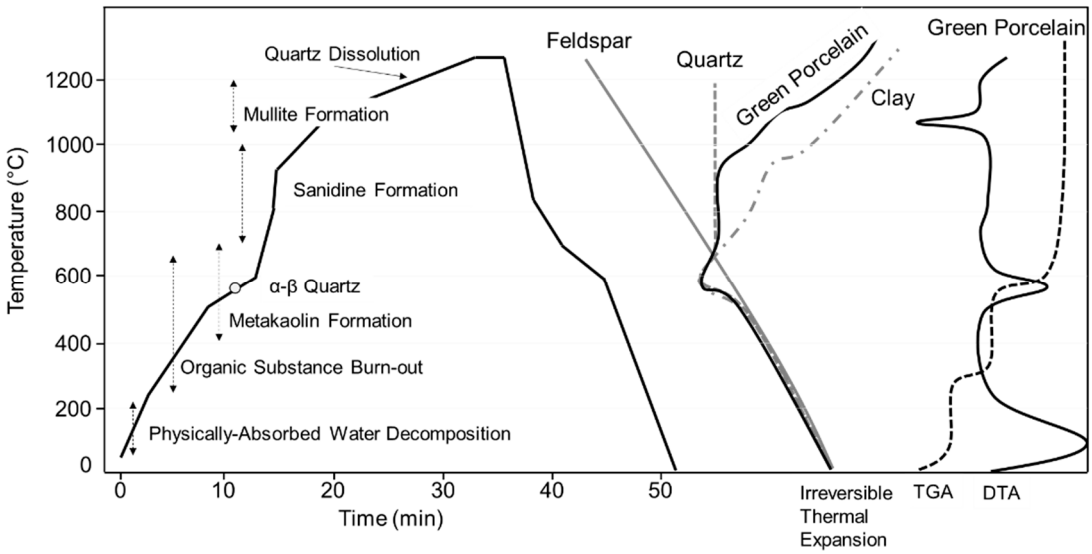

Figure 3.19: Sketch illustrating the chemical reactions of a typical porcelain body during sintering from room temperature to 1300 °C. The irreversible thermal expansion of the three main constituents, and a green porcelain body are presented as well as thermal behaviours using TGA/DTA [author's figure].

Furthermore, metakaolin transforms to a spinel-type structure, and liberates amorphous silica at ~950 to 1000 °C. This amorphous silica helps to form an eutectic point as previously addressed [119,120]. Decomposition of metakaolin forms fine needles of primary mullite discussed in detail in the next section. Quartz dissolution starts at above 1200 °C which increases the viscosity of the liquid glass [42,121,122].

3.9.2.2 Mullite formation

Mullite ($3Al_2O_3 \cdot 2SiO_2$) is the only stable intermediate compound in the Al_2O_3-SiO_2 binary system at atmospheric pressure. It has chemistry (alumina/silica ratio) ranging from silica-rich mullite (3/2) to alumina-rich mullite (2/1) which are 60 and 66 mol.% of Al_2O_3, respectively, and was initially believed to be sillimanite (1/1) but later identified as mullite [123]. Mullite is a major constituent of many whitewares and refractory products [42,106]. Mullite has several useful technological properties i.e. low thermal expansion, good chemical and thermal stability, high thermal shock and creep resistance, and good corrosion resistance in severe conditions [124-128]. Mullite is stable in orthorhombic crystal structure having lattice parameters a=7.545 Å, b=7.689 Å, and c=2.884 Å (JCPDS Card#15-776) but the tetragonal structure is also observed and referred to as an

unstable phase [129-131]. The lattice parameters of mullite, moreover, are dictated by its chemistry; the a and c-parameters increasing with increasing alumina content while b decreases [124,132-135]. Mullite can be produced in large quantities either as a solid solution of alumina-silica mixture or by transformation of kaolinitic clays [136-140]. Mullite produced from kaolinite, however, is the main topic of this thesis and hence, the other production routes will not be addressed.

Mullite formation from kaolinitic clays under normal heat treatment condition (pressureless with heating rate of 5-60 °C/min) is well known, starting from dehydroxylation at around 450-600 °C and formation of metakaolinite ($Al_2O_3 \cdot 2SiO_2$) with a disordered crystal structure. Metakaolinite, later transforms to a spinel structure in the temperature range 950-1050 °C and liberates highly reactive amorphous silica as a by-product. However, some authors suggest that metakaolinite transformation at 980 °C can be Al-Si spinel, γ-alumina or primary mullite depending on its chemistry (Fig. 3.20) [42,106,110,119,120,147-159].

Although there are debatable results about the mullite transformation at 980 °C, it is fundamental to investigate how the metastable spinel phase transforms into mullite above 1100 °C and how this transformation can be used to design microstructure. For example, mullite in porcelains has been reported as primary, secondary and tertiary (all of which exhibits orthorhombic crystal structure) depending on its source and aspect ratio [122]. Primary mullite is generally located in the clay relicts exhibiting low aspect ratio (1-3:1). Secondary mullite is found embedded in the glassy matrix (feldspar relicts) with high aspect ratio of (3-10:1), while tertiary mullite, which is rarely formed, is located at the interface between alumina particles and glassy matrix [122]. Since mullite is typically produced from cheap and naturally occurring raw materials, the level and types of impurity (i.e. TiO_2, Fe_2O_3, alkali/alkali earth) also play an important role in its properties. For example, Fe^{3+} and Ti^{4+} can enter the mullite structure by substituting for Al^{3+} at the octahedral site resulting in a reduction in its mechanical strength [141-144]. In addition, alkali and alkaline earth elements can react with alumina and silica producing liquid phase at lower temperatures (1450-1550 °C compared to 1587 °C in pure system) [145-146].

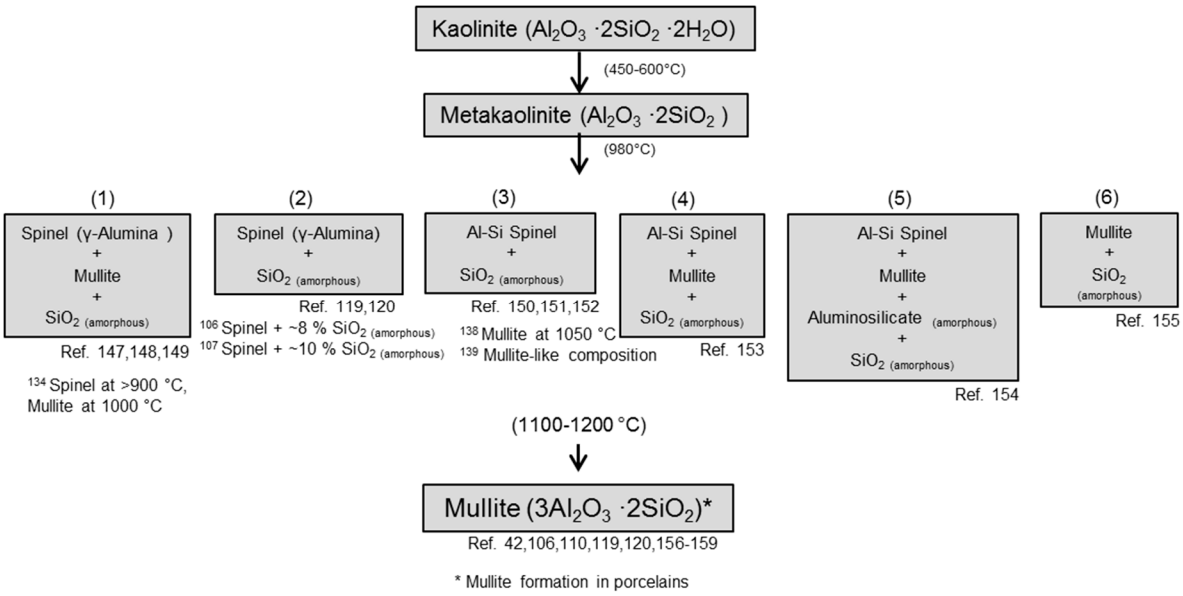

Figure 3.20: Tree diagram of proposed kaolinite-mullite phase evolution from 400-1200 °C reported in the literature. The phases evolve from kaolinite to metakaolinite at 450-600 °C then 6 routes of mullitization at 980 °C have been suggested [42,106,110,119, 20,147-159] [author's figure].

Mullite formation in porcelains under conventional firing has been also extensively studied, and it is clear that mullite starts to form between ~1050-1200 °C and its transformation completes in the temperature range of 1200-1400 °C [106,160-162,163,164]. In general, porcelains contain two types of mullite; primary and secondary mullite. The primary mullite forms ~1100 °C in clay relicts whilst secondary mullite forms at above 1200 °C in the melt. From the chemistry point of view, primary mullite is believed to have 2:1 (Al_2O_3:SiO_2) because it is purely derived from the decomposition of clay species whereas secondary mullite tends to have 3:2 (Al_2O_3:SiO_2) resulting from the chemical reaction of feldspars, clays, and quartz [161,165]. In porcelains, moreover, the amount of mullite is believed to be independent of temperature, dwell time, and heating rate above 1200 °C [110,160].

The amount of mullite formed in a porcelain body can be calculated by using the concept of 'glass composition boundary' which is described in section 3.9.2.4 [110,160]. Mullite crystallite size also increases as a function of temperature, dwell time, and chemical composition [105,166-168].

3.9.2.3 Quartz dissolution

Quartz in porcelain bodies provides excess silica for the glass phase, but the dissolution rate is insignificant below 1200 °C [169-171]. Quartz dissolution in a fast-fired porcelain body, however, was reportedly observed at 1100 °C [163]. It is widely accepted that the dissolution rate of quartz is dependent on starting particle size [172-173]. In contrast, a recent work has demonstrated that quartz dissolution is independent of particle size, with the dissolution rate limited by the diffusivity [111]. Dissolution of quartz is a function of dwell time, and temperature regardless of the heating rate effect [160]. Due to the dissolution of quartz, silica in the glass phase increases; thus increasing the viscosity of the liquid glass, and reducing the tendency for pyroplastic deformation at peak temperature [171].

3.9.2.4 Glass formation boundary and its chemistry

Liquid glass in porcelains is produced at different temperatures depending on the chemical compositions, especially the types of fluxing agents used as previously mentioned. The amount of glass phase formed in a porcelain body is determined by the amount of flux ($RO+R_2O$), dwell time, and peak temperature [171]. In general, the amount of glass phase formed in typical porcelain bodies is about 30-70 vol.% [121,165]. Recent research shows that chemistry of the glassy phase in porcelains can be calculated using the overall chemistry of porcelain composition.

It is proposed that compositions of the glassy phase locate on 'the glass phase composition boundary' over the temperature range of 1200-1400 °C in a flux–alumina–silica system [171]. The glass phase composition boundary is a practical approach allowing ceramists to calculate the chemistry of glass phase, and amount of mullite formed in porcelains. The amount of alumina which dissolves in the glass phase is proposed on the molar basis as 1.19±0.1: 1 [Al_2O_3 :($RO+R_2O$)]. Any excess alumina in the system is used for mullite formation. This ratio is measured to be constant over industrial firing temperatures and it can be applied to all commercial porcelain compositions [110,160].

The glass chemistry, however, changes above the quartz dissolution temperature which resulted from introducing more silica into the glass phase. Consequently, the silica level in the glass chemistry is increased while the alumina

to alkali ratio remains constant [174]. However, in the literature, it is reported that glass chemistry in porcelains has different compositions because alumina, and silica have different dissolution limits at different temperatures [175-178].

3.10 Densification and microstructural development of porcelains using a conventional sintering process

Densification of a porcelain body is dictated by the development of apparent bulk density (Fig. 3.21a-d). With increasing temperature, the density increases which results from elimination of open pores via vitrification process [179-181]. Generally, densification in a porcelain body is insignificant from room temperature to ~1000 °C because there is a small change in chemical reactions and phase transformation (a) [106,182]. The apparent bulk density sharply develops above 1000 °C (b) to the peak temperature (e.g. 1200 °C) by formation of liquid glass. The density remains constant at peak temperature for a certain time (c) before it decreases due to bloating (d) [37,42,121,164].

Due to the presence of liquid phase around solid particles, wetting plays an important role in the densification process. The wetting mechanism is penetration of liquid phase in a porous structure of solid particle clusters via capillary action. Capillary action brings particles closer together, resulting in shrinkage and lower porosity leading to densification [37,183]. It has been proposed that surface tension in porcelain systems can be negligible since it is not changed much by altering the composition [184,185].

Fig. 3.21e-g schematically presents the microstructural evolution during development of porcelain density based on SEM study. As mentioned in section 3.9.2 several chemical reactions occur. At 600 °C (Fig. 3.21e, the mixture of clays, feldspar and quartz particles is evident because there is little reaction. At >1000 °C (Fig. 3.21f), spinel forms in the clay relict and feldspar melts to form liquid glass while quartz remains intact. At this stage, pores can develop in the liquid glass. At >1200 °C (Fig. 3.21g) mullite develops from reaction between spinel and liquid glass and quartz starts to dissolve into the glassy phase. Pores are enlarged at higher temperatures.

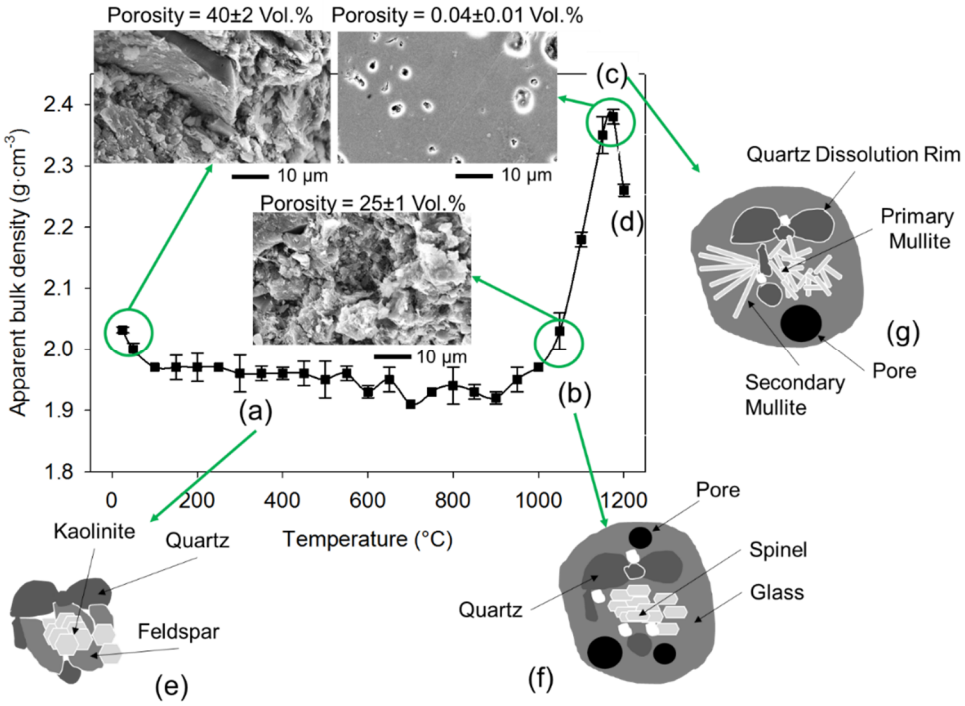

Figure 3.21: Development of apparent bulk density (a-d) and microstructure development (e-g) of a porcelain body sintered using a conventional sintering process (5 °C/min) [author's figure].

3.11 Case studies in rapid sintering techniques of porcelains

To the best of the author's knowledge there is little works has been done on the field assisted sintering of porcelain materials. In this section some recent works are reviewed and summarised.

3.11.1 Spark plasma sintering

A utilisation of the SPS technique to porcelain materials was reported by Tsukada et al., [186]. A zirconia/porcelain functionally graded composite was used as the starting material to fabricate restorative dental porcelain. The SPS conditions used to sinter this dental porcelain composite were 1380 °C peak temperature, 4 minutes dwell time, 88 °C/min heating rate, and partial vacuum under 10 MPa uniaxial pressing.

The results showed that when the porcelain powder was mixed with Y-TZP (70:30 by volume), the porcelain peaks were not observed in the XRD patterns at 1350 °C because the fusing point of this porcelain body in a conventional sintering process was 1290 °C. The author concluded that porcelain was completely

transformed to glassy phase and this glassy phase was believed to exist between the Y-TZP particles. In addition, the glassy phase was believed to prevent the generation of the plasma during sintering process in the SPS, which resulted in lower density of the 70/30 Y-TZP/porcelain composite compared with the pure SPS sintered Y-TZP [186].

3.11.2 Flash sintering

Flash sintering of whiteware was first reported by Trombin and Raj [91]. They developed a sintering map using current density, holding time, and furnace temperature to study microstructure of a whiteware body. The whiteware composition used was reported as a mixture of feldspars and 10 vol.% of calcium silicate glass. The sintering temperature of this whiteware composition using conventional firing process is 1150 °C. The experimental setup of flash sintering used in their work was simple using two metal punches which acted as electrodes. A cylindrical sample was pressed under 1 MPa uniaxial pressure between the two electrodes. Instead of using a combination of constant applied electric field and increasing furnace temperature at constant heating rate, they used a constant furnace temperature and applied a step function in time of electric field. The good microstructure (the detail of the good microstructure was not provided but can be indicated as 'no localised melt') indicated the suitable sintering conditions. For this whiteware body, the furnace temperature 950 °C was kept as constant. The maximum current density and the holding time which gave good microstructure (no localised melt) were 1.4 mA/mm^2 and 2-70 s, respectively. They suggested that the liquid glass phase formed at lower temperature and flowed abruptly under applied electric field to bond the other constituents [91].

3.11.3 Microwave sintering

Porcelains and their raw materials are poorly microwave absorbing materials, all of which do not couple well with microwaves at room temperature, but they can effectively absorb microwaves above a critical temperature [138,187]

Uses of microwave energy to sinter porcelains have been reported. Menezes et al.,[188] conducted a microwave sintering experiment on porcelains. Different porcelain compositions including sanitaryware, dental porcelain, and electrical

porcelain were successfully sintered using microwaves. The microwave sintered samples were compared to conventionally sintered samples. A 2.45 GHz hybrid microwave sintering system (a combination of infrared heat, susceptor and microwave radiation) was used for the microwave sintering study. The microwave sintered samples exhibited better bulk density and modulus of rupture compared with conventionally sintered samples. The water absorption was in a similar range for both processes, but the peak temperature of the microwave sintering was higher than conventional process by ~20 °C. However, a substantial reduction of dwell time was the advantage of microwave sintering. For example, the similar water absorption was obtained by dwelling 6-10 minutes at the peak temperature using microwaves whereas conventional sintering process required 60 minutes [188].

Another study on a high voltage porcelain insulator was conducted by Satapathy [189]. Satapathy showed that microwave sintering produced better final properties of the samples compared to conventionally sintered samples at the same peak temperature. The total firing cycle was also reduced approximately 80% by using a 6kW/2.45 GHz microwave power. The porcelain samples were sintered at 1240 °C and dwelled for 65-70 hours in conventional process but 8-10 hours in microwave sintering. The apparent bulk densities were 2.35 and 2.38 g/cm^3 for conventional and the microwave sintered samples respectively. The three-point bending strength of the microwave sintered samples was slightly higher than conventional sintered ones. Moreover, the microwave sintered samples exhibited better dielectric properties [190].

Allan et al., [191] successfully produced a large-cross section (12 cm of diameter) electrical porcelain insulator using Microwave Assisted Technology (MAT), a combination of electric furnace and microwave heating, with 5 times shorter processing time compared to the conventional process.

A recent experiment conducted by Santos et al., [190] used 1kW/2.45 GHz microwave power in a multimode cavity furnace. A SiC slab was used as a susceptor. Whole pieces of tableware (with glaze): a dish, a cup and a bowl were successfully sintered at 1284 °C and the total cycle time was 150 minutes whereas these products needed to be fired at 1380 °C for 200 minutes in the conventional

firing cycle. The MWSed porcelains showed similar impact resistance, porosity, water absorption, and phase compositions to conventionally sintered porcelains. The microwave sintering process was faster resulting in lower processing costs. An important aspect of their work was the effect of microwave power distribution in the cavity resulting in homogeneity in the sample. A critical problem in microwave sintering was thermal runaway due to inhomogeneous microwave absorption. To combat the inhomogeneous microwave absorption problem, Monteiro et al., [192] developed a control system which created a uniform electromagnetic field and therefore more uniform heating, even at high heating rates. Even though there have been several studies dealing with microwave sintering of porcelains, none have reported in detail the effect of microwave heating on microstructural evolution.

Chapter 4

Experimental methodology

4.1 Material

The material used in this work was an industrially processed porcelain composition obtained from a porcelain tile factory in Thailand, which composes of clays, feldspar, and quartz. The powder was received in a sprayed dried powder form and this powder was used throughout the work. The powder was characterised in terms of chemical composition, particle size distribution, thermal behaviours including thermal expansion, electrical and physical properties.

Fig. 4.1a shows spherical morphology of the porcelain spray dried powder, which also varied in its size, about 50-300 μm. Fig. 4.1a (inset) also indicated that the powder has donut shape resulting from the spray dried process. Fig. 4.1b show a high magnified SEM image of the spray dried powder showing clay particles with particle size <5 μm.

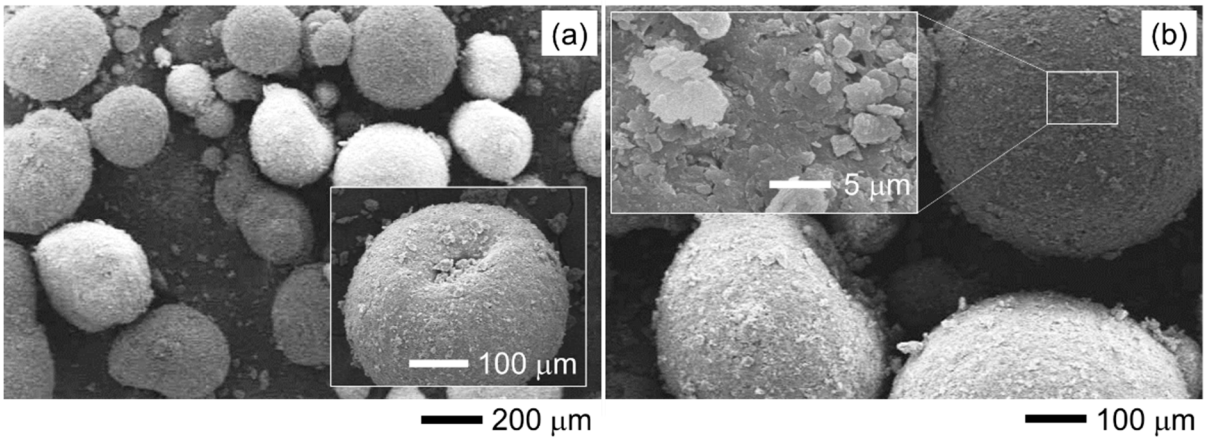

Figure 4.1: SEM images of the spray dried powder obtained from the porcelain tile factory [author's figure].

4.2 Inductively Coupled Plasma-Atomic Emission Spectroscopy (ICP-AES)

ICP-AES is an analytical technique used for detection of trace elements (0.002-1000 ppm) and all elements in the Periodic Table can be identified. The basic principle of the ICP-AES is to use high temperature argon plasma to thermally excite electrons from their ground to an excited state (the argon plasma temperature is ~6000 to 10000 K). When electrons fall back to their ground state they emit a unique energy (wavelength) dependent on their electron configurations. Thus, different elements can be differentiated from their specific emitted energy. The intensity of the energy emitted, moreover, is representative of the concentration of elements in the sample. Thus, by comparing their emitted energy and intensity with reference elements, the ICP-AES can qualitatively and quantitatively determine the elements in the sample [193,194].

Fig. 4.2 presents a work diagram of ICP-AES, the sample, which is in a liquid form, is transported by the pump into the nebulizer where the liquid sample turns into an aerosol and goes into the ICP torch. The high temperature argon plasma in the ICP torch turns the sample into ionised ions. The ionised ions emit their characteristic wavelength, which is sorted by the diffraction grating and collected by a photodetector, to lose their energy. The photodetector converts the collected photons to an electrical signal, which is amplified and processed, which is then displayed and stored in the computer. The total number of emitted photons is directly proportional to the elements concentration in the sample [194].

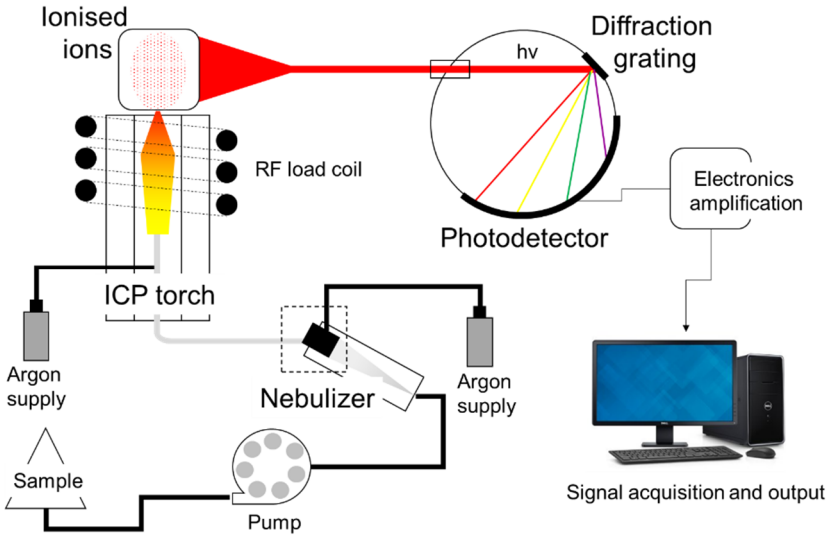

Figure 4.2: Schematic diagram of an inductively coupled plasma-atomic emission spectroscopy [author's figure].

In this study, ICP-AES (iCAP 6500, Thermo Scientific, Cambridge, UK) was performed at the Imaging and Analysis Centre (IAC)&Earth Sciences, Natural History Museum, London. 2 g of the porcelain spray dried powder was well sampled from the mass of 5000 g at different part of the container using a small spatula. There is no settlement or composition gradient since every spray dried powder has similar composition, only different in granulation size. The 2 g of the porcelain spray dried powder was melted to a glass form before being dissolved in HNO_3 solution. The solution was then feed into the spectroscope where it was atomised. The atomised solution was carried into the argon plasma via argon gas.

To ensure the accuracy of the ICP-AES measurements, three reference materials were analysed alongside the porcelain sample as presented in Table 4.1. The chemical composition of the reference materials obtained from ICP-AES were compared to the certified values and used to calculate the percentage of difference of each atom. Measurements were reported 3 times to calculate mean and standard deviations of the sample.

Table 4.1: Calculation of accuracy of the ICP-AES measurements.

Oxide	Al_2O_3	CaO	Fe_2O_3	K_2O	MgO	Na_2O	SiO_2	TiO_2	Total
	wt.%	wt.%	wt.%	wt.%	wt.%	wt.%	wt.%	wt.%	wt.%
Analysed reference materials									
SdAR-L2	11.55	1.11	3.64	4.11	0.42	2.71	74.95	0.64	99.31
DBC-1	31.33	0.18	0.88	2.61	0.33	0.39	51.48	1.12	88.39
WG-1	14.11	8.18	11.24	0.84	7.32	3.13	52.44	1.75	99.46
Certified values									
SdAR-L2	11.58	1.06	3.63	4.10	0.43	2.66	74.48	0.62	98.74
DBC-1	31.82	0.00	0.94	2.64	0.36	0.00	51.98	1.12	88.92
WG-1	14.35	8.40	11.31	0.84	7.55	3.10	52.23	1.74	99.95
Difference (%)									
SdAR-L2	0.24	4.36	0.24	0.22	2.42	2.17	0.64	3.59	0.58
DBC-1	1.55	0.00	5.96	0.97	6.95	0.00	0.97	0.05	0.60
WG-1	1.66	2.59	0.61	0.28	3.06	1.11	0.39	0.58	0.50
Average % difference	**1.15**	**2.32**	**2.27**	**0.49**	**4.14**	**1.09**	**0.67**	**1.41**	
Sample									
Porcelain	**17.43**	**0.74**	**1.24**	**1.24**	**0.49**	**3.77**	**74.32**	**0.68**	**100.00**
Standard deviation	**0.27**	**0.02**	**0.04**	**0.01**	**0.03**	**0.06**	**0.68**	**0.01**	**n/a**

Thus, chemical composition of the porcelain powder was 74.32±0.68 wt.% SiO_2, 17.43±0.27 wt.% Al_2O_3, 0.68±0.01 wt.% TiO_2, 1.24±0.04 wt.% Fe_2O_3, 0.74±0.02 wt.% CaO, 0.49±0.03 wt.% MgO, 1.24±0.01 wt.% K_2O and 3.77±0.06 wt.% Na_2O.

4.3 Particle size distribution

The particle size distribution measurement is determined using a laser particle size analyser. The technique relies on the relationship between light and particle scattering. The technique measures particle size by measuring the scattering angle and intensity of the incident light passes through a dispersed sample (a laser beam (λ=nm) is employed). Large particles scatter light at small angles relative to the laser beam and small particles scatter light at large angles as illustrated in Fig. 4.3.

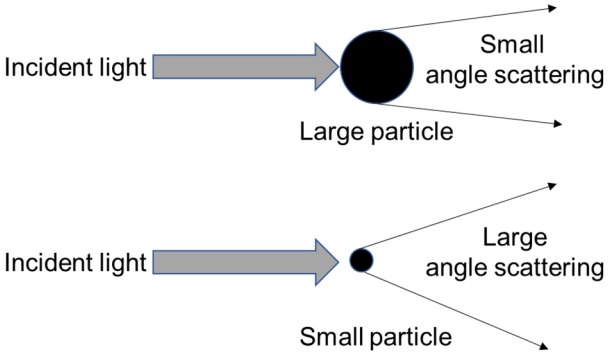

Figure 4.3: Light scattering from large and small particles [author's figure].

When light strikes a particle, several phenomena occur: diffraction, refraction, reflection, and absorption. The large particle (>1 μm) is determined from small scattering angle and high intensity of diffracted light, which is easy to calculate the particle size using Fraunhofer diffraction approximation. However, small particles (<1 μm), refraction is more pronounced because the diffracted light becomes wide angle and low intensity, which make the Fraunhofer diffraction approximation invalid. The current generation of laser particle size analysers employ the Mie theory to calculate the particle size [195], but the absorption coefficient and refractive index of both the materials and medium must be known for an accuracy measurement otherwise an error becomes large. The particle size is reported as volume equivalent sphere diameter [196].

Particle size distribution of the porcelain powder was measured, 3 measurements, by using a laser particle size analyser (Mastersizer 2000, Malvern Instruments Ltd., Malvern, Worcestershire, UK) and the refractive index of the

sample was not considered. Fig. 4.4 shows the particle size distribution of the porcelain sample having mean particle size (D_{50}) of 10-20 µm.

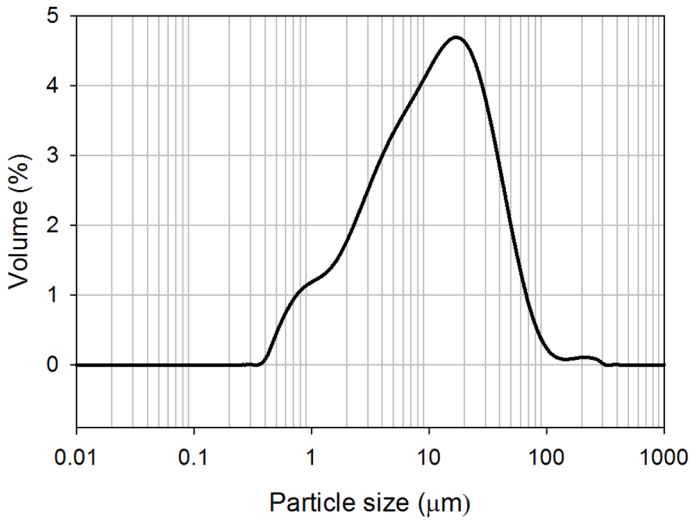

Figure 4.4: Particle size distribution of the porcelain spray dried powder measured using laser diffraction analyser.

4.4 Thermal analysis

Thermal analysis (TA) is a set of analytical techniques measuring physical (dimension, mass) and chemical (phase) property changes of materials as a function of temperature. The gained thermal energy increases vibration and rotation of atomic bonds resulting in events such as phase transformation, glass transition, melting, sublimation, and thermal decomposition such thermal events arises from heat (Q) flow between the material and its surroundings and can be *endothermic (absorbing heat) and exothermic (releasing heat)*. The change of internal energy (ΔU) at constant pressure (P) is the amount of heat (Q) give to the system, minus the amount of work done (W) by the system on its surroundings, the work done by the system is defined as volume change in the system under constant pressure (ΔV). In addition, enthalpy (H) is a thermodynamic parameter which can be directly determined by the change of heat flow (Q). Eq. 4.1-4.5 present the relationship of enthalpy and heat flow [197].

$$\Delta U = Q - W \tag{4.1}$$

$$\Delta U = Q - P\Delta V \tag{4.2}$$

$$H \equiv U + PV \tag{4.3}$$

$$\Delta H \equiv \Delta U + P\Delta V = (Q - P\Delta V) + P\Delta V \tag{4.4}$$

$$\Delta H = Q \tag{4.5}$$

The three major types of the thermal analysis are thermogravimetry (TG), differential thermal analysis (DTA), and differential scanning calorimetry (DSC). The schematic diagram of the three techniques are presented in Fig. 4.5 a, b and c respectively.

TG is generally employed to determine mass changes as a function of temperature. DTA and DSC are generally used for examining phase change with temperatures [197].

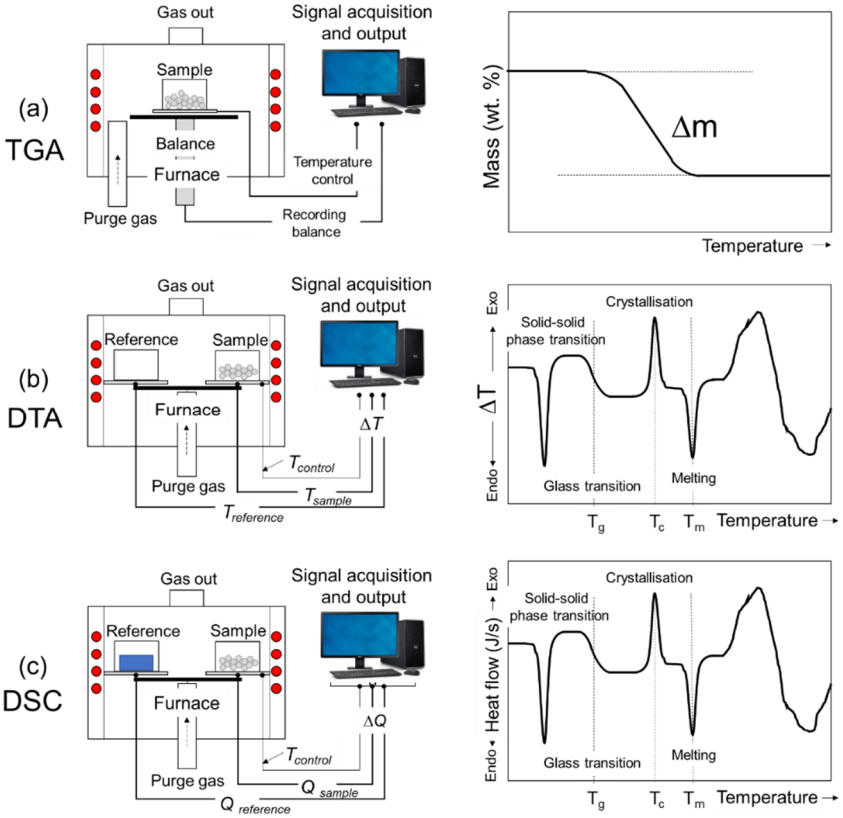

Figure 4.5: Schematic diagrams of different instruments used in thermal analysis: (a) thermogravimetric analysis (TGA), (b) differential thermal analysis (DTA), and (c) differential scanning calorimetry (DSC) [author's figure].

TGA (Fig. 4.5a) measures changes of sample mass upon increasing temperature using a highly accurate balance. Samples are subjected to a controlled temperature change and in a controlled atmosphere. The mass change is plotted against temperature. The working principle of DTA (Fig. 4.5b) is that a sample and a reference in crucibles are simultaneously heated under identical conditions. The temperature difference (ΔT) between sample and reference is recorded then plotted against time or temperature. DTA determines the difference in temperature between a sample and a reference by keeping heat flow constant. DSC (Fig. 4.5c) measures the amount of heat needed to increase sample temperature and the heat required to increase the reference temperature. The measured signal is the temperature difference between the sample and the reference and this difference in temperature is used to calculate the heat flow.

In this study, thermal behaviour (TGA, DTA) of the porcelain powder was characterised using simultaneous thermogravimetry-differential thermal analysis in a TG-DTA (Netzsch STA 449C, Jupiter, Selb, Germany) from 25 to 1200 °C at a heating rate of 10 °C/min and instrument cooling rate. The instrument operated under continuous air flow at a rate of 50 ml/h. DSC was used to determine Cp of the porcelain sample which is discussed in section 4.5.

4.5 Heat capacity

Heat capacity (Cp) can be determined using a DSC. Heat capacity is directly proportional to the heat flow in DSC. To determine heat flow in a DSC, a slow heating rate (5 °C/min) is used to ensure that the system reaches equilibrium. The measurement starts with measuring an empty pan, reference material (known Cp i.e. sapphire), and the porcelain sample. The Cp of the porcelain sample is then obtained from Eq. 4.6.

$$Cp_s = \left(\frac{H}{h} \cdot \frac{M_r}{M_s}\right) \cdot Cp_r \tag{4.6}$$

where Cp_s is Cp of the porcelain sample, H is heat different between sample and empty pan, h is heat difference between reference and empty pan, M_r is mass of the reference, M_s is mass of the sample, and Cp_r is Cp of the reference [198,199].

In this study, a small amount (0.2 g) of the porcelain sample was pressed into 5mm diameter and 1mm thick pellet and stored in an oven at 110 °C prior to the Cp measurement, which was performed in a DCS instrument (Netzsch STA 449C, Jupiter, Selb, Germany) using sapphire as the standard. The measurement was done from 25-1200 °C at a heating rate of 5 °C/min and with instrument cooling rate after switching off. The instrument operated under continuous air flow at a rate of 50 ml/h. The Cp result was used to calculated thermal conductivity of the porcelain sample, which is discussed in section 4.6.1.

4.6 Thermal conductivity and thermal diffusivity by laser flash method

4.6.1 Thermal conductivity

Thermal conductivity (k) represents the transport of heat through the mass of materials resulting from a temperature gradient. In ceramics heat propagates from the surface to the mass of materials largely via lattice vibration waves or phonons. Phonons are predominantly responsible for thermal conductivity in traditional clay-based ceramics since thermal conduction from electrons is small. In addition, at high temperature (>800 °C), heat can also move via phonon radiation. Factors which affect thermal conductivity in ceramics are types of chemical bonding, purity, and density. Strong bonds, high packing density of atoms, high crystallinity, and light elements are the keys for having high thermal conductivity because of high mean free path of phonons [22,200,201].

In general, to quantify thermal conductivity, a relationship between heat flow over time (dq/dt) and the temperature gradient (dT/dx) through an area (A) is employed as expressed in Eq. 4.7.

$$q = -k\frac{dT}{dx} \tag{4.7}$$

where q is heat flow per unit time per unit area, k is thermal conductivity, and dT/dx is temperature gradient through the material. However, this equation is valid only for steady state condition [201].

In addition, a simple, fast, and reliable method to determine thermal conductivity is to employ the relationship between thermal diffusivity (a), density (ρ) and specific heat capacity (Cp) as presented in Eq. 4.8.

$$k(T) = \rho(T) \cdot Cp(T) \cdot a(T) \tag{4.8}$$

4.6.2 Laser Flash Analysis (LFA)

The term thermal diffusivity (a) is defined as how fast temperature change in unit volume of material during changes of surrounding temperature as a function of time. In other words, it measures the rate of transfer of heat from the hot side to the cold side of a material.

A versatile technique to measure thermal diffusivity (a) is the laser flash method which uses a laser pulse to heat the sample on one side and a detector measures temperature versus time on the opposite side [202,203]. The laser flash method employs non-contact sensing, which greatly reduces error from the contact thermal resistance [204].

Fig. 4.6a presents a laser flash analyser (LFA) which is comprised mainly of a laser source, a furnace, and an IR detector, and a data acquisition system. The sample is heated and stabilised in the furnace at desired temperatures. The pulse laser strikes and is absorbed by the front surface of the sample, which rises the sample temperature only 0.5-2 °C. The heat pulse then travels through thickness of the samples and reach the back of the sample. An infrared detector measures the temperature rise at the back of the sample with respect to time and sends this information to the data acquisition system. The temperature obtained at the back of the sample is plotted as a function of time (Fig. 4.6b) and Eq. 4.9 is used to calculated thermal diffusivity.

$$a = 0.1388 \frac{d^2}{t_{1/2}} \tag{4.9}$$

where d is the thickness of the sample, $t_{1/2}$ is the time where the increase in temperature (ΔT) is at half of the maximum.

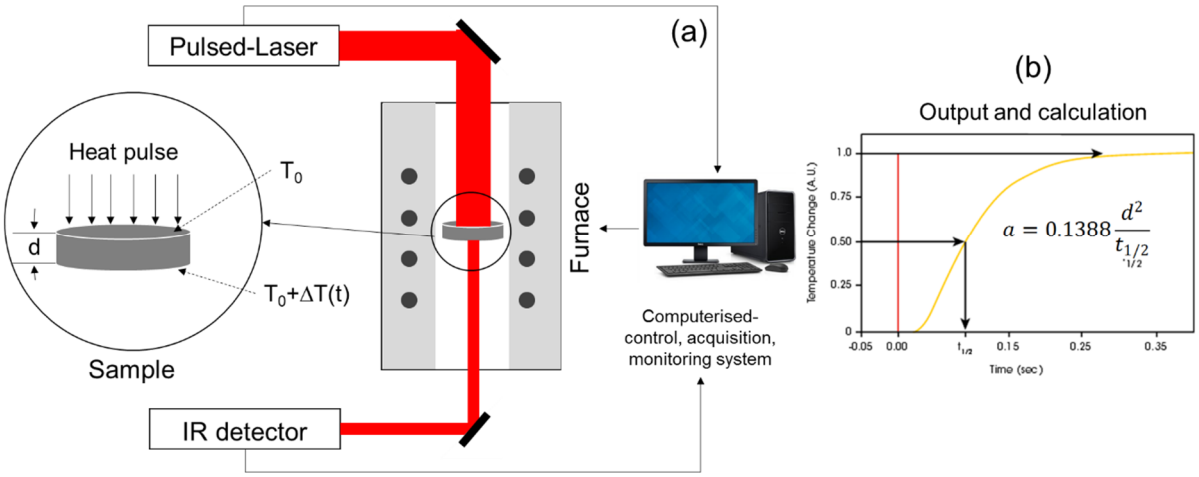

Figure 4.6: Schematic diagram of a laser flash analyser (LFA) [author's figure].

A pellet (well plane-parallel) sample is required for the laser flash analysis. Samples must be coated by a thin layer of graphite emulsion (~5 μm) to help increase the energy absorbed on the laser side and to increase the temperature signal on the detector side.

In this study, a porcelain pellet with 10 mm diameter and 2 mm thick was coated by graphite spray (Graphit 33) on both sides. 2-3 spray passes over the samples and allow it to dry on forming a graphite layer (~5 μm). The pellet then was examined in a LFA instrument (LFA 427 (Netzsch, Selb, Germany). The measurement was made from room temperature to 1200 °C with increments of 100 °C. Three measurements were made at each temperature obtaining average values and standard deviations. The thermal diffusivity result was used to calculated thermal conductivity of the porcelain sample using Eq. 4.8. However, the errors in the sample thickness and density measurements can result the overall error of the thermal conductivity results.

4.7 Dilatometry

Dilatometry is a technique to measure dimension change caused by a physical or chemical process as a function of temperature. The coefficient of thermal expansion is calculated using Eq. 4.10 [205].

$$\alpha = \frac{1}{L_0}\frac{\Delta L}{\Delta T} \tag{4.10}$$

where α is the coefficient of thermal expansion, L_0 is initial sample length, ΔL is change in length of the sample, ΔT is temperature change.

In this study, the porcelain powder was uniaxially cold pressed into 5mm diameter and 20 mm long pellets at 35 MPa using a metallic uniaxial die. Measurements were made in a dilatometer (Netzsch 402E dilatometer, Netzsch, Selb, Germany) using a heating rate of 10 °C/min from room temperature to 1200 °C under normal atmosphere (air).

4.8 Impedance Spectrometry

Impedance Spectroscopy (IS) is an in-situ technique used to measure electrical resistivity of a circuit (then the resistivity is converted to electrical conductivity). It is a useful tool for studying bulk conduction of materials and electrochemical reactions at interfaces of an electrolyte and electrodes. IS can measure resistivity of solid and liquid electrolytes involving movement of ions, dipole rotation (grain interior), and electronic conduction. IS can also determine the electrical responses from different components in a multiphase material and can identify conduction types (magnitude of the electrical response) because conduction steps have a unique time constant depending on frequency. Brantervik and Niklasson [206] suggested that the four main conduction mechanisms are (i) polarization effects at a molecular level, (ii) conduction through the solid bulk, (iii) conduction of ions through the pore network, and (iv) ion conduction at the bulk-electrode interface.

The IS measurements (setup shown in Fig. 4.7) are made with a frequency response analyser (FRA) which is controlled by a computer. The setup employs a two electrodes configuration, usually Pt electrodes, where sample is placed between the electrodes. Both surfaces of the sample are Pt-coated to establish a good electrical contact to the electrodes. During the measurement the sample is place into a tube furnace whose temperature is controlled by a thermocouple close to the sample. The AC signal is set cross the sample and the corresponding current as a function of frequency is recorded by the FRA.

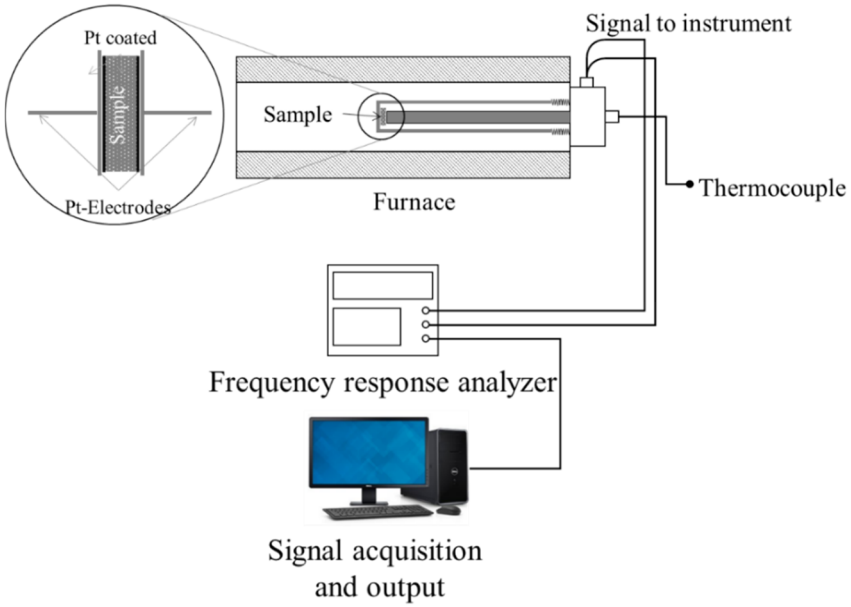

Figure 4.7: Schematic diagram of the impedance spectroscopy apparatus. The inset shows the coated sample and two electrodes which were used [author's figure].

IS measures electrical response using a small amplitude of AC potential (100mV) applied across the sample and measuring the phase angle of current as a function of frequency. Once the AC potential is applied ($V(t)$), the current ($I(t)$) is measured and the impedance ($Z(t)$) is obtained as expressed by Eq. 4.11 [207].

$$Z(t) = \frac{V(t)}{I(t)} \tag{4.11}$$

where $V(t) = V_0 \sin \omega t$

$I(t) = I_0 \sin(\omega t + \theta)$

θ = Phase angle between $V(t)$ and $I(t)$

The data from an IS measurement is given in the form of the Nyquist plots, the real impedance (Z') and the imaginary impedance (Z'') are obtained as shown in Fig. 4.8a [208].

$$Z = Z' + Z'' \tag{4.12}$$

where Z is impedance, Z' is the real part, and Z'' is the imagination part.

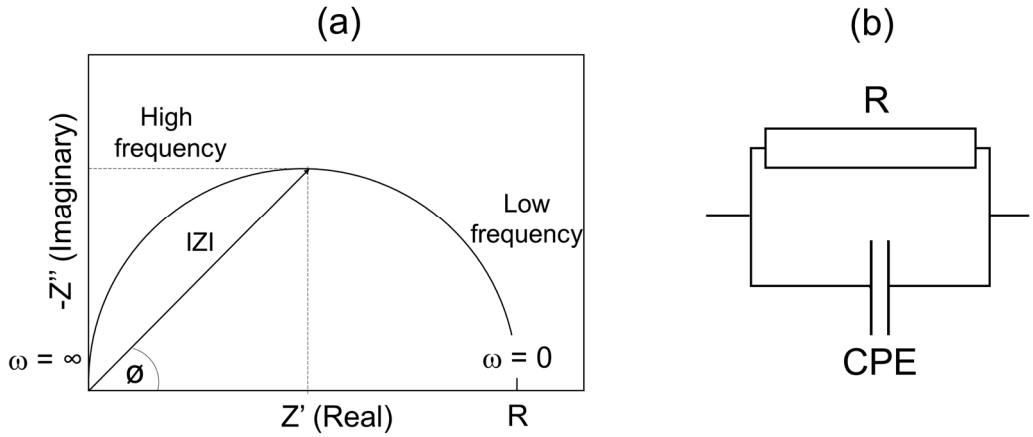

Figure 4.8: (a) Nyquist plot with impedance vector, (b) schematic diagram showing equivalent circuit (R (resistance)-CPE (constant phase element)) [208,209].

To obtain impedance data, an equivalent circuit analysis is employed. An equivalent circuit is a set of resistors and capacitors arranged either in series or in parallel. The constant phase element (CPE) is widely used in equivalent electrical circuits for fitting an experimental impedance data. It is used to replace the capacitor in an equivalent parallel circuit of an R which has a practical advantage for the conductivity.

In the case of mantle minerals (i.e. olivine, anorthite, diopside) and ceramics; pores, cracks or grain boundaries do not contribute significantly to the IS data [210-213].

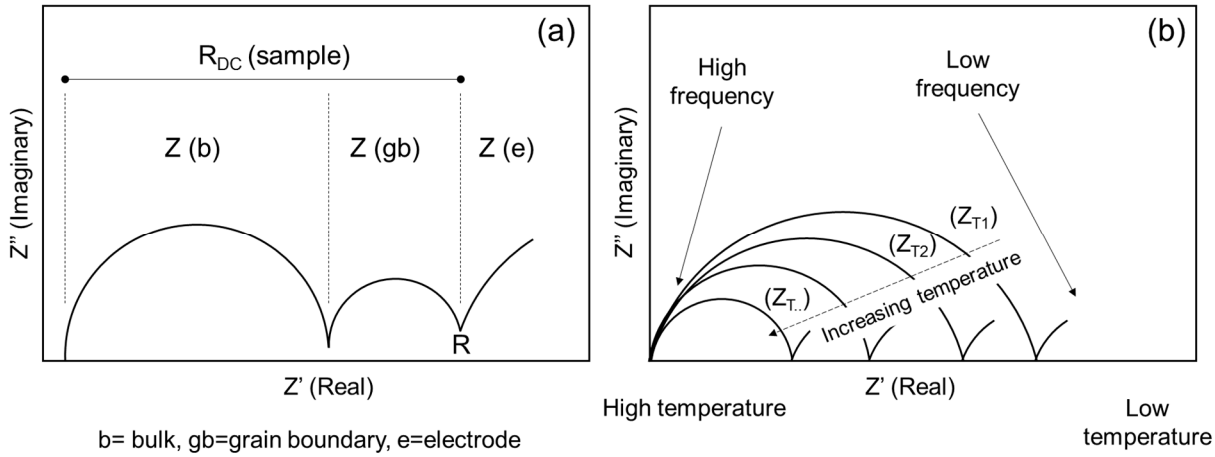

Figure 4.9: (a) Ideal impedance spectra employed by analysing IS data, (b) resistance as a function of temperature [adapted from Ref. 214].

Fig. 4.9a depicts using IS to identify different types of resistance. A Nyquist plot shows the imaginary Z against the real Z of a material. The overall resistance (R_{DC}) of the sample can be broken down into 2 arcs. The arc at the high frequencies is attributed to the bulk resistance (Z_b). The intermediate arc is attributed to the grain boundary resistance (Z_{gb}). The third arc is measured at low frequencies which attributes to the electrode resistance (Z_e). Fig. 4.9b represents a decrease in impedance as a function of temperature suggesting that at elevated temperature resistivity of the material decreases.

To perform IS measurements, both surfaces of the green porcelain pellet were coated with platinum paste and dried for 1h at 110 °C prior to IS measurement. Impedance data were collected from 100 °C to 950 °C at 50 °C intervals using a Solartron 1260 frequency response analyser (FRA), coupled with a Solartron 1296 dielectric interface (Solartron Analytical, Farnborough, Hampshire, UK). A 100 mV-AC current was applied over the frequency range 1 mHz-1.3 MHz, with 30 data points collected per decade; at each point, 10 s integration time was applied for data collection. IS measurement was performed during both heating and cooling conditions to investigate the hysteresis of resistivity. The IS data were analysed using the Zview package (v3.2, Scribner Associates, Southern Pines, NC, USA) to calculate the conductivity of the porcelain sample from the obtained resistivity.

4.8.1 Electrical conductivity

To extract electrical conductivity values from the impedance measurement, an equivalent circuit with R (resistance)-CPE (constant phase element) was used in this study as presented in Fig. 4.8b. In this porcelain sample, only one R-CPE component was used for the fitting of the impedance data, as the grain boundaries contribute little to the overall resistance. The overall resistance (R) of the sample was determined as the interception of the real part (Z') of the impedance at low frequency on the x-axis. The resistances from the impedance were used to calculate the conductivity. The total conductivity (σ) was calculated using Eq. 4.13.

$$\sigma = \frac{1}{R} \cdot \frac{l}{A} \tag{4.13}$$

where R is the resistance obtained from the fitted impedance data, l is the sample thickness, and A is sample area.

As IS was performed to determine electrical conductivity at different temperatures thus the change of the electrical conductivity on temperature can be evaluated by the Arrhenius Equation, Eq.4.14.

$$\sigma = \sigma_0 exp \frac{E_a}{kT} \tag{4.14}$$

where σ_0 is the pre-exponential factor, E_a is activation energy, k is the Stefan-Boltzmann constant, and T is temperature in Kelvin.

4.8.2 Dielectric constant (k) and loss tangent ($tan\ \delta$)

Dielectric constant (k) and loss tangent ($tan\ \delta$) were calculated from the impedance data. From Eq. 4.12, Z' is the real part of the impedance relating to a resistance of the system (R) while Z'' is the imaginary part relating to capacitance as expressed using Eq. 4.15 [215].

$$Z'' = \frac{1}{j\omega C} \tag{4.15}$$

where j=√-1 and ω is angular frequency ($2\pi f$). In this study capacitance (C) is obtained from a Nyquist plot. Then dielectric constant (k) can be calculated using Eq. 4.16.

$$C = k\varepsilon_0 \frac{A}{d} \tag{4.16}$$

where k is dielectric constant, ε_0 is permittivity of the free space (8.854x10^{-12} F/m), A is the area of the sample, and d is the separation of the two plates, either side of the sample.

Loss tangent ($tan\ \delta$) can be estimated using the electrical conduction value and dielectric constant at a particular frequency as presented by Eq. 4.17 [216].

$$tan\delta = \frac{\sigma}{2\pi f k \varepsilon_o} \tag{4.17}$$

4.9 X-ray Diffraction (XRD)

X-ray diffraction is a powerful tool to determine structure of crystals. Generally, X-rays are produced in a vacuum tube by heating a filament (i.e. tungsten, W) to produce electrons via thermionic emission. The produced electrons are accelerated and collide with a metal target i.e. copper by applying a high voltage of 40 kV. Once high energy electrons collide with the Cu target, they excite the electrons in Cu atoms and cause X-ray to emit. Many X-rays are produced during the collision, but the two useful X-rays produced by Cu, namely $Cu_{k\alpha}$, and $Cu_{k\beta}$ correspond to 1.5406 Å and 1.392 Å. However, the 1.5406 X-rays are widely used to determine crystal structure because of their high intensity [217].

When a crystalline material is irradiated with a parallel monochromatic X-ray beam (with high energy electromagnetic radiation (10 eV to 100 keV), the atomic lattice of the materials diffracts the X-ray to specific angles which satisfy Bragg's Law;

$$n\lambda = 2d \sin\theta \tag{4.18}$$

where n is an integer, λ is the wavelength of the X-ray, d is the atomic lattice spacing (d-spacing), and θ is half of the diffraction angles. The crystal structures can be identified against databases using the atomic lattice distances (or peak positions) and peak intensities.

In this study, phase contents of the samples were characterized using a Bruker D2 Phaser diffractometer (Bruker, Coventry, UK). XRD data were collected from 15° to 65°2θ with $Cu_{K\alpha}$ radiation (λ=0.154 nm) at 30 kV and 10 mA with a step size of 0.03° and a count time of 1 s. Diffraction patterns were analysed using commercial software (X'pert high score plus software, PANalytical, Almelo, Netherlands). The phases in the samples were listed as albite ($NaAlSi_3O_8$,

(Triclinic), JCPDS: 09-0466), kaolinite ($Al_2Si_2O_5(OH)_4$), (Triclinic), JCPDS: 14-0164), quartz (SiO_2, (Trigonal, alpha quartz), JCPDS: 65-0466), and mullite ($Al_6Si_2O1_3$, (Orthorhombic), 15-0776). Please note that the samples (CS, DS, SPS and MWS) were ground using a mortar and pestle to obtain fine powder and passing through 325 mesh before performing XRD for mullite crystallite size (section 4.10), chemical composition of mullite (section 4.11) and phase quantification using modified Internal Standard (section 4.12). However, the study of mullite orientation in SPSed samples was performed using polished samples (pellets).

4.10 Mullite crystallite size calculated by Debye-Scherrer's equation

Mullite crystallite size was evaluated from line profile analysis of the (110) reflection. All the observed XRD peaks were approximated by using the Pearson VII functions in commercial software (Origin 2015, OriginLab, Northampton, MA, USA). The Scherrer equation was employed to evaluate the mullite crystallite coarsening. The Scherrer constant (K) of 0.94 was used [147]. Therefore, in this case the Scherrer equation was given in Eq. 4.19.

$$L_{(110)} = \frac{0.94\lambda}{\mathrm{B}\ cos\theta} \tag{4.19}$$

where B is Full Width Half Maximum of the diffraction peak, L is the mullite crystallite size (nm), θ is the diffraction angle from X-ray diffractometer, λ is wavelength of the incident X-ray.

4.11 Chemical composition of mullite using Ban and Okada's method

Mullites formed in porcelains may have different chemical composition compared to mullite formed via solid solution of alumina and silica powder (60 mol.% alumina). This is because mullite in porcelains forms via decomposition of clays and further reaction may occur between liquid phase and the mullite. Ban and Okada [135] used the ratio of integral XRD peak areas of the (220) and (111) reflections to estimate the alumina content (mol.%) of mullite and this method is applicable for both tetragonal and orthorhombic mullite because it uses both of (220) and (111) reflections. The two reflections are suitable for obtaining reliable

data because they have strong intensities, and no overlap with other peaks. Ban and Okada found that the integral area of the two reflections relates directly to the structure of mullite, both atomic positions and chemical composition. The change of area of these two peaks arises from change of mullite chemistry. More Al^{3+} can be accommodated in mullite structure by replacing Si^{4+} at tetrahedral site and creating oxygen vacancies to maintain charge neutrality. When the substitution occurs, position of the cations (Al, Si) changes. However, taking the peak area ratio to determine the chemical composition is not easy since the peak area is governed by crystal structure, elements, substitutions, thermal vibrations, diffractometer geometry, variable or fixed apertures, X-radiation and homogeneity of the sample. In addition, the lattice parameters indicate where the peaks appear in the XRD graph while the structure of the crystals is responsible for the peak intensity. Whether alumina contributes more to (220) than to (111) depends on the electron density, because Al^{3+} has larger atomic radius (68 pm) compared to Si^{4+} (54 pm) so, when S^{4+} is substituted by the larger Al^{3+}, the intensity of the plane is greater. This is described by the term in the structure factor. In summary, when mullite has more alumina in its crystal structure Al^{3+} moves closer to the (220). So, the use of (111) and (220) peaks area ratio suggests that if I_{220}/I_{111} is high, there is a greater number of Al^{3+} and if I_{220}/I_{111} is low, there is a smaller number of Al^{3+}. This calculation is known to be simple and reliable [135]. In this study, the chemistry of mullites formed in the porcelain samples under different sintering conditions was determined using the Ban and Okada method, the calculation is simple as presented in Eq. 4.20.

$$Al_2O_3\ (mol.\%) = 41.77\left(\frac{I_{220}}{I_{111}}\right) + 27.6 \qquad (4.20)$$

where I_{220} and I_{111} are the integrated peak areas of the mullite (220) and (111) reflections. The XRD patterns of porcelain were obtained as presented in section 4.9. The integrated peak area was calculated from Person VII functions using commercial software (Origin 2015, OriginLab, Northampton, MA, USA).

4.12 Phase quantification using modified Internal Standard

XRD is also useful for phase quantification and the reference intensity ratio (RIR) method takes advantage of the XRD data based on measuring the intensity of one or more peaks of the phases of interested and comparing to an added internal standard (i.e. corundum). Quantification is done by mixing corundum and the sample (analyte) at 50:50 wt.% and calculating the RIR ($I_{analyte}/I_{corundum}$) from the most intense peak of the analyte ($I_{(hkl),\ analyte}$) and the most intense peak of corundum ($I_{(113),\ corundum}$). The RIR method can be simplified by discarding the effect of matrix absorption (matrix flushing) [218,219]. The simplified equation of the RIR is shown in Eq. 4.21, which is fully explained elsewhere [220].

$$RIR_{i,s} = \left(\frac{X_s}{X_i}\right)\left(\frac{I_{(hkl)i}}{I_{(hkl)s}}\right) \tag{4.21}$$

where X is the weight fraction, I is integrated peak intensity of the respective peaks in the XRD, and the subscripts i indicates the unknown phase and s is the standard phase, respectively. Furthermore, to quantify the concentration of any phase (X_i), the RIR is used as presented in Eq.4.22.

$$X_i = \left(\frac{X_{cor}}{RIR_{cor}}\right)\left(\frac{I_{(hkl)i}}{I_{(113)cor}}\right) \tag{4.22}$$

where X_{cor} is the weight fraction of corundum, $I_{(113)cor}$ and $I_{(hkl)i}$ are the XRD integrated peak intensity of the most intense corundum peak, and from the most intense peak from phase i, in a 50:50 mixture by weight, respectively. RIR_{cor} is the ratio of $I_{(hkl)i}/\ I_{(113)cor}$.

In this study, CaF_2 is used as the standard instead of corundum because it has no peak overlap with mullite. The standard mullite (mullite, Sigma-Aldrich, Gillingham, UK) is dry mixed with the standard calcium fluorite (CaF_2, Sigma-Aldrich, Gillingham, UK) at 50:50 wt.% in a mortar using a pestle and then the mixed powder is characterised by XRD. The RIR of mullite and fluorite (RIR_{mf}) is calculated from a peak of fluorite (111) and three peaks of mullite (001,220,111) to

minimise any effect of preferred orientation of the mullite, which may occur during the powder mounting in a front-loading holder by applying a shear motion to make the surface of the powder mount smooth and flat [160]. The X-ray background is estimated via the Pearson-VII distribution function (with residual error less than 5%) as shown in Fig. 4.10.

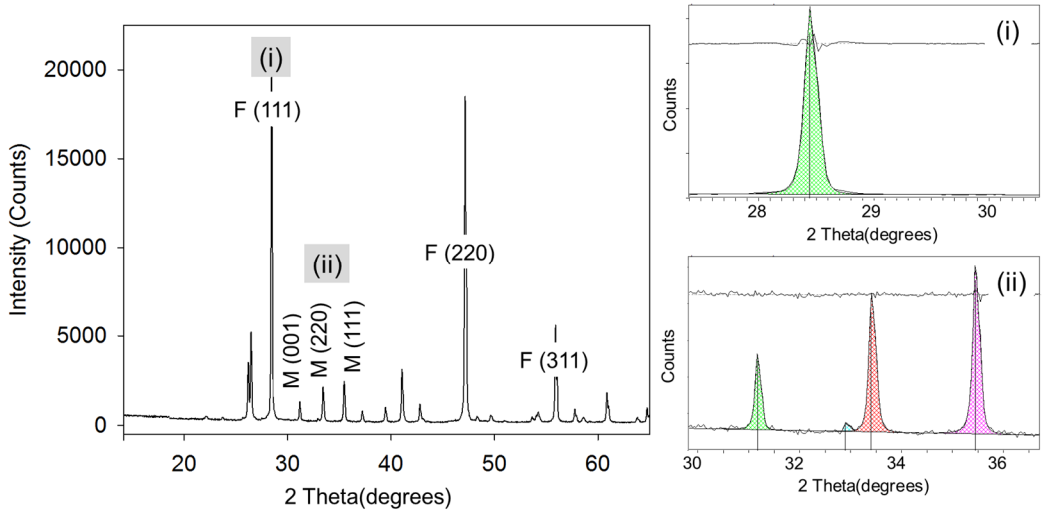

Figure 4.10: XRD pattern of the mixed powder—fluorite (F) and mullite (M). i and ii present the area under peaks for the RIR calculation, (i) fluorite (I_{111}), and (ii) mullite ($I_{001,220,111}$) [author's figure].

RIR_{mf} is calculated using Eq. 4.23.

$$RIR_{mf} = \left(\frac{x_f}{x_m}\right)\left(\frac{I_{(001)m} + I_{(220)m} + I_{(111)m}}{I_{(111)f}}\right) \tag{4.23}$$

$$RIR_{mf} = \left(\frac{50}{50}\right)\left(\frac{18574}{61754}\right) = 0.301$$

where x_f is the weight fraction of fluorite, x_m is the weight fraction of mullite. $I_{(hkl)m}$ is integrated peak intensities of mullite, and $I_{(111)f}$ is integrated peak intensity of fluorite. The RIR_{mf} calculated from Eq. 4.22 is 0.301.

In addition, to determine the reliability of the RIR_{mf}, porcelain samples (conventionally sintered at 1200 °C, 5 °C/min, 15 min dwelled) were mixed with different wt.% of fluorite to determine mullite in the porcelain because the

porcelains sintered at the same temperature produce the same amount of mullite [110,160].

Table 4.2 presents three mixtures of porcelain and fluorite with different wt.% used to determine the reliability of the RIR_{mf}, for example, mixture no.1 is composed of 90 wt.% porcelain and 10 wt.% fluorite. The mixtures were characterised by XRD to obtain integral peak intensity of the particular peaks as mentioned in Eq. 4.23. The wt.% mullite (X_m) in porcelain was then determined using Eq. 4.24.

$$X_m = \left(\frac{X_f}{RIR_{mf}}\right)\left(\frac{I_m}{I_{(111)CaF_2}}\right) \tag{4.24}$$

where X_m and X_f are wt.% of mullite and fluorite respectively, RIR_{mf} is 0.301, I_m is mullite integrated peak intensity found in the porcelain sample ($I_{(001)m} + I_{(220)m} + I_{(111)m}$) and $I_{(111)CaF_2}$ is fluorite peak intensity.

Table 4.2: Quantifying phase contents using RIR.

Mixture no.	$X_{porcelain}$	X_{CaF_2}	I_m	$I_{(111)CaF_2}$	X_m
1	90	10	4677	16476	9.44
2	80	20	3975	27544	9.59
3	50	50	3777	61940	10.13
				Average	9.72
				StDev	0.21

Table 4.2 shows that mullite is found in this porcelain sample (conventionally sintered at 1200 °C, 5 °C/min, 15 min dwelled) at a level of 9.72 wt.% with standard deviation of 0.21 wt.%.

4.13 Scanning Electron Microscopy and Energy Dispersive X-ray Spectroscopy

Scanning Electron Microscopy (SEM) is one of the most useful instruments for analysing microstructural characteristics of materials. An electron beam is used to examine the sample surface instead of the light because electrons give high resolution thanks to their short wavelength (i.e. the wavelength of an electron beam generated from 20 kV is 0.06 nm while an optical microscope uses white light with wavelength about 500 nm). Images are produced by interaction of the

electron beam and the sample (Fig. 4.11a). When an electron strikes the sample, several events occur i.e. production of backscattered electrons, secondary electrons, characteristic X-rays, Auger electrons, cathodoluminescence etc. but the major events of interest regarding to image production are production of backscattered electrons (BSE) and secondary electrons (SE).

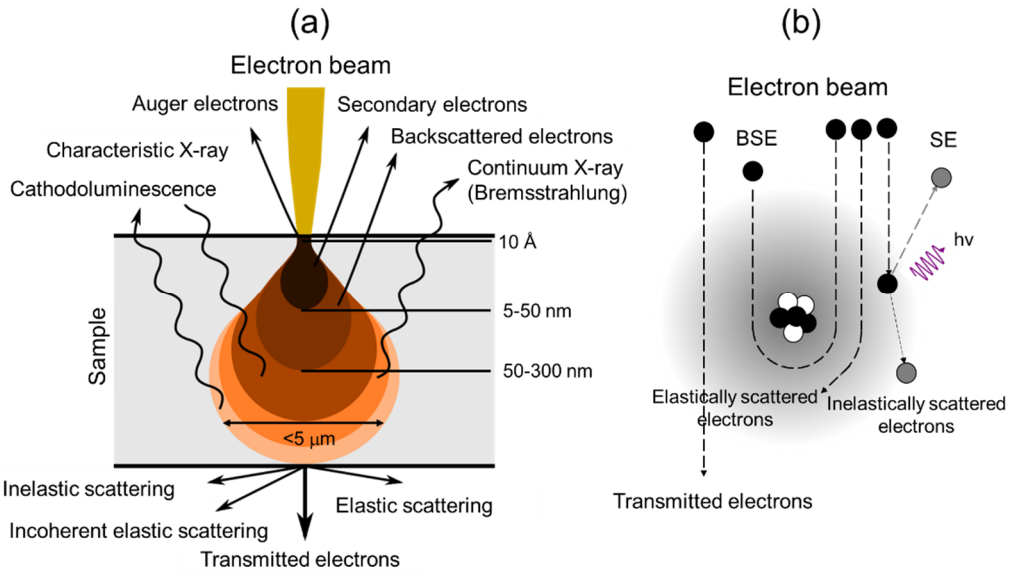

Figure 4.11: (a) The interaction zone of a primary electron beam and the sample bulk showing relative interaction volume, (b) a schematic diagram represents electron beam interacts with an atom [adapted from Ref. 197].

Fig. 4.11b illustrates that electrons (in the incident electron beam) interact with atoms in the sample. BSEs are produced when the electron beam elastically scatters with a sample atom and loses no energy. Thus, BSEs have the same energies as those of the primary electron beam (up to 10's of keV). On the other hand, SEs are generated by inelastic scattering and have low energy (typically ~20 eV). SEs can escape from the sample surface to a detector from a depth of 5-50 nm whilst BSEs come from about 50-300 nm. Therefore, SEs give better resolution of the sample topography than BSE. In addition, BSE signal is dependent on the atomic number of the atoms in the sample it interacts with so BSEs can provide information about the compositional contrast in the sample. The larger atomic number will, therefore, appear brighter as higher energy electrons can reach the BSEs detector [197,221].

Energy dispersive spectroscopy (EDS) takes advantage of the production of characteristic X-rays during the interaction between the electron beam and sample atoms. The high energy electron strikes core shell electrons leaving electron holes then the higher energy electrons from higher energy shell fall to fill the holes producing characteristic X-rays associated with the atom type (element). A typical EDS instrument is capable of detecting characteristic X-rays of elements above boron (Z=5) since a Be window is used. The energy of the characteristic X-ray emission of the K series ranges from 0.185 keV for boron to tens of kilo-electron-volts for heavy elements.

The penetration depth of the electron beam depends on its accelerating voltage and the sample density. For example, the interaction volume at 30 kV for an iron sample (ρ=7.874 g/cm^3, Z=26) reaches a depth of 3.1 μm, and at 5 kV;a depth of 0.16 μm [222].

Generally, the interaction volume (penetration depth x penetration width) of SEM depends on the accelerating voltage and density of the sample. The interaction volume of the SEM can be estimated using the Eq. 4.25-4.26 [223].

$$Penetration\ depth\ (x) = \frac{0.1\ E^{1.5}}{\rho} \qquad 4.25$$

The width of the excited volume (y) can be approximated by

$$Penetration\ width\ (y) = \frac{0.077\ E^{1.5}}{\rho} \qquad 4.26$$

where E is accelerating voltage in kV, and ρ is density of the sample (g/cm^3).

In this study, all samples were 10 nm-chromium-coated using a high-resolution sputter coater with chromium target (Q150T-S, Quorum Technologies, Lewes, UK) before undergoing a SEM-EDS analysis. A SEM (Auriga, Carl Zeiss, Oberkochen, Germany) equipped with an EDS unit (X-Max 20, Oxford Instrument, Abingdon, UK) was employed and the signal was analysed using a commercial software (Inca, Oxford Instrument, Abingdon, UK). Accelerating voltages of 5 and 20 kV were used for all measurements. Working distance was 5 mm. 5 kV was used to give high-resolution due to the presence of nanoscale

mullite. Eq. 4.25 and 4.26 suggest that the interaction volume of mullite (density 3.17 g/cm^3) at 5 kV is about 0.35x0.27 μm (depth x width). So, it can be deduced that the semi-quantitative EDS analysis at 5 kV to determine the chemical composition of the mullite is reasonable because the interaction volume indicates a significant proportion of the mullite needles.

4.14 Transmission Electron Microscopy

Transmission electron microscopes (TEMs) are instruments used to generate images at the nanometre scale revealing ultrafine detail of materials. To achieve high resolution, TEMs operate at high acceleration voltages of 100-200 kV. The electron beam interacts with the sample in different ways—diffraction, transmission, and absorption. High-resolution images are produced by transmitted and diffracted electrons whilst absorbed electrons play a minor role in TEM [197].

4.14.1 TEM sample preparation

TEM samples must be thin enough to allow the incident electron beam to pass through (<100 nm). In this study, the samples were prepared using a grinding and ion milling apparatus [197,224].

Porcelain samples were cut into small 3x3 mm^2 squares with thickness of 0.5 mm using a diamond saw (Fig. 4.12a(i)). The samples were then mounted on metallic stubs and put in a hand grinding jig then polished down to 100 μm thick using 2000-4000 grit-SiC papers (Fig. 4.12a(ii)). The samples were polished again using a dimple grinding machine (Fig. 4.12b) to produce a dimple area with thickness of 20 μm in the centre (Fig. 4.12a(iii)). The samples were then mounted to a copper ring using thermoplastic wax to strengthen the sample during ion milling.

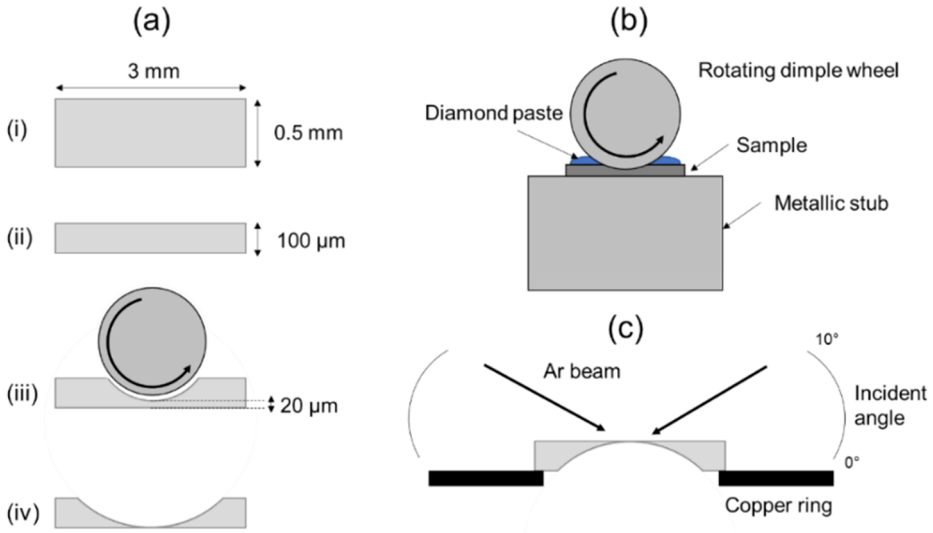

Figure 4.12: Schematic diagram of TEM sample preparation, (a) thickness of the sample at each stage of grinding and polishing, (b) dimple machine, and (c) ion milling machine [adapted from Ref. 197].

The dimpled samples (Fig. 4.12a(iv)) were ion milled in an Ar ion beam thinner (Gatan Precision Ion Polishing System: PIPS™ Model 691, Gatan Inc., Pleasanton, CA, USA) as shown in Fig. 4.12c. The ion beam energies, angles and milling time used are shown in Table 4.3.

Table 4.3: The condition used in the ion milling process (PIPS).

Energy (keV)	Current (µA)	Angle (degree)	Time (min)
5	2	10	90
5	2	8	90
4	2	6	60
3	2	4	60
2	2	2	60

4.14.2 Operation modes

TEMs have two operation modes, the image modes and diffraction modes (DP). The difference between image and diffraction modes is that in diffraction mode, the lenses in the imaging system are adjusted (objective aperture is moved out, the selected-area diffraction (SAD aperture is moved in) allowing the back-focal plane (BFP) of the objective lens acts as the object plane for the intermediate lens (Fig. 4.13a). In image mode, the intermediate lens are readjusted which its object plane is the image plane of the objective lens (Fig. 4.13b) [197,225].

Images obtained via DP can be (1) spots arranged in rings for polycrystalline materials, (2) halos for amorphous compounds and (3) ordered spots for single crystals. When ordered spots for a single crystal are obtained, it is possible to determine the d –spacing of the investigated compounds by using Bragg's law. The investigated compound is then identified for the possible phases present in the system by comparison of the calculated d –spacing with the ones in the PDF from the ICDD database [225].

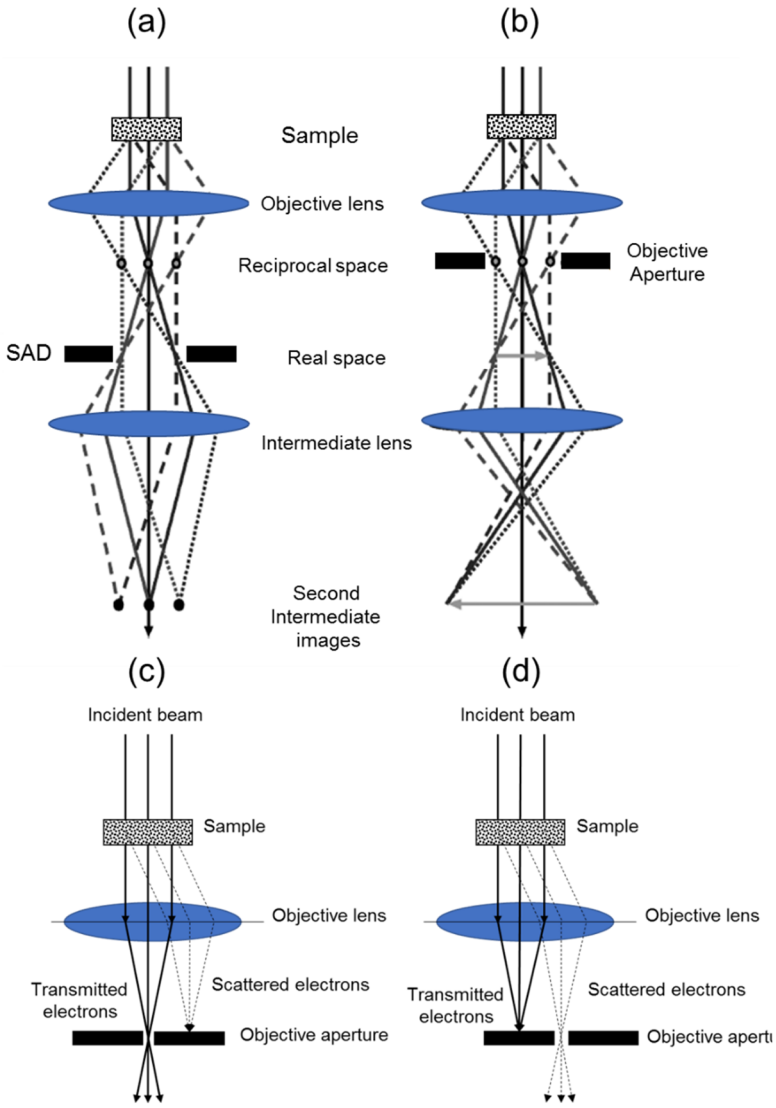

Figure 4.13: The two-operation mode of TEMs, (a) diffraction mode (DF), (b) image mode, (c) a BF image formed from the transmitted electrons, (d) DF image formed with a specific off-axis scattered electrons [adapted from Ref. 197,225].

The two imaging modes in a TEM—bright field (BF) and dark field (DF). In general, BF is used to produce general images while the DF is used to study defects in crystals. BF images are produced by using the transmitted electrons (unscattered electrons) to generate images. In other words, the BF image is a shadow of the sample, more electron transmitted area is brighter. DF images are produced by the scattered electrons which are selected by objective aperture, more scattered electrons detected is brighter (Fig. 4.13c and d).

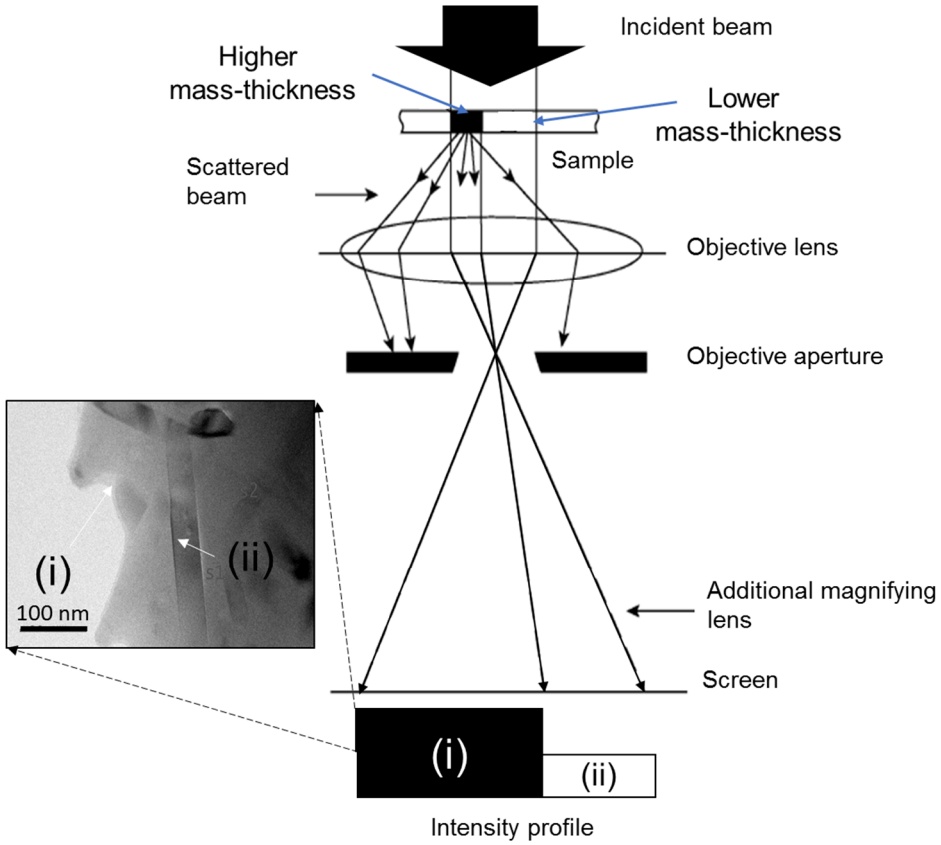

Figure 4.14: BF image formation in the TEM showing different intensity of the image depends on mass-thickness contrast (i) aluminosilicate glass, (ii) mullite. [adapted from Ref. 197,225].

The contrast of phases present in a sample depends on the thickness and density (mass-thickness contrast) (Fig. 4.14) [22,197]. For example, in BF imaging thicker areas appear dark because fewer electrons are transmitted. Consider the same thickness areas, high atomic number produce dark region in the resulting images because there is more probability of interaction, or diffraction, between the electrons and the nucleus in high atomic number areas (Fig. 4.14). Fig. 4.14 shows

the mass-thickness on a BF image generation of a porcelain. The low intensity area (i) is glass, which has lower density compared to mullite needle (ii). In comparison to BF imaging, DF imaging acts in a opposite way, thicker and high atomic number areas result in bright region in the resulting images (Fig. 4.14).

In this study, JEOL 2100Plus microscope (JEOL, Tokyo, Japan) was used to examine mullite in fired porcelain samples. Double tilt holder was employed, allowing samples to be tilted along two axes. Bright-field (BF) micrographs and selected-area diffraction (SAD) patterns were also taken. The TEM was operated at an accelerating voltage of 200 kV. Imaging in TEM was done primarily in the bright-field and SAD modes. The SAD patterns were indexed by matching the d_{hkl} values with PDF reference patterns obtained from the ICDD database, thanks to Dr. Ayan Bhowmik at Imperial College London.

4.15 Physical property measurements

Apparent bulk density (ABD) and water absorption (WA) were obtained using an immersion method based on a modified ASTM standard (C20-00). Bulk density was calculated using Eq.4.27 [226].

$$ABD = \frac{D}{(W - S)} \tag{4.27}$$

where D is dry weight (weight of the sample after drying at 110 °C for 24 h), W is saturated weight which has been saturated with water after removing of external-residue water, S is suspended weight after boiling for 2 hours and suspended in water. Water absorption (WA) was calculated using Eq. 4.28.

$$WA = \frac{(W - D)}{D} x100 \tag{4.28}$$

At least 5 samples were used for each measurement to calculate the standard deviation of the average values. Although the 5 pellets were crushed to produce 10 samples and the 10 broken-samples were used to determine ABD and WA. In this sense, the mean and standard deviation value are sufficient to represent the result

since the WA and ABD are continuous data (not binary). It has been shown to be accurate for small sample sizes [227,228]. In this study, descriptive statistic (mean and standard deviation) was used to present the experimental data to show how the average value and spread of data would be. In addition, green density of the porcelain sample was determined in the same fashion but using kerosene with density of 0.81 g/cm^3 as the medium.

4.16 Porosity analysis

While average porosity may not be the best way to present the mechanical properties of the porcelain, it is acceptable and well established as indicated by numbers of references [229-236]. Stathis et al., [229] reported that the bending strength of sanitaryware porcelain decreased with increased total porosity with no effect of pore size or shape was reported. Kurama et al., [230] demonstrated that Young's modulus of porcelain tiles measured by ultrasonic testing was solely dependent on total porosity values. Cannillo et al., [231] studied a relationship between elastic modulus and total porosity at the different part of porcelain tiles. They found that total porosity significantly controlled the elastic modulus of the porcelain tile samples. Maity et al., [232] was another example of using total porosity as an indicator to develop high strength whiteware body. They concluded that total apparent porosity affected modulus of elasticity of the whitewares, the higher porosity value, the lower modulus of elasticity. Pérez and Romero [233] also pointed out that lower porosity of fired porcelain tiles produced higher values of bending strength. In addition, a decrease of 8% total porosity increase 34% bending strength of the porcelains. Batista et al., [234] compared fracture toughness and Young's modulus of bone china and hard porcelain using percentage porosity. They concluded that the hard porcelain had lower fracture toughness but higher Young's modulus, which was believed to result from its lower porosity.

Nyongesa et al., [235] studied thermal shock in porous clay ceramics using total porosity. They found that residual strengths after thermal shock were strongly dependent on the volume fraction of porosity. Thermal shock resistance parameter (an ability to resist crack propagation under loading and reduction of strength on thermal shocking), in addition, increased with an increasing volume

fraction of porosity while the room-temperature residual strengths decrease with increasing porosity fraction.

Martín-Márquez et al., [236] studied effect of microstructure (open and closed porosity and mullite) on bending strength, Young's modulus, Vickers hardness, and fracture toughness of porcelain stoneware. Their results showed that by plotting the bending strength against percentage porosity, the decreased bending strength resulted from increasing open porosity but independent on closed porosity. They also concluded that Young's modulus and Vickers hardness had similar behaviour to bending strength and these properties were controlled by the same factors (porosity), no effect of pore size or shape was reported.

Thus, in this study, the effect of average percentage porosity on mechanical strength of porcelain is considered rather than the pore size distribution. In this study, we attempt to understand the effect of firing conditions (heating rate, dwell time and temperature) on apparent bulk density and water absorption and the water absorption is directly related to the percentage open porosity, not the pore size.

ImageJ® (National Institute of Mental Health, Bethesda, MD, USA) was used to determine pores (2D pores) in samples via SEM or optical microscopy images. A segmentation process is required to convert grey scale images (standard 8-bit digital images having 256 intensity levels, ranging from pure black (lowest intensity of 0) to pure white (highest intensity of 255) into binary images (black and white) based on the grey scale histogram. An automatic thresholding function, which is calculated based on the Isodata algorithm [237], integrated in ImageJ is employed to binarize the images. The images are converted into black and white in which white usually represents solid phase and black represents pores. After a well-binarized image is obtained, the Analyze function in ImageJ is employed to calculate the percentage area of interest (i.e. black-porosity) present in the images.

To determine percentage porosity of a sample begins with scale setting (Fig. 4.15a) and selecting the area of interest (Fig. 4.15b). Fig. 4.15a shows that the 250 pixels are equal to 50 µm (yellow line above the SEM scale bar) while Fig. 4.15b shows the selected area used to calculate the percentage porosity.

To transform the selected image (grey scale image) to a binary image (black and white), requires using Image>Adjust>Threshold (Fig. 4.16a,i). At first, the automatic threshold value is generated based on the Isodata function (yellow box in Fig. 4.16a,i). The red area (Fig. 4.16a, ii), which represents pores, is dependent on the threshold value.

However, if the automatic thresholding value is not satisfied by the visual examination, the threshold value can be manually optimised (red box in Fig. 4.16a, i) to obtain the best red area according to the actual pores. So, the threshold value needs to be carefully adjusted. After applying the best threshold value, the binary image of the selected area is obtained (Fig. 4.16a, iii), which contains black (pores) and white (solid phase).

To calculate the percentage area of pores, requires using Analyze>Set Measurements (enable Area, and Area fraction)>Measure (Fig. 4.16b, i).

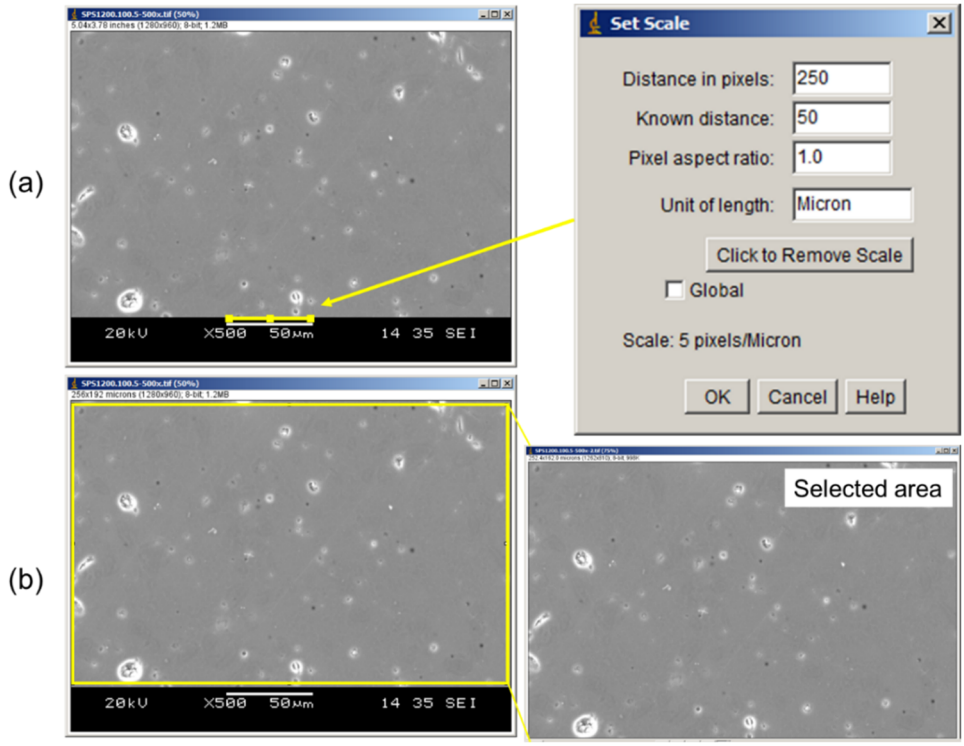

Figure 4.15: Image preparations, (a) scale setting, (b) image area selection [author's figure].

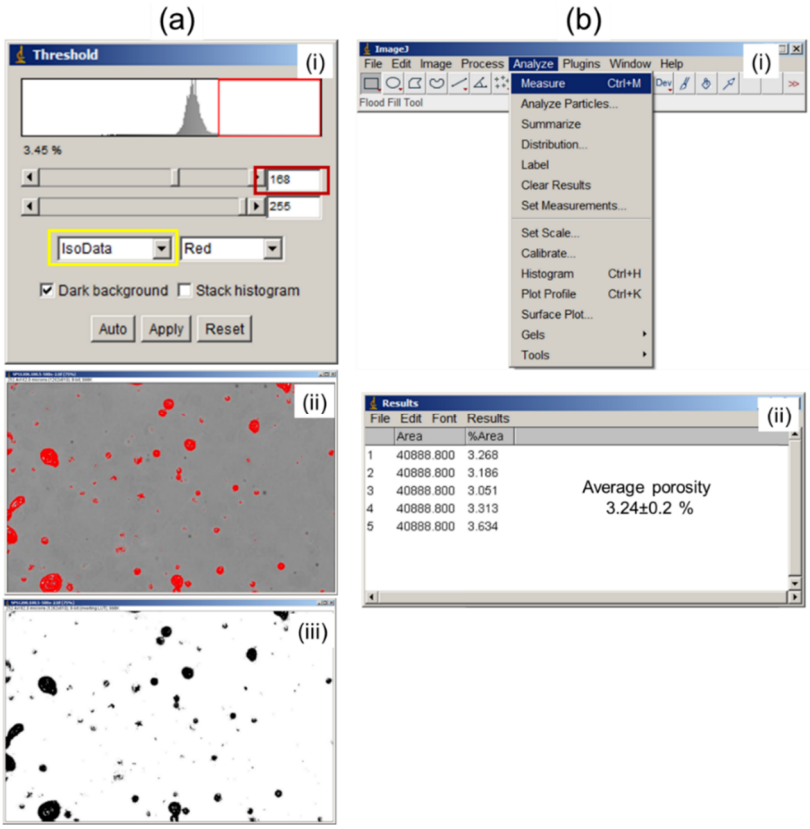

Figure 4.16: Calculation of percentage porosity of the SPSed 1200 °C, 5 min dwell sample, (a) segmentation with thresholding window, and (b) Analyse window [author's figure].

In this study, three areas of each sample were chosen, and 5 replications were made to obtain average and standard deviation of porosity for each area by automatic and manual adjustment of the threshold (Fig. 4.16b, ii). Features smaller than 5 μm^2, which is about 10 pixels on the images (yellow arrow in Fig. 4.17), were not included as pores because features at this size could be mistaken for background noise.

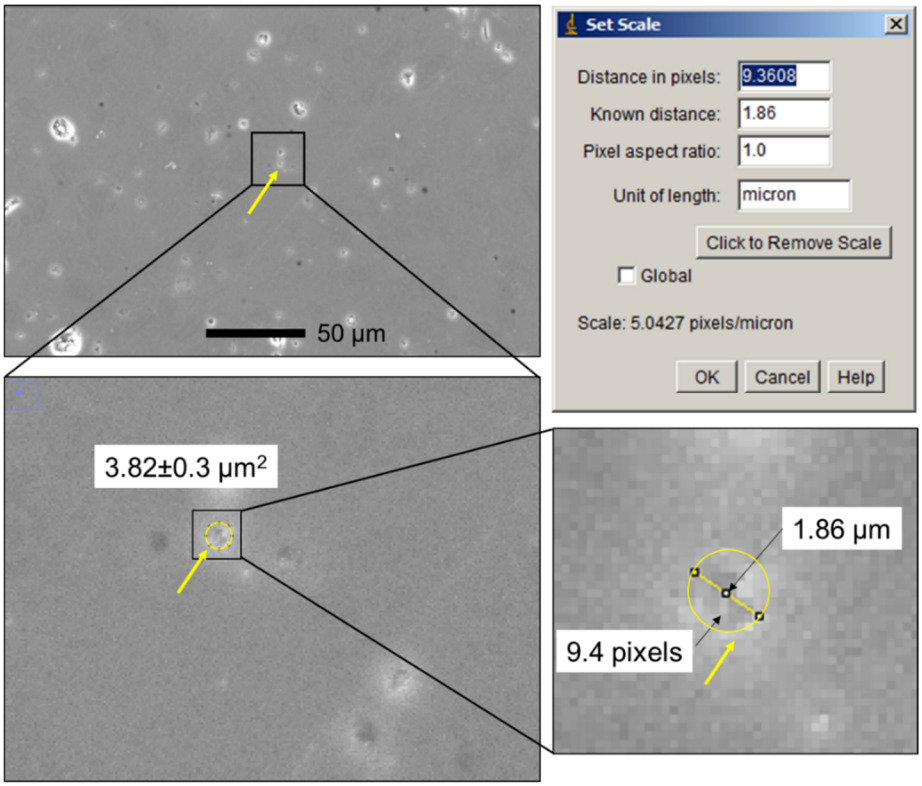

Figure 4.17: Small features (≤5 µm² or 10 pixels) presented as yellow arrow and found in the SPSed 1200 °C, 5 min dwell [author's figure].

4.17 Mechanical testing

4.17.1 Diametral compressive strength

Diametral compressive strength (DCS) or diametral tensile strength (DTS) are alternative measures of strength of brittle materials with no plastic deformation [238]. They are simple, reproducible, and reliability techniques and have been used to test the tensile or compression strength of several materials such as rocks [239], ceramics [240] and glass-ceramics [241]. The load applied in DCS generates compressive stress at the top and bottom of the sample while tension is generated in the samples (Fig. 4.18).

DCS is different from bending strength testing in that latter employs rectangular bar samples subjected to three- or four-point bending. The tensile stress is generated on the lower surface of the sample because the compressive stress is generated on the upper surface, where load is applied [238,240].

DCS is done by subjecting pellets (or discs) of samples to compressive loads in the diametral plane until the samples fail. The maximum load is used to calculate the strength as shown in Eq. 4.29.

$$\sigma_t = \frac{2P}{\pi DT} \tag{4.29}$$

where σ_t is diamentral strength, P is the maximum applied load, D is sample diameter, and T is sample thickness.

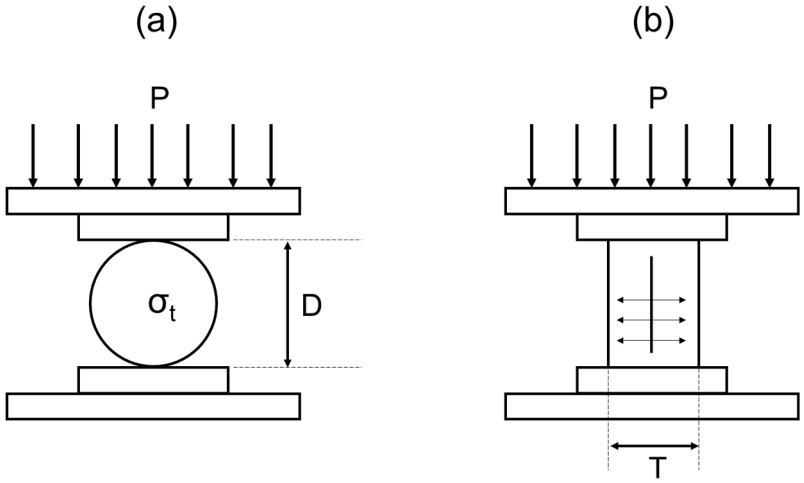

Figure 4.18: Schematic diagram of the experimental setup of DCS, (a) front view, (b) side view [author's figure].

In this study, a diametral compressive strength (DCS) measurement of the sintered samples under different sintering condition was made using a Zwick/Roell Z010 (Zwick-Roell, Ulm, Germany) at a crosshead speed of 1 mm/min with load applied until sample failure. Please note that the DCS was only performed for the conventionally sintered samples (CS) and direct sintering sample (DS) because this test was intended to compare mechanical properties of these two processes only. The sample dimension used in the DCS is ~12 mm diameter and ~7 mm thick (see more detail in section 4.18.1 and 4.18.2). 5 samples of each process were used to calculate the mean and standard deviation. The report of the mean and standard deviation of the experimental data (continuous data, not categorical data) is sufficient for the small number of samples because a practical way, number of samples is limited, cannot run many experiments. This allows to

calculate the sample mean and standard deviation [242]. In this study, descriptive statistic (mean and standard deviation) was used to present the experimental data to show how the average value and variability of data. Please note that the small number of samples can increase the spread of data compared with the large number of samples [242].

Furthermore, compressive strength in ceramics is known to increase with the crosshead speed because ceramics exhibit slow crack growth [243,244]. At the slower crosshead speed, more time allows to store strain energy to generate cracks, leading to more crack propagation with lower stress. On the other hand, at high crosshead speed, materials need more strain energy to generate cracks. Thus, at high crosshead speed may cause overestimation of DCS while at too low crosshead speed may cause underestimation of the strength. It has been suggested that reasonable crosshead displacement rates for metal tests are ~2 to 3 mm/min. Polymers may be tested between 2 and 500 mm/min. Ceramic and inorganic glasses are usually tested at cross head speeds of 1-2 mm/min. In other words, the greater the expected elongation of materials, the higher the crosshead speed [245,243]. Thus, in this study, 1 mm/min crosshead speed was used to determine diametral compressive strength.

Weibull testing would have required 10-15 samples as a minimum. It was not chosen as there was insufficient material to prepare this number of samples

4.17.2 Vickers hardness and fracture toughness

Indentation hardness test measures an ability of materials to resist plastic deformation when they are subjected to a penetration load, it is usually done at a microscale. Hardness of materials is not an intrinsic property and it is dependent on the measurement procedure such as Rockwell, Brinell, Vickers, and Knoop hardness testing [246].

The Vickers hardness (H_V) is calculated from the size of imprint produced by a square-based pyramid diamond indenter (with an angle of 136° between the opposite faces) on the sample surface. The indenter is pressed into the surface of the sample at load ranging up to 120 kgf to produce size of the imprint <0.5 mm. The diagonal lengths of the imprint (d) are measured (Fig. 4.19a) then the Vickers hardness (H_V) is calculated by Eq. 4.30 [247].

$$H_V = \frac{1.8544P}{d^2} \tag{4.30}$$

where P is the applied load (kgf), and d is the length of diagonal.

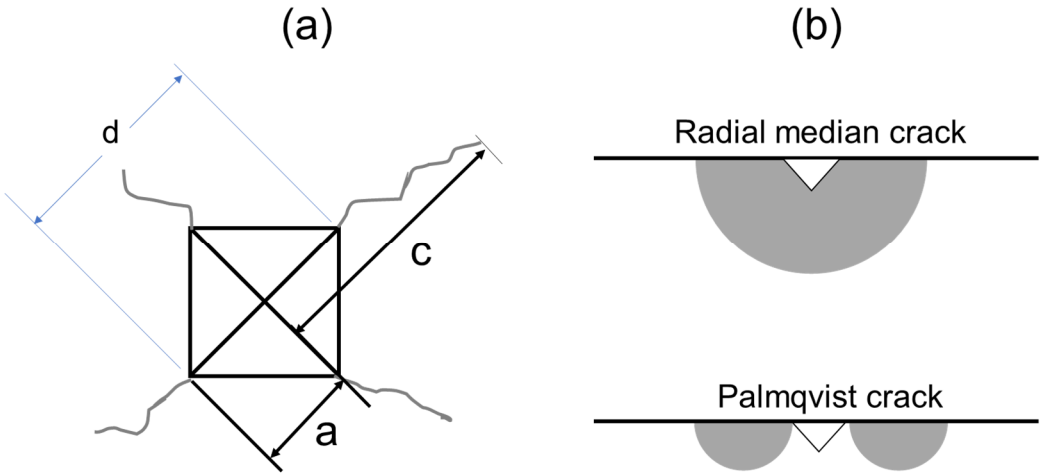

Figure 4.19: (a) Cracks generated by the indenter and the measurement parameters, (b) the two types of cracks generated in porcelains [adapted from Ref. 248].

In this study, Vickers hardness testing (H_V) was used to evaluate the hardness and fracture toughness of the porcelain samples because it is simple, economical, and reliable. In porcelains, the cracks generated by an indenter can be classified into two types including radial median cracks (half penny) and Palmqvist cracks (Fig. 4.19b). The half penny crack is used to measure low toughness porcelains while the Palmqvist is for high toughness porcelains [246].

The equation used to calculate fracture toughness (K_{IC}) of the samples is derived from Evans and Charles as shown in Eq. 4.31 [249].

$$K_{IC} = 0.16(H_V)(a^{\frac{1}{2}})(\frac{c}{a})^{-3/2} \tag{4.31}$$

where H_V is Vickers hardness (GPa), a is half of the indentation impression diagonal length and c is the crack length measured from the centre of the indentation to the crack tip (Fig. 4.19b) [249]. In addition, the hardness is strongly dependent on the indentation load, the hardness decreases as the indentation load

increases because when a high magnitude of the load is applied, the indenter penetrates through the surface of the sample, cover larger area and reaches the deep microstructure of the materials. On the other hand, when a small magnitude of the load is applied, the indenter may not penetrate and reach the deep microstructure. Thus, the hardness of the same materials can be different for different applied load. 1 kgf is used in this study since it has been shown to be suitable for porcelains because this indentation load satisfies the requirement that the pattern be well developed (c>2a) [246].

The duration of the indentation is also needed to ensure that the loading is stationary and to prevent dynamic loads, which will enlarge the indent size leading to inaccurate hardness reading. The maximum duration of the indentation is 10 s which is suggested by ASTM E384-17 [247].

Spacing of indents is also important because indentation produces plastic deformation and a stress field around the indent. If the spacing is too small, the new indent will be affected by the strain field around the previous indent. The stress field produced by the indentation is about the crack length ($2C_0$) as presented in Fig.4.20. Fig. 4.20a depicts a typical indent crack system in brittle solids with 'PZ' indicates plastic zone; 'RC' indicates ring crack; 'C_0' is median indent crack size; 'A' represents prospective locations of radial and ring crack origin, and 'C' represents the location of lateral crack initiation. Thus, the stress field under indent is about $2C_0$. In the brittle materials, i.e. calcium magnesium aluminosilicate and soda lime silica glass, C_0 is directly proportional to the indentation load applied (P); $\log C_0 \approx \log P^{2/3}$ [250].

The spacing between indentations is at least 2.5 Dv (where Dv is Vickers indenter diagonal) as also suggested by ASTM E384-17 [247]. In this study, the indent spacing was at least 3 times Dv and at least 2 times from the crack tip. Fig. 4.20 shows SPSed sample sintered at 1200 °C, heating rate 100 °C/min, and dwell 5min. Thus, the measurement of each indent was not interfered by others. Also, the indentation was done on the dense area, so the effect of pores should be minimal.

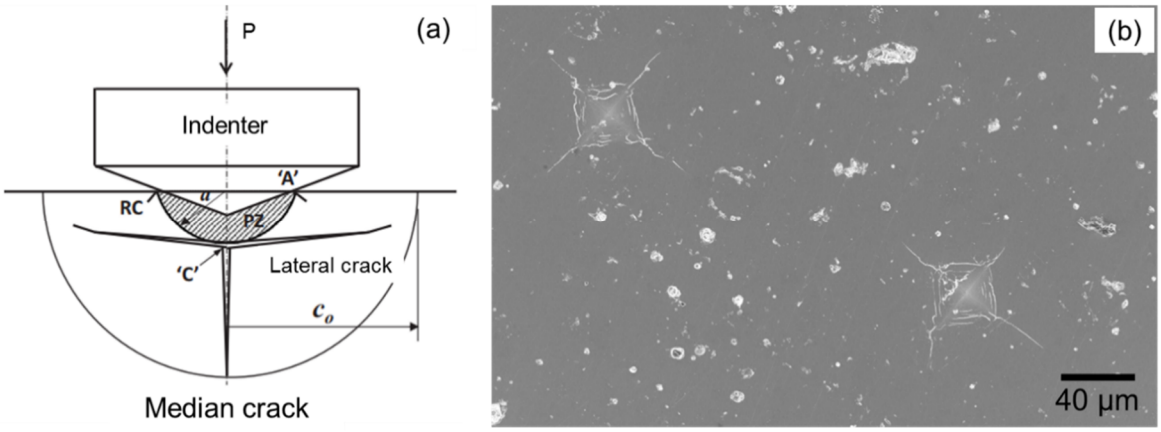

Figure 4.20: (a) Schematic diagram shows stress field produced by the indentation [250] and (b) the spacing between indentations made on SPSed sample sintered at 1200 °C, heating rate 100 °C/min, and dwell 5 min [author's figure].

15 indents were made for each sample and used to calculate the average value and standard deviation using a microhardness tester Zwick/Roell Indentec ZHV (Zwick GmbH, Ulm, Germany) integrated with computer software at 1 kgf load (9.8 N), and loading duration of 10 s. The report of the mean and standard deviation of the experimental data is sufficient for the small number of samples as addressed in section 4.17.1. The sample surface, in addition, was polished finish using 400 grits SiC paper in order to minimise errors from the measurement of the a and c parameters. However, some indentations produced crack length <2a which may be a source of the Vickers hardness and fracture toughness measurements error.

4.18 Sintering of porcelain samples

4.18.1 Conventional sintering (CS)

Porcelain pellets were produced by uniaxially cold-pressing at 35 MPa in 13 mm diameter and 7 mm thick in a steel die, each pellet weighs 2±0.05 g. The pellets were also dried overnight at 110 °C and stored in an oven until further experiments. Conventional sintering was performed by heating porcelain pellets in a front-loading box furnace (Carbolite CWF 1200, Carbolite, Sheffield, UK) using 5 °C/min to sintering temperatures of 1150, 1175 and 1200 °C and dwell for 15 min. 5 pellets were produced for each sintering condition. The sample then was

cooled to 700 °C at 30 °C/min followed by natural cooling in furnace to room temperature. The sintered samples were used for further investigations.

4.18.2 Direct sintering (DS)

Porcelain pellets were produced by uniaxially cold-pressing using the same condition to the CS samples and 5 pellets were produced for each sintering condition. Direct sintering was performed by transferring porcelain pellets directly into a preheated front-loading box furnace (Carbolite CWF 1200, Carbolite, Sheffield, UK) at sintering temperatures of 1150, 1175 and 1200 °C. All samples were dwelled for 15 min at the peak temperatures then was cooled to 700 °C at 30 °C/min followed by natural cooling in furnace to room temperature. The sintered samples were used for further investigations.

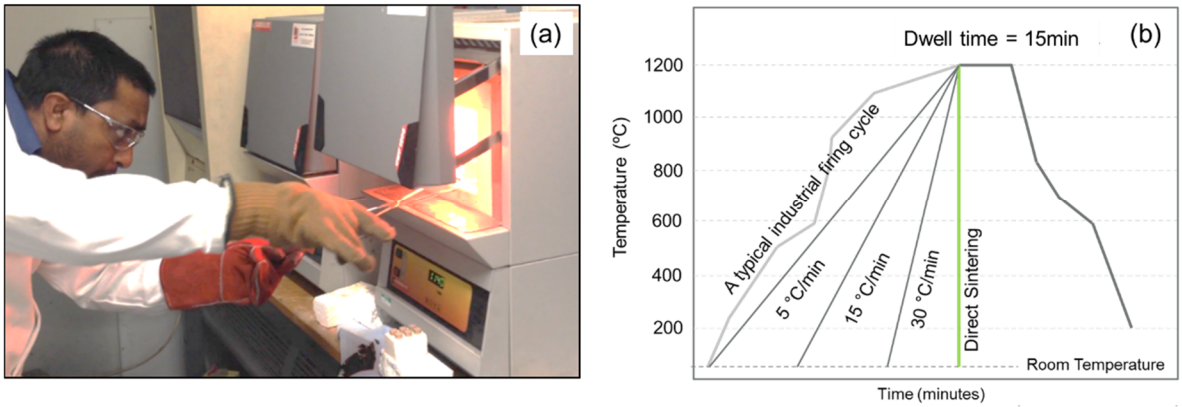

Figure 4.21: (a) Photo shows insertion of samples in the preheated furnace, and (b) temperature-time profiles with respect to change in heating rates [author's figure].

4.18.3 Spark plasma sintering (SPS)

Spark plasma sintering of the porcelains was conducted using the SPS furnace at Queen Mary University London (FTC HP D20; FCT Systeme GmbH, Rauenstein, Germany) (Fig. 4.22a). The SPS has integrated computer software to input sintering conditions and retrieve post-sintering data for further analysis.

The porcelain powder was loaded into a 20 mm diameter graphite die (Fig. 4.22b) and sandwiched between 0.3 mm thick graphite foils. The die was placed between the graphite punches which act as electrodes, and graphite felt was also wrapped around the die to reduce heat loss. A constant vacuum of 5 Pa

was used during the sintering. Three different SPS processing temperatures are used, 1000, 1100 and 1200 °C, with a constant heating rate of 100 °C/min, constant dwell time of 5 min and constant pressure of 25 MPa (the pressure is applied cold and left on until the end of the processing to study the effect of temperature).Four dwell times were also used, 0, 5, 10 and 15 min, at 1100 °C to study the effect of time. The samples were then cooled to room temperature at 100 °C/min. Sample temperature was measured using a pyrometer focused inside a hole in the top punch at a distance of 4 mm from the sample.

One sample was produced for each sintering condition due to the high cost of each experiment. However, physical and mechanical properties measurement were done in various point of the samples. However, the sample was examined at various points across the sample body. Thus, each sample was representative of the sintering condition. SPSed samples were also polished using silicon carbide papers to get rid of any graphite foil contamination. The graphite contamination was examined by visual inspection.

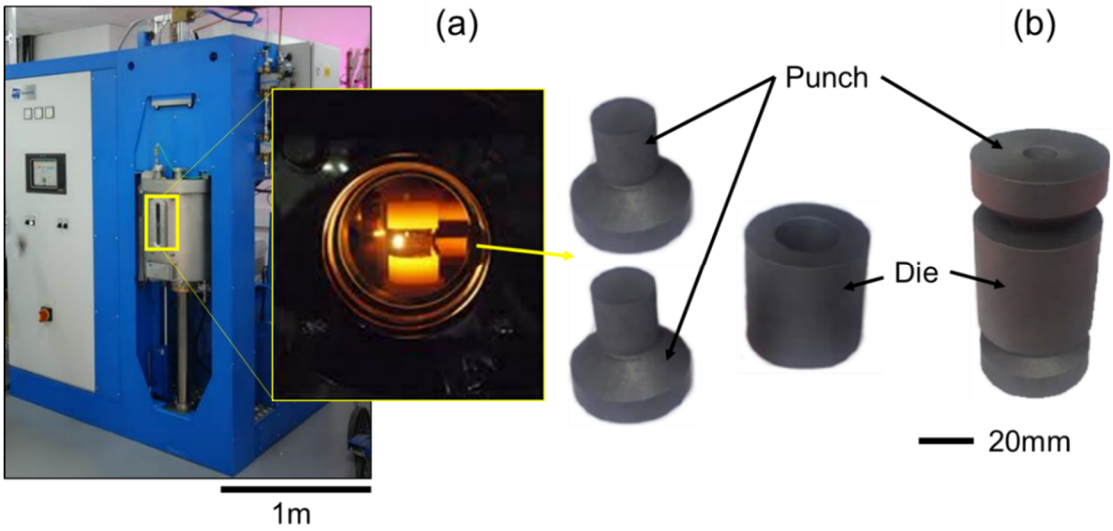

Figure 4.22: (a) The SPS machine, and (b) graphite die and its assembly [author's figure].

4.18.4 Microwave sintering (MWS)

The microwave sintering process was done in a collaboration with the Instituto de Tecnología de Materiales (ITM) and Instituto de Aplicaciones de las Tecnologías de la Información y de las Comunicaciones Avanzadas de la

Universitat Politécnica de Valencia (ITACA) at Universitat Politécnica de Valencia, Spain. Fig. 4.23a shows an MWS components including magnetron, waveguide, tuner, sample cavity and pyrometer. The basic operation of MWS is that microwave energy produced by the magnetron (microwave power source) then is transported to the sample cavity by the wave guide. The tuner is used to match the impedance between the sample (in the cavity) and the microwave power source.

Porcelain pellets used in the microwave sintering process were produced as in the DS experiments. One sample was produced for each sintering condition due to the high cost of each experiment. However, physical and mechanical properties measurements were done at various points of the samples. Thus, each sample was representative of the sintering condition. The pellets were sintered under air in a single mode cylindrical microwave cavity operating in the TE_{111} mode at a resonant frequency of 2.45 GHz (Fig. 4.23a). The TE_{111} mode is a fundamental mode of cylindrical cavity, which is widely used for material property characterisation [251]. In short, the electric field vectors are perpendicular to the cavity with the maximum field magnitude at the centre, where the samples are located (Fig. 4.23b) [252,253] thus the microwave power is greatly absorbed. The cavity has radius of 104 mm, and 200 mm height, which contains a quartz tube as the sample holder, the sample was being heated in the quartz tube (Fig. 4.23c).

The final temperatures reached were 850, 900, 1000 and 1100 °C using a heating rate of ~30 °C/min with 5 min of holding time at the respective temperatures. The temperature of the sample was monitored using an infrared radiation thermometer (Optris CT-Laser LT, 8–14 μm), focused on the sample surface as presented in Fig. 4.23a.

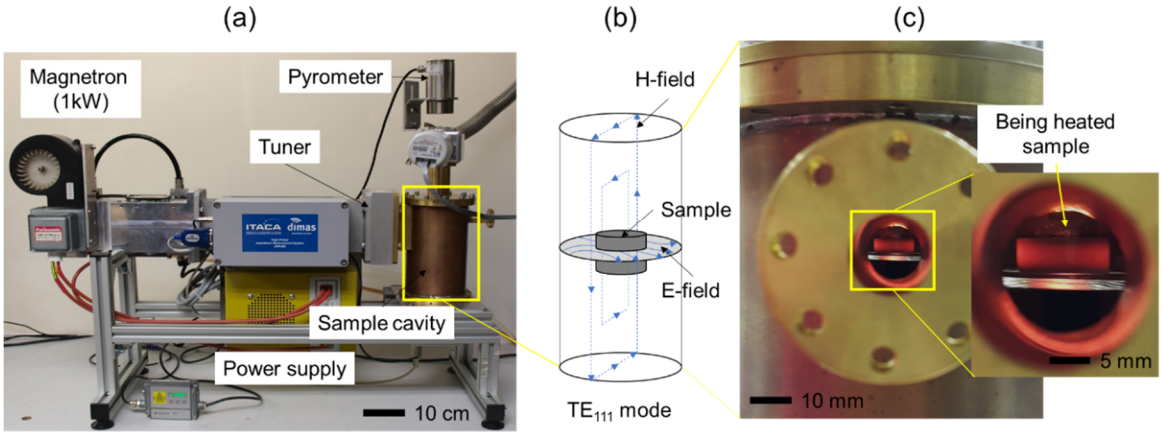

Figure 4.23: (a) MWS system integrated with a computer software, (b) E-field distribution in TE_{111} mode cavity, and (c) the sample was being heated in the quartz tube [author's figure].

4.18.4.1 Pyrometer calibration

Sample temperature monitoring in a microwave cavity not possible by using a thermocouple since the thermocouple can interfere with the process. To determine the sample's temperature and control the heating rates during microwave sintering, a pyrometer was used to monitor real-time temperature information. Pyrometers measure temperature of objects using the Stefan-Boltzmann's law, which relates to thermal radiation (j) and temperature (T) of the objects. In this sense, thermal radiation of objects also relates to emissivity (ε) of the objects as presented in Eq. 4.32.

$$j = \varepsilon\sigma T^4 \tag{4.32}$$

where σ is the Stefan-Boltzmann constant (5.670×10^{-8} $W \cdot m^{-2} \cdot K^{-4}$).

In this study, emissivity of porcelain sample at elevated temperature (800 and 1200 °C) was determined using an Optris CT Laser 2MH CF2 pyrometer (Optris GmbH, Berlin, Germany). A porcelain pellet was heated at 5 °C/min to the given temperatures and dwelled for 15 min at each temperature before the emissivity was measured (in an electrical laboratory furnace in air). The emissivity and temperature results are presented in Table 4.4.

However, emissivity of materials also depends surface conditions i.e. roughness and viewing angles but both were kept the same during the

measurement to minimise the error. In this study, the accuracy of the pyrometer was considered as ±5 °C, since the maximum difference between pyrometer and furnace temperature was 3 °C at the 1000 °C of furnace temperature (Table 4.4).

Table 4.4: Emissivity of the porcelain sample at the temperature range of 800-1200 °C.

Furnace temperature (°C)	Transmission (t)	Emissivity (ε)	Pyrometer temperature (°C)
800	1	0.980	800±1
900	1	0.962	900±2
1000	1	0.957	1000±3
1100	1	0.956	1100±1
1150	1	0.980	1150±2
1200	1	0.983	1200±1

4.18.5 Flash sintering (FS)

Flash sintering was performed in the Department of Materials, University of Oxford. The porcelain powders were uniaxially pressed to pellets at 35 MPa to 13 mm diameter and 2 mm thick dimension. One sample was produced for each sintering condition due to the high cost of each experiment. However, the sample was examined at various points across the sample body. Thus, each sample was representative of the sintering condition.

The pellets were coated using Pt paste on both sides for establishing homogeneous electrical contacts. Pt wires (0.5 mm diameter) were bent making spiral coils and used as electrical conductors (Fig. 4.24a). The pellets were sandwiched between the two Pt wire spirals and some platinum paste was used to ensure homogeneous electrical connection. An alumina casing was used to provide a small pressure (~0.1 MPa) making better electrical conduction (Fig. 4.24b).

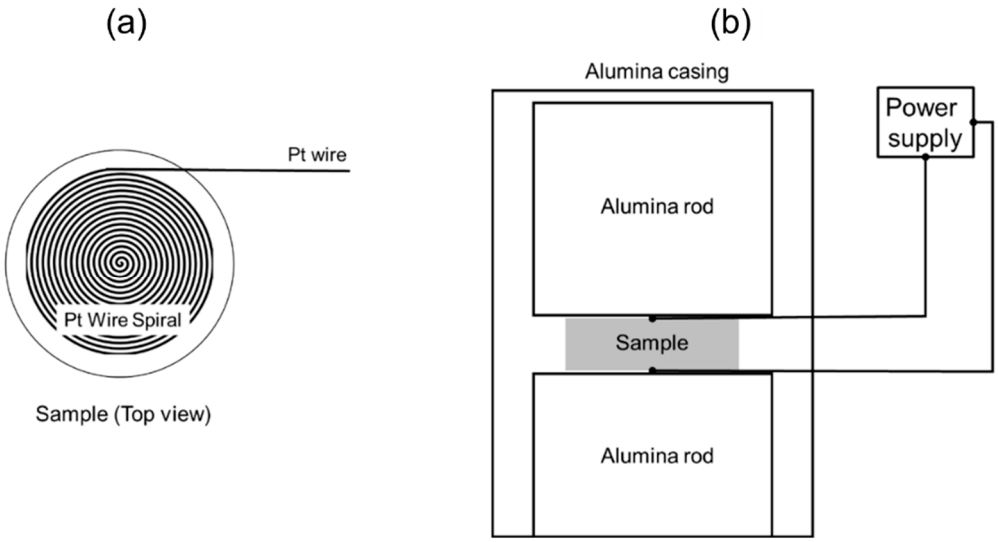

Figure 4.24: Experimental setup of FS, (a) Pt spiral coils used as electrical conductors, and (b) the porcelain sample in the alumina casing [author's figure].

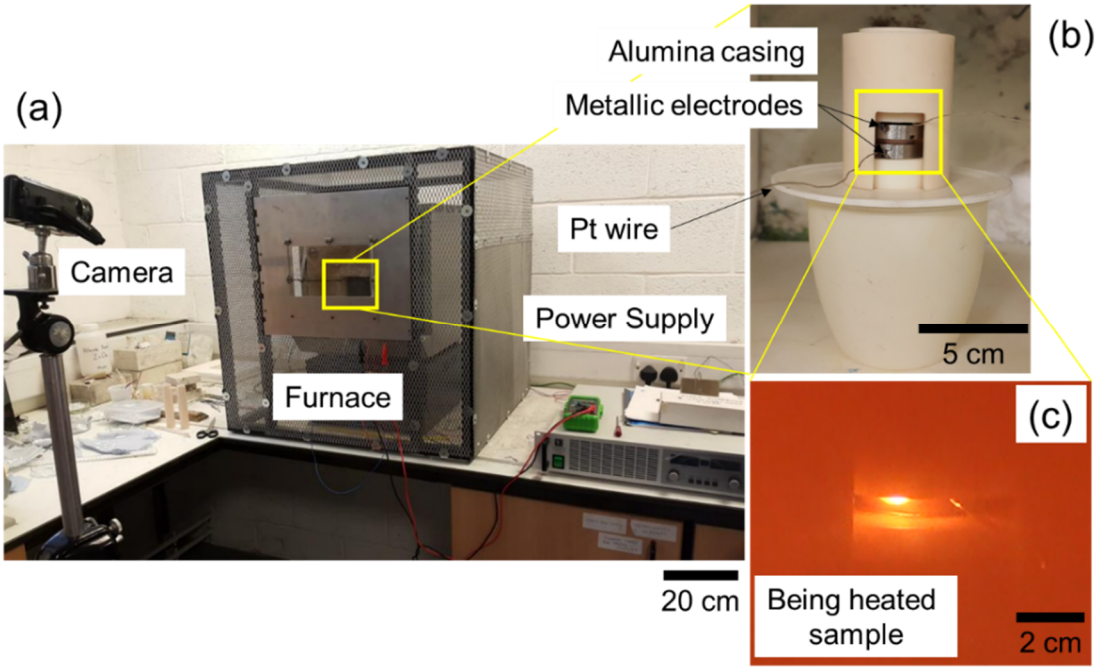

Figure 4.25: (a) The FS apparatus and its assembly, (b) the porcelain sample in the alumina casing, (c) the porcelain sample was being flash sintered [author's figure].

Fig. 4.25 shows the FS apparatus and its assembly. The samples and the alumina casing (Fig. 4.25b) then were placed in a modified box furnace (Fig. 4.25a). A digital camera was place next to the furnace (Fig. 4.25a) and used to observe the flash events (Fig. 4.25c).

Electric fields were applied to the specimen through a closed electrical circuit using a commercial DC power source (360 V, 15 A, 1500 W, Elektro-Automatik, Viersen, Germany). Voltages and electric current data were recorded using a data logger (NI USB 6008, National Instruments, Austin, TX, USA) and displayed by Labview software (National Instruments, Austin, TX, USA). The furnace was heated at a rate of 5 °C/min to the hold temperature of 850, 900, 950 and 1000 °C as measured by the furnace thermocouple. When the furnace reached the respective temperatures, a series of electric fields of 0.5, 1.0 and 1.5 kV/cm was applied for 60 s each. The current control limit was controlled at 0.2 A. using a programmed power supply. A constant voltage was employed but was switched automatically to current control when the current limit was reached.

Sample temperatures during the flash events were estimated using a non-equilibrium development of the black body radiation model of Raj as presented in Eq. 4.33 [254].

$$T_s = \left[T_f^4 + \frac{W}{A\varepsilon\sigma}\right]^{1/4} \tag{4.33}$$

where T_s is the sample temperature, T_f is furnace temperature, W is the electrical energy dissipated in the sample, σ is the Stefan-Boltzmann constant, ε is emissivity of the porcelain sample at the furnace temperature, and A is the surface area.

4.19 Evaluation of energy consumption in the rapid sintering techniques

4.19.1 Energy measurement in CS and DS

The potential energy savings of the various sintering processes were determined including careful consideration of the energy losses. In this study, energy consumption of the CS (the energy consumption in CS was measured for comparison purposes), and DS were measured using a power meter (Floureon Power Meter, NY, USA) attached to the laboratory furnace as presented in Fig. 4.26a. Power data (watts) were manually recorded with a 30 s time interval and then plotted using a commercial software (Origin 2015, OriginLab, Northampton, MA, USA) to obtain the power against time (Fig. 4.26b). The

integrated area under the plot represents energy consumption (power*time, (W · s is Joule) of the CS and DS process.

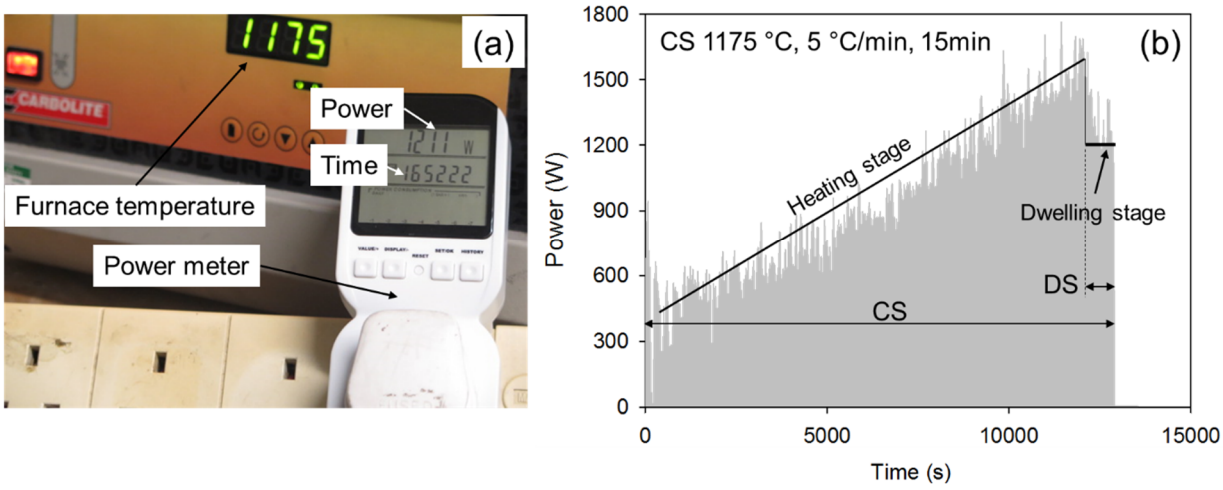

Figure 4.26: (a) Power meter attached to an electric furnace, (b) graph of power vs time obtained from the power meter in CS and DS [author's figure].

The energy consumption in CS was determined from the fully sintered CSed sample at 1175 °C. The energy consumption was measured during heating (with 5 °C/min) and dwelling stages but excluding the cooling stage (Fig. 4.26b, also see section 4.18.1 and 4.18.2). The energy consumption of DS was obtained from the fully sintered DSed sample (1175 °C with 15 min dwell) during the dwelling stage only (Fig. 4.26b) and the energy loss during sample insertion was not considered since it was for about 5 s only (see section 4.18.1 and 4.18.2, Fig. 4.21a).

4.19.2 Energy measurement in SPS

The SPS unit has integrated computer software to create, save and upload sintering conditions and to download the sintering data after sintering for further analysis. Power consumption of the SPS was calculated from the voltage and the current which were measured by sensors in the SPS unit (Fig. 4.27a). These values are referred to the power employed by the SPS machine. The power data were replotted against time to obtain energy consumption (Fig. 4.27b).

The energy consumption in the SPS was determined from the fully sintered SPSed sample (SPSed 1100 °C, 100 °C/min, 5 min dwell).

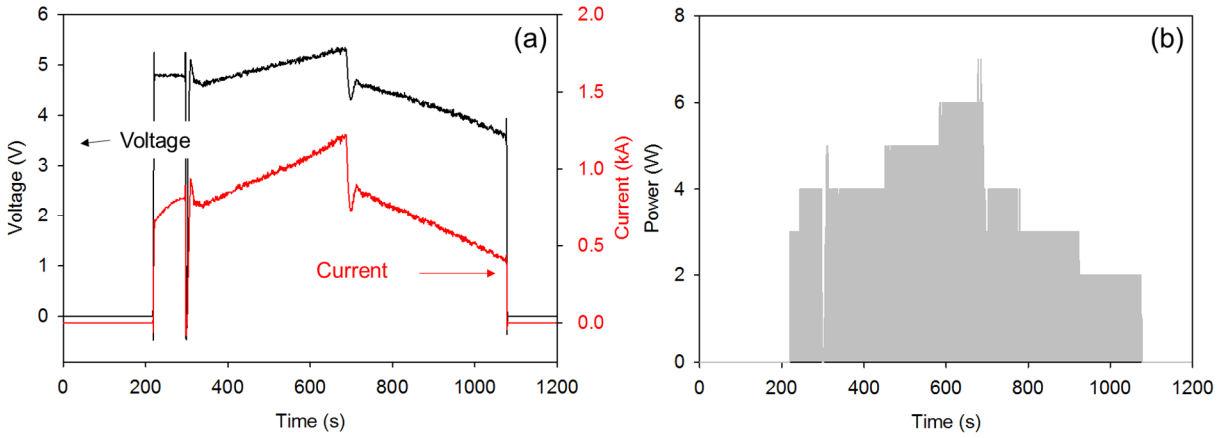

Figure 4.27: (a) Electrical current and voltage profiles, (b) power vs time of SPSed 1100 °C, 100 °C/min, 5 min dwell, and 25 MPa [author's figure].

4.19.3 Energy measurement in MWS

The microwave sintering furnace has integrated computer software to create, control sintering conditions and to download the sintering data after sintering for further analysis.

The software measures the energy input, which is produced by the magnetron, to the cavity and measures the energy output from the cavity, so the energy absorbed by the sample is known. Fig. 4.28a shows an example of the software user interface showing microwave power input (500 W), sintering curve (heating rate, dwell time, temperature), and control mode. The energy absorbed by the sample was extracted using the software and replotted (power vs time) as shown in Fig. 4.28b.

Fig. 4.28b shows that the sample absorbed power as a function of tuner position, which controls the sample position to get the best microwave absorption in the cavity. In this study the energy consumption of MWS was obtained from the fully sintered MWSed sample (MWSed 1100 °C, 50 °C/min, and 5 min dwell).

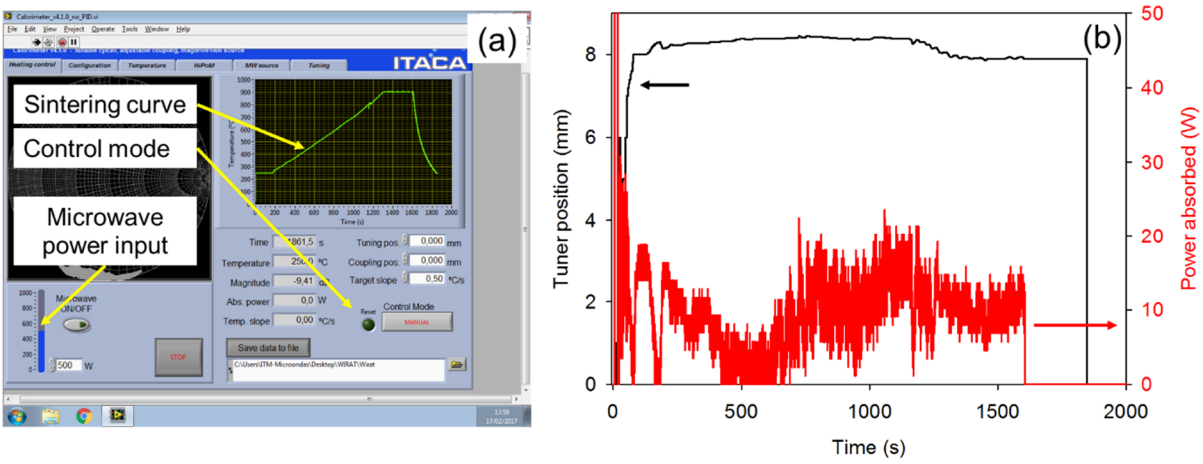

Figure 4.28: (a) MWS integrated software user interface shows sintering curve, control mode, and power input, and (b) an example of power consumption of MWS 1100 °C, 50 °C/min, and 5 min dwell [author's figure].

4.19.4 Energy measurement in FS

4.19.4.1 Energy measurement in FS (furnace)

In the case of FS, before the electric current was applied to the sample to produce flash sintering, the sample was heated in the furnace to the set temperature. The energy consumed by the furnace was estimated using the same procedure as used in CS and DS (Fig. 4.26). In this FS, 950 °C of furnace temperature, 5 °C/min heating rate were used. The energy consumed at dwelling stage was only included only during the flash event.

4.19.4.2 Energy measurement in FS (Joule heating in the sample)

The power supplied (watts) to the samples (to produce Joule heating) was obtained from the instant voltage and instant current using a data logger (NI USB 6008, National Instruments, Austin, TX, USA) and displayed by Labview software (National Instruments, Austin, TX, USA) (Fig. 4.29a, also see section 9.3).

The power was calculated from voltage and current obtained from the data logger. The power then was replotted using commercial software (Origin 2015, OriginLab, Northampton, MA, USA) to obtain the power against time giving energy consumption.

The energy consumption of FS is a combination of energy used to heat the sample in the furnace (section 4.19.4.1) and energy used to produce Joule heating in the sample (section 4.19.4.2).

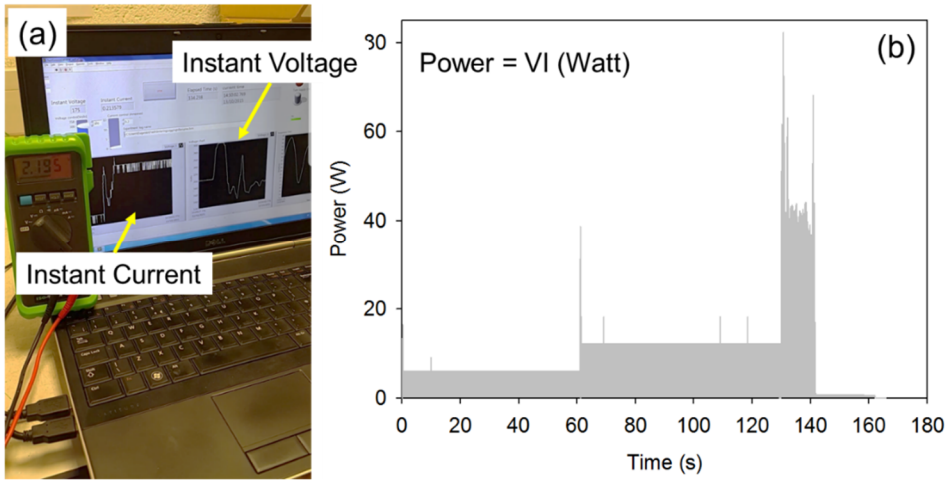

Figure 4.29: The data logger used to record the voltage and current data and displayed by Labview software in a personal laptop [author's figure].

However, the measured energy consumption in the studied sintering processes was not only consumed by the porcelain sample but also by the furnace structure, setter materials, and losses. Thus, the energy losses were empirically calculated to compare between the studied sintering processes.

4.19.5 Heat balance and energy consumption

The basis of energy consumption of a sintering process is the energy balance, which is the relationship between energy input (the energy measured either by power meter or integrated computer software) and energy output (energy required by the samples, and setters) and losses. In this study, it is assumed that;

(i) The energy inputs of CS and DS processes ($Q_{CS,DS}$) were used to heat the porcelain ($Q_{porcelain}$), and the alumina setter (Q_{setter}), the rest of the energy was considered to be lost (Q_{losses}) to the furnace wall, and the opening gaps.

$$Q_{CS,DS} = Q_{porcelain} + Q_{setter} + Q_{losses} \quad (4.34)$$

(ii) The measured energy input in SPS (Q_{SPS}) was mainly used to heat graphite components ($Q_{graphite}$), porcelain ($Q_{porcelain}$), and the rest is lost (Q_{losses}) to the water cooling of the SPS structure.

$$Q_{SPS} = Q_{porcelain} + Q_{graphite} + Q_{losses} \quad (4.35)$$

(iii) The energy input of MWS (Q_{MWS}) was assumed to be solely absorbed by the porcelain ($Q_{porcelain}$) because neither the furnace structure, microwave cavity nor quartz tube absorbed microwaves (they are designed to be transparent to microwaves).

$$Q_{MWS} = Q_{porcelain} \quad (4.36)$$

(iv) In FS, the energy consumption is a combination of the electrical power supplied directly to the porcelain ($Q_{porcelain}$) producing Joule heating and the furnace energy ($Q_{Furnace}$) to heat the sample at the flash event. The rest of the energy was considered to be lost (Q_{losses}) to the furnace wall, and the opening gaps.

$$Q_{FS} = Q_{porcelain} + Q_{Furnace} + Q_{losses} \quad (4.37)$$

Table 4.5 shows the furnace model and furnace parameters used to calculate the energy losses in this study.

Table 4.5: The furnace model and furnace parameters used in this study.

Process	Furnace model	Furnace components
CS, DS	Laboratory chamber furnace 	1. Furnace chamber volume = 4.5 Litres 2. Chamber dimensions (W*L*H) = 0.14*0.25*0.13 cm
SPS	FCT HPD 25; FCT Systeme GmbH 	Graphite dimension 1. Graphite spacer (Dia./Height) =60/30 Graphite punch (Dia./Height) =20/20 2. Graphite die (Dia./Height) =20 (inside),40(outside)/40
MWS	MWS integrated with a computer software. 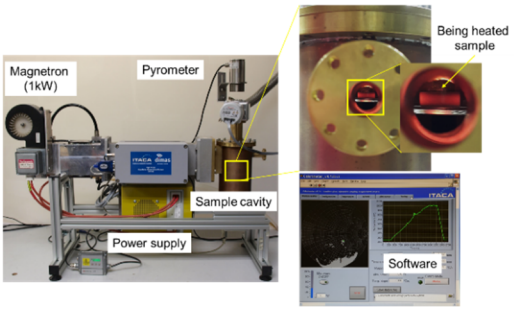	Cavity dimension 1. Diameter =104 mm 2. Height =200 mm
FS	Flash sintering apparatus integrated with a computer software. 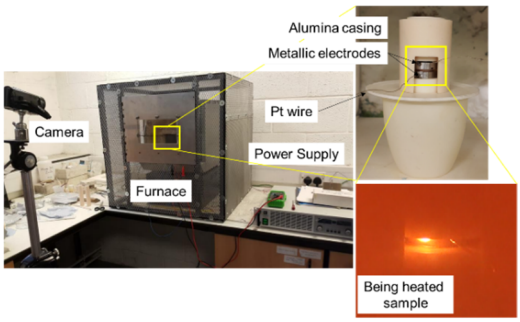	1. Furnace chamber volume =4.5 Litres (estimated) 2. Chamber dimensions (W*L*H) =0.14*0.25*0.13 cm

Chapter 5

Porcelain powder and body characterisation on heating

5.1 Chapter review

Understanding porcelain sample behaviour as a function of temperature is key to this study because it helps to set the appropriate sintering process parameters and will enable discussion of interpret the empirical results. Different characterisation techniques including XRD, DTA-TGA, dilatometer, DSC, Laser flash apparatus, and impedance spectroscopy were used to measure the temperature-dependent properties of the porcelain.

The mineral composition of the porcelain obtained using XRD is given in section 5.2., while the thermal behaviour of the porcelain powder is given in section 5.3. The dilatometry, and heat capacity by DSC are given in section 5.4 and 5.5 respectively. Thermal diffusivity and thermal conductivity are presented in section 5.6. Electrical conductivity of the porcelain is explained in section 5.7 and finally dielectric constant and loss tangent are presented in section 5.8. The obtained data show how the porcelain sample physically, and chemically changes with elevated temperature.

5.2 Mineral composition of porcelain powder by XRD

XRD was used to determine the mineralogical composition of the porcelain powder sample. Fig. 5.1 shows the three main minerals found in the porcelain powder are albite ($NaAlSi_3O_8$, (Triclinic), JCPDS: 09-0466), kaolinite ($Al_2Si_2O_5(OH)_4$), (Triclinic), JCPDS: 14-0164), and quartz (SiO_2, (Trigonal, alpha quartz), JCPDS: 65-0466). As described in section 4.2, the chemistry of the

porcelain powder examined by ICP-AES is 74.32±0.68 wt.% SiO_2, 17.43±0.27 wt.% Al_2O_3, 0.68±0.01 wt.% TiO_2, 1.24±0.04 wt.% Fe_2O_3, 0.74±0.02 wt.% CaO, 0.49±0.03 wt.% MgO, 1.24±0.01 wt.% K_2O and 3.77±0.06 wt.% Na_2O. The ICP-AES data suggest that the porcelain powder possibly contains minor amounts of microcline ($KAlSi_3O_8$), dolomite ($CaMg(CO_3)_2$), hematite (Fe_2O_3), and rutile (TiO_2); all of which are considered as impurities because they are not detected in significant levels by XRD.

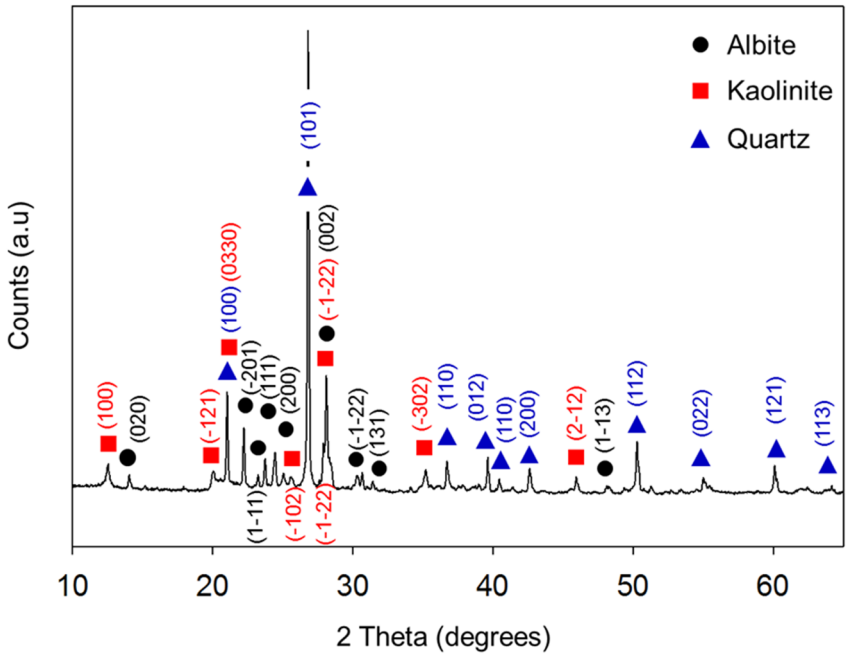

Figure 5.1: XRD of as-received porcelain powder reveals albite, kaolinite, and quartz.

5.3 Thermal property of porcelain powder by DTA-TGA

The thermal behaviour of the porcelain powder was measured from room temperature to 1200 °C using DTA-TGA analysis (Fig. 5.2). Three main thermal events (labelled as i, ii, and iii) including two endothermic and one exothermic are revealed Fig. 5.2a.

The two large endothermic peaks at 100-200 °C and 450-600 °C, correspond to (i) evaporation of physically bound water and (ii) dehydroxylation of chemically bound water of kaolinite, respectively [42,106,121,150]. The small exothermic peak at 942 °C (iii) suggests the initial formation of the spinel-alumina phase from the kaolinite, and then eventually transform to mullite above this temperature

[37,94,108,137]. The endothermic reaction at above 942 °C indicates the formation of a liquid phase resulting from the melting of albite [42,106,121,150].

The total weight loss of this porcelain body presented in Fig. 5.2b is ~5% associating with ~1.1 wt.% from physically bound water evaporation, and ~3.7 wt.% from chemically bound water during decomposition from kaolinite. In this case, burning of organic matter is negligible.

An endothermic peak of quartz inversion (α to β) at ~560 °C is masked by overlap with the dehydroxylation peak of the kaolinite, but it can be seen by the change in thermal expansion in Fig. 5.3.

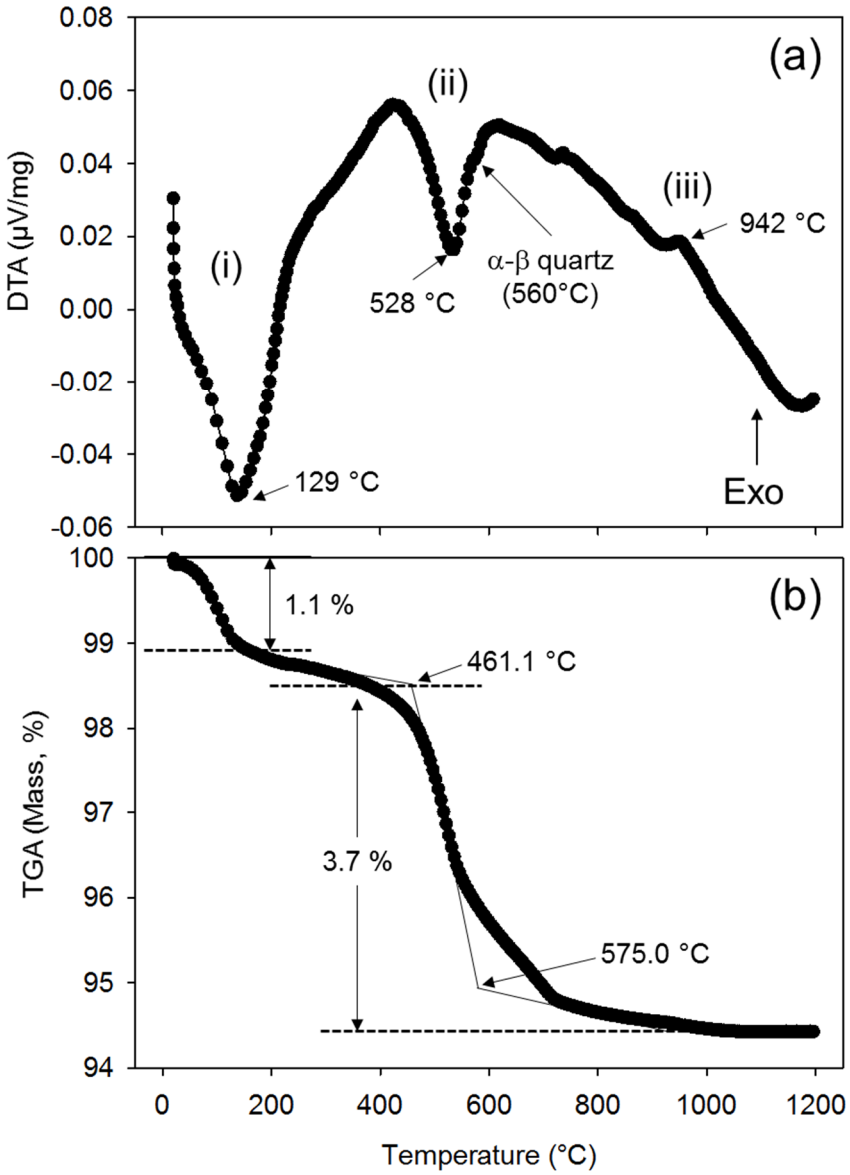

Figure 5.2: (a) DTA, and (b) TGA of porcelain powder as a function of temperature, from 25-1200 °C.

5.4 Dilatometry

Dilatometry (Fig. 5.3) reveals that the green porcelain sample has coefficient of thermal expansion (CTE) of 11.17×10^{-6} K^{-1} (50-900 °C) which corresponds to about 0.95% linear expansion. At ~560 °C, there is a slight jump in the CTE caused by the volumetric change of quartz (α to β polymorph) indicated by the 1st derivative of the dilatometry curve. The green porcelain starts to contract at 950 °C due to melting of albite. The contraction from 950-1200 °C is about 7%. The dilatometry curve suggests that under a conventional sintering process this porcelain sample starts to densify at 950 °C.

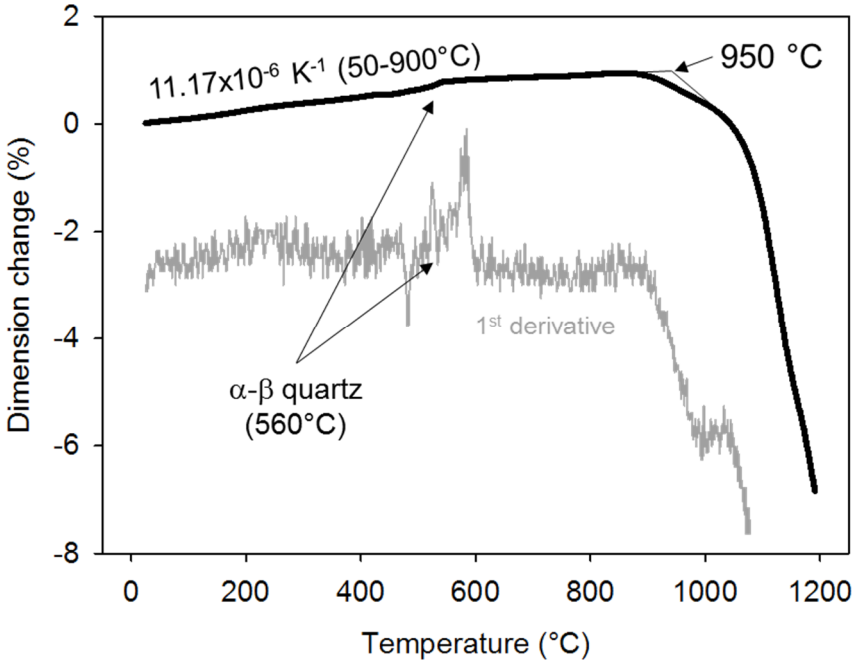

Figure 5.3: Thermal expansion/shrinkage of the porcelain sample. The 1st derivative shows the quartz inversion.

5.5 DSC and heat capacity (C_p)

Fig. 5.4 shows DSC curve of porcelain powder and a sapphire standard plot against temperature. The integrated area under peaks (shaded area) is the change of heat at the thermal events (the integrated area unit of mW/mg · time (s) is equal to mWs/mg which equals J/g).

For the porcelain sample, the heat needed for evaporating physically bound water is about 13 J/g, while more heat (90.44 J/g) is required for the

dehydroxylation process at about 550 °C. The exothermic reaction at ~970 °C corresponds to the conversion of meta-kaolinite to mullite (approx. 10.70 J/g).

The DSC curve of the porcelain sample is compared to the DSC curve of the standard sapphire to calculate the heat capacity (C_p) using the ratio method.

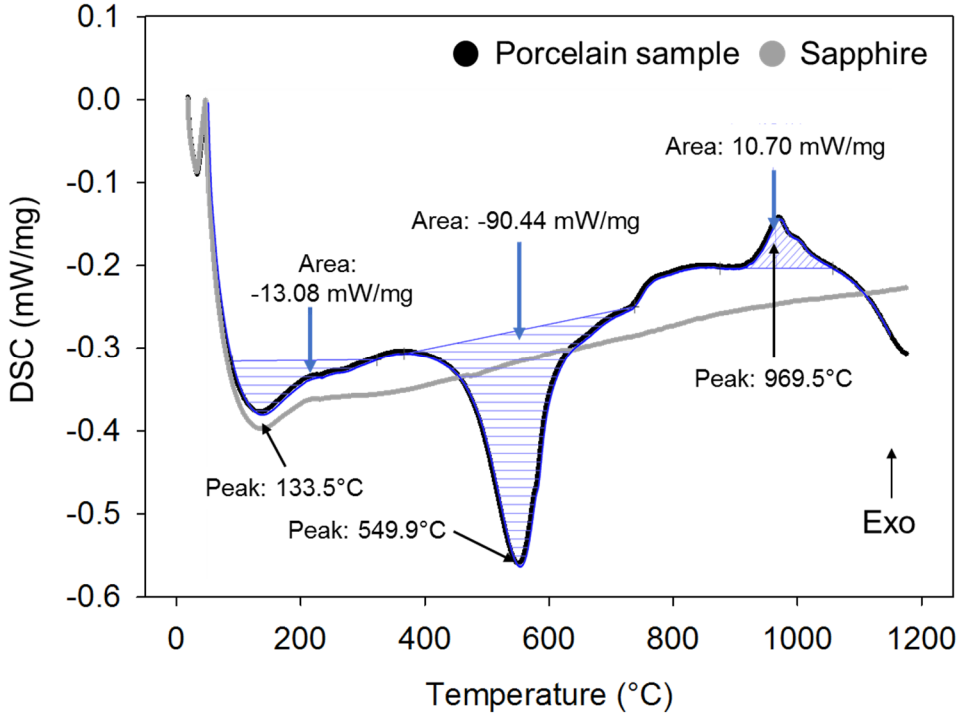

Figure 5.4: DSC of porcelain sample and sapphire standard.

The heat capacity (C_p) of the porcelain sample (Fig. 5.5) slightly increases as temperature increases from 25-450 °C, with a peak at ~560 °C then sharply increases above 1000 °C. The increase in C_p from 800-1100 J/kg·mol from 25-450 °C is due to latent heat required for evaporating 2 wt.% physically bound water. The peak at 550 °C (C_p ~2100 J/kg·mol) occurs due to two events (i) dehydroxylation of the kaolinite, and (ii) α-β polymorphic transformation of quartz. The large peak at 560 °C starts from 450-600 °C presenting that a large latent heat required for dehydroxylation of chemically bound water in the kaolinite and polymorphic transformation of quartz.

The heat required for dehydroxylation of kaolinite is reported as 42-250 kJ/mol [105, 255] while the heat for α-β quartz inversion is 0.385 kJ/mol [256]. In the case of quartz inversion, it is not detected at 573 °C but it is detected at 560 °C (from DTA result (section 5.3), and dilatometry curve (section 5.4)). The shifted in

α-β polymorphic transition temperature of quartz might be attributed to its crystallinity and impurity in its crystal structure [257].

C_p increases again at the temperature of mullite formation (~942 °C) and melting of albite above 1000 °C. It is worth noting that when feldspars (albite) melt, their heat capacity changes and the vibrational and configurational heat capacity accounts for the change of heat capacity [257].

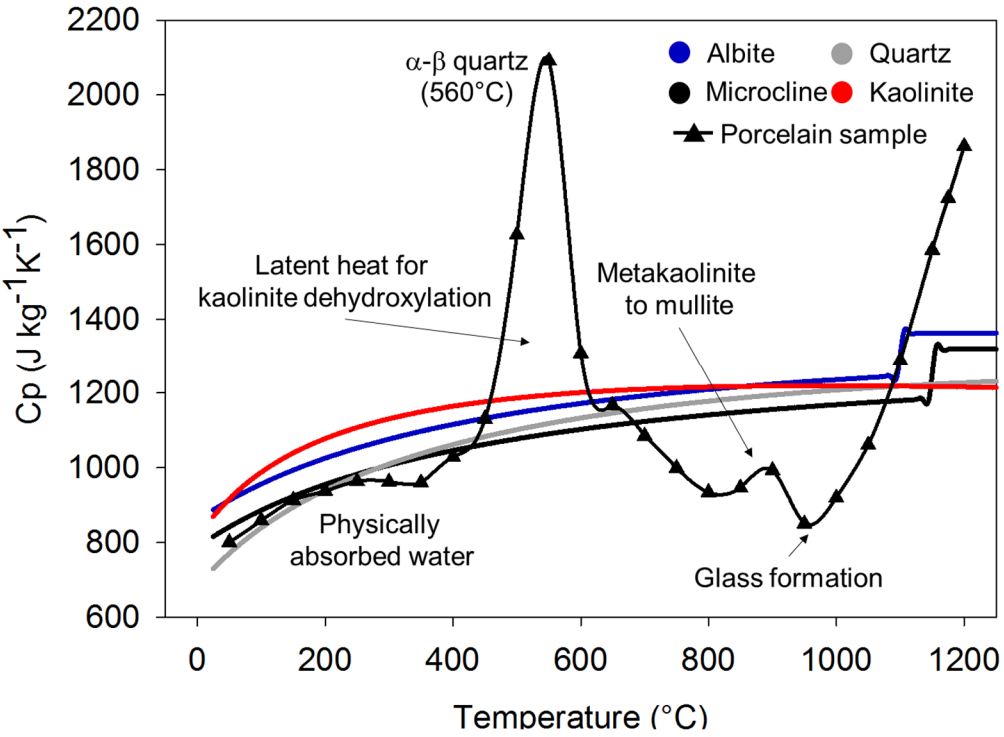

Figure 5.5: Heat capacity (C_p) of the green porcelain sample as a function of temperature obtained from the experiment and the C_p of minerals calculated from literature.

At low temperature (below the melting point of feldspars), the vibrational heat capacity increases as temperature increases because there is not enough heat energy to excite the vibrations but at high temperature (at the melting point of feldspars), the vibrational heat capacity decreases because melting of feldspar produces low density resulting from an increase of the interatomic distance. On the other hand, the configurational heat capacity increases when feldspars melt because the melting process needs energy, which is not to increase the temperature, but to achieve equilibrium with a new configuration (solid to liquid). Therefore, the elevated temperature increases heat capacity [258]. Thus, from this

study, the rapid increase of the heat capacity of the porcelain sample above 1000 °C is due to the formation of liquid glass from the melting of albite.

In general, C_p of substances as a function of temperature can be determined using Eq. 5.1 [259]. Thus, the C_p of the porcelain sample can also be calculated and explained using its composition. The heat capacity coefficients (a, b, c, and d) of minerals are presented in Table 5.1.

$$C_P = a + bT + cT^{-2} + dT^{-1/2} \quad (5.1)$$

where a, b, c, and d are the empirically determined coefficients, and T is temperature (K).

To the best of the author knowledge, the heat capacity coefficients are well documented, comprehensive, and critical compilation which can be used with confidence. However, it suggests that although the calculated and experimental heat capacity are well correlated, but the difference can be ~2%. Thus, the heat capacity coefficients used in this study are considered as ±2% accuracy.

Table 5.1: Heat capacity coefficient of minerals found in the porcelain sample.

Minerals	a	b (10^5)	c	d
Albite ($NaAlSi_3O_8$)	0.4520±0.009	-1.3364±0.026	-1275.9±25.5	-3.9536±0.079
Microcline ($KAlSi_3O_8$)	0.4488±0.009	-1.0075±0.020	-1007.3±20.1	-3.9731±0.079
Kaolinite ($KAlSi_3O_8$)	0.4367±0.009	-3.4295±0.068	-4055.9±81.1	-2.6991±0.053
Quartz (SiO_2)	0.1107±0.002	-0.5189±0.010	0	-1.1283±0.022
Albite (liquid), 1118 °C	0.3585±0.007	-	-	-
Microcline (liquid), 1150 °C	0.3673±0.007	-	-	-

The a, b, c, and d are constants for the heat capacity (C_p) computed using Eq. 5.1 ($J/K \cdot mol$) [260].

Fig. 5.5 shows the calculated heat capacity of the albite, microcline, kaolinite and quartz as a function of temperature. The heat capacity of these minerals increases as temperature increases. For example, the heat capacity of kaolinite increases from 830 kJ/mol at room temperature to 1270 kJ/mol at 1200 °C but the calculation does not account for any phase transformation.

Fig. 5.5 also suggests that the C_p of the porcelain sample is in a good agreement with the C_p of its composition. In general, heat capacity of minerals

increases as increase temperature [258]. The C_p of albite and microcline increase rapidly at their melting points (1118 °C for albite and 1150 °C for microcline respectively). However, the liquid glass formation in this porcelain sample found at lower temperature (950 °C) is due to a eutectic reaction between kaolinite, feldspars and quartz making the C_p of the sample increases from this point.

5.6 Thermal diffusivity and thermal conductivity

Thermal diffusivity data of the porcelain sample are plotted against temperature as presented in Fig. 5.6. At 25 °C, the thermal diffusivity of the porcelain sample is ~3.69x10^{-3} cm^{2}s^{-1}, gradually decreasing to 1.92x10^{-3} cm^{2}s^{-1} as temperature increases to 900 °C. Decrease of thermal diffusivity with elevated temperature of the porcelain sample is due to (1) high volume fraction of porosity and (2) increasing lattice vibration which obstructs the flow of heat (phonon scattering) [261].

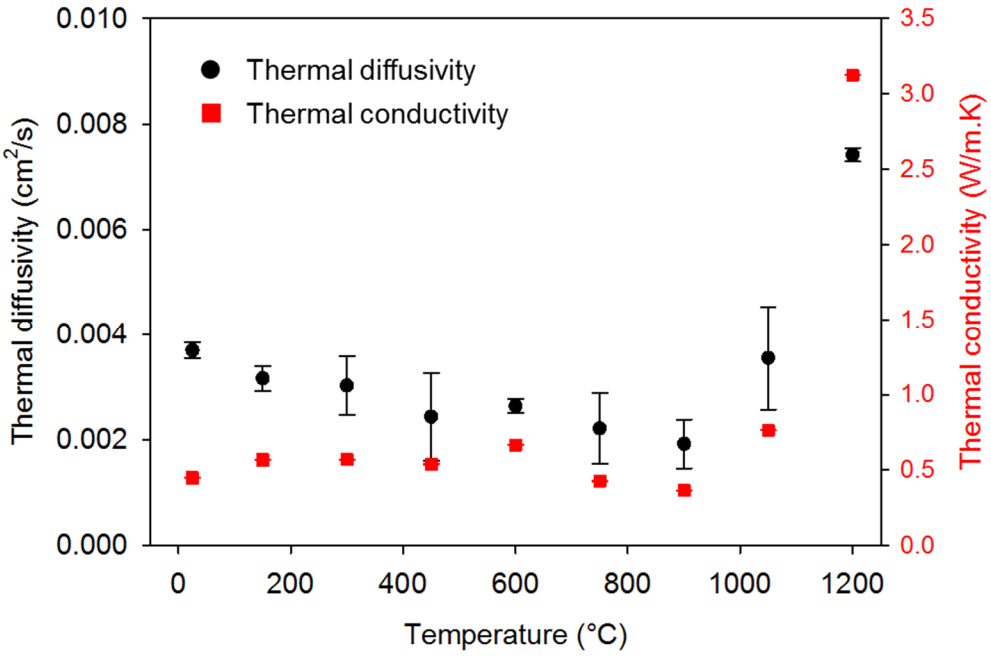

Figure 5.6: Thermal diffusivity and thermal conductivity of the porcelain sample as a function of temperature.

Since thermal diffusivity is related to the volume fraction of solid and air space in the sample body; solids give high thermal diffusivity while air space has low thermal diffusivity. According to Fig. 5.7, the porosity in the porcelain sample

is about 40±0.2 vol.% and remains constant from 25-950 °C. Because there is no change in porosity between 25-950 °C; so the only factor in decreasing of the thermal diffusivity is phonon scattering. Even though there are several thermal events occur during heating the porcelain such as evaporation of physically bound water, and dehydroxylation but the dilatometry suggests that the porcelain expands as temperature increases suggesting that the porosity in the sample is not decreased (Fig. 5.3). From this point of view, it can be seen that at 25-950 °C, phonon scattering plays an important role in decreasing of the thermal diffusivity.

In addition, during dehydroxylation (450-600 °C), the thermal diffusivity and conductivity remains constant because the sample has less contact between particles resulting from dehydroxylation and no change in the porcelain sample density as presented in Fig. 5.7. Thermal diffusivity (Fig. 5.6) shows a broad hump at 500-600 °C, this may result from the displacive quartz inversion, but diffusivity continues decreasing to 1000 °C. Decreasing of thermal diffusivity between 600-1000 °C resulted from dehydroxylation of kaolinite producing metakaolinite, which has disorder crystal structure, low thermal diffusivity.

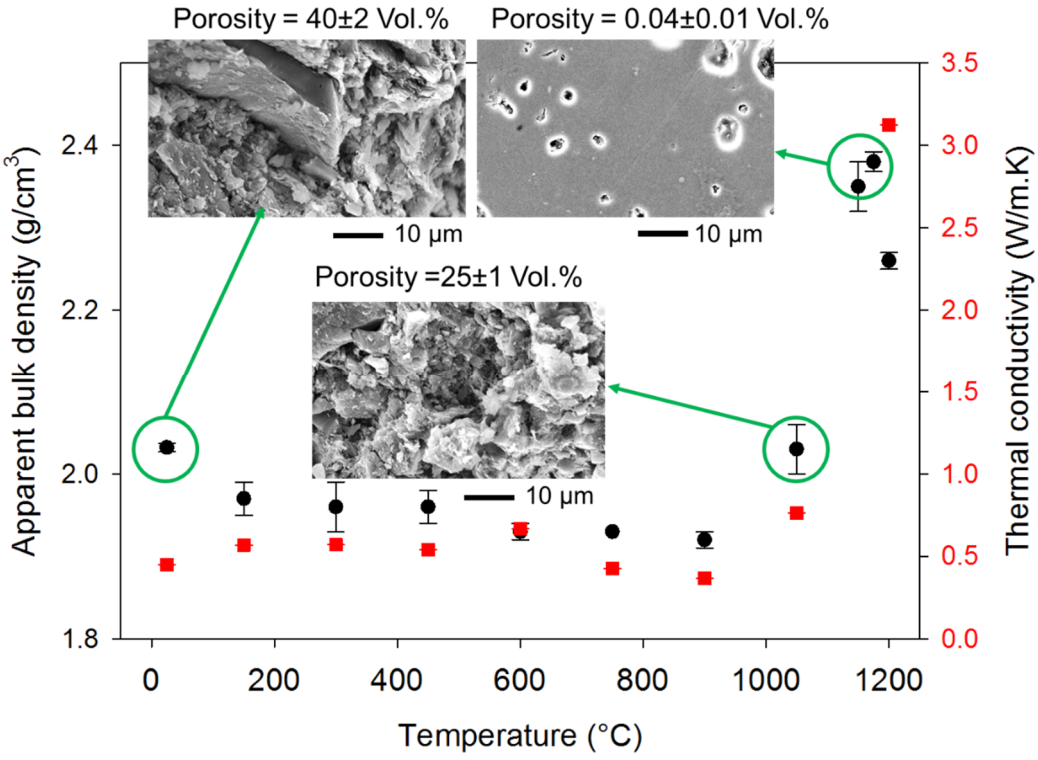

Figure 5.7: Bulk density and thermal conductivity of the porcelain sample as a function of temperature.

Increasing thermal diffusivity and conductivity above 1000 °C is due to increasing of bulk density via melting of albite which provides heat transfer paths and brings closer particle packing, reducing porosity to 25±1 vol.% (Fig. 5.7). The microstructure of the porcelain sample at 1175 °C in Fig.5.7 is similar to that of commercial porcelain, which contains about 0% open porosity.

However, it should not be confused that formation of liquid glass generally lowers thermal diffusivity because liquid phase has disordered structure, which has a poorer thermal conductivity than solids. Liquid phase also provides convection and radiation but in this experiment condition, these heat transfer mechanisms are minimal because (1) glass liquid does not move because of its inertia so, there is no convection, (2) the measurement time is short, and thickness of the sample is small producing minimal radiation [262]. Thus, in this case the effect of bulk density on thermal diffusivity and thermal conduction is greater than the effect of melting of albite.

Fig. 5.6 also presents thermal conductivity of the porcelain sample as a function of temperature. It is clear that the thermal diffusivity and conductivity follow the apparent bulk density trend (Fig. 5.7)

5.7 Electrical conductivity

Fig. 5.8 shows examples of the impedance spectra of the porcelain sample influenced by temperature (e.g. 400-650 °C). On heating (Fig. 5.8a), the diameter of the semicircles (which is fitted as shown in the inset of Fig. 5.8a) is reduced as temperature increases. This figure represents a decrease of overall resistance of the porcelain sample with increasing temperature. In other words, the electrical conductivity of the porcelain sample increases as temperature increases.

Fig. 5.8 also reveals different resistances of the porcelain sample between (a) heating and (b) cooling cycles. Both cycles exhibit different semicircle diameters at the same temperatures and it is clear that the electrical conductivity of the porcelain sample in the cooling cycle is greater than that in the heating cycle.

In addition, the impedance spectra in Fig. 5.8 show one semicircle (each temperature) in both heating and cooling corresponding to bulk conduction. The single semicircle in each temperature suggests that the effect of grain boundaries is not observed (the grain boundary effect is generally observed by the presence of

a second semicircle in the impedance spectra). It is possible that the conduction path in this porcelain sample is along the particle surface with no obstruction (fast electrical conduction pathway); even in the green porcelain sample having high porosity. Moreover, the tails at low frequency correspond to the electrode/sample interface normally present in impedance measurement.

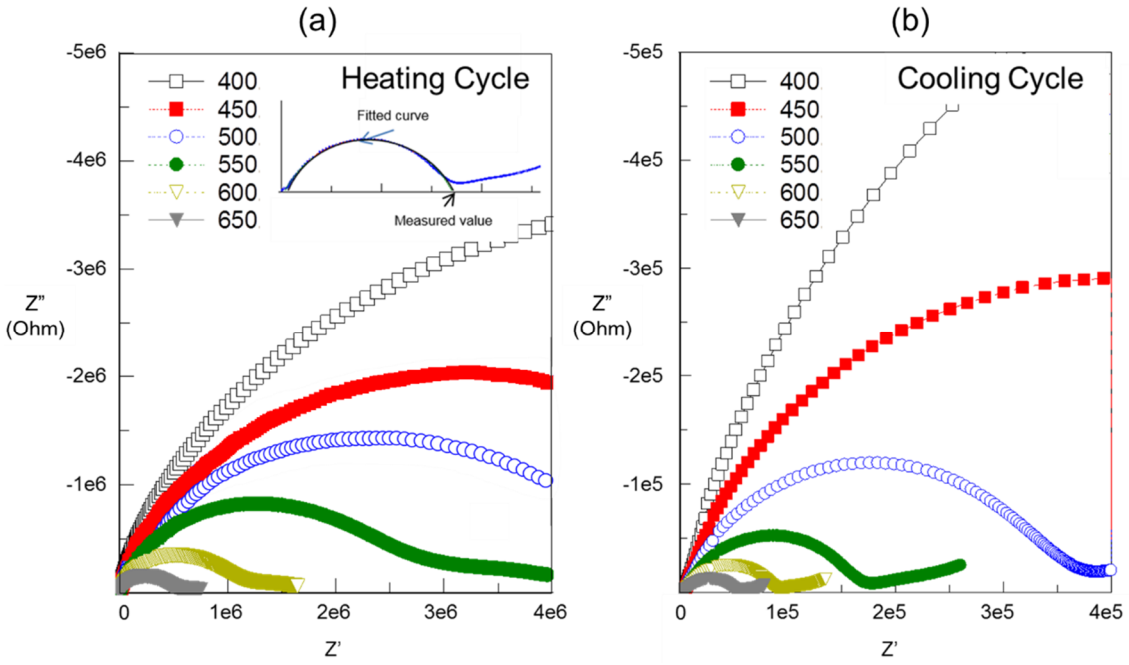

Figure 5.8. Nyquist plots of porcelain sample as a function of temperature with different stages: (a) heating and (b) cooling. Note that the scale of the heating cycle is higher by one order of magnitude.

The intercept at x axis present in the inset of Fig. 5.8a is the resistance which is used to calculate the electrical conductivity and the calculated electrical conductivity values are used to generate an Arrhenius equation to calculate the activation energy, which is presented in Fig. 5.9.

An Arrhenius plot (prepared as described in section 4.8.1) of electrical conductivity against reciprocal absolute temperature of the porcelain sample (Fig. 5.9) reveals that on heating the electrical conductivity fits to three regions with different slopes here referred as low, medium and high temperature regimes. In the low temperature regime at 100-250 °C, the conductivity increased slightly from 4.8 x 10^{-10} to 1.7 x 10^{-9} Scm^{-1}. The electrical conductivity in this temperature range is caused by ionization of physically bound water which produces H^+ and

OH^- ions [262]. It is also possible that migration of Na^+, K^+ and Ca^{2+} ions, which are usually present in porcelains, contribute to the conductivity [263]. However, the mobility of Ca^{2+} (and other divalent ions) is much lower than Na^+ and K^+ since Ca^{2+} has bigger atomic radius and higher charge than Na^+ and K^+ ions.

In addition, the electrical conductivity of dry quartz and feldspars are steady in the low temperature regime (below 500 °C) as previously reported [264] thus they do not contribute to the conductivity in this temperature range. Therefore, the H^+, OH^- and monovalent ions should be responsible for the conductivity in this low temperature regime [265].

This result also suggests that in the absence of water molecules in the porcelain sample, electrical conductivity is very low (10^{-8} Scm^{-1}). This is consistent with the observation that the electrical conductivity of this porcelain in the low temperature regime is dominated by H^+ and OH^- conduction with activation energy lower than 1 eV [266].

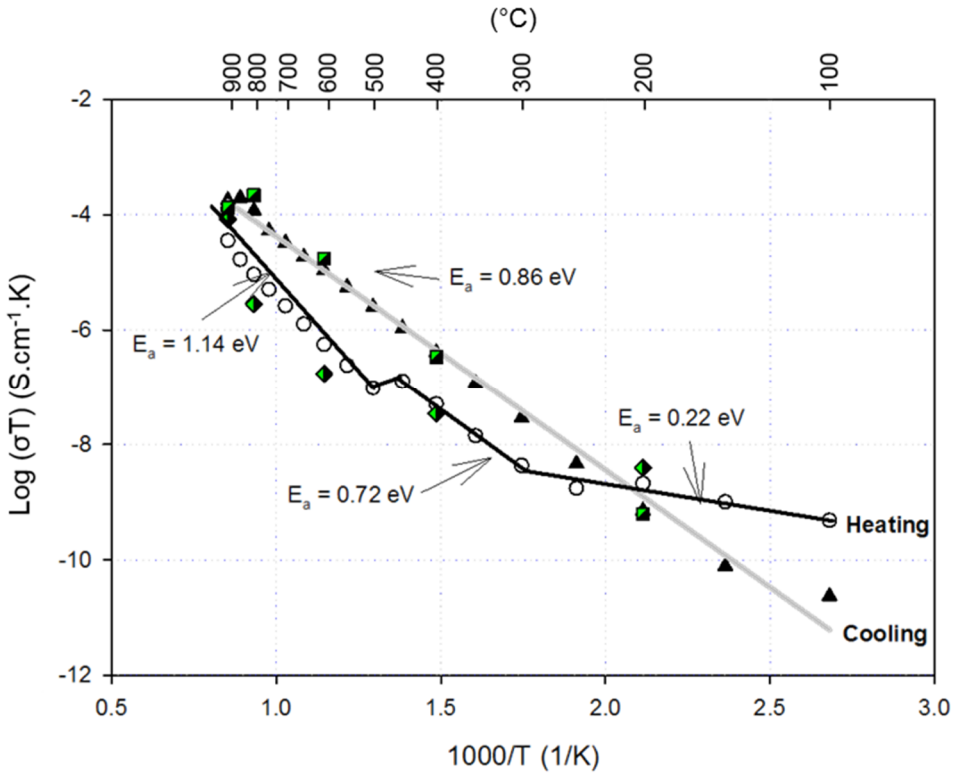

Figure 5.9. Arrhenius plot of the electrical conductivity against reciprocal absolute temperature of porcelain sample during heating (open circles) and cooling (filled triangles). Repeating experiments are performed to check reliability of the results. The semi-filled diamonds represent the heating, and the semi-filled squares represent the cooling stage.

The conductivity drops at 200-250 °C due to the removal of physically bound water decreasing the numbers of charge carriers then increases again above 250 °C. Between 250-450 °C (medium temperature regime), the conductivity increases from $1.74x10^{-9}$ to $1.27x10^{-7}$ Scm^{-1}, mainly driven by monovalent ions (Na^+, K^+), but H^+ and OH^- ions are not involved because they are completely evaporated. Some reports suggest that electrical conductivity in this temperature range results from 'hopping conduction' which occurs in silicate minerals with ferrous impurity [266,267]. It is also reported that the hopping conduction in silicate minerals occurs by transport of electron-hole pairs especially in the ferrous ion (Fe^{2+}) and the activation energy of this conduction is relatively low, less than 0.01 eV [266].

At the dehydroxylation temperature of clay substances, 450-600 ºC, the main charge carriers are monovalent ions, H^+ and OH^- ions. The decrease of conductivity observed at 500 ºC might result from the loss of H^+ and OH^- ions [263]. Moreover, a study on dehydroxylation of kaolinite to metakaolinite suggests that the structure of metakaolinite is distorted which obstructs the migration of the K^+ ion [268] and the Al^{3+} ion [269] by collapsing the kaolinite structure. Above 500 °C (high temperature regime), the electrical conductivity increases gradually with an activation energy of 1.14 eV. This activation energy is consistent with previous examination of a green porcelain composed of 50 wt.% of kaolinite (1.03 eV) [270]. Over this temperature range (450-600 ºC), the conductivity is potentially the result of migration of Na^+, K^+, Ca^{2+}, and Fe^{3+} ions [270]. At low and medium temperatures, the conductivity correlates well with the thermal analysis as the conductivity of the porcelain body is closely linked with the physically and chemically bound water.

Fig.5.10 illustrates the correlation between the thermal behaviour and the electrical conductivity of the porcelain sample. The DTA-TGA curve reveals good agreement of correlation between the thermal behaviour and the electrical conductivity. However, changes in conductivity at the phase transition points of quartz at 573 °C (α-β) and 870 °C (β-quartz to tridymite) were not observed in this study. This might result from only a few data points being taken in these regions.

However, the result is consistent with a previous study which found that there is no clear change in conductivity during this transition [263].

When the porcelain sample cools from 950 °C, it exhibits irreversible behaviour of electrical conductivity (Fig. 5.9) and the electrical conductivity on cooling is greater than the conductivity in the heating stage at any given temperature. This result is attributed to change in the phase composition and porosity of the sample. The dimension change (Fig. 5.3) confirms that liquid glass started to form ~900 °C revealed by the shrinkage of the porcelain sample and this shrinkage is more pronounced above 950 °C. The liquid glass changed the overall electrical conductivity of the sample by forming continuous glass-pathway allowing the charge carriers easily to move (high diffusion pathway) along the pathway without experiencing significant blocking.

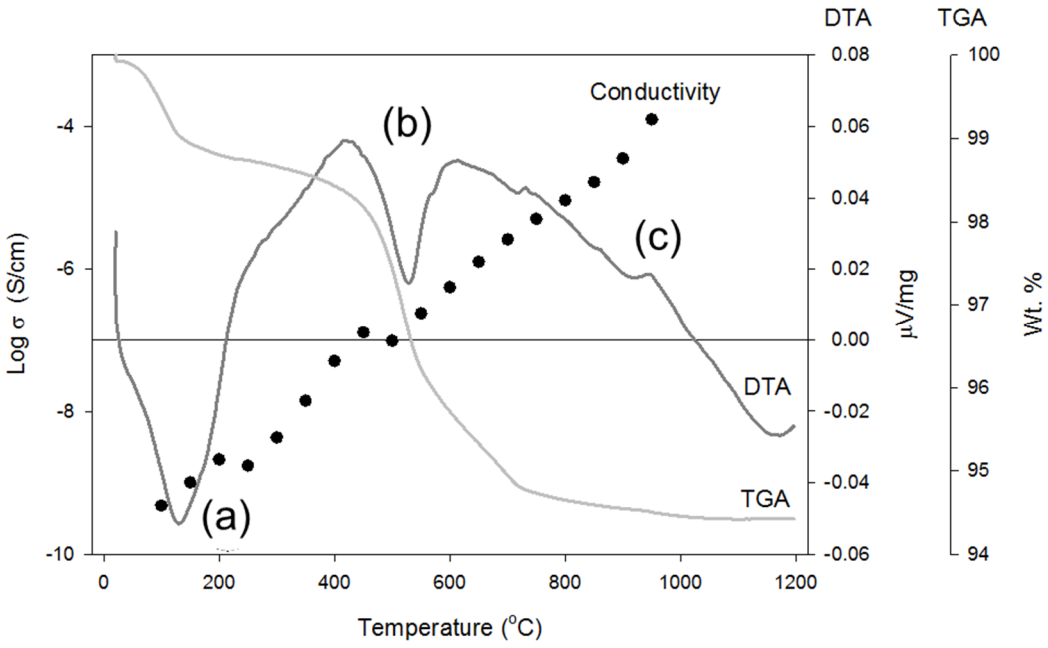

Figure 5.10: DTA-TGA plots of thermal behaviour of the porcelain sample associated with the electrical conductivity. The letters represent (a) removal of physically bound water, (b) removal of chemically bound water, and (c) spinel formation.

XRD revealed the expected phases in the green and fired porcelain (Fig. 5.11). Kaolinite, albite and quartz are the main constituents in the green porcelain body. The sample fired at 950 °C contains a small amount of glassy phase which was ~19.4±0.7 vol.% from albite melt calculated by decreasing in area of the

albite peaks. Kaolinite also transformed to metakaolinite (450-600 ºC) and spinel at 942 ºC (Fig. 5.2a) which is observed as "S" in the inset of Fig. 5.11. [94,93,271]. As a result, the different electrical conductivity arises from the changing phase composition.

Previous studies suggest that electrical conductivity of feldspars is reversible for both heating and cooling cycle below their melting point whereas quartz has irreversible behaviour because of the polymorphic transformations [265]. This result reinforces that electrical conductivity in the porcelain sample is irreversible.

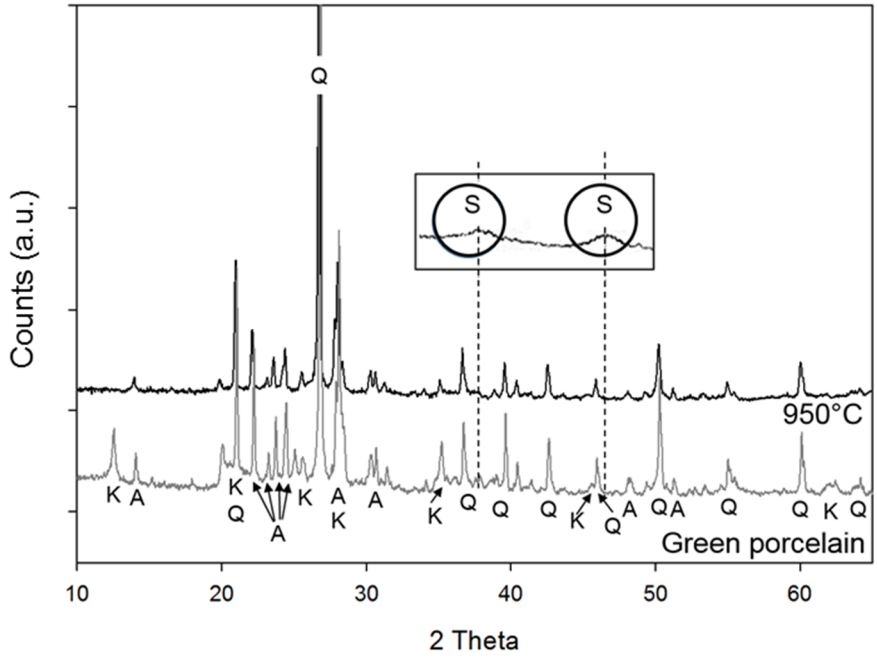

Figure 5.11: XRD of green porcelain and fired porcelain after 15 minutes at 950 °C revealing different phase compositions. K is Kaolinite, Q is Quartz, A is Albite and S is Spinel. The inset represents an enlargement of spinel peaks taken from Ref. 271.

SEM images (Fig. 5.12) of both the green and the fired porcelain sample reveal that porosity of the porcelain sample after thermally treated is smaller compared to the green porcelain. The apparent porosities of both green and fired samples were quantified using immersion method according to the ASTM C20-00 and were ~40±2 vol.% for the green sample and ~25±1 vol.% for sample heated at 950 °C, respectively (as also presented in Fig. 5.7).

The high magnification SEM image (Fig. 5.12e) shows evidence of glass formation locating around the solid particles. The glassy phase acts as a binder to bring all grains into closer contact reducing porosity.

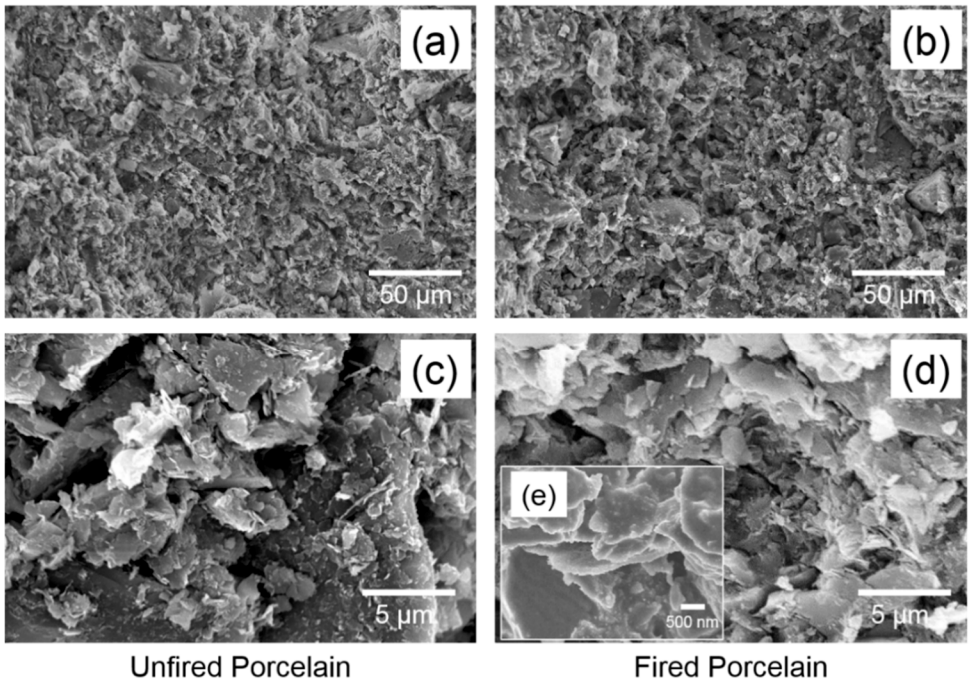

Figure 5.12: SEM images of the porcelain microstructures and porosity, (a) green porcelain, (b) porcelain fired at 950 °C for 15 min, (c) green porcelain at high magnification, and (d) porcelain fired at 950 °C for 15 min at high magnification, and (e) nanoscale image suggesting formation of glass around the particles.

In addition, the microstructures show in Fig.5.12 are similar to commercial porcelain products sintered at 950 °C being composed of high-interconnected porosity, clay particles, unmelted feldspars, and quartz [42,106,272]. At the temperature of 950 °C, there is little change in phases or reactions such as little melting of feldspars (significant above 1050 °C), and no quartz dissolution (significant above 1200 °C) thus the sample is still porous because it experiences little densification.

Due to the limit of the Impedance Spectroscopy instrument, the temperature of 950 °C was chosen to prevent any contamination or damage to the test rig. At this particular temperature, the sample shows good electrical behaviour which is useful for further experimental study of the FS process. However, after firing at 1200 °C, the microstructure has the typical features of a

well-fired ceramic body including glassy phase, mullite and quartz [42, 106,160,272].

5.8 Dielectric constant (k) and loss tangent ($tan\ \delta$)

Dielectric constant (k) and loss tangent ($tan\ \delta$) are calculated based on the obtained electrical conductivity result (from section 5.7). The k is calculated using the capacitance, sample dimension and the permittivity of free space as described in section 4.8.2. Capacitance data can be extracted from the impedance spectra (Fig. 5.8), the sample dimension is obtained from the dilatometry data (Fig. 5.3).

The result in Fig. 5.13 shows that the dielectric constant decreases as temperature increases because (1) the sample loses its ability to store charge (charges move resulting in electrical conductivity), and (2) thermal motion which decreases the polarizability of the minerals in the porcelain sample.

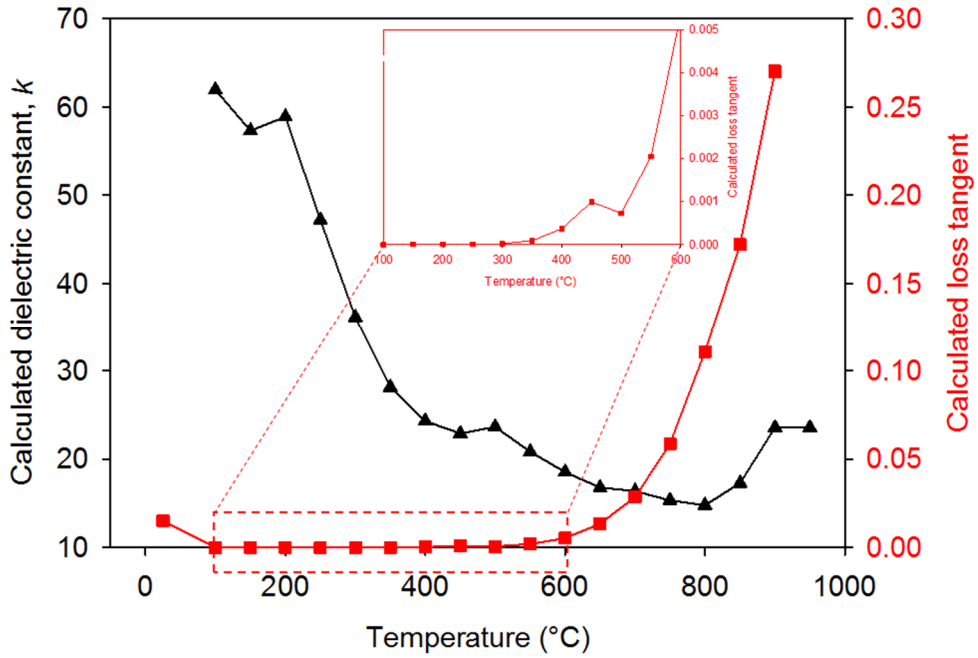

Figure 5.13: Calculated dielectric constant (black line) and calculated loss tangent (red line) as a function of temperature. Inset shows the calculated loss tangent at 100-600 °C.

At low temperature (<200 °C), high dielectric constant (k ~60) arises from the physically bound water (dielectric constant of water at 20 and 200 °C is 80.1 and 34.5 respectively [273]). At 200-400 °C the dielectric constant rapidly decreases as a result of evaporation of the physically bound water. Decrease in the

dielectric constant from 600-800 °C may result from the temperature effect because over this temperature range there is neither physical nor chemical change in the porcelain sample.

At elevated temperature (i.e. 600-800 °C) the dielectric constant of the porcelain sample decreases because the polarizability of the minerals in the porcelain sample decreases due to increasing thermal motion. Quartz, and albite contribute little to the overall dielectric constant since the dielectric constants (at room temperature) of quartz (k ~4.4), and albite (k ~5.4) are small compared to water and kaolinite [274] but still their dielectric constants decrease on increasing temperature.

After formation of metakaolinite via kaolinite dehydroxylation, the disordered crystalline structure of metakaolinite has lower density (2.37 g/cm^3) compared to kaolinite (2.65 g/cm^3) and this disordered structure generally increases dielectric constant due to the ease of polarization. Thus, in this temperature range (600-800 °C) the major factor to decrease the dielectric constant is the temperature (thermal motion), not the crystal structure changes.

Increase of the dielectric constant from 800 °C to 950 °C is unexpected because over this temperature range there is little change in terms of physics and chemistry of the sample. The presence of liquid phase from albite melting would increase the polarizability of the sample due to the ease of polarisation under applied electric field. However, 800 °C, no such liquid glass is produced (liquid glass is observed around 950 °C).

This behaviour was also observed by Leluk et al., [275] who explained by the removal of chemically bound water during dehydroxylation at 400-800 °C producing free volumes (in the metakaolinite structure). The free volume provides higher movements and/or oscillations of polar molecules, and so the dielectric constant should increase [275]. In this study it is possible that the increase of dielectric constant above 800 °C is due to the formation of metakaolinite since there is large fraction of kaolinite found in the porcelain sample.

Moreover, increase in the dielectric constant can result from the space charge polarization because in a multiphase solid where one phase has a much

larger electrical resistivity than the others, charges can accumulate at the phase interfaces [276].

Loss tangent ($tan\ \delta$) as a function of temperature of the porcelain sample is calculated using the electric conductivity (Fig. 5.9) and dielectric constants (Fig. 5.13). From 50-500 °C the loss tangent is very small (about ~10^{-6}) but drops at 500 °C resulting from the dehydroxylation of kaolinite (presented in the inset of Fig. 5.13).

The loss tangent increases sharply at above 600 °C from 10^{-6} to 0.27 which can be explained by increasing of three loss mechanisms: conductive loss (flow of charge carriers), dipole loss (rotation of dipole), and vibration loss (vibration of charge carriers) [277].

At low temperatures (<600 °C), the loss tangent is low because of the low values of conduction, dipole and vibration losses. However, above 600 °C, the three losses contribute significantly to the loss tangent (such as through increase of electrical conductivity, and greater effect of thermal motion) leading to an increase in the loss tangent with increasing temperature. Thus, a combination of these three losses produces a large loss tangent.

The conduction loss plays the most important role in rising the loss tangent because it significantly increases the mobility of the charge carriers (i.e. Na^+ and K^+). The loss tangent increases exponentially above 950 °C due to the presence of liquid glass, which produces a great electrical conductivity (great conduction loss).

5.9 Conclusions

This chapter summarises the effect of elevated temperature on the porcelain sample properties. The key findings are;

1. The porcelain sample composes of albite, kaolinite, and quartz while other oxides found by ICP-AES are considered as impurities.
2. The porcelain sample starts to sinter at 950 °C and fully sintered with total shrinkage of 7% at 1200 °C.
3. Heat capacity of the porcelain increases with increase temperature. The melt of albite substantially increases the heat capacity above 1000 °C.
4. Thermal conductivity as a function of temperature of the porcelain sample decreases by the phonon scattering at low temperature before

the melting of albite, once the albite melts thermal conductivity increases substantially due to increasing of density of the porcelain.

5. Electrical conductivity of the porcelain is divided into 3 regimes; low, medium and high temperature regimes. Conductivity at 100-250 °C increased mainly arising from H^+ and OH^- generated from the physically bound water. At >250 °C, a combination of H^+, OH^-, Na^+ and K^+ dominated the conductivity. During the cooling, the change of phases in the sample produced greater electrical conductivity at the same temperature.
6. All of these measured properties in this chapter is used to set the appropriate sintering process parameters and will enable discussion of interpret the empirical results.

Chapter 6

Effect of DS process on porcelain

6.1 Chapter review

In the direct sintering (DS) process, porcelain samples are transferred into a preheated furnace at certain sintering temperatures, followed by dwelling and cooling in the furnace to room temperature. DS employs fast heating rates (from room to peak temperature in seconds) compared with conventional sintering (typically 5-20 °C/min); so, minimizing the total energy consumption and total processing time. The aim of this work is to understand the effect of the rapid heating rate of 780 °C/min (this value is calculated in section 6.8) on densification, phase evolution, and mechanical properties. The results also give an idea how rapidly this porcelain composition can be successfully sintered.

Densification of porcelain samples sintered at different heating rates and temperatures is presented in section 6.2, and the physical properties are presented in section 6.3. Phase evolution, microstructure and mechanical properties are presented in sections 6.4, 6.5 and 6.6, respectively. The DSed 1175 °C samples are examined in more detail in section 6.7. Finally, section 6.8 describes heat transfer to porcelain samples during the DS process.

6.2 Densification

Porcelain pellets were densified using DS under different sintering conditions (heating rates, dwell times, and temperatures). The densification of the porcelain samples is determined from apparent bulk density (ABD), and water absorption (WA) measurements. Preliminary results presented in section 5.4 revealed this porcelain composition starts to densify at ~950 °C indicated by its

linear shrinkage (under a conventional sintering process with heating rate of 5 °C/min) and fully densified at 1200 °C (see Fig. 5.3). This initial result was used to set firing temperatures of 1150 °C, 1175 °C, and 1200 °C for more extensive study.

The DS process aims to densify the porcelains more efficiently. The firing schedule showed in Fig. 6.1 represents the relative processing time, and relative energy consumption of the DS process compared with the conventional firing process using 5, 15 and 30 °C/min with a peak temperature of 1200 °C. Fig. 6.1 shows that the bars, which represent processing time and relative energy consumption (% relative energy consumption) located below the firing schedules are significantly reduced with increase heating rates.

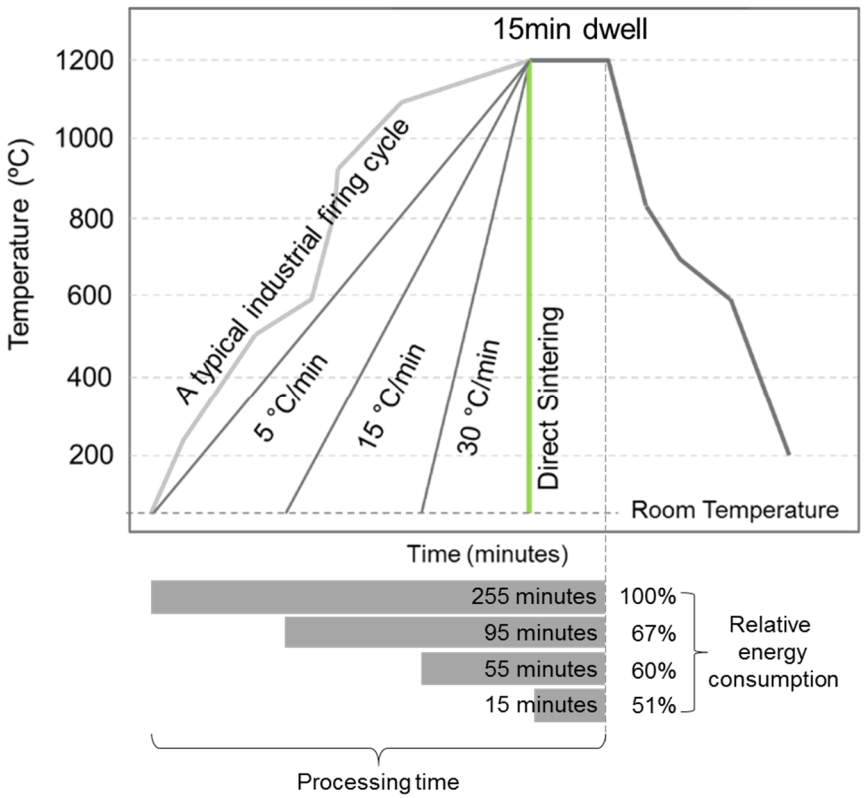

Figure 6.1: Temperature-time profiles and change in total porcelain processing time with respect to change in heating rate. Bars at the bottom of figure represent the processing time, reduction in energy consumption with the change in processing time calculated by the area under curves.

The relative energy consumption of each firing schedule is calculated using the area under the sintering curve and the 5 °C/min firing schedule is used as the

baseline representing 100% energy consumed and the energy usage values for other firing runs are normalised to this baseline. Because the same furnace and sample masses were used, the energy losses are considered as the same for all the heating cycles. The reduction of energy in this study comes from the reduction of processing time (area of the sintering curve). It is also well-established that a conventional furnace can significantly save energy by a small increase in heating rate. This can be done by the improvement of heating power of furnaces through designing a better heat transfer or utilizing more thermally insulative materials and/or heat recovery strategies [278].

Fig. 6.1 reveals that by increasing the heating rate to 15 °C/min, the total energy is reduced by 33% while DS can reduce the energy used by 49%. From this point of view, the DS process has a potential to reduce the processing time and the energy usage. However, it should be noted that the processing time and energy reduction must induce suitable final properties in the sintered products.

6.3 Physical properties

Apparent bulk density (ABD) and water absorption (WA) of the porcelain samples sintered under different conditions are shown in Fig. 6.2 and Table 6.1. Fig. 6.2a shows ABD of porcelain samples as a function of heating rate and sintering temperatures with 15 min dwell. Fig. 6.2a indicates that the change in heating rate has little influence on ABD of the samples sintered at 1150 °C and 1175 °C ranging between 2.36 g/cm^3 to 2.40 g/cm^3.

However, the samples sintered to 1200 °C show a significant difference in ABD with the heating rates, which are 2.25±0.02 g/cm^3 (5 °C/min), 2.26±0.02 g/cm^3 (15 °C/min), 2.31±0.03 g/cm^3 (30 °C/min) and 2.33±0.02 g/cm^3 for the directly sintered samples (DSed samples). Two interesting features were observed in the samples sintered to 1200 °C. Firstly, ABD of all the 1200 °C samples are lower compared to the samples sintered to 1150 °C and 1175 °C. Secondly, the DSed samples sintered to 1150, 1175 and 1200 °C has little change in ABD (the blue diamond in Fig. 6.2a, and Table 6.1a).

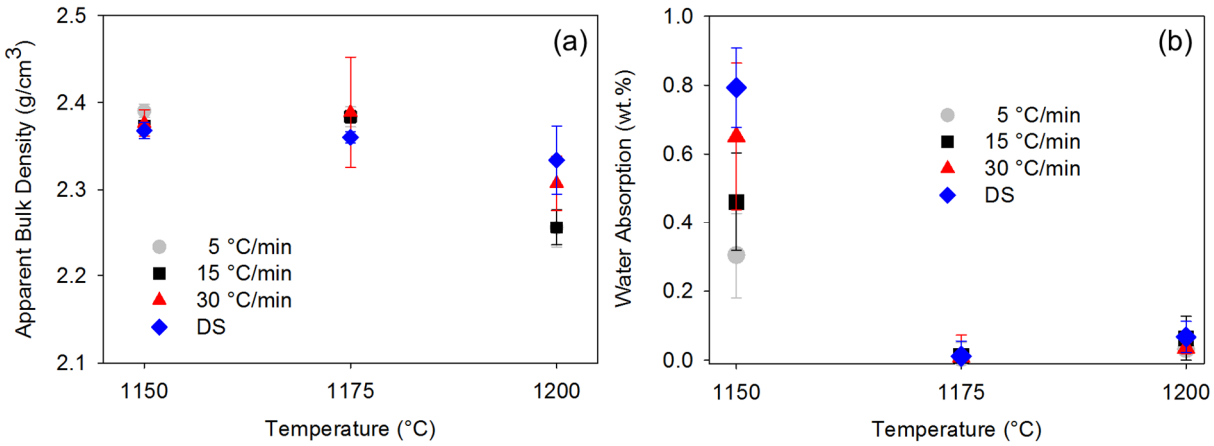

Figure 6.2: (a) ABD, and (b) WA of porcelain samples sintered under different conditions, all dwell 15 min at temperature.

The lower ABDs for the 1200 °C samples at 5, 15 and 30 °C/min is due to bloating, which can be seen from the microstructure (discussed in section 6.5, and Fig. 6.8c). However, the DSed 1200 °C sample has higher ABD compared to the 1200 °C samples at 5, 15 and 30 °C/min, but has similar ABD to the DSed samples sintered at 1150 °C and 1175 °C (2.33-2.37 g/cm^3) because all the DSed samples (1150, 1175 and 1200 °C) have similar densification degree, similar processing time (there is no difference in heating rate effect, Fig. 6.1) thus, the DSed 1200 °C sample may have had insufficient time for bloating to occur resulting in higher ABD compared to the samples sintered to 1200 °C with 5, 15, and 30 °C/min.

Table 6.1: (a) ABD and (b) WA of porcelain samples as a function of heating rate and temperature.

Temperature (°C)	(a) ABD (g/cm^3)			
	5 °C/min	15 °C/min	30 °C/min	Direct sintering
1150	2.39±0.01	2.38±0.01	2.37±0.01	2.37±0.01
1175	2.38±0.01	2.38±0.01	2.39±0.01	2.36±0.01
1200	2.25±0.02	2.26±0.02	2.30±0.03	2.33±0.04

Temperature (°C)	(b) WA (wt.%)			
	5 °C/min	15 °C/min	30 °C/min	Direct sintering
1150	0.30±0.12	0.46±0.14	0.65±0.21	0.79±0.10
1175	0.01±0.04	0.01±0.01	0.00±0.01	0.01±0.04
1200	0.03±0.02	0.06±0.06	0.04±0.01	0.06±0.04

The decrease of ABD in the 1200 °C samples is due to bloating which, however, is not affected by the heating rate because there is no correlation between the heating rates and ABD. In other words, bloating has much greater effect than heating rate when samples are sintered beyond their optimal temperature. The occurrence of bloating is when gas, which is released from burning of volatile matter, is trapped and expands in the liquid glassy phase formed in the samples during sintering process [279].

Fig. 6.2b reveals that the samples sintered to 1150 °C exhibit greater WA at higher heating rates while samples sintered at 1175 °C have lowest WA, which is ~0 wt.%, and independent of heating rates. At 1200 °C, the samples have an increased WA (~0.1 wt.%) compared with the 1175 °C samples.

The increasing of WA of the 1200 °C samples is due to the bloating as also can be seen from the ABD in Fig. 6.2a. Thus, the samples sintered at 1175 °C are the most promising samples in terms of ABD and WA.

Interestingly, in the case of DSed samples (the blue diamond in Fig. 6.2b), once sintering is complete, heating rate does not much affect the WA as revealed by the DSed sample sintered to 1175 °C and 1200 °C. The reason is that the liquid glass fully fills pores eliminating open pores; the less open pores, the less WA.

6.4 Phase evolution

Fig. 6.3 reveals phase evolution of the porcelain samples sintered under DS condition at different temperatures. The as-received porcelain powder composes of three major phases which are albite, kaolinite, and quartz (as also shown in Fig. 5.1, section 5.2). After sintering to 1150 °C, kaolinite peaks disappear from the XRD pattern while residual albite is still observed, and quartz remains constant. Mullite, moreover, is observed in the DSed samples sintered to 1150 °C and above.

Glassy phase is observed in the DSed samples sintered at 1150-1200 °C indicated by a broad hump at ~ 25°2θ (Fig. 6.3a). The glassy phase formed in this porcelain body at ~950 °C due to the decomposition of kaolinite to metakaolin liberating amorphous silica as a by-product. This amorphous silica interacts with albite forming a eutectic melt at ~1050 °C [42,160].

Since, melting of albite is affected by sintering temperature (Fig. 6.3b) the volume of the glassy phase in the samples should increase but a significant change

in the glassy phase volume (suggested by amorphous hump area) is not observed by XRD. In addition, albite completely melts by 1175 °C as revealed by the disappearance of its peaks, thus the volume of glassy phase should remain constant above 1175 °C.

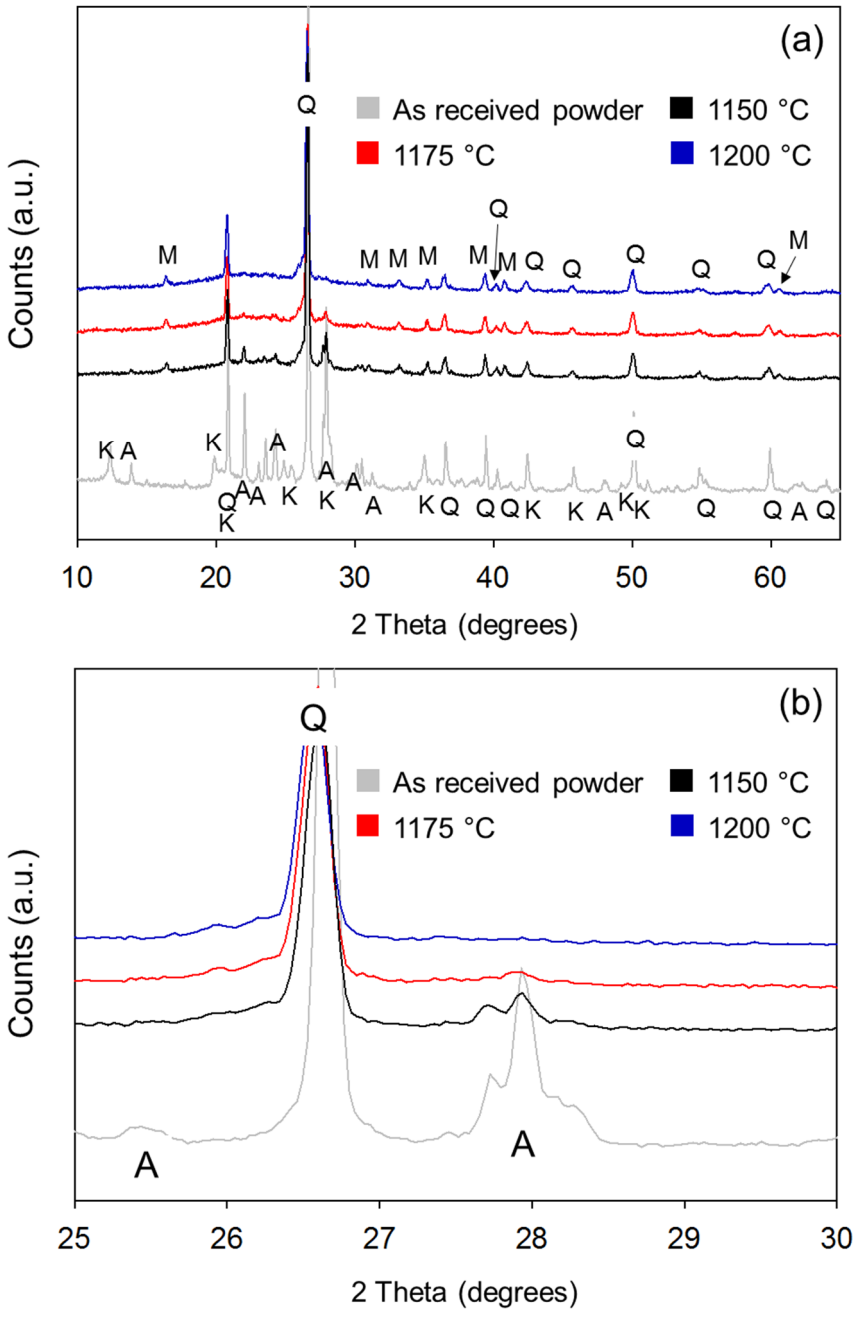

Figure 6.3: XRD showing (a) phase evolution of the DSed porcelain samples at different temperatures, and (b) disappearance of albite peaks with increased sintering temperature. A is albite, K is kaolinite, M is mullite, and Q is quartz.

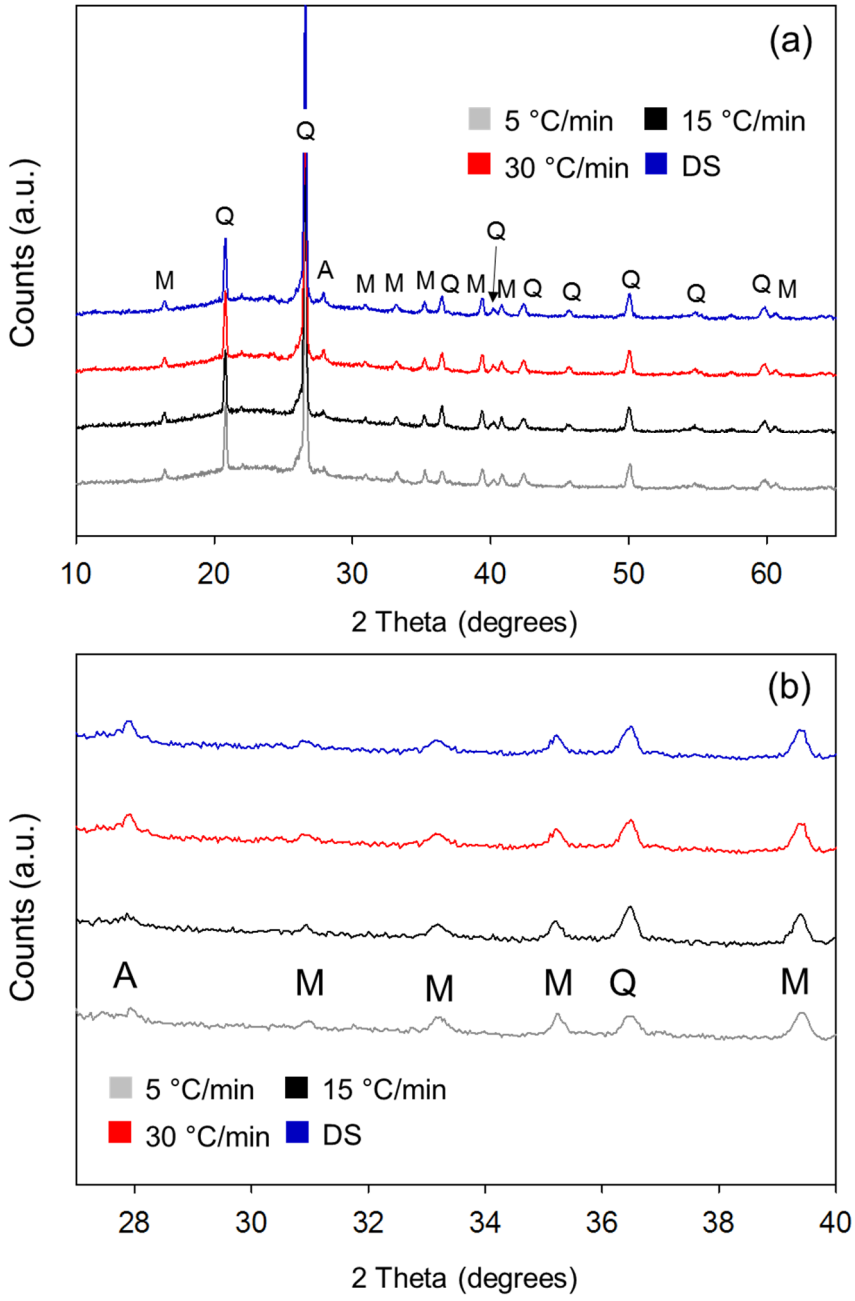

Figure 6.4: XRD of 1175 °C samples showing (a) phase evolution as a function of heating rate, and (b) a closer look at albite and mullite peaks. A is albite, K is kaolinite, M is mullite, and Q is quartz.

Fig. 6.4b shows detail of the decreasing intensity of albite peaks as a function of heating rate in the 1175 °C samples. The XRD patterns show that albite is observed in all samples sintered to 1175 °C, but less amount compared to the sample sintered to 1150 °C. The albite peak area (at 28°2θ) increases with increasing heating rate. However, the XRD shows no clear pattern of how the

melting of albite is affected by the heating rate. To clarify this the albite peak area was plotted against the sintering conditions as presented in Fig. 6.5a.

Fig. 6.5a confirms that the total albite peak area decreases with increase in sintering temperature and is also affected by the heating rate. The albite amount in the samples sintered to 1175 °C are 17-23 vol.% in 5-30 °C/min and 35±1 vol.% in DS process which are less than that in the samples sintered to 1150 °C. In other words, the melting of albite is affected by both temperature and heating rate. The higher the heating rate, the lower the amount of albite melts. However, albite completely melts by 1200 °C.

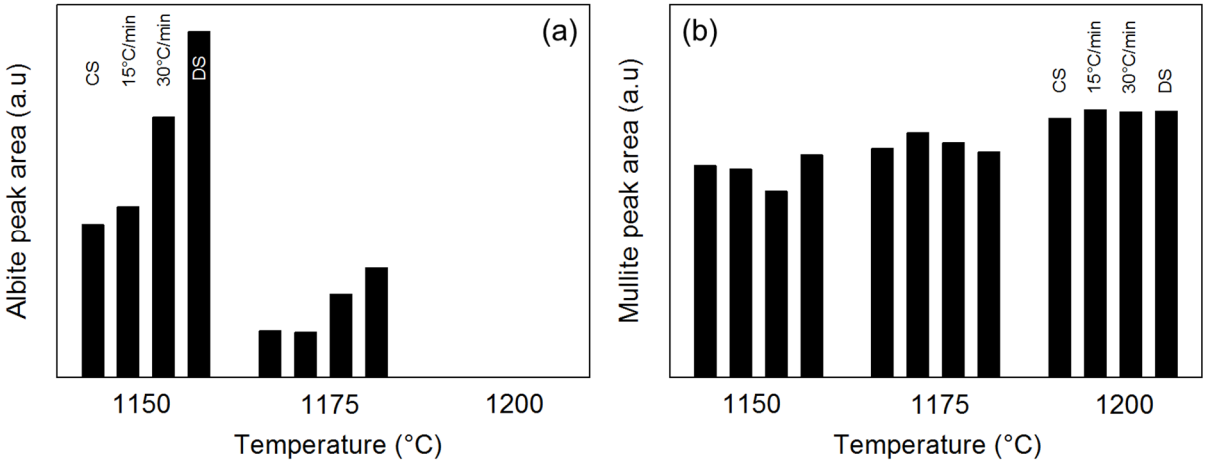

Figure 6.5: (a) Albite and (b) mullite XRD peak areas in porcelain as a function of sintering temperature and heating rate.

Fig. 6.5b reveals that mullite is observed in all samples sintered at 1150, 1175 and 1200 °C irrespective of the heating rate. The mullite peak area, although not strictly indicative of the volume of phase formed, is found to increase with increased sintering temperature and remain constant with changing heating rate.

Interestingly, mullite formed in the samples sintered at 1200 °C is independent on the heating rates. In other words, mullite forms completely at 1200 °C regardless of heating rate. The observed mullite is from two mechanisms. Primary mullite forms directly from kaolinite phase decomposition while secondary mullite forms by reactions between albite, kaolinite and quartz [122,161]. The microstructures reveal that both primary mullite (formed in the

clay relict) and secondary mullite (found in the glassy region) are present (further discussed in section 6.5).

ABD, WA (Fig. 6.2a and b), and XRD results (Fig. 6.3 and 6.4) indicate that despite the samples fired to 1175 °C having the highest ABD and lowest WA, they still contained residual albite. This observation suggests that the formation of glassy phase in the samples sintered at 1175 °C is not complete, even though full densification can be achieved. In other words, when a sufficient amount of liquid phase is obtained; further melting of albite is unnecessary for densification. Thus, in this study the optimal glassy phase content for achieving full densification can be estimated from the albite XRD peak area.

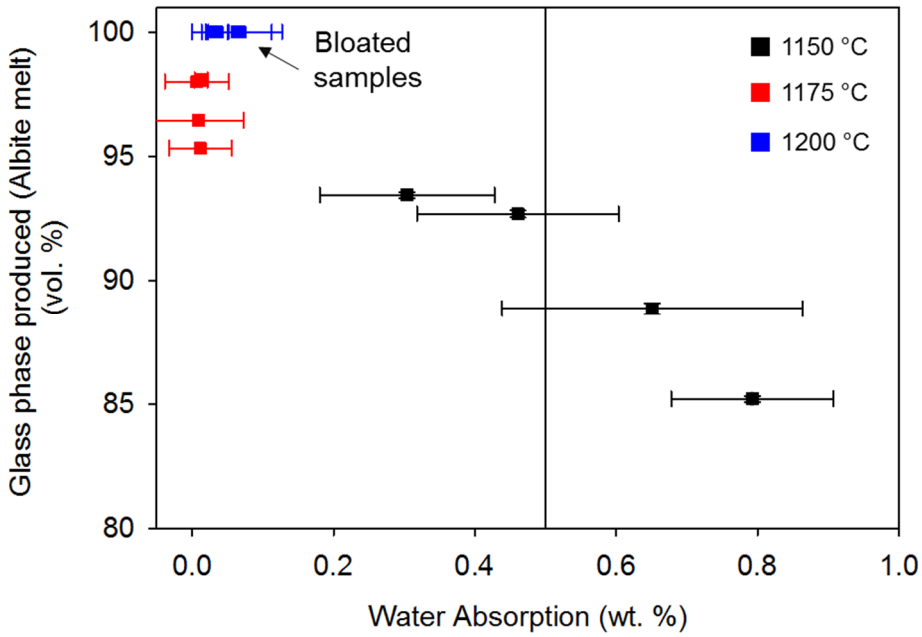

Figure 6.6: Optimal glass content of the porcelain calculated from total albite peak area. The industrial standard for porcelain tiles (0.5 wt.% WA) is referred as ISO 13006 [280].

Fig. 6.6 presents the optimal glassy phase content of this porcelain composition which is calculated using the albite peak area in the XRD patterns (100 vol.% of albite is calculated using albite peak area of the green porcelain). This plot reveals that this porcelain composition needs ~95 vol.% of the albite to melt to achieve a fully densified product (WA ~0 wt.%). From the industrial standard point of view (WA <0.5 wt.%), the optimal glassy phase content is when ~90 vol. % of the albite melts. In other words, the sample sintered at 1150 °C with

5 °C/min is also promising for industrial use. Furthermore, melting of more than 95 vol.% of the albite does not further improve densification of the samples. In contrast, this study reveals that 100 vol.% albite melting leads to bloating.

The XRD result was also used to calculate mullite crystallite size as presented in Fig. 6.7. Fig. 6.7 shows the mullite crystallite size calculated using the Scherrer equation (see section 4.9.1 in Experimental chapter) which suggests that mullite crystallite size increases with increasing temperature but does not change with the heating rate because there is no clear correlation between mullite crystallite size and heating rates. The mullite size in the sample sintered to 1150 °C ranges from 33-37 nm while it is 37-40 nm in the 1175 °C samples. The 1200 °C sintered samples have a slightly larger mullite crystal size than the 1175 °C samples, ranging between 37-44 nm.

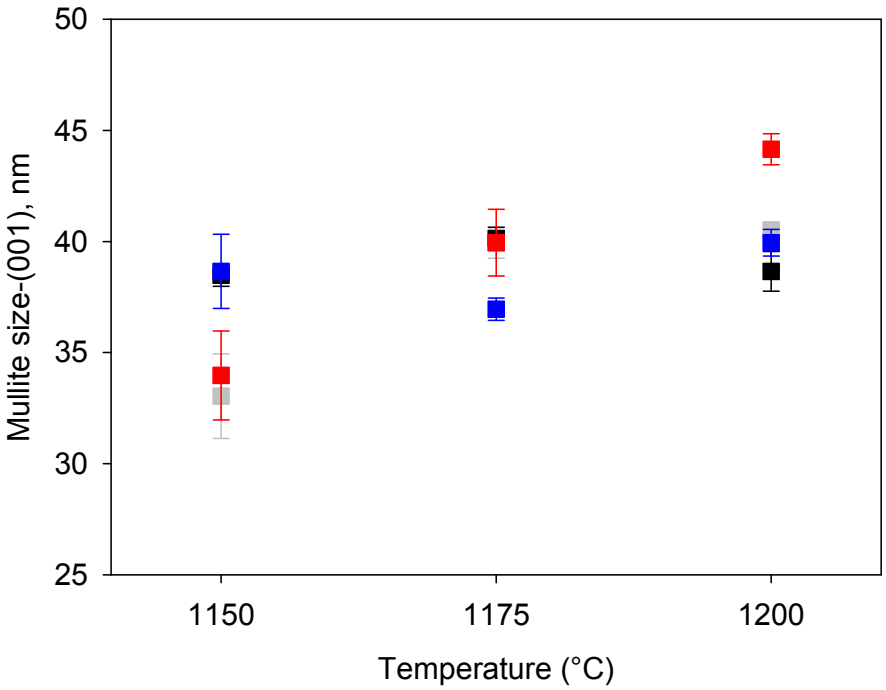

Figure 6.7: Mullite crystallite size as a function of heating rates, and temperature calculated using Scherrer equation.

6.5 Microstructure

Microstructural analysis of the DSed samples sintered at different temperatures (Fig. 6.8) reveals that the DSed samples fired at 1150 °C (Fig. 6.8a) contain porosity (green colour calculated using image analysis) of 22.7±2% and it is higher than the samples fired at 1175 °C and 1200 °C having 10.9±2% and

14.9±5%, respectively. In addition, the DSed sample sintered at 1175 °C (Fig. 6.8b) contains some irregular-shaped pores while DSed 1200 °C samples (Fig. 6.8c) has isolated pores, which are more rounded due to them starting to fill with gas (bloating).

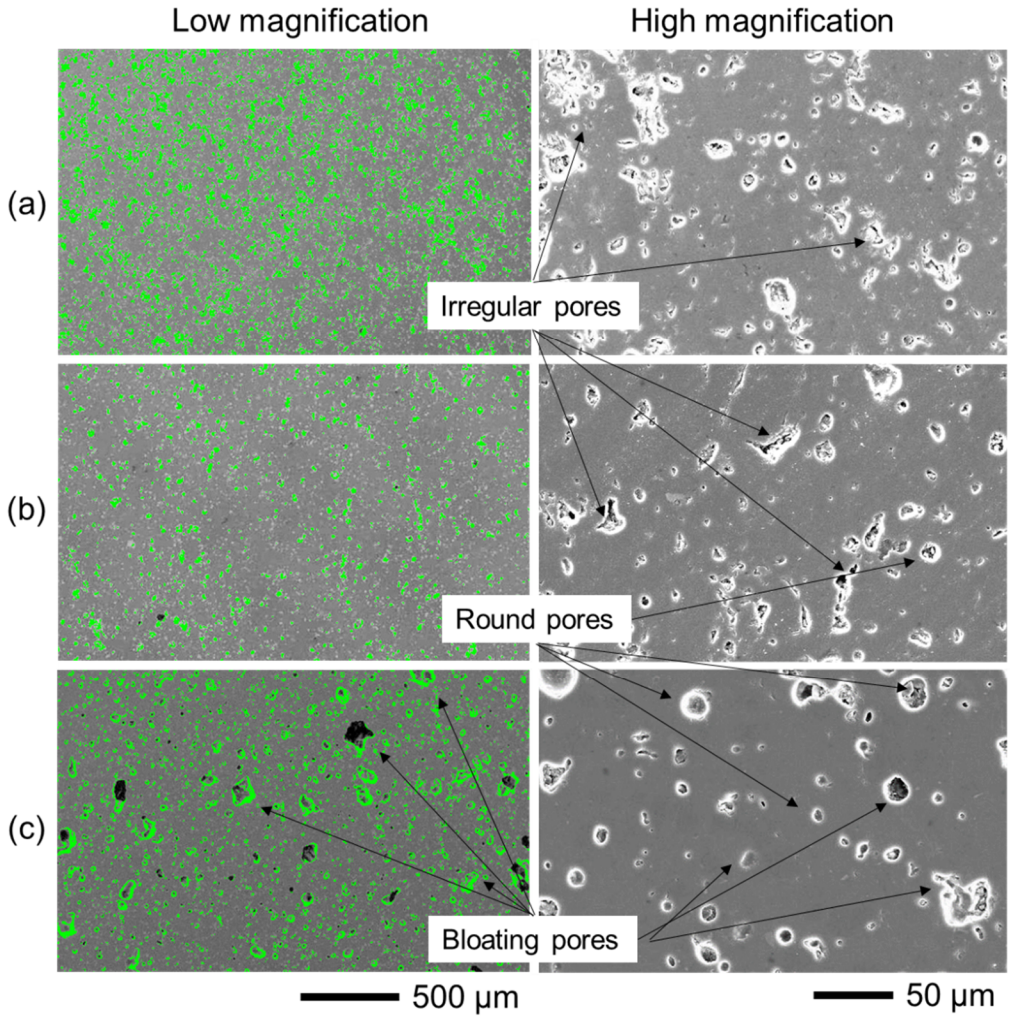

Figure 6.8: SEM images at low (left column) and high (right column) magnification of DSed porcelain samples fired 15 min at different temperatures, (a) 1150 °C, (b) 1175 °C, and (c) 1200 °C showing different pore shapes, the green area in the left column represents calculated porosity.

Low magnification SEM images (left column in Fig. 6.8) also represent uniformly sintered microstructures; the 1150 °C sample has interconnected irregular-shape pores due to incomplete sintering. The 1175 °C contains a number of isolated pores (6 pores/50x50 µm^2 of size >20 µm) while the 1200 °C shows a

large number of rounded-pores resulted from bloating (15 pores/50x50 μm^2 of size >20 μm).

Fig. 6.9 presents the etched microstructure revealing mullite, glass and quartz in DSed samples sintered at different temperatures. SEM reveals mullite in all DSed samples has different size and shape. Mullite formed at 1175 °C has an average size of ~1±0.2 x 0.07±0.03 μm (length x thickness) (Fig. 6.9c) when compared with the needles observed in samples sintered at 1200 °C (~2±0.1 x 0.1±0.02 μm) (Fig. 6.9b).

However, the mullite size observed by SEM is larger from the mullite size calculated using Scherrer's equation (see Fig. 6.7) because SEM gives grain sizes which may contain several crystallites, whereas XRD gives the individual crystallite sizes. Scherrer's equation gives values of 37±0.5 and 40±0.6 nm in samples sintered at 1175 °C and 1200 °C respectively.

In addition, the Scherrer equation determines the mullite crystallite size from larger sampling areas volume (cm^3) whereas SEM images show mullite needles in a small area (μm^2). However, both observations of mullite size agree that mullite formed in the DSed samples at 1200 °C is larger than that in 1175 °C samples.

More mullite is present in the DSed samples sintered at 1200 °C (~10 vol.% greater than that formed in samples sintered at 1175 °C determined from XRD peak area (Fig. 6.5b). In addition, the DSed 1200 °C sample contains no albite while albite relicts (indicated by A in Fig. 6.9a) are observed in samples fired at lower temperatures.

The microstructures presented in Fig. 6.8 and 6.9 are similar to the commercial porcelain products having typical features of a well-fired ceramic body including glassy phase, mullite and quartz [42,106,160,270]. However, the DSed sample and commercial porcelain products have different amounts and size of mullite because they have different chemistries. The apparent porosity of the DSed sample and commercial porcelain is also different because they may have different firing treatments although the WA of both is similar (~0 wt.%). The dense porcelains generally have about 0 wt.% water absorption which corresponds to almost zero open porosity regardless of the pore shapes. According to the

industrial standard (ISO 13006), the open porosity (water absorption) of typical commercial porcelain tiles is <0.5 wt. %.

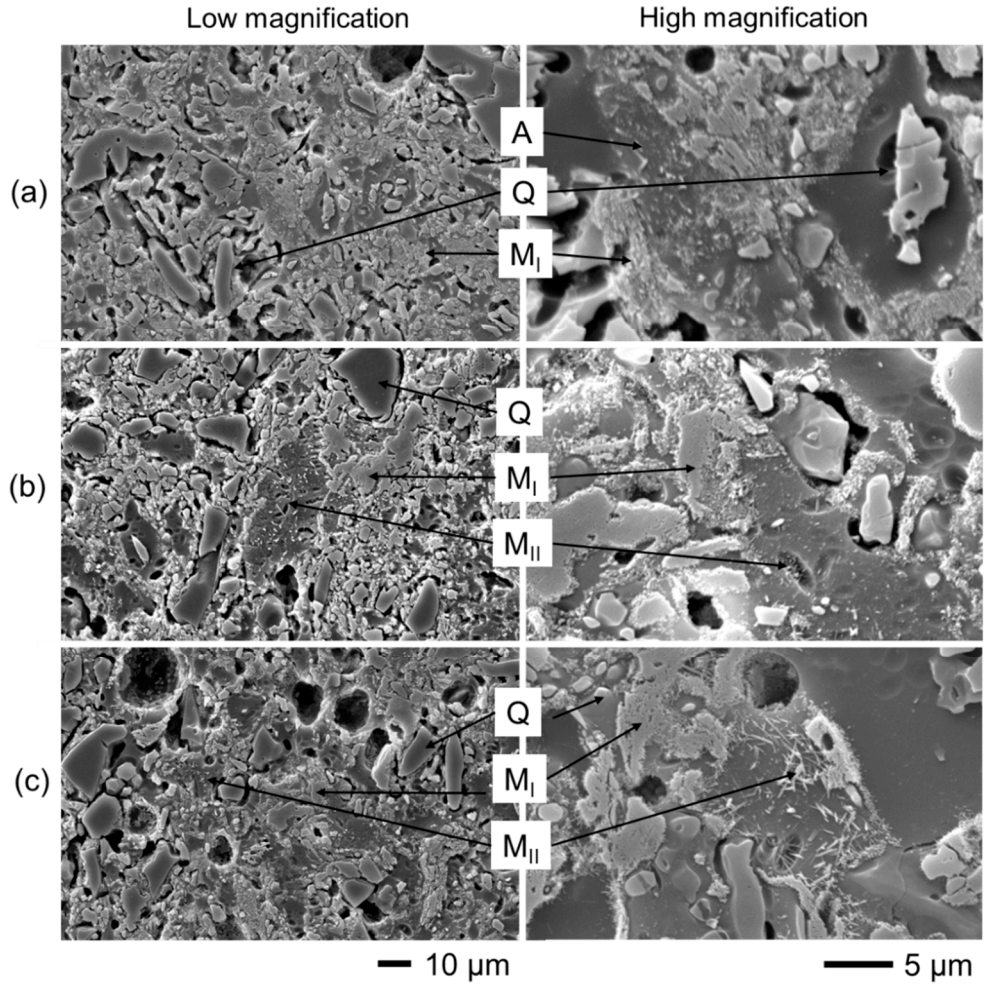

Figure 6.9: SEM images at low (left column) and higher (right column) magnification of DSed porcelain samples, sintered for 15 min at different temperatures, (a) 1150 °C, (b) 1175 °C, and (c) 1200 °C showing etched samples using 20% HF. (A is albite relicts, M_I is primary mullite, M_{II} is secondary mullite and Q is Quartz).

6.6 Mechanical properties

The diametral compressive strengths (DCS) determined as described in section 4.14.1 of the porcelain samples sintered under different conditions are shown in Table 6.2 and Fig. 6.10a.

Considering the 5 °C/min heating rate samples (the grey circle in Fig. 6.10a). The DCS of samples sintered to 1150 °C is relatively low (23±5 MPa) compared to those sintered to 1175 °C (26±3 MPa) but similar to those sintered to

1200 °C (~23±2 MPa). The low DCS of samples sintered at 1150 °C is due to their incomplete sintering (high porosity), while the low DCS of samples sintered at 1200 °C is due to gas take up in pores prior to eventual bloating.

The porcelain samples sintered to 1175 °C with different heating rates has a range of DCS of 26±3, 26±3, 32±4 MPa for heating rates of 5, 15, and 30 °C/min, respectively, while DSed 1175 °C sample shows the lowest DCS of 21±2 MPa. Samples sintered to 1200 °C also exhibit a range of DCS; the DSed sample has lowest DCS (18±4 MPa) compared to samples fired at slower heating rates due to pore growth from gas ingress prior to bloating (Fig. 6.8c).

Table 6.2: DCS of porcelain samples as a function of heating rate and temperature.

Temperature (°C)	DCS (MPa)			
	5 °C/min	15 °C/min	30 °C/min	Direct sintering
1150	23±5	21±3	23±5	20±4
1175	26±3	26±3	32±4	21±2
1200	23±2	24±4	25±3	18±4

Examining the samples sintered to 1175 °C in more detail reveals that the relation between the DCS and heating rate is complex. The slow heating rates of 5 and 15 °C/min produced similar DCS (26±3 MPa) while the highest DCS is obtained at 30 °C/min (32±4 MPa). DCS drops to its lowest value for DSed samples (21±2 MPa); so, there is no clear trend between heating rate and DCS.

It might be expected that faster heating rates providing less time for densification would give the most porous microstructure, but this is not the case. Thus, the variation of the DCS appears to be due to the nature of the pores (size, shape and distribution) in the sintered samples (discussed further in section 6.7). However, the samples sintered to 1175 °C at 30 °C/min have highest DCS likely due to a slightly higher density (2.39±0.02 g/cm^3) compared to the others, see Table 6.1a.

In the case of DS process (the blue diamond in Fig. 6.10a), the DCS of DSed samples sintered to 1150 and 1175 °C are similar (20-21 MPa) while the DSed samples sintered to 1200 °C exhibit lower DCS which is 18±4 MPa, which is due to bloating.

The DCS of samples sintered at 1200 °C with the heating rates of 5, 15 and 30 °C/min varies over a narrow range (23-25 MPa). Nevertheless, among the DSed samples, the 1175 °C sample has the highest DCS due to its higher ABD and lower WA (Table 6.1a and b).

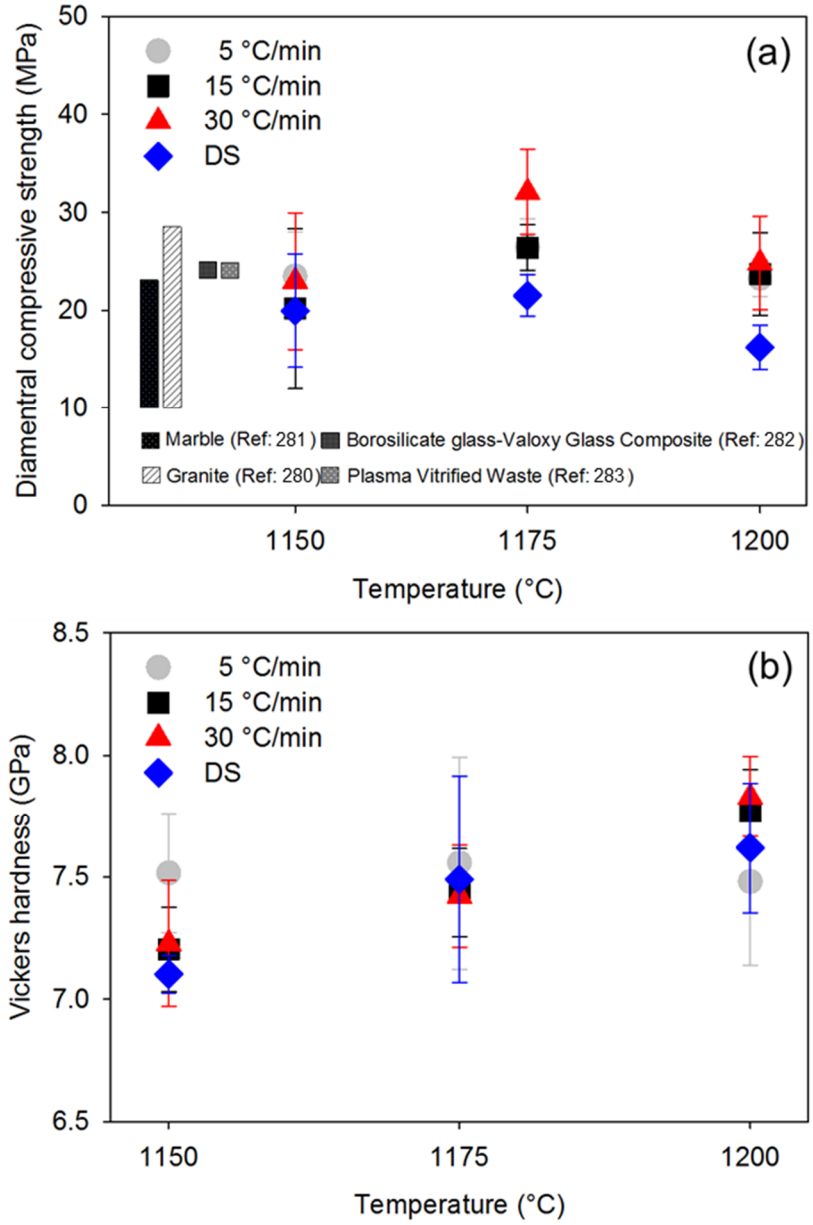

Figure 6.10: (a) DCS of fired porcelain samples compared with selected commercial building materials [281-283], (b) Vickers hardness of sintered samples as a function of heating rate and temperature.

Mechanical strengths measured by DCS of porcelains sintered to 1175 °C for all heating rates suggest that they are promising and potentially usable commercially compared to current building materials such as marble (10-28 MPa)

[281] and granite (10-23 MPa) [281], as well as glass composite building materials derived from borosilicate-Valoxy glasses (24 MPa) (the Valoxy are alumina-rich wastes produced from recycling aluminium salt slags [282]), and from plasma vitrified wastes (24±2 MPa) [283].

Vickers hardness (H_V) values (Fig. 6.10b) are similar for samples sintered to 1175 and 1200 °C and a little higher than samples sintered to 1150 °C. This is attributed to the microscale density and varying phase compositions. For example, samples sintered to 1175 °C have high H_V because they have highest ABD, while samples sintered to 1200 °C exhibit lower ABD but they contain more mullite and a denser microstructure (not at the bloated area, yellow circles in Fig. 6.11) thus the samples sintered to 1200 °C also have high H_V.

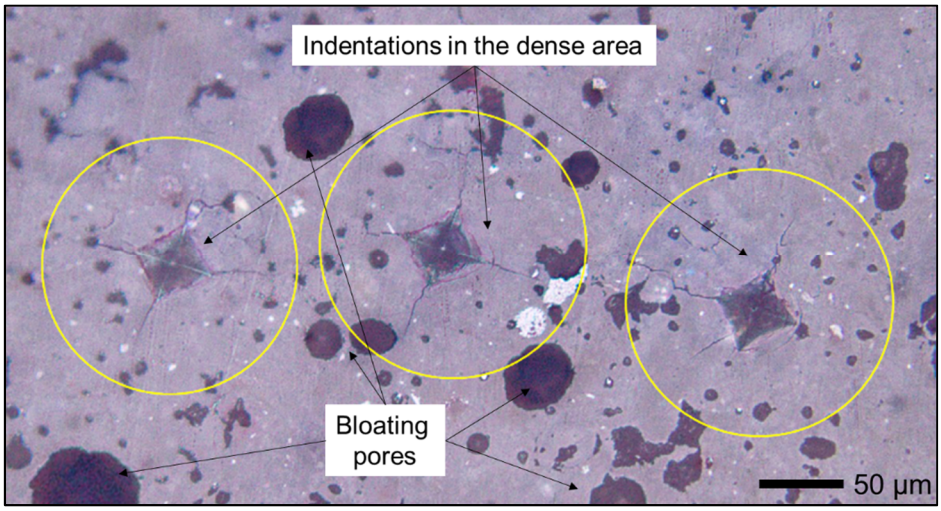

Figure 6.11: The yellow circles show the indentation areas, which were selected from the dense and pore-free area, the bloating pores were observed in the DSed 1200 °C sample.

Previously reported H_V of porcelains (sintered 2 h at 1250 °C) are comparable to those of this study being in the range of 6-8 MPa [284,285]. However, it should be noted that the difference of DCS and H_V results from the examination scales. DCS measures strength of the samples by measuring force to break the samples, which is considered as macroscale behaviour, while H_V measures the material surface resistance to the plastic deformation, which is in microscale [285].

Mechanical strength measured using DCS gives lower values than other testing methods. A comparative study of the DCS to flexural strength (3-point bending) of composite resins shows the DCS of 35.61±5.4 MPa is equivalent to 87.75±3.8 MPa of 3-point bend flexural strength [286]. Furthermore, the DCS of a glass ionomer cement for dental restorations of 8.27±0.475 is equivalent to 70.26±6.05 of compressive strength [287]. Therefore, based on this information, the samples sintered using DS are likely to have sufficient mechanical strength to be used as flooring materials.

The promising physical properties, phase compositions, and mechanical properties in the dense areas were successfully obtained by the DS process. Therefore, this study suggests that if dense porcelains without bloating pores can be produced using the direct sintering technique, they could have comparable technical properties to current commercial materials and with less processing time and energy.

6.7 Detailed examination of porcelain samples sintered to 1175 °C

SEM images of cross sections of the porcelain samples sintered to 1175 °C (Fig. 6.12a) show that the samples sintered using different heating rates have different pore structures and percent porosity (Fig. 6.12b). The 5 °C/min porcelain sample is highly porous (20.4±2% porosity) whereas the 15 °C/min sample has a denser microstructure (14.7±1% porosity) but still contains numbers of irregular-pore clusters. The sample sintered at 30 °C/min also has a denser microstructure (15.7±2 % porosity) with a slightly higher ABD (2.39±0.01 g/cm^3) compared to 1175 °C samples sintered using different heating rates (see Table 6.1a). The DSed sample exhibits similar microstructure in terms of ABD and percent porosity to the 30 °C/min sintered sample (14.9±1% porosity) which can also be seen from Fig. 6.12b.

This 30 °C/min sample has more irregular-pore clusters (yellow circles in Fig. 6.13a) distributed throughout its cross section compared with the DSed sample but having better DCS. The DSed 1175 °C contains less irregular pore clusters (yellow circles in Fig. 6.13b) but larger (~60-80 µm) than that present in the 30 °C/min sample (~30-50 µm) which explain the lower DCS. From the microstructure point of view, this may explain why the sample sintered at

30 °C/min has highest DCS. It is well documented that strength of ceramics is related to both the amount of porosity and pore characteristics. Strength decreases as porosity increases. In other words, higher density porcelains have higher strength. It is also known that irregular pores act as fracture flaws reducing strength but isolated spherical pores with a size of 5-20 μm can enhance the strength because energy of crack is distributed around the spherical pores, cracks can be stopped [288-290]. Although there are round pores in both samples but the major factor dictating DCS between 30 °C/min and DSed sample is the size of the irregular-pore clusters.

Another possibility for the reduction of DCS in the DSed sample is that a more viscous glass forms tending to entrap volatile matter in the bulk of the material, which otherwise would escape. Such entrapped gas increases the stresses at the interfaces between particles leading to lower DCS [282].

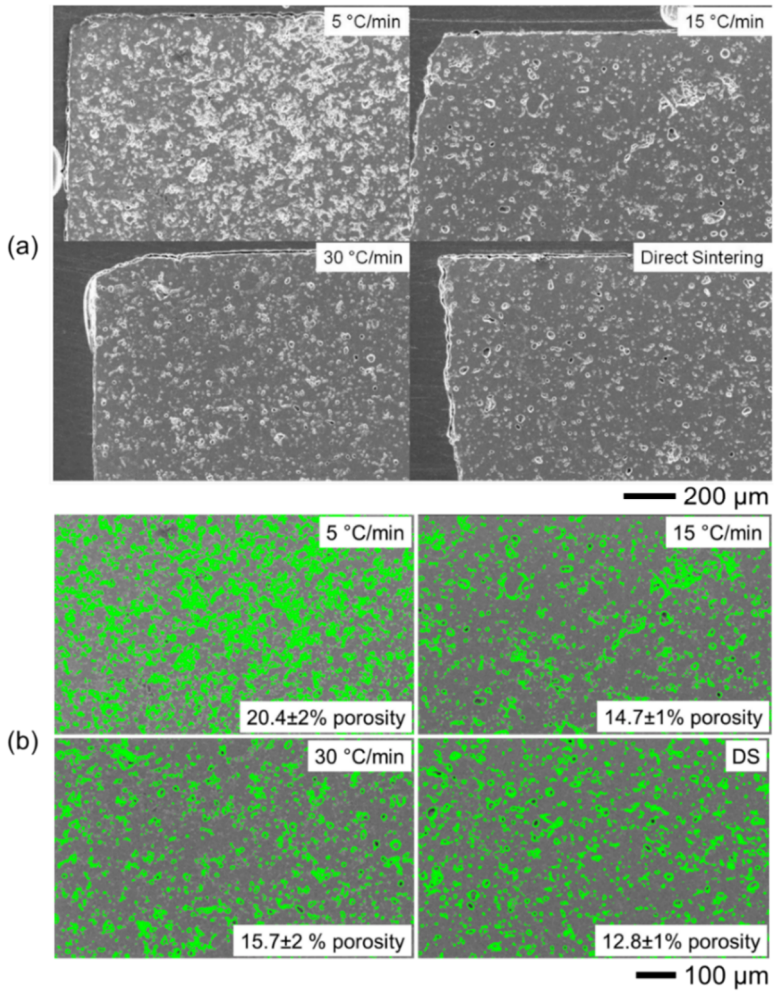

Figure 6.12: SEM cross-sections of porcelains sintered for 15 min at 1175 °C, (a) with different heating rates, (b) the green area shows calculated porosity.

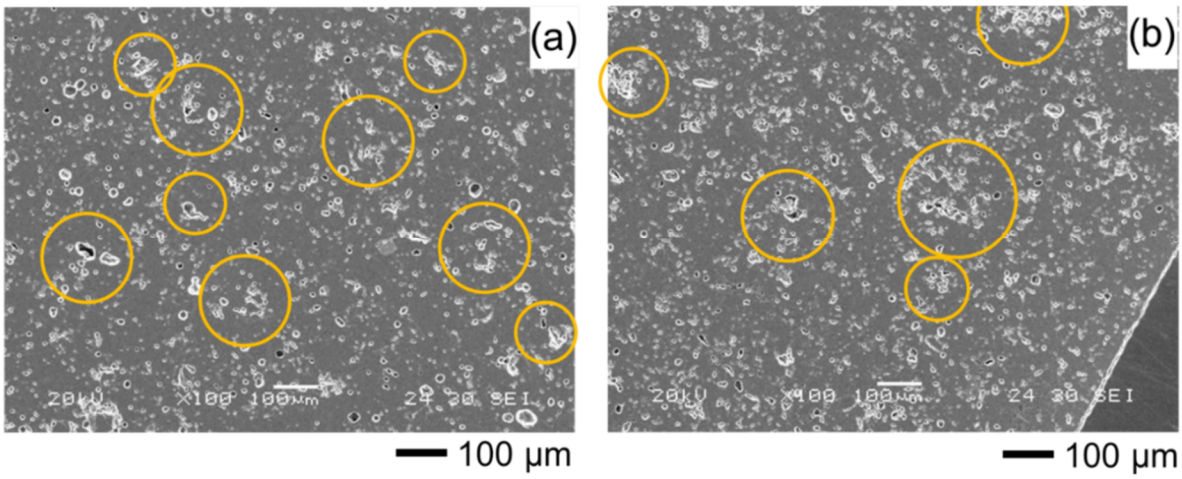

Figure 6.13: SEM images of the DSed 1175 °C samples with different heating rates, (a) 30 °C/min, and (b) DS. The green area represents calculated porosity. The yellow circles represent the irregular pore clusters.

In addition, a study of the effect of heating rate effect on leucite-based dental porcelains showed that the heating rates did not affect densification of the porcelain [291]. In other words, there was no obvious trend how heating rate affects densification and properties of porcelains. Presumably the ease of melting and viscosity of the liquid glass formed is the key in porcelain densification and this may vary significantly between systems impacting also the shape and distribution of any remaining pores, which affects the mechanical properties.

6.8 Heat transfer in porcelain via DS

The DS process employs a rapid heating rate to sinter the sample where surface and bulk experience a temperature gradient for a short period of time. In this section the temperature gradient is analysed to determine how much time is needed to sinter samples homogeneously.

Consider a green porcelain pellet with a certain dimension being heated in an electric resistance furnace (Fig. 6.14). In this case, the furnace is preheated to 1200 °C, a typical porcelain sintering temperature. At a steady state (time =0), the porcelain is directly subjected to the furnace temperature, so heat is transferred from the furnace atmosphere to the porcelain sample. It is assumed that the heat transfer from the surroundings to the porcelain is only by radiation because (1)

high temperature above red heat is used and (2) there is no air circulation in the furnace cavity (no convection).

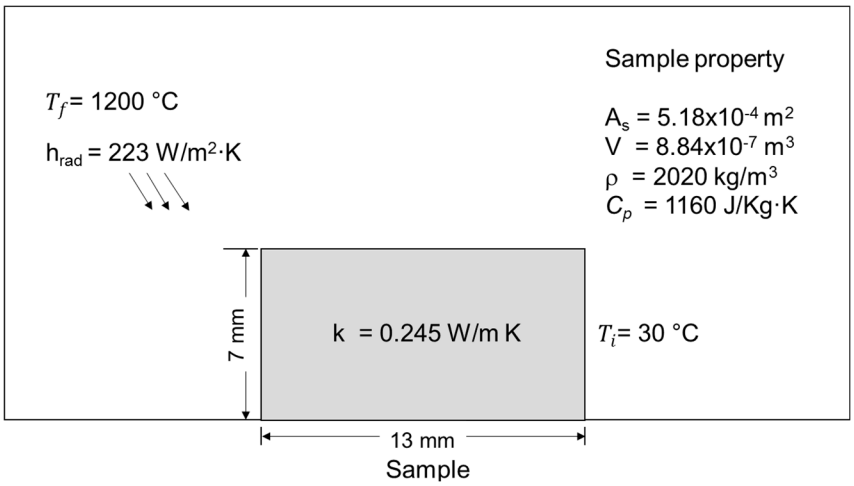

Figure 6.14: Schematic diagram of porcelain pellet in a furnace and its properties at 1200 °C.

In this case, the furnace temperature (T_f) is fixed and the porcelain temperature ($T_{porcelain}$) is variable so the time giving $T_{porcelain} = T_f$ can be estimated and this estimation can be representative of the heating rate used in the DS process. It is also assumed that (1) temperature gradient in the sample bulk is negligible, (2) there is homogeneous thermal conduction throughout the sample body, and (3) the porcelain properties (i.e. C_p, thermal conductivity etc.) are not a function of temperature (C_p, and thermal conductivity were taken at 1200 °C from section 5.5 and 5.6 respectively). Under this assumption, the heat transfer from the furnace to the porcelain sample can be expressed by using the energy balance equation as presented in Eq.6.1 and 6.2 [292].

$$hA_s(T_f - T_s)dt = mC_p dT \tag{6.1}$$

$$\frac{d(T_s - T_f)}{(T_i - T_f)} = -\frac{hA_s}{\rho V C_p}dt \tag{6.2}$$

where h is heat transfer coefficient (W/m²·K), A_s is surface area of the sample, m is mass of the sample, ρ is density of the sample, V is sample volume, C_p is heat

capacity of the sample at constant pressure, and T_i, T_s, and T_f are initial temperature of the sample, final temperature of the sample and the furnace temperature, respectively. Integrating from time t=0, at T_s=T_i to any time t, at T=$T(t)$ yields;

$$ln\frac{(T_s(t)-T_f)}{(T_i-T_f)} = -\frac{hA_s}{\rho V C_p}t \tag{6.3}$$

$$\frac{(T_s(t)-T_f)}{(T_i-T_f)} = e^{-bt} \qquad \text{where } b = \frac{hA_s}{\rho V C_p} \tag{6.4}$$

As previously mentioned, it is assumed that heat transfer from a laboratory electric furnace is due to radiation only. The h_{rad} from the temperature difference between 1200 °C and 30 °C is calculated using Eq. 6.5.

$$h_{rad} = \varepsilon\sigma(T_f^2 + T_s^2)(T_f + T_s) \tag{6.5}$$

$$h_{rad} = 0.98\sigma(1473^2 + 303^2)(1473 + 303) = 223.2\ \mathrm{W/m^2K}$$

where h_{rad} is radiative heat transfer coefficient (W/m^2·K), ε is emissivity of the sample obtained from the pyrometer calibration data in section 4.15.3.1, σ is the Stefan-Boltzmann constant (σ = 5.67 x 10^{-8} W/m^2·K^4), T_f is temperature from emitting surface (furnace) (K), and T_s is temperature of absorbing surface (sample) (K).

To calculate time required to heat a porcelain pellet uniformly under the direct sintering process Eq. 6.4 is employed.

Using, the following equation to calculate b.

$$b = \frac{hA_s}{\rho V C_p} \qquad \text{b = 0.063 s}^{-1}$$

$$\frac{(1468-1473)}{(303-1473)} = e^{-0.063t} \qquad \text{t= 86.60 s or ~1.5 min}$$

In this case, it is assumed that the interior temperature of the DSed sample is 1195 °C. Therefore, in the DS technique with a preheated furnace of 1200 °C, the porcelain sample with a dimension of 13x7 mm (diameter x height) needs about 1.5 min to be heated uniformly as presented in Fig. 6.15. In other words, the heating rate used in the DS process is about 780 °C/min.

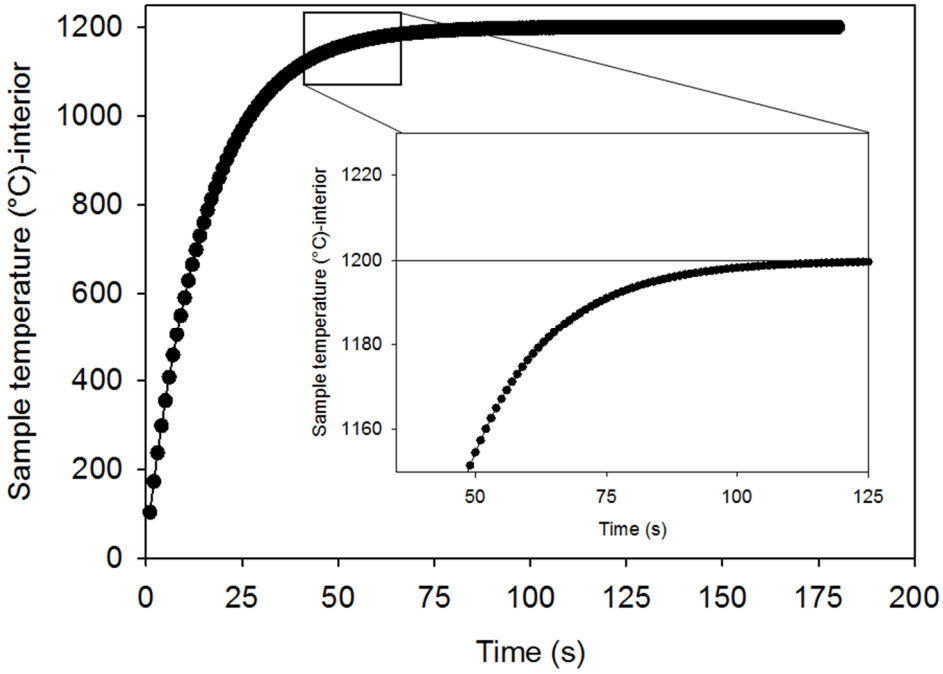

Figure 6.15: Graph shows development of porcelain sample temperature as a function of time.

In addition, the porcelain pellet experiences a temperature gradient at t=0 due to thermal conduction. To demonstrate how the temperature distributes in the sample at a steady state (t=0), the finite difference approximation (FDA) is employed [293].

Consider the 2D (x, y space) heat diffusion equation, the finite difference approximation can be expressed as;

$$\frac{\partial T}{\partial t} = k\left(\frac{\partial^2 T}{\partial x^2} + \frac{\partial^2 T}{\partial y^2}\right) + \frac{Q}{\rho C_p} \tag{6.6}$$

and

$$\left.\frac{\partial^2 T}{\partial x^2}\right|_{m,n} \approx \frac{T_{m+1,n} - 2T_{m,n} + T_{m-1,n}}{(\Delta x)^2} \tag{6.7}$$

$$\left.\frac{\partial^2 T}{\partial y^2}\right|_{m,n} \approx \frac{T_{m+1,n} - 2T_{m,n} + T_{m-1,n}}{(\Delta y)^2} \tag{6.8}$$

where T is temperature, t is time, Q is heat generation, ρ is material density, $C_p$is heat capacity, k is thermal conductivity, x and y are direction of heat propagation, m, n are the location of the nodal points (two indices for space).

To solve this heat equation in the steady state, the finite difference approximation of the 2D heat diffusion equation is;

$$\frac{T_{m+1,n} - 2T_{m,n} + T_{m-1,n}}{(\Delta x)^2} + \frac{T_{m+1,n} - 2T_{m,n} + T_{m-1,n}}{(\Delta y)^2} + \frac{Q}{\rho C_p} = 0 \tag{6.10}$$

Due to the complexity of this numerical analysis, the temperature distribution is solved using MS Excel as presented in Fig. 6.16.

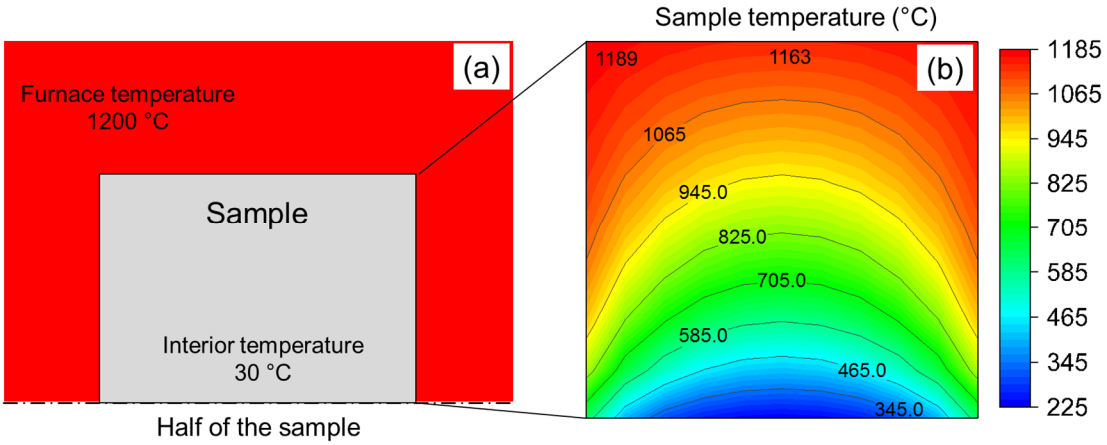

Figure 6.16: (a) Schematic diagram of the DSed sample in the preheated furnace, (b) contour plot of temperature distribution in the DSed porcelain sample at 1200 °C and t=0.

Fig. 6.16 shows that there is a large temperature difference in the DSed porcelain sample at the steady state (t=0). It is clear that the surface temperature of the DSed sample is about 40 °C lower than the furnace temperature (1163 °C at the top-middle of the sample) whilst the interior temperature at the middle of the sample is about 330 °C.

Please note that the boundary condition at the bottom of the model represents half of the sample, which has temperature of 30 °C inherited from room temperature. However, this DSed sample is uniformly heated at t=86 s as shown in Fig. 6.15. In this study, moreover, all the DSed samples are held at the peak temperature for 15 mins thus, it is certain that all sintered microstructures are uniform.

6.9 Conclusions

Porcelain was successfully sintered by the DS process with comparable physicomechanical properties to porcelain sintered using conventional processes as measured by DCS and H_V in the dense areas of the microstructure. Compared with porcelains sintered conventionally at heating rates of 5 °C/min DS requires less processing time and consumes less energy at this laboratory scale. However, to be commercialised sufficient process control would be needed to eliminate bloating, and ensure a homogeneous microstructure. FDA analysis of temperature distribution shows that the actual heating rate of the DS is 780 °C/min and the porcelain samples require about 1.5 min to achieve thermal equilibrium.

This study also confirms that heating rate has little affect mullite formation but significantly affects glass formation, the slower the heating rate, the more glass produced and the optimal glass content to obtain full densification can be estimated.

DCS values alone suggest that DS produces a sufficiently mechanically strong porcelain body which is comparable to selected commercial building materials. However, it is worth noting that the present experiments are based on controlled variables included starting materials, furnace conditions and experimental procedures. Moreover, a homogeneous microstructure does not result as there are bloating holes. For a real industrial process, the energy consumption may be different depending on the process variables and a more homogeneous microstructure would need to be obtained.

Chapter 7

Effect of SPS process on porcelain

7.1 Chapter review

In this chapter the effect of spark plasma sintering (SPS) on porcelain densification, physical property (ABD and WA), microstructure, and phase evolution is examined. 100 °C/min was the only heating rate used because the heating rate has little effect on densification and phase evolution as revealed by the DS process results in Chapter 6. External pressure was applied to the sample from the beginning to the end of the SPS process and its effect on densification, physical property, microstructure, mullite formation and mullite dissolution is discussed.

An example of the SPS experimental conditions for an SPSed 1100 °C, 5 min dwell sample is shown in Fig. 7.1. 6±1 kN (25±1 MPa) of external pressure is applied throughout the test. At the experiment stabilisation period <400 °C (t=0-250 s), the pressure increases from zero to the setpoint (6 kN) producing a punch displacement of ~1 mm. The punch displacement decreases from 400-900 °C because of an expansion of the sample. Displacement rapidly increases above 920 °C since the liquid phase forms as a result of melting of albite. This displacement represents the rate of densification. In this sample, densification is completed at ~1060 °C and there is no further densification during the dwelling period. A thermal contraction of the graphite die occurs when temperature decreases showing a large displacement at the cooling regime. From this point of view, this porcelain composition is densified at 1060 °C under these SPS conditions.

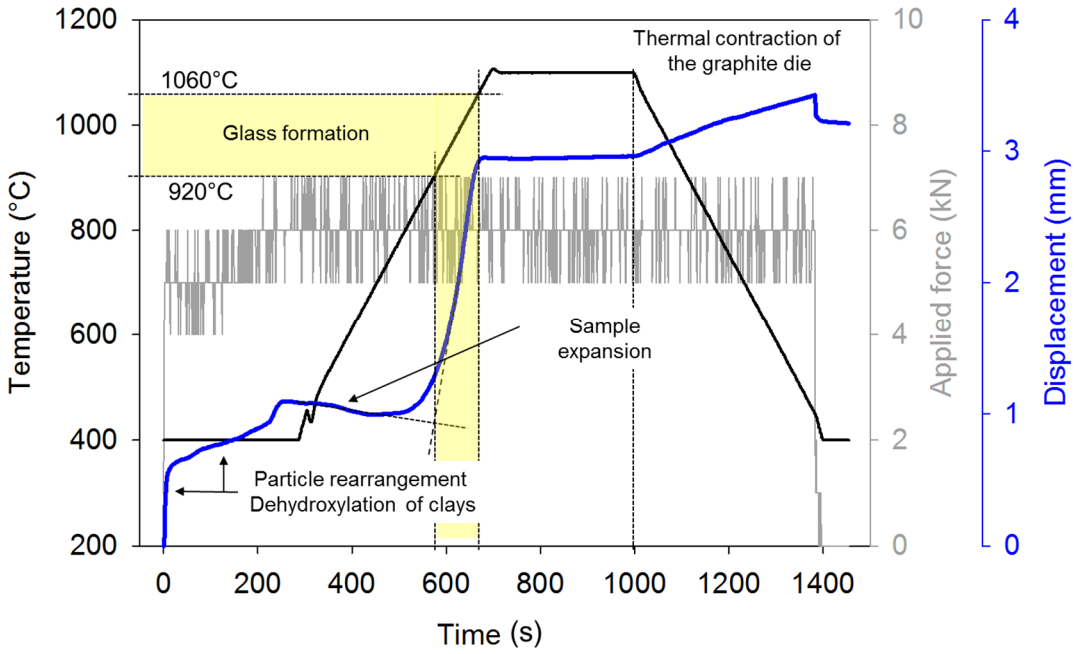

Figure 7.1: An example of SPS conditions used: temperature, applied pressure, and displacement of the SPSed 1100 °C, 5 min dwell sample.

7.2 Densification

Fig. 7.2a shows densification behaviour of the SPSed samples sintered from 1000-1200 °C, at a heating rate of 100 °C/min and dwell time of 5 min. The initial stage of sintering of the three samples starts with punch displacement between 25-400 °C (i in Fig. 7.2a), which is produced by a combination of cold compaction and particle rearrangement under applied pressure. The particle rearrangement arises from the plate-like kaolinite particles which randomly arrange in the spray dried powder. Under the applied pressure the kaolinite particles tend to rearrange perpendicular to the compressive plane. The punch displacement associated with the shrinkage of the samples at 400-500 °C (ii) results from dehydroxylation of kaolinite; the process involves losing the chemically bound water in its crystal structure, so the kaolinite structure collapses under the applied pressure [294,295]. Between 600-900 °C (iii), there is no change in the punch displacement.

At ~900 °C, a significant displacement is observed in all samples resulting from the melting of albite to form liquid glass (iv) (Fig. 7.2a). For the SPSed 1000 °C sample, the punch displacement is small compared to the samples with higher firing temperatures, suggesting that the amount of liquid glassy phase

produced is insufficient to promote significant densification. The punch displacement continues to contract during the dwell step (v) which is a consequence of further liquid glassy phase formation (albite continues to melt). However, the densification is not completed in the 5 min dwell time as indicated by the low displacement at the dwelling region.

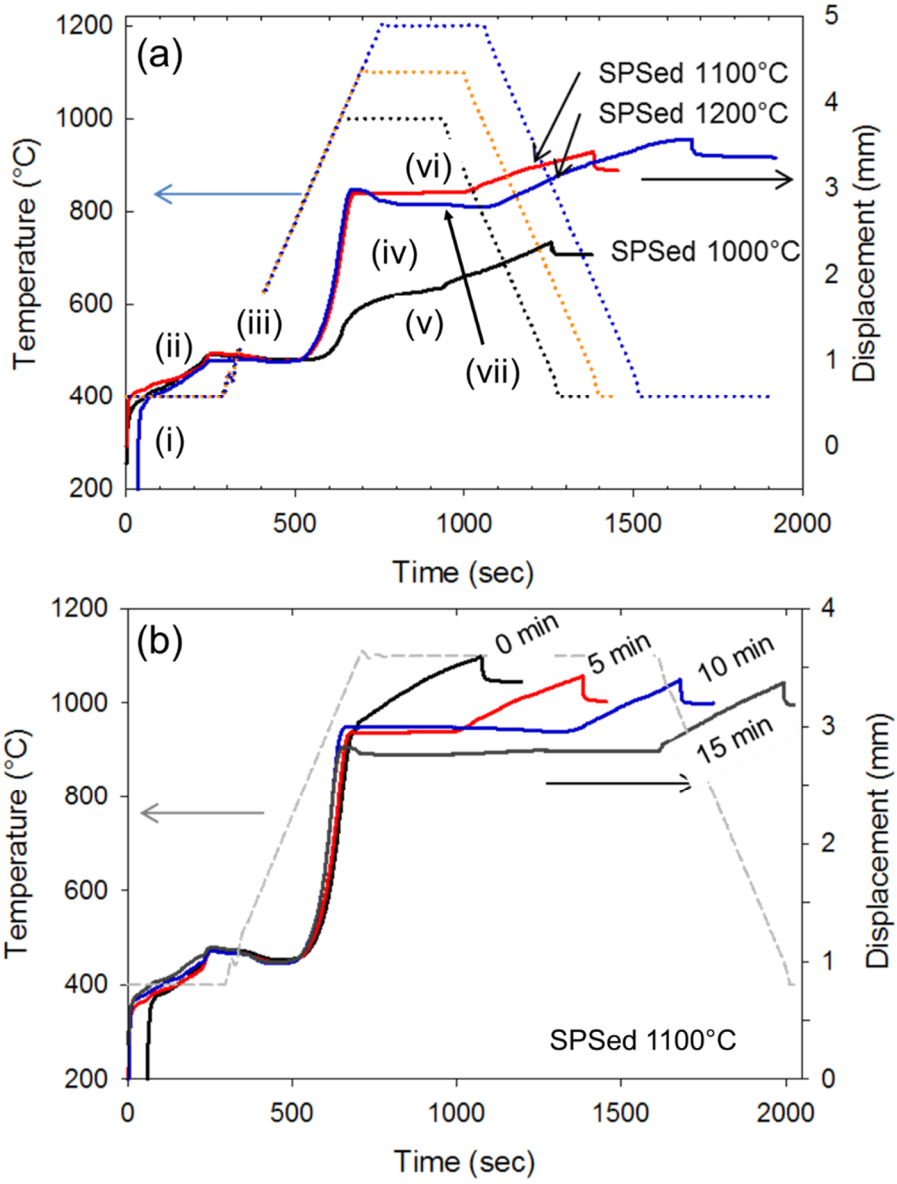

Figure 7.2: (a) Densification behaviour of SPSed samples sintered at 1000, 1100 and 1200 °C respectively with 100 °C/min and 5 min dwell, (b) densification behaviour of SPSed samples sintered at 1100 °C with dwell times of 0-15 min respectively, and with 100 °C/min.

The SPSed samples sintered at 1100 °C in Fig. 7.2(a) (red line) show great punch displacement as a consequence of the large amount of liquid glass produced with increasing temperature, and the glass formation is likely to be completed at this temperature because there is no further densification (vi) during the dwell step as mentioned earlier. The same scenario is also observed in the SPSed samples sintered at 1200 °C (blue line in Fig. 7.2(a)) which show no densification during the dwell step. In contrast, the punch displacement shows expansion of the sample due to gas evolution on bloating (vii), which can be observed from the microstructure (shown in section 7.4).

Fig. 7.2b reveals the effect of dwell time on densification using SPSed 1100 °C samples. The large displacement suggests that substantial volumes of liquid glass start to form at about 900 °C. The effect of dwell time shows that there is no change of punch displacement of 0-10 min dwell once the temperature reached 1100 °C. However, displacement of the 15 min dwell sample is the lowest perhaps caused by a measurement error. The effect of bloating is indicated by SPSed the 1200 °C sample (Fig. 7.2a) which is seen to expand after the sample reached dwelling period.

7.3 Physical properties

Fig. 7.3a shows development of apparent bulk density (ABD) and water absorption (WA) of the SPSed samples sintered using 100 °C/min and 5 min dwell at different temperatures. The SPSed 1000 °C sample shows a high level of WA which is 4.4±0.1 % associated with an ABD of 2.31±0.01 g/cm^3. At 1100 °C, the ABD increases to 2.46±0.01 g/cm^3 with WA of 0.01±0.01 %. The ABD of the SPSed 1200 °C sample drops to 2.41±0.01 g/cm^3 with WA of 0.07±0.01%. The drop of ABD in the SPSed 1200 °C sample is due to bloating consistent with the punch displacement (Fig. 7.2a) and its microstructure (Fig. 7.5).

Fig. 7.3b presents the effect of dwell time on the SPSed samples sintered at 1100 °C. The maximum density of this porcelain sintered at 1100 °C with 0 min of dwell time is 2.52±0.02 g/cm^3 with water absorption of 0.1±0.01 %. ABD decreases from 2.52 to 2.42±0.01 g/cm^3 with increasing dwell time from 0 to 10 min and remains constant to 15 min dwell. This decrease of ABD is due to melting of albite, which is a high-density phase (2.62 g/cm^3) to glass (lower density phase,

2.39 g/cm^3). WA is in the low range of 0.01±0.01 % with 0-10 min dwell but increases to 0.07±0.02 wt. % with 15 min dwell indicating bloating.

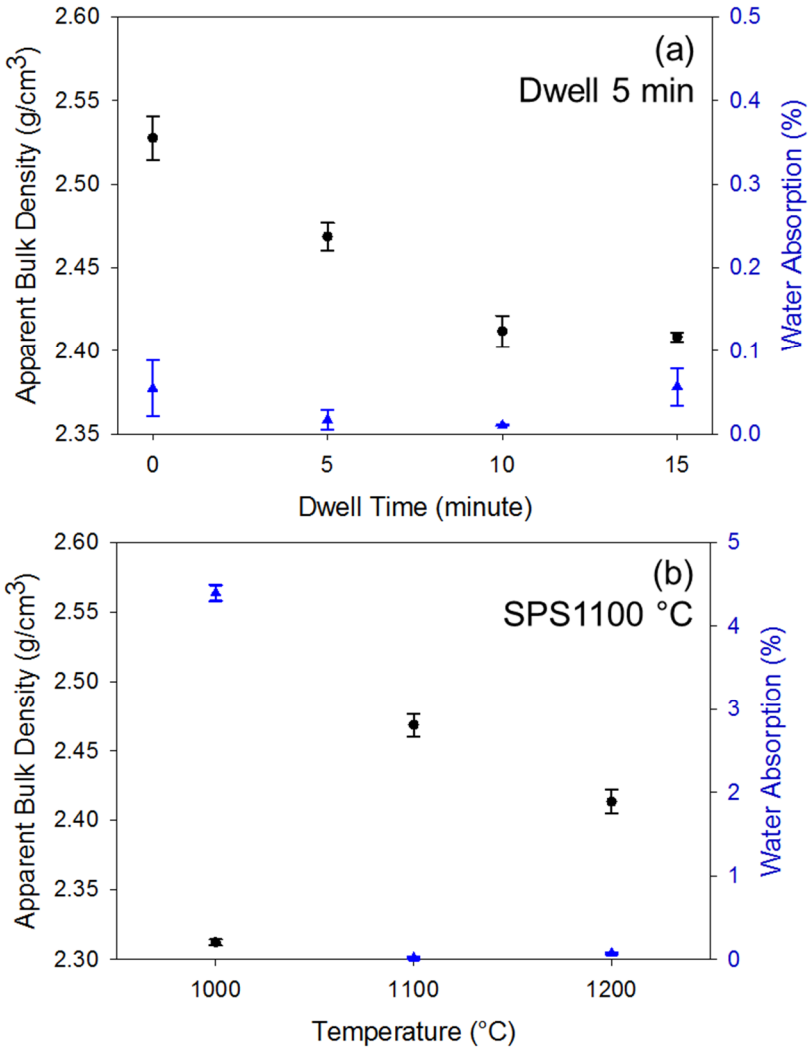

Figure 7.3: (a) Physical properties (ABD and WA) of SPSed samples sintered at 1000-1200 °C with 100 °C/min, 5 min dwell, (b) SPSed 1100 °C with different dwell times of 0-15 respectively.

Fig. 7.4a-c presents a contour plot of ABD, WA, and apparent porosity (AP) of the SPSed samples sintered determined using Archimedes principle. The SPSed sample sintered at 1000 °C with 5 min dwell has high AP of 10.2±0.2 vol.% while the AP decreases to 8.5±0.5 vol.% for the sample SPSed at the same temperature but with 10 min dwell (see also Fig. 7.5). It is clear that the optimal parameters to sinter this porcelain composition to obtain suitable physical properties (high ABD, low WA and AP) are 1100 °C and 5 min dwell. As previously mentioned, however,

this porcelain composition can be densified at a relatively low temperature of 1060 °C with no dwelling under SPS condition. In other words, the applied pressure of 25 MPa has a great effect on the densification and physical properties of porcelains, this effect will be discussed in the next section. In addition, Fig. 7.4d shows the apparent porosity determined using the image analysis which is discussed in section 7.4.

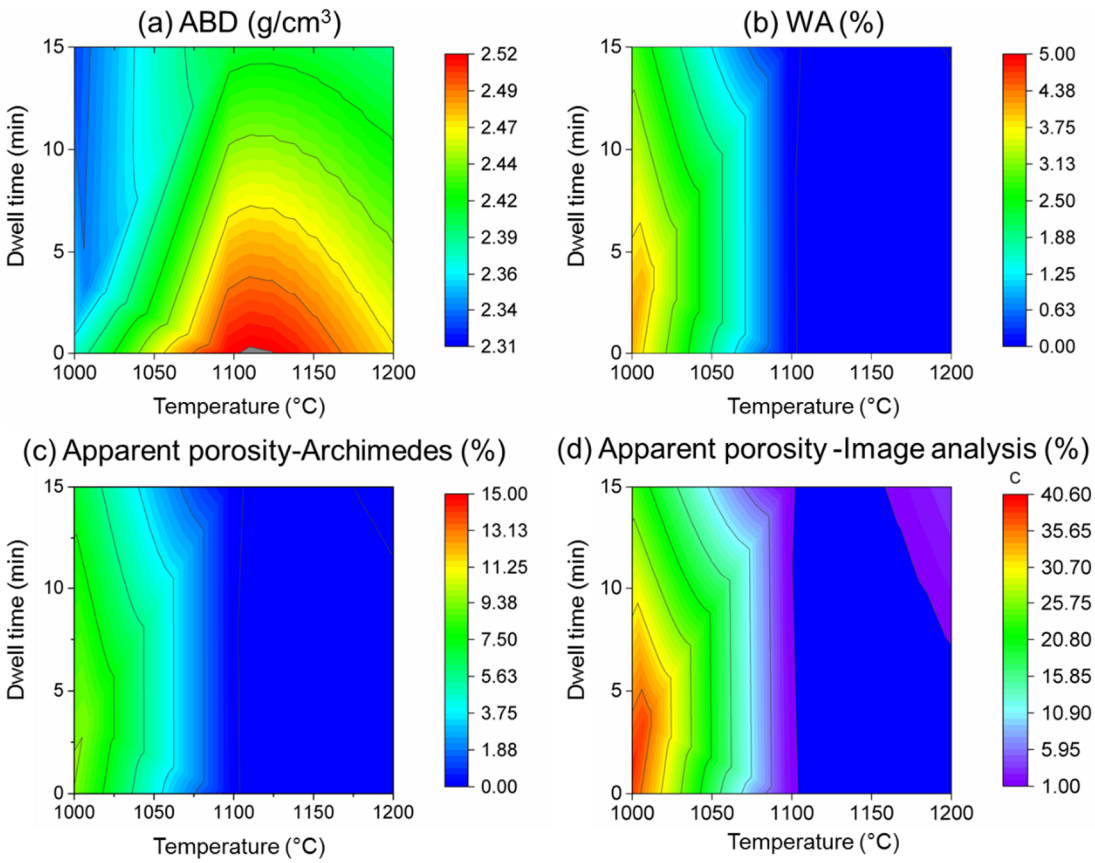

Figure 7.4: Contour plot of (a) apparent bulk density, (b) water absorption, and (c) apparent porosity of the SPSed porcelain samples sintered under different conditions, and (d) apparent porosity of the SPSed samples determined using image analysis.

7.4 Microstructure

SEM images of microstructures of polished SPSed samples sintered under different conditions are shown in Fig. 7.5. Image analysis shows that the SPSed 1000 °C, 5 min dwell sample contains ~40.51±5 % porosity whilst SPSed 1000 °C, 10 min dwell has ~30.50±3 % porosity. The polished surfaces also reveal the interconnected pores (open pores) of the two samples (SPSed 1000 °C, 5 min and

10 min) resulting in high level of porosity. The SPSed 1100 °C samples, in contrast, have small fraction of porosity and only closed pores are observed.

Porosities presented in the SPSed 1100 °C samples are in the same range of 1.0-1.6% for all dwell times. Porosity slightly increases to ~3.5% in the SPSed 1200 °C samples and only closed porosity is observed. Interestingly, the polished surface of the SPSed 1100 °C, 15 min sample and SPSed 1200 °C samples show round-closed pores consistent with bloating. The pore size in the SPSed 1200 °C sample, in addition, is small (3-5 μm) with small standard deviation (0.7-3.5). Table 7.1 summarises physical property data including pore sizes of the SPSed samples.

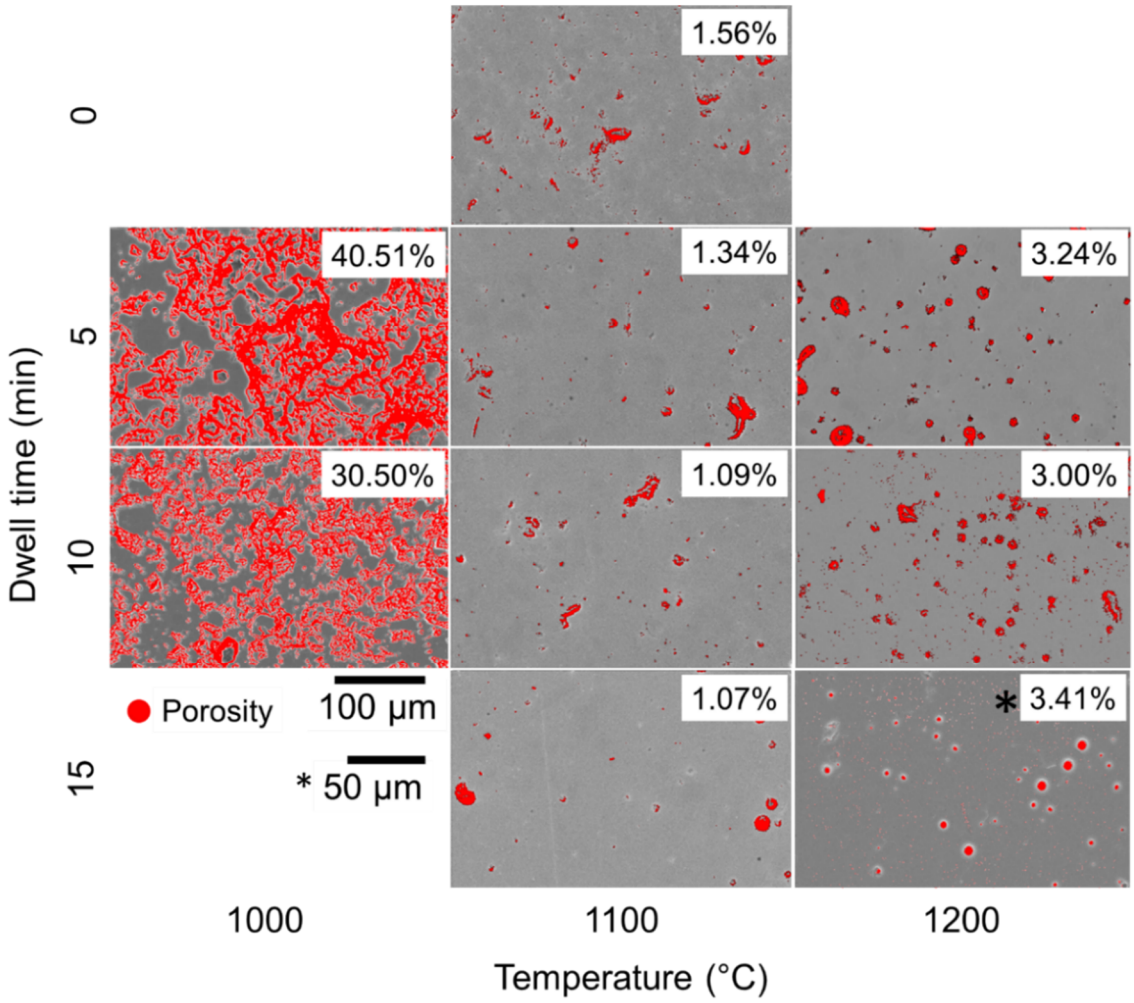

Figure 7.5: SEM images of the SPSed porcelain samples sintered under different conditions, the red area representing calculated porosity.

Table 7.1: Physical properties of SPSed samples.

Sample (Temp-Dwell)	ABD (g/cm^3)	WA (%)	App. Porosity* (Vol.%)	Porosity** (%)	Pore size** (μm)
1000-5	2.31±0.01	4.39±0.10	10.17±0.22	40.51	n/a
1000-10	2.32±0.01	3.56±0.15	8.51±0.10	30.50	n/a
1100-0	2.52±0.01	0.05±0.03	0.14±0.09	1.56	7.05±3.4
1100-5	2.46±0.01	0.01±0.01	0.04±0.03	1.34	4.65±1.1
1100-10	2.41±0.01	0.01±0.01	0.03±0.00	1.09	8.27±7.3
1100-15	2.41±0.0	0.05±0.02	0.14±0.05	1.07	6.30±3.2
1200-5	2.41±0.01	0.07±0.01	0.17±0.02	3.24	5.61±3.5
1200-10	2.41±0.01	0.01±0.01	0.24±0.05	3.00	3.82±0.7
1200-15	2.39±0.01	0.02±0.01	0.28±0.07	3.41	3.98±1.4

* ASTM C20-0, ** Image analysis, n/a = pore size not determined due to interconnected pores.

7.5 Phase composition

Fig. 7.6 shows XRD of as-received porcelain powder and SPSed samples sintered to different temperatures of 1000-1200 °C. The as-received powder was composed mainly of albite (A), kaolinite (K) and quartz (Q). Fig. 7.6 also shows that after sintering at 1000 °C under the SPS conditions the powder undergoes a slight phase change; the intensity of the kaolinite and albite peaks decreases compared to the as-received powder.

Mullite peaks become pronounced in the SPSed samples sintered at 1100 and 1200 °C as well as a large hump observed at 20-30°2θ, which indicates the formation of glassy phase from the melting of albite. XRD also suggests that the fraction of glassy phase increases slightly at 1200 °C due to quartz dissolution (due to decreased quartz peak intensity).

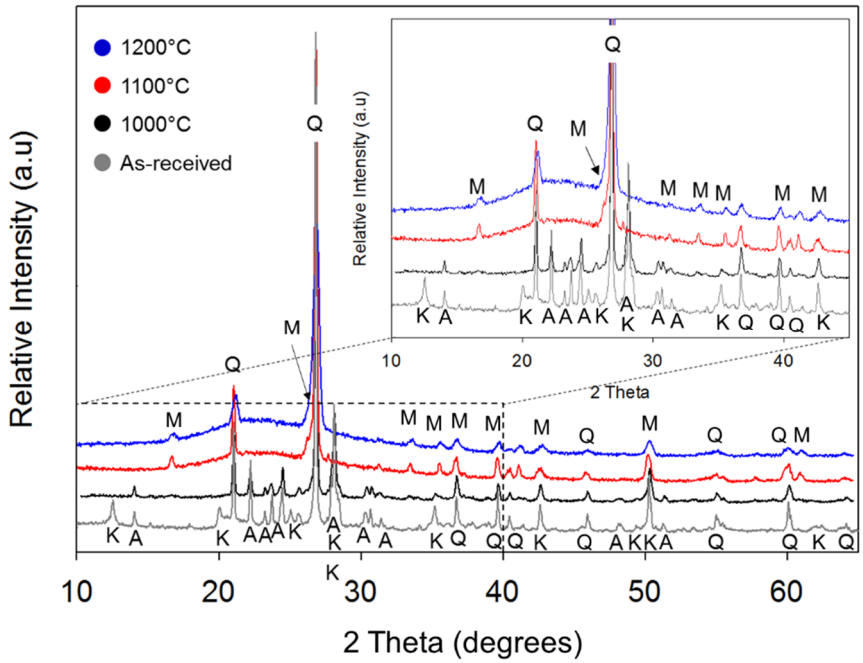

Figure 7.6: XRD of porcelain samples sintered using SPS to different temperatures. A is albite, K is kaolinite, M is mullite, and Q is quartz.

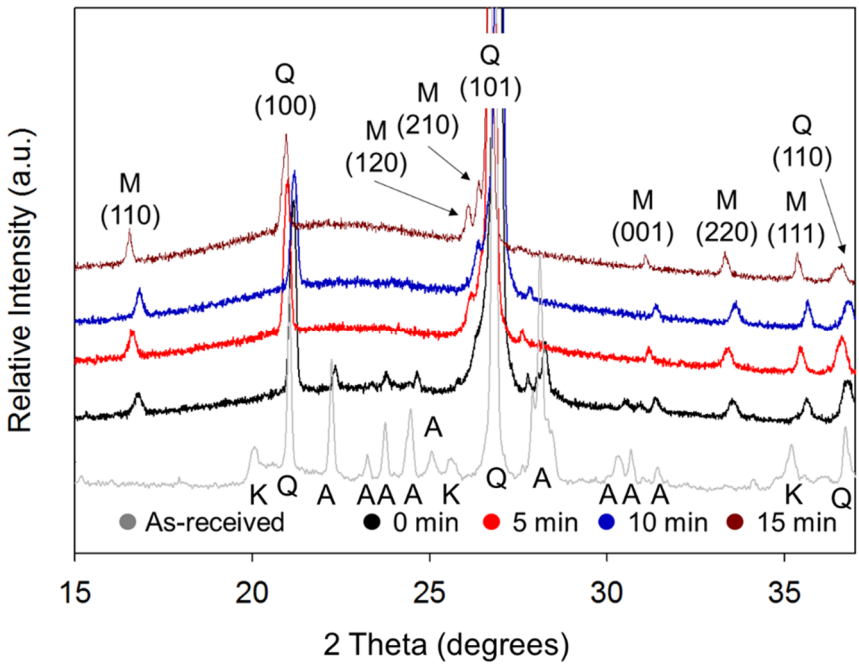

Figure 7.7: XRD of porcelain samples sintered using SPS to 1100 °C with different dwell times. M is mullite and Q is quartz.

Fig. 7.7 reveals the effect of dwell time on the SPSed samples sintered to 1100 °C. Mullite peaks are observed at 0 min and become more pronounced with increasing dwell time. At short dwell times of 0 and 5 min, residual albite is still

observed but vanishes after 15 min suggesting that it completely transforms to glassy phase. The quartz peaks shift to lower angles, which may result from compressive stresses in the quartz lattice which are generated on cooling in the SPS process. It is well understood that XRD peaks can shift for three main reasons. First, due to strain contribution. Second, due to the zero drift from XRD itself (which can be corrected using software). Third, the shift can also be caused by temperature. In this case, lattice strain could be the important reason of the quartz peaks shifting because cooling rate used by the SPS is as fast as 100 °C/min.

Fig. 7.8 compares fully dense samples sintered using conventional sintering (1175 °C) and in the SPS (1100 °C). The SPSed 1100 °C sample is composed of three major phases including mullite, glass and residual quartz while the conventionally sintered sample is composed of residual albite, mullite, glass and residual quartz. It is also clear that the SPSed sample contains more mullite, glass and less residual quartz (discussed further in section 7.6.3).

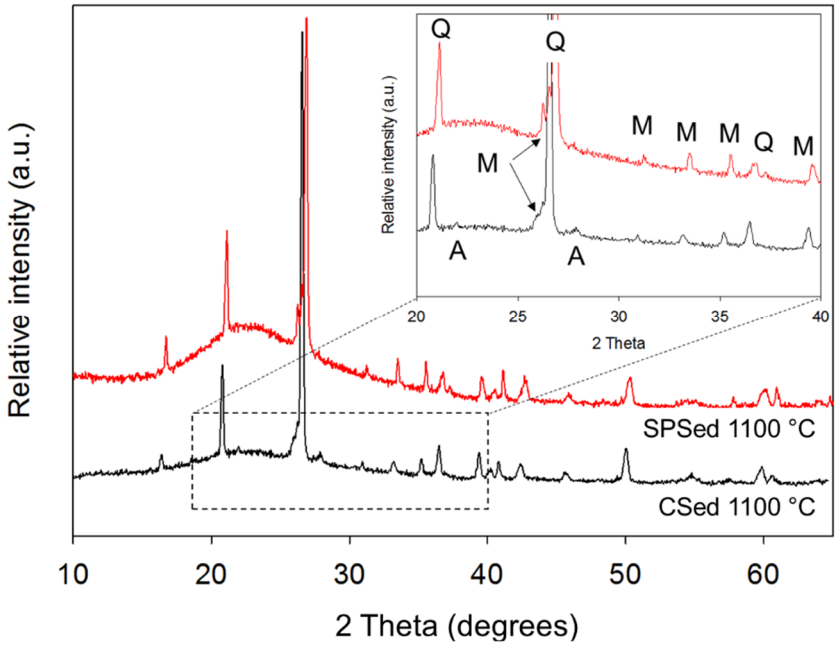

Figure 7.8: XRD of sintered porcelain, SPSed 1100 °C and CSed 1175 °C samples. A is albite, K is kaolinite, M is mullite and Q is quartz.

7.6 Mechanical properties

The Vickers hardness (H_V) measurement is carried out on sample cross-sections (C1 and C2) and on the surface perpendicular to the compressive plane of SPS (P) as schematically shown in the inset of Fig. 7.9 and 7.10.

Fig. 7.9 reveals the H_V of the SPSed samples (5 min dwell) is significantly increased with increased temperatures from 1000-1100 °C then remains relatively constant at temperature of 1100-1200 °C, explained by their denser microstructures (Fig. 7.5). The H_V values in C1 and P are not different in the SPSed 1100 °C and 1200 °C samples but the SPSed 1000 °C samples show a little greater H_V at C1 compared to H_V in the surface (P). However, in the samples sintered at 1000 °C H_V ranged between 1-1.5 GPa while in the samples sintered at 1100-1200 °C it ranged 6-7 GPa.

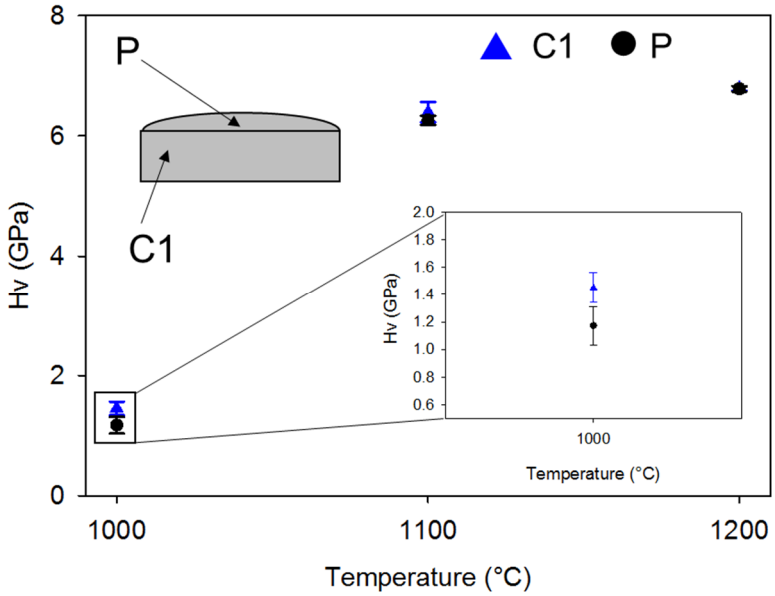

Figure 7.9: Vickers hardness (H_V) of samples sintered using the SPS as a function of sintering temperature. C1 (cross-section, outer layer) and P (perpendicular to the compressive plane, top surface in the centre).

However, visual microstructural observation suggests that the SPSed samples sintered at 1100 °C with short dwell times (≤5 minutes) exhibit variation of microstructure from the outer layer and inner layer which is attributed to the rapid heating rate [296]. This variation of microstructure is not observed in samples using dwell times greater than 10 min (Fig. 7.10). This may be due to a

lack time for bulk diffusion to occur in the ≤5 min dwell SPSed sample. To understand this heterogeneity SPSed 1100 °C samples were examined in more detail. The H_V measurement is performed at C1 (cross-section, outer layer), C2 (cross-section, sample centre mid-thickness) and P (perpendicular to the compressive plane, top surface in the centre), as shown in the inset of Fig. 7.10.

The H_V results suggest slightly different hardness, with the outer layer (C1 and P) having lower H_V compared to centre of the samples (C2). This result is attributed to different phase compositions suggested by XRD (Fig. 7.11) while H_V shows decreases at all tested points for the SPSed 1100 °C samples dwelled 10 and 15 mins (Fig. 7.10). H_V is similar throughout the sample cross-section (no difference is seen between C1 and C2 and P) suggesting there is no uneven sintering at these dwell times.

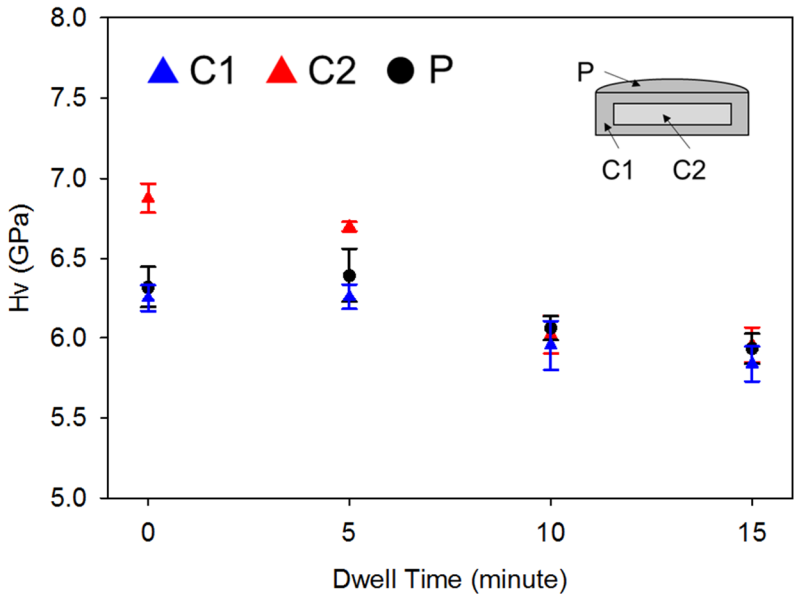

Figure 7.10: Vickers hardness (H_V) of samples sintered using SPS sintered at 1100 °C with different dwell times. C1 (cross-section, outer layer), C2 (cross-section, sample centre mid-thickness) and P (perpendicular to the compressive plane, top surface in the centre).

XRD (Fig. 7.11a) reveals the phase composition in the SPSed 1100 °C sample with 5 min dwell. The centre of the samples (C2) contains more residual albite, indicated by the greater intensity of albite peaks compared to the peak intensity of the outer layer (P). The presence of a small hump for the glass phase reinforces the presence of residual albite in C2. According to previous modelling

of the temperature distribution in samples during heating on SPS, the temperature at C2 is lower than C1 and P, this results in preferential sintering near its location (with also increased pressure applied) [296].

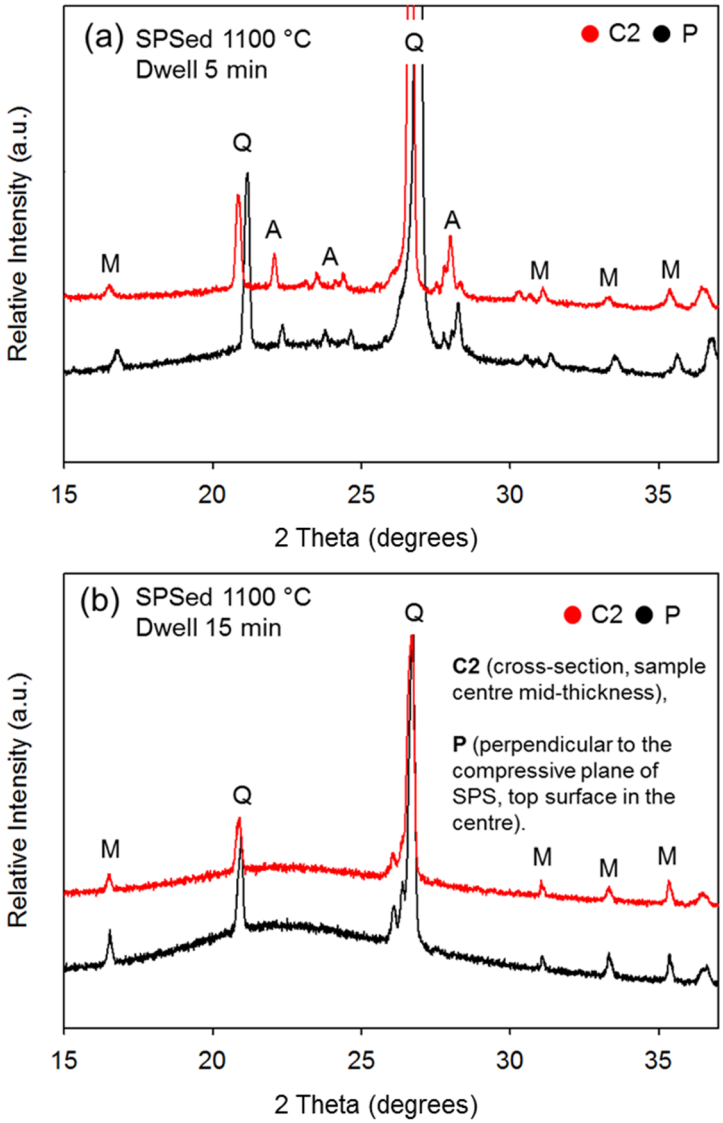

Figure 7.11: XRD shows mineralogical compositions of outer (P) and inner layers (C2) of the SPSed 1100 °C sample with (a) 5 min and (b) 15 min dwell.

The absence of albite peaks in the SPSed 1100 °C with 15 min dwell (both in C2 and P) shown in Fig. 7.11b suggests that the glassy phase is completely formed (from melting of albite) as confirmed by XRD. In addition, it can be concluded that the SPSed 1100 °C samples with 0-5 min dwell have greater H_V because there is residual albite present, further formation of glassy phase (dwell time of 10-15 min) decreased H_V because, among the mineralogical phases in

porcelains (mullite, albite, quartz and glass), the glassy phase has the lowest H_V [297-302]. The quartz peak at about 21°2θ shifted due to strain because the cooling rate used by the SPS is as fast as 100 °C/min as previously mentioned.

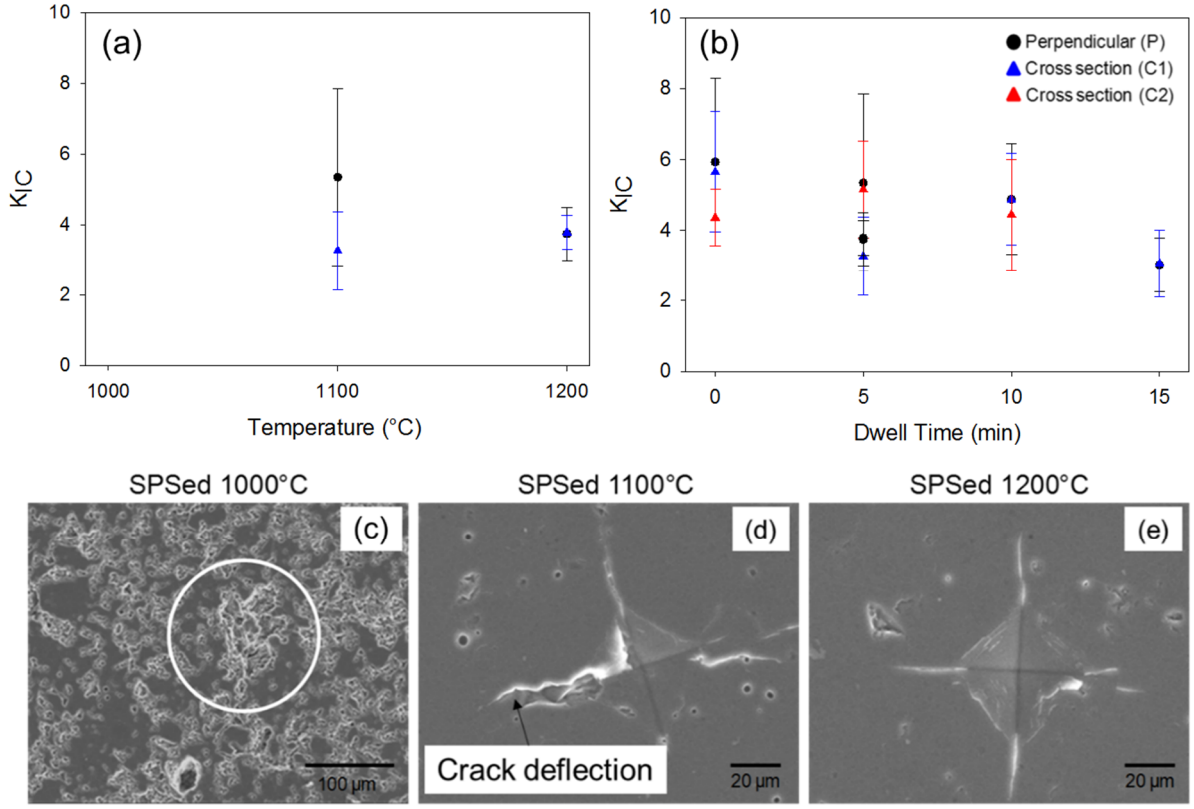

Figure 7.12: Fracture toughness (K_{IC}) of SPSed samples as a function of (a) temperature, and (b) dwell time. Images (c – e) show cracks generated labelled as SPSed 1000, 1100 and 1200 °C. The white circle represents the indented area in the SPSed 1000 °C sample with unidentified H_V.

Fig. 7.12 shows K_{IC} of SPSed samples as a function of temperature and dwell time along with images of Vickers indentations. Cracks could not be observed in samples sintered at 1000 °C due to their highly porous nature so that it was not possible to determine K_{IC}. The radial cracks in the samples sintered at 1100 °C and 1200 °C are clearly observed. Crack deflections are observed in the 1100 °C samples (arrowed in Fig. 7.12d), which produced higher fracture toughness compared with the 1200 °C samples. This can be explained by the residual crystalline phases (albite, mullite and quartz) dispersed in the dense glassy matrix of the samples SPSed at 1100 °C. In the 1200 °C sample straight

cracks are observed, suggesting that the samples contain high levels of brittle glassy phase, which results in lower fracture toughness compared to the 1100 °C samples.

In SPSed samples sintered at 1100 °C, K_{IC} decreases slightly as a function of dwell time (Fig. 7.12b). The presence of residual albite, quartz and mullite in the glassy matrix tends to increase the fracture toughness of the samples by crack deflection while as more glass forms the fracture toughness decreases because glass has the lowest toughness among the phases present in the porcelains as presented in Table 7.2.

Thus, in this study, the slight decrease of K_{IC} of 1200 °C SPSed sample compared to 1100 °C SPSed samples is likely due to the presence of residual albite, quartz and mullite in the glassy matrix.

In addition, large standard deviation of the K_{IC} observed in Fig.7.12 is likely due to the presence of residual albite, quartz and mullite in the glassy matrix, which causes heterogeneous microstructure of the porcelain samples and the heterogeneous microstructure may lead to inaccurate crack lengths.

Table 7.2: Summary of material properties [298,301,302].

Mineral	Density (g/cm^3)	H_V (GPa)	K_{IC} ($MPa \cdot m^{1/2}$)	Reference
Albite	2.62	6-6.5	0.75-1.3	301
Mullite	3.14	10-11	2.3-2.8	298,302
Quartz	2.65	12	1.6-2.4	301
Glass	2.39	3-6	0.6-0.7	301

7.7 Discussion

7.7.1 Effect of applied pressure on porcelain densification

As previously discussed in section 7.2, the densification of porcelains depends on the formation of liquid phase. When the liquid glass phase is formed, the liquid phase brings the solid particles (kaolinite, mullite, residual albite and quartz) together creating volume shrinkage and closed pores so that a large fraction of the microstructure is filled with glass. The pressure, furthermore, forces liquid glass phase to fill the pores increasing densification rate. The liquid glass flows into capillaries in proportion to the applied pressure and densifies the

porcelain. Densification from viscous flow under applied pressure can be expressed by Eq.7.1 [303].

$$\frac{d\rho}{dt} = \frac{3P}{4\eta}(1-\rho) \tag{7.1}$$

where ρ is density, P is the applied pressure, η is viscosity of the liquid glass and (1- ρ) is volume fraction of porosity. Note that increasing pressure can result in increased viscosity of the liquid glass but to increase viscosity of liquid glass significantly, pressure has to be high (GPa) [304]. Thus, in this study, the glass viscosity is considered to be unchanged with increasing pressure. The increased densification is solely governed by applied pressure. Although, there is always some remnant porosity as trapped gas cannot escape through highly viscous vitreous phase.

A comparison with conventional sintering (CS) suggests that SPS allows densification of this porcelain body to be achieved at a lower temperature (1060 °C, 25 MPa) compared to a conventional sintering which is 1175 °C in pressureless conditions (Fig. 7.13a). These results suggest that applied pressure promotes a rapid densification rate via vitreous sintering. Because of its rapid heating in combination with applied pressure, the major benefit of SPS over conventional sintering is that the processing times for vitreous phase sintering can be significantly reduced.

The different densification behaviour of samples sintered by the various sintering processes can be highlighted by plotting the rate of change of the apparent bulk density as a function of the sintering temperature (Fig. 7.13b). The densification rate of the SPSed samples is highest at 900-1000 °C (time interval of 60 s) while the conventionally sintered sample has the highest rate at 1050-1100 °C (600 s). Note that densification rate during the conventional firing process is higher than during SPS because the rate is accelerated over the SPS cycle with an initial densification below 600 °C.

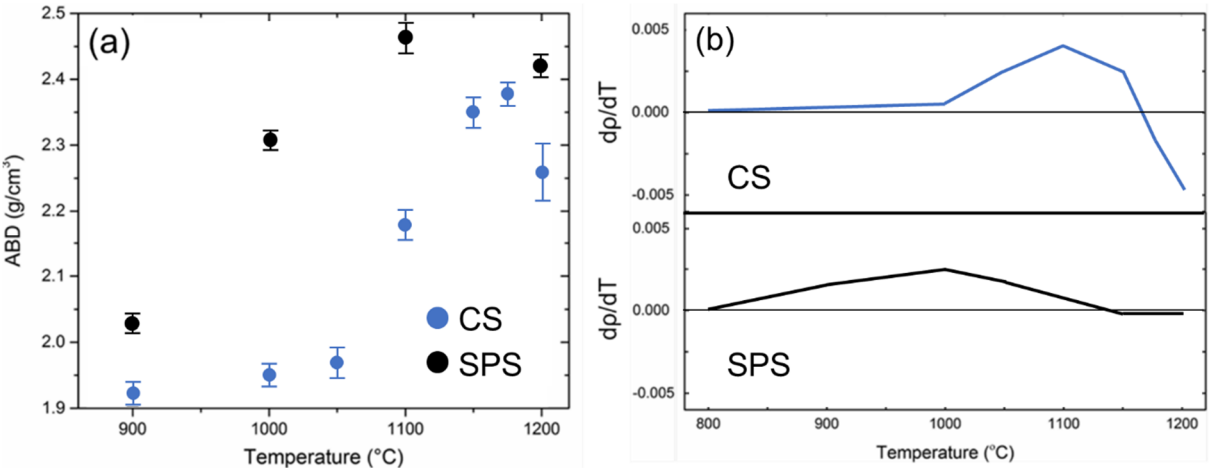

Figure 7.13: (a) Apparent bulk density (ABD) of the samples sintered using the SPS and the conventional sintering process, (b) rate of change of apparent bulk density, dρ/dT sintering temperature.

7.7.2 Melting of feldspars under applied pressure

Understanding feldspar melting under applied pressure helps interpret porcelain densification. The densification (Fig. 7.2) and phase evolution (Fig. 7.6) show that when liquid glass is formed; the albite is disappearing, and no other intermediate phases are found (Fig. 7.6). In other words, albite melts congruently under pressure resulting in uniform liquid glass viscosity. Thus, it is worth discussing how applied pressure affects the melting of feldspars.

Firstly, at atmospheric pressure, pure albite ($NaSi_3O_8 \cdot SiO_2$) melts congruently at ~1100 °C but when some amount of quartz is added, the temperature of solidus of albite decreases from 1100 to 970 °C. At high pressure (~15 kbar or 1500 MPa) the addition of quartz does not lower the solidus temperature of albite because increasing pressure alters the composition of the albite-quartz eutectic. For instance, the eutectic of albite-quartz at atmospheric pressure is ~ 40:60 wt.% albite: quartz while it is ~96:4 wt.% albite: quartz at 15 kbar (1500 MPa) [305].

Secondly, anorthite ($CaAl_2Si_2O_8 \cdot SiO_2$) at atmospheric pressure, melts congruently at ~1533 °C but at a high pressure of 10 kbar (1000 MPa) anorthite melts incongruently to corundum and a silica-rich glass. If a fraction of quartz (40 wt.%) is added the melting point of anorthite decreases to ~1320 °C at the atmospheric pressure but again quartz does not lower the melting point of

anorthite at high pressures ~10 kbar (1000 MPa). This result can be explained by the same mechanism as the albite melting behaviour because the eutectic composition of anorthite and quartz is changed i.e. being ~45-50:55-50 wt.% anorthite: quartz while it is ~70-75:30-25 wt.% anorthite: quartz at 18 kbar (1800 MPa) [305].

Finally, sanidine ($KAlSi_3O_8 \cdot SiO_2$) at atmospheric pressure, melts incongruently to leucite and silica-rich glass at ~1050 °C and melts incongruently at ~980 °C when quartz is added. Microcline melts incongruently to sanidine and silicate melt at 1055 °C [305]. In other words, microcline converts to sanidine and glass melt before it fully melts to an aluminosilicate liquid. In addition, orthoclase melts incongruently to leucite at about ~1530 °C but melts congruently to aluminosilicate melt when excess quartz (~30 wt.%) is present [306].

At high pressures, the melting points of potash feldspars increase, and they can be estimated using the Clausius-Clapeyron equation. i.e. meting temperature increases 10 °C, 25 °C, and 4 °C by increasing pressure to 1000 atm (101 MPa) for orthoclase, albite, and anorthite respectively [305]. In contrast, the melting temperature of potash feldspars decreases when they are under hydrothermal conditions (in the presence of pressure and water). For instance, the melting temperature of sanidine is lowered to 750 °C from ~1050 °C with the presence of 18 kbar (1800 MPa) and water [307]. Thus, in this experiment, albite and quartz form a eutectic melt at ~1000 °C, and congruently melt because there are no other intermediate feldspars found in the XRD patterns (Fig. 7.6-7.7). The pressure of 25 MPa (0.25 kbar) applied during SPS in this study is unlikely to change the melting temperature of albite because it is small compared to the pressures that were reported in the literature [305-307].

7.7.3 Mullite formation under SPS

7.7.3.1 Mullite formation as a function of SPS conditions

Under hot pressing conditions (with applied pressure of 55 MPa and heating rate of 50 °C/min), Blair and Chaklader [308] produced a larger fraction of mullite at a temperature of 800 °C compared to conventional pressureless sintering at 1100 °C. Weiss et al., [309] also reported that mullite formation from kaolinite was possible at 600 °C using 250 kbar (2500 MPa).

However, in this study (as shown in Fig. 7.14a), mullite peaks are not pronounced at 1000 °C. XRD of samples SPSed at 1000 °C reveals a small hump at 16.42°2θ implying that kaolinite initially undergoes phase transformation to either spinel or small mullite crystallites but at this stage it is not pronounced because the basal plane (001) reflection at 31°2θ is not observed suggesting that the mullite crystals are not elongated. However, in spite of the crystals having elongated morphology, the (001) mullite peak may be hidden by peaks of un-melted albite. This result is supported by the SEM image shown in Fig. 7.14b revealing that either spinel or mullite crystals (as arrowed) formed but they are small in size (<50 nm).

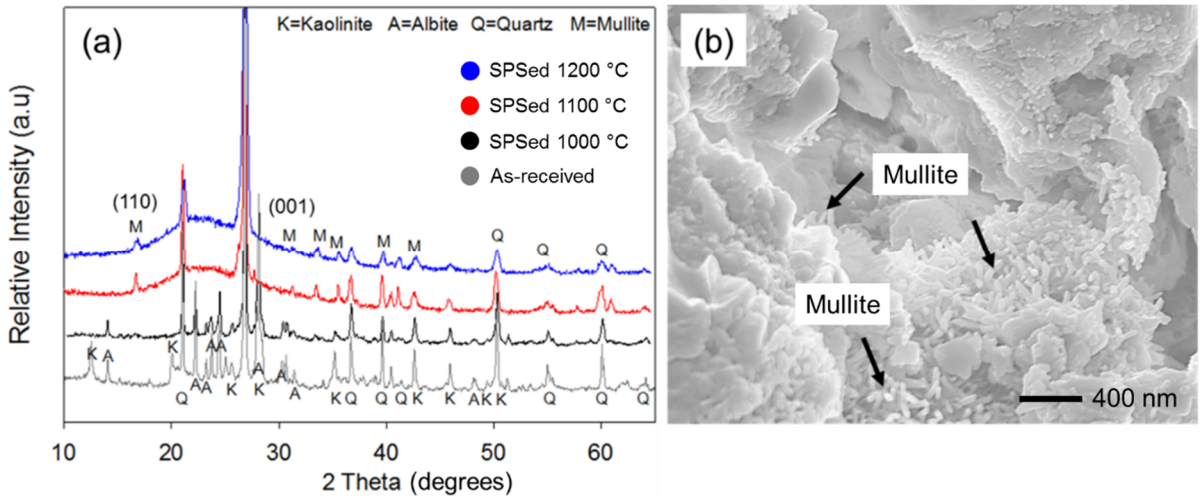

Figure 7.14: (a) XRD of SPSed porcelain samples as a function of temperature with a dwell of 5 mins, and (b) SEM image of the SPSed 1000 °C sample showing small crystals (arrowed).

After sintering at 1100 °C, pronounced mullite peaks are revealed suggesting significant mullite formation. A large glassy hump is also found at around 22°2θ. It suggests that the applied pressure of 25 MPa in this SPS condition is significant for mullite formation because of the plastic deformation combined with a heating rate of 100 °C/min that triggers the transformation of kaolinite in porcelain at lower temperature compared to transformation in pure kaolinite under pressureless sintering as reported previously [310]. After sintering at 1200 °C (Fig. 7.14a), mullite peaks are also clearly observed but the shape of the peaks is different compared to at 1100 °C. This is believed to have resulted

from dissolution of mullite needles in the liquid aluminosilicate glass which will be discussed in section 7.7.3.3.

Fig. 7.15 compares mullite formation of the SPSed 1100 °C sample and the CSed 1100 °C sample. SPS produces a greater amount of mullite than the CS process does as presented in Fig. 7.15. In addition, it can be deduced from the XRD that the presence of kaolinite peaks in CSed 1100 °C sample suggests mullite formed less because kaolinite does not completely decompose to mullite. Greater amount of mullite in SPSed sample is also confirmed by the SEM images in Fig. 7.15c and d.

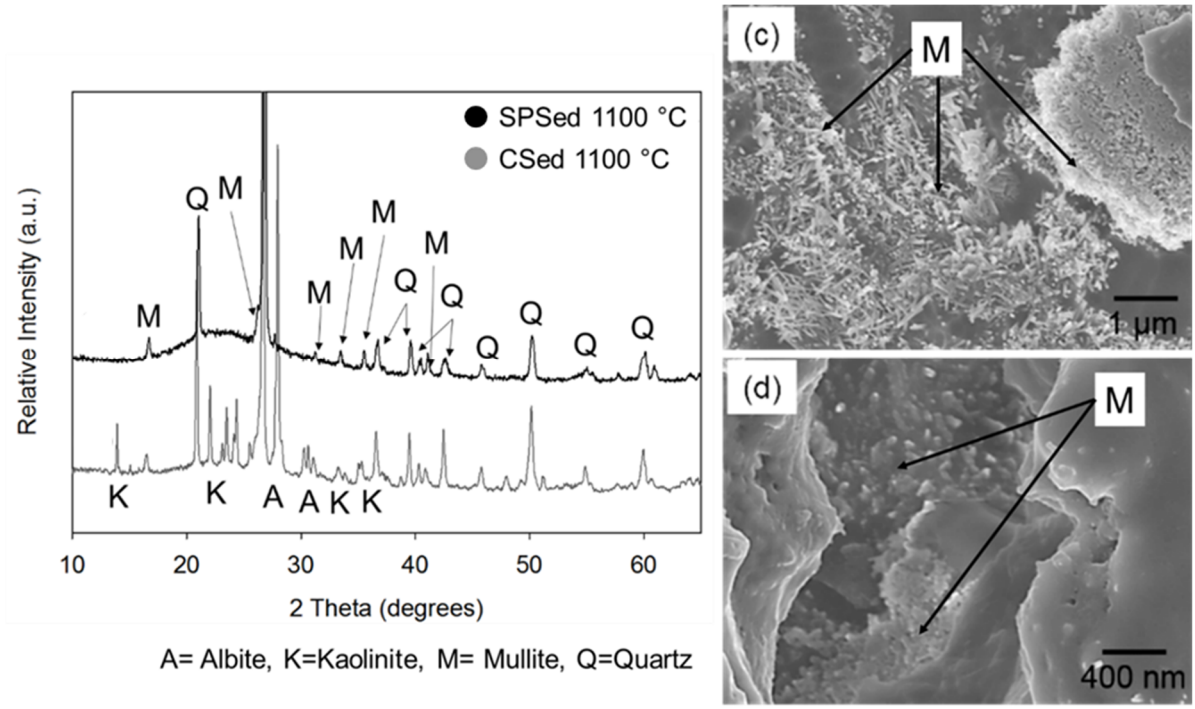

Figure 7.15: Comparison of mullite formation at 1100 °C, (a) SPS (100 °C/min, 5 min dwell) and (b) conventional sintering (5 °C/min, 15 min dwell), and SEM images showing different mullite crystallites, (c) SPSed 1100 °C (100 °C/min, 5 min dwell), and (d) CSed 1100 °C (5 °C/min, 15 min dwell).

Interestingly, Fig. 7.14a (SPSed samples) also shows that the mullite peak (marked as M (001) peak) at ~31°2θ disappeared after SPS at 1200 °C but other peaks are still pronounced. This observation suggests that mullite formed in the SPSed 1200 °C sample does not disappear but develops a preferred orientation.

The integrated (001) peak area of mullite (Fig. 7.16) decreases as a function of temperature as well as dwell time (Fig. 7.16 a and b) in the temperature range of 1100-1200 ºC due to a preferred orientation. In addition, the orientation of mullite needles remains reasonably constant in the SPSed 1200 °C samples as revealed by XRD peak area in Fig. 7.16b.

SEM images (Fig. 7.16c-j) show that the mullite needles formed under the SPS conditions at 1100-1200 °C with different dwell times have preferential orientation compared to the conventionally sintered sample (Fig. 7.16j). The mullite in the CSed 1200 °C samples oriented randomly while the SPSed 1100-1200 °C samples (Fig. 7.16c-i) shows mullite needles oriented against the compressive plane of the SPS process.

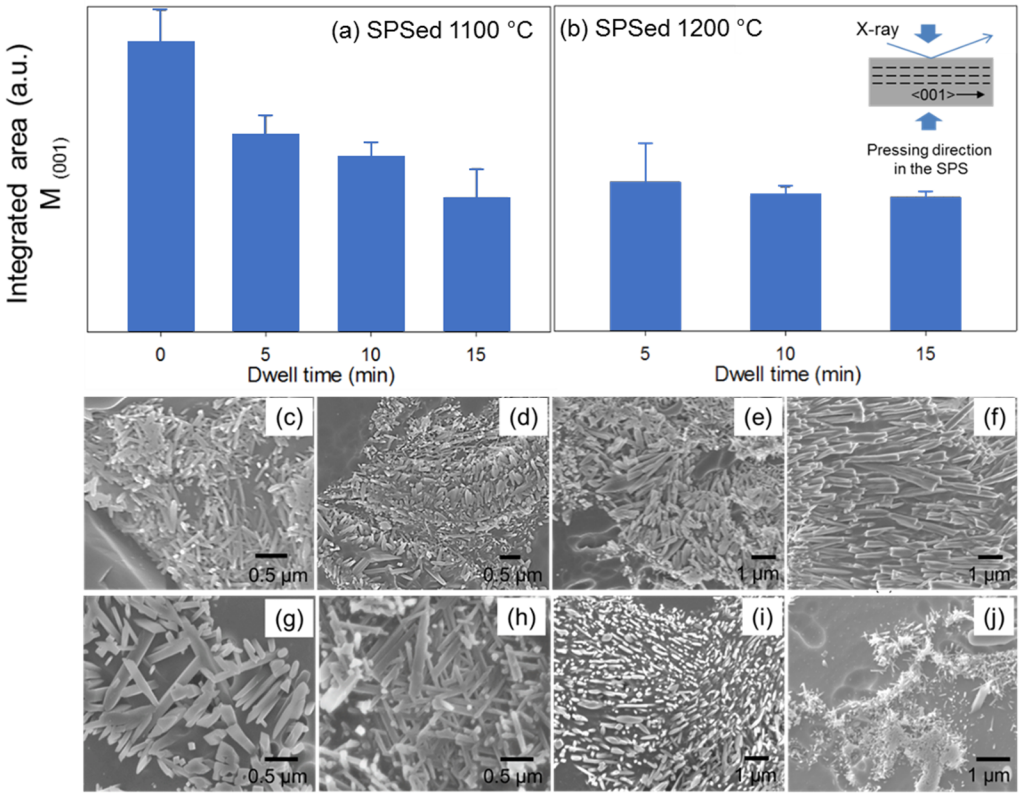

Figure 7.16: (a-b) Plots of integrated area of M (001) mullite peak for porcelains SPSed at 1100 and 1200 °C with varying dwell time and SEM images showing mullite orientation resulted from SPS conditions. The SPSed 1100 °C samples for dwell times of (c) 0, (d) 5, (e) 10, and (f) 15 min respectively, the SPSed 1200 °C samples for dwell times of (g) 5, (h) 10, (i)15min respectively. The CSed 1200 °C sample for dwell time of (j) 15 min.

Once mullite starts to grow, it usually shows acicular morphology. The growth of (001) plane is due to it has higher surface energy other {hk0} planes [311]. Mullite needles align perpendicularly to the compressive direction of the SPS. The orientation of mullite is likely to be constant once the porcelain had been sintered for 15 mins at 1100 °C and there was no further re-orientation in the SPSed 1200 °C samples. A similar result was reported by Shinoda et al., [312] who showed that mullite orientation (c-axis of mullite) in Al_2O_3-SiO_2-SiC composites sintered using SPS is perpendicularly oriented to the compressive plane. Thus it can be concluded that the applied pressure in the SPS significantly influences mullite orientation.

The bright-field TEM images in Fig. 7.17 (a and c) shows mullite crystals dispersed in an amorphous glass matrix in a sample SPSed 1100 °C with 15 min dwell. The mullite polymorph was identified by tilting to various zone axes in the TEM. Two populations of the mullite crystals are identified in the TEM – one in the form of needles (Fig. 7.17a) and the other as bulk crystals (Fig. 7.17c). The diffraction patterns obtained from the mullite needle marked 'A' in Fig. 7.17a and shown in Fig. 7.17b are indexed as belonging to zone axes [113] and [114] for an orthorhombic mullite (a = 7.567 Å, b = 7.709 Å, c = 2.902 Å) single crystal. These two zone axes are separated by an angle of ~8.2° along the -110 Kikuchi band.

As shown in Fig. 7.17a, the mullite needles are typically about 100-200 nm long and <100 nm wide. The small crystallite sizes make tilting challenging, so the diffraction patterns shown in Fig. 7.17b are not exactly on the zone axes but slightly off-centred because the mullite particles were very small (<200 nm) and it was difficult to tilt to exact zone axes but that did not prevent us from identifying the crystal structure from the diffraction patterns.

Also, the amorphous halo from the glassy matrix made the job of tilting to the zone axis even more difficult. The bigger particle shown in Fig. 7.17c, marked 'B', was also identified to be orthorhombic mullite as shown in Fig. 7.17d but there was no evidence of tetragonal mullite as also revealed by the XRD (section 7.5 Fig.7.7).

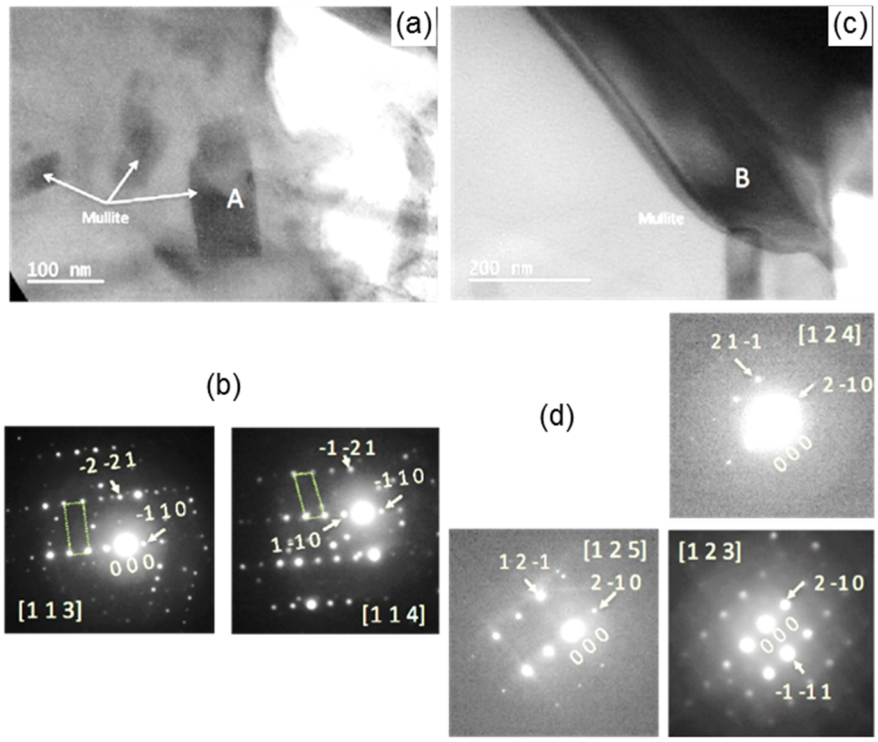

Figure 7.17: (a) Bright-field TEM image of mullite needles in the SPSed 1100 °C with 15 min dwell, (b) SAD patterns obtained from particle marked 'A' in (a) corresponding to orthorhombic mullite zone axes [113] and [114] – the green polygons act as a guide to the eye for identification of the diffracting planes from mullite in the zone axes since stray reflections from the matrix could not be avoided owing to the small mullite crystallites. (c) Bright-field image of a larger mullite particle, 'B' and (d) SAD patterns obtained from 'B' and identified as [123], [124] and [125] as described in section 4.14.2 of the Experimental Chapter.

The applied pressure not only affects the mullite orientation but also alters the phase transformation temperature for its formation. Thus, the effect of pressure on mullite formation needs to be explained in light of thermodynamics to understand why mullite is not observed in the SPSed 1000 °C sample. This can be expressed using the Clausius-Clapeyron equation as shown in Eq. 7.2 [313,314].

$$\frac{dT}{dP} = T\frac{\Delta V}{\Delta H} \tag{7.2}$$

where T is temperature, P is pressure, ΔV is the change of molar volume, and ΔH is the change of enthalpy. The integral form of the Clausius-Clapeyron equation

reveals how the respective temperature of mullite formation changes when the applied mechanical pressure changes.

$$ln\frac{T_2}{T_1} = \frac{\Delta V}{\Delta H}(P_1 - P_0) \quad (7.3)$$

For the SPS conditions used in this study, the positive change of the pressure (P_1 is applied pressure of 25 MPa, and P_0 is no applied pressure) means that;

(1) if the molar volume and enthalpy changes of metakaolinite to mullite are the same sign (-/- or +/+), the result will be $ln\,(T_2/T_1) > 0$ which produces $T_2 > T_1$; thus, the applied pressure will increase the transformation temperature.

(2) if the change of volume and enthalpy are different signs (-/+ or +/-), then $T_2 < T_1$.

Table 7.3 shows the molar volume and enthalpy changes of kaolinite to mullite transformation revealing that;

1. Kaolinite to metakaolinite transformation temperature increases with increasing pressure because $(+\Delta V/+\Delta H) \cdot (+\Delta P)$ yields $T_2 > T_1$.
2. Metakaolinite to spinel transformation temperature also increases with increasing pressure ($(-\Delta V/-\Delta H) \cdot (+\Delta P)$ yields $T_2 > T_1$).
3. The change of spinel to mullite should not be easy since the Clapeyan-Clausius's equation also yields $T_2 > T_1$ suggesting spinel to mullite transformation temperature under applied pressure must be higher compared to a pressureless process.

This calculation suggests that the applied pressure does not decrease the mullite formation temperature. However, experimentally, mullite is observed to fully form by 1100 °C (the XRD peak intensities reached maximum) suggesting that the mullite formation temperature under applied pressure is relatively low compared to mullite formation in pressureless sintered porcelains which is normally completed around 1200-1400 °C. In other words, mullite formation can be considered as a pressure driven phenomena or that pressure enhances mullite

formation kinetics. Blair and Chaklader [308] suggested that a positive enthalpy changes for metakaolin to spinel and spinel to mullite transformations can be possible yielding $T_2<T_1$ but they are small (+7.5 kJ/mol) and hidden by crystallization of amorphous silica to crystalline silica. However, decreasing the mullite transformation temperature is not significant because of the moderate pressure used in this study.

Table 7.3: Density, unit cell volume, molar volume and enthalpy of kaolinite transformation at ambient pressure [308,315-319].

Phase	Theoretical Density (g/cm^3)	Unit cell volume (Å^3)	Molar volume (cm^3/mol)	$\Delta H_{f,298}$ (kJ/mol)	ΔH (kJ/mol)
Kaolinite ($Al_2Si_2O_5(OH)_4$)	2.63 [315]	329.89 [315]	99.35 [315]	-3953.9 [317]	
Metakaolinite ($Si_8Al_8O_{28}$)	2.37 [308]	621.84 [308]	374.37 [308]	-3362.7 [317]	(1) +632 [319]
Spinel ($Si_8Al_{34}O_{32}$)	3.26 [308]	490.42 [308]	295.33 [308]	-955.75 [318]	(2) -230 [319]
Mullite ($Si_2Al_6O_{13}$)	3.17 [316]	167.44 [316]	100.86 [316]	-7547.9 [319]	(3)-84 [319]

(1) Kaolinite to metakaolin, (2) metakaolinite to spinel, (3) spinel to mullite

7.7.3.2 Chemistry of mullite as a function of SPS conditions

The effect of time and temperature on mullite formation during SPS process is indicated by the mullite chemistry which can be inferred from XRD analysis. By taking the relationship of the peak intensity ratio (I_{220}/I_{111}) from Ban and Okada [135], the alumina content (mol.%) in mullite can be obtained (see section 4.11 in Experimental chapter).

The calculation suggests that mullite chemistry is modified; mullite produced under the SPS tends to be an alumina-rich phase having 66-73 mol.% of alumina (compared to the stoichiometric mullite having 60 mol.% of alumina) with respect to temperature and dwell time (Fig. 7.18). The SPSed 1100 °C sample has highest alumina content when the dwell time is zero, and its alumina content decreases when the dwell time increases. The decreasing of alumina content in

mullite at 1100 °C and 1200 °C is likely to be related to its crystal structure (see Fig. 7.19).

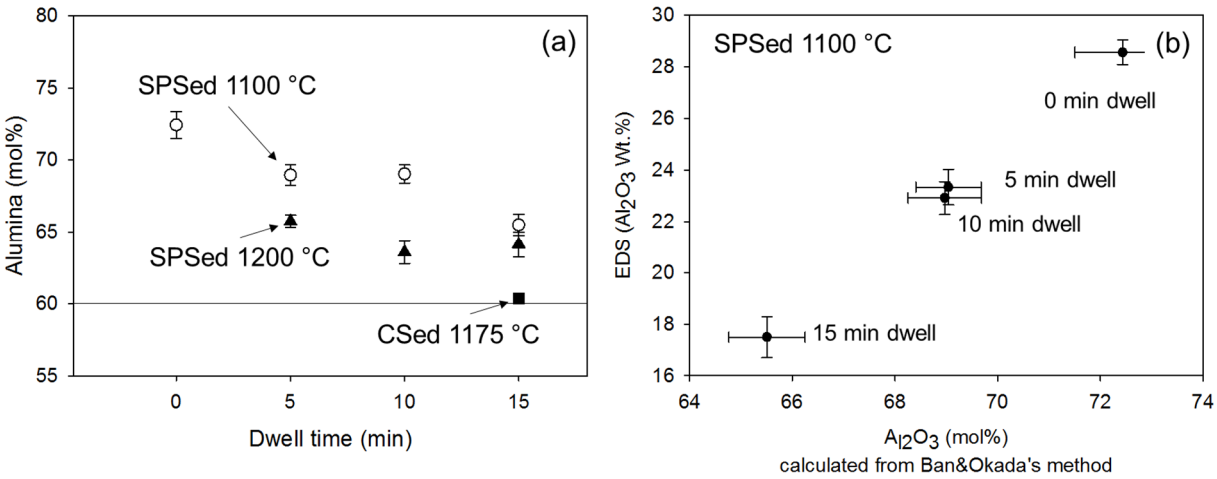

Figure 7.18: (a) Chemistry of mullite produced under the SPS as a function of temperature and dwell time, the CSed sample sintered at 1175 °C, 5 °C/min, and 15 min dwell, (b) the plot of the EDS results against the calculated alumina content in mullite using the Ban and Okada's method.

Energy Dispersive Spectroscopy (EDS) by SEM was performed and plotted against the calculations by the Ban and Okada equation (Fig. 7.18b). The they are found to be in good agreement. Thus, it can be deduced that mullite chemistry varies with time and temperature in SPS.

The effect of atmosphere can superimpose on the effect of applied pressure since both are applied simultaneously. The effect of vacuum (as was used in the SPS) on mullite formation was reported by MacKenzie et al., [320] who showed that firing kaolinite clay in vacuum produces higher mullite fraction and silica-rich mullite compared with that fired in O_2, air, Ar, N_2, H_2, NH_3, and CO_2. Considering samples SPSed at 1100 °C reveals pronounced mullite peaks (Fig. 7.19) compared to those conventionally sintered (Fig. 7.15) in agreement with MacKenzie et al., [320].

At 0 s dwell time, mullite is alumina-rich but alumina content decreases with increasing dwell time or temperature both 1100 °C and 1200 °C). Mackenzie et al., [320] explained that the silica component in the mullite is affected by vacuum, which tends to increase, while the alumina component remains

unaffected. Thus, sintering under vacuum produces lower alumina molar ratio (increasing silica content) compared to sintering in air as in oxidizing environments.

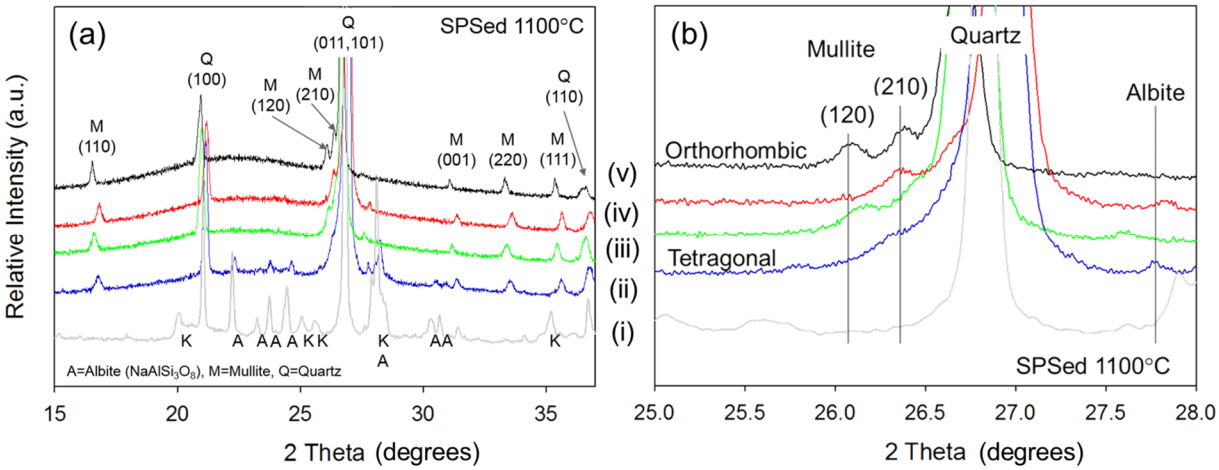

Figure 7.19: (a) Mullite formation in SPSed sample as a function of dwell time at 1100 °C, (i) green porcelain sample, (ii) 0 min, (iii) 5 min, (iv) 10 min, and (v) 15 min. (b) Mullite crystal structure by splitting of the 120 and 210 peaks showing transformation from tetragonal to orthorhombic mullite.

XRD (Fig. 7.19) also reveals that mullite formed at 1100 °C has different crystal structure depending on dwell time. With 0-10 min dwell times non-splitting (120/210) peaks suggest that mullite formed in these conditions is the tetragonal polymorph having higher alumina content [321] but changes to orthorhombic after 15 mins dwell time (the orthorhombic mullite is revealed by splitting of the 120 and 210 peaks). As previously mentioned tetragonal mullite is unstable and eventually transforms to orthorhombic structure.

The XRD result is consistent with the TEM results (Fig. 7.17) which also showed the mullite needles or clusters to have an orthorhombic crystal structure. Thus, at longer dwell time and higher temperature, mullite is in the orthorhombic form. This is strongly dependent on its chemistry because mullite is unstable above 75 mol.% and metastable above 63 mol.% alumina [322,323]. Thus, mullite that forms in porcelains in the SPS is unstable and metastable from a chemistry point of view and it needs sintering at higher temperature and/or longer dwell time to become a stable phase.

7.7.3.3 Dissolution of mullite in aluminosilicate melt

Mullite is observed to dissolve in the liquid melt as revealed by decrease of the integral area of mullite XRD peaks (Fig. 7.20). Fig. 7.20a shows that the amount of mullite formed during SPS is likely to be maximum at 1100 °C after 5 min dwelling time. Mullite content decreases as a function of dwell time after 5 min. The effect of SPS temperature is also observed at 1200 °C (Fig. 7.20b). Although mullite is recognized as a chemically and thermally stable material this result shows that it can dissolve in the aluminosilicate liquid melt. A similar result reported by Baudin and Villar [324] revealed that mullite dissolved in the presence of alkaline salts (~0.3% of Na_2O, K_2O and CaO) from 900-1630 °C under conventional firing conditions. Baudin and Villar pointed out that dissolution of mullite is masked by grain growth, which is greater than dissolution, and formation of liquid by reaction of mullite and alkalis during the firing process [324]. Ribeiro et al., [325] also reported that small (<5 µm) mullite grains dissolve in the liquid phase at high temperature (1250-1650 °C).

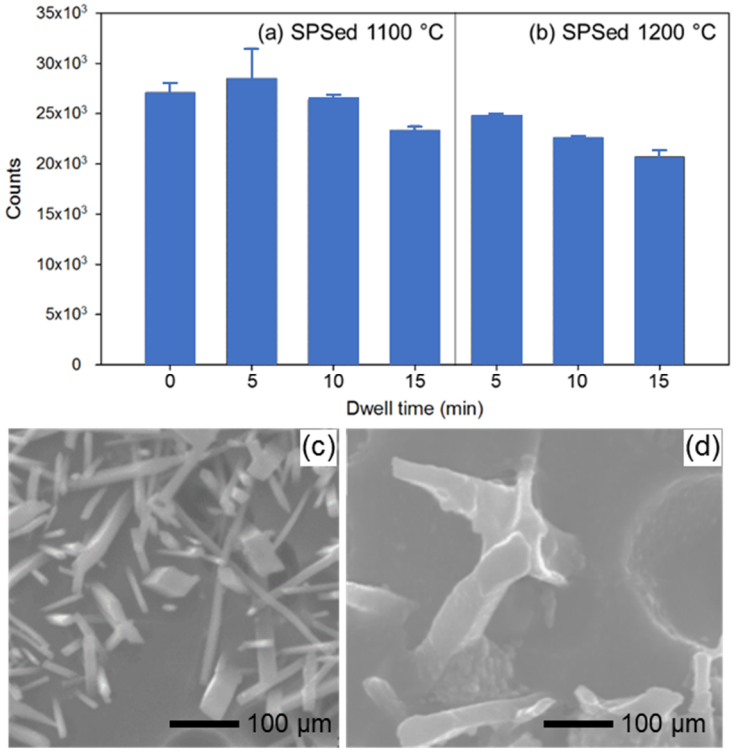

Figure 7.20: (a-b) Integral XRD peak area of mullite showing decreasing as function of dwell time and temperature. SEM images represent (c) well crystallized mullite in SPSed 1200 °C, 5 min dwell, and (d) partially dissolved mullite in SPSed 1200 °C, 15 min dwell, both samples were etched for 10 s in 5 %HF.

Microstructural analysis (Fig. 7.20d) shows partially-dissolved mullite needles emphasizing that mullite can dissolve at relatively low temperature (~1100-1200 °C) in the SPS.

7.7.3.4 Reprecipitation of mullite by Ostwald ripening

The Debye-Scherrer equation can be employed to calculate mullite crystallite size from the (110) reflection in XRD representing *a* and *b* lattice parameters as described in section 4.10. Fig. 7.21 suggests that mullite crystallite size increases as a function of dwell time and temperature (1000-1100 °C) in agreement with the study of mullite formation in porcelain by Lerdprom [160]. However, at 1200 °C, the mullite crystallite size decreases with increase in dwell time suggesting that mullite dissolved into the aluminosilicate liquid by alkali attack which is consistent with the dissolution results in section 7.7.3.3.

In addition, at 1100 °C mullite crystallite size increases as dwell time increases in contrast to the dissolution result (Fig. 7.20 mullite content decreases with increase dwell time). This can be explained by the Ostwald ripening effect resulting in the dissolved mullite re-precipitating into larger needles or clusters. Larger mullite needles were also in fact clearly observed in the TEM of the 1100 °C SPSed sample dwelled for the longest time (section 7.7.3.1).

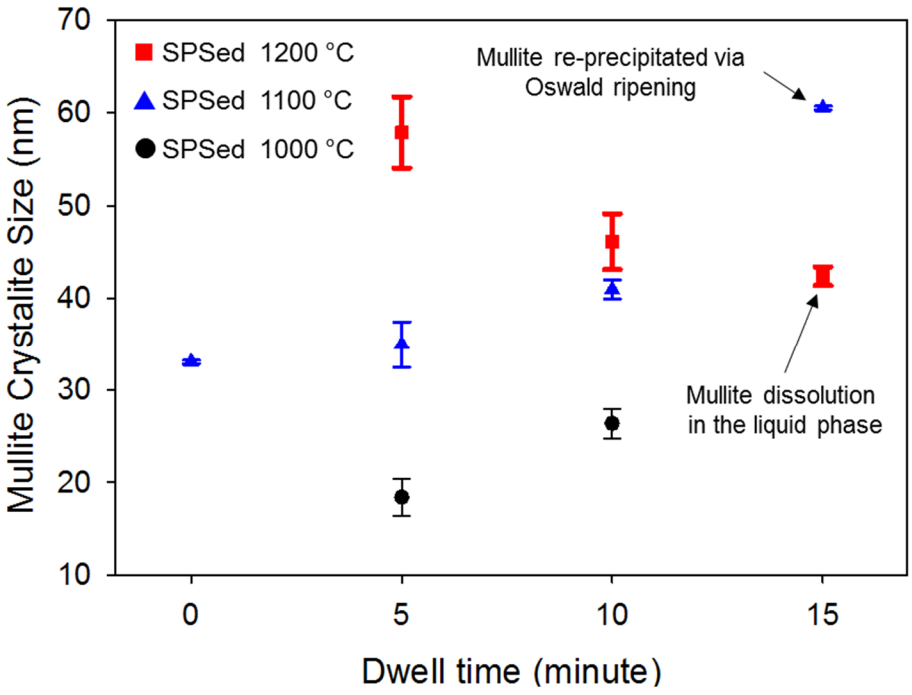

Figure 7.21: Mullite dissolution in aluminosilicate liquid and re-precipitation via Oswald ripening affected by dwell time and temperature.

7.8 Conclusions

SPS is an effective process to produce highly-dense porcelain requiring lower temperature and shorter sintering times compared to conventional sintering processes. The applied pressure has a huge influence on the densification. SPSed samples exhibit high ABD (2.46±0.01 g/cm^3), low WA (~0%), high Vickers hardness (6-7 GPa), and fracture toughness (4-6 MPa · m$^{1/2}$), all of which resulting from a combination of the highly-dense microstructure and mineralogical composition.

Several effects of SPS conditions on mullite formation with the overall scenario summarised schematically in Fig. 7.22. Mullite starts to form at 1000 °C with dwell time of 5 min. Initially, it forms as small crystallites (<50 nm) which are considered to be either spinel or mullite. Thermodynamic calculations suggest that the phase formed at 1000 °C tends to be mullite not spinel. At 1100 °C, substantial amount of mullite forms in the SPS process compared with conventional sintering due to the applied pressure and vacuum. Mullite needles align perpendicular to the compressive plane of the SPS with partial dissolution of mullite observed at 1100 °C as a function of dwell time and temperature. However, the dissolved mullite can re-precipitate on the small needles (40 nm) via Oswald ripening making larger mullite needles (60 nm).

Mullite chemistry changes with atmosphere, dwell time, and temperature resulting in different crystal structures, tetragonal or orthorhombic, depending on dwell time – tetragonal structure is formed for short dwell time of sintering which then transformed to orthorhombic with longer dwell times. Mullite produced under the SPS tends to be an alumina-rich phase having 66-73 mol.% of alumina (compared to the stoichiometric mullite having 60 mol.% of alumina).

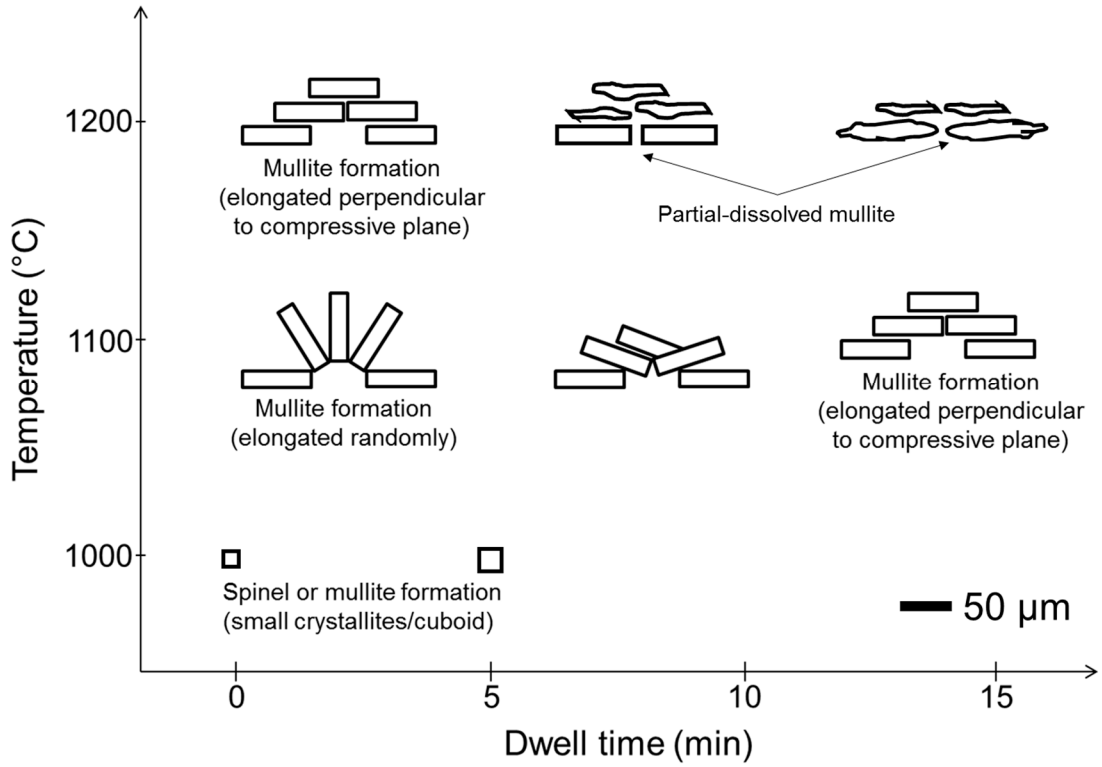

Figure 7.22: Schematic of the mullite formation, orientation, and dissolution under SPS conditions (dwell times and temperatures).

Chapter 8

Effect of MWS process on porcelain

8.1 Chapter review

In this chapter the effect of microwave radiation on porcelain is described. The green porcelain pellets were sintered by microwave radiation in a monomode cavity. Analysis of the temperature distribution in porcelain samples during microwave sintering is presented in section 8.2 because of the low thermal conductivity of porcelain. The microwave power absorption by porcelain resulting from the change of dielectric properties is discussed in section 8.3 revealing that porcelain pellets absorb microwaves at room temperature, heating to the sintering temperature and densify. Densification, physical property (ABD and WA), and microstructure are presented in section 8.4. The mechanical properties (Vickers hardness and fracture toughness) of the porcelain samples are reported in section 8.5 while section 8.6 considers mullite formation under microwave sintering, including its different morphologies.

8.2 Porcelain sample temperature distribution

Porcelain samples start to sinter under microwave radiation (MWSed samples) at relatively low temperature (~850 °C, surface temperature measured using a pyrometer) compared with samples sintered in the absence of microwave radiation, which start to densify at ~950 °C (see conventional sintering samples presented in section 5.4). However, the interior temperature of the samples produced by microwaves is higher than that at the surface since microwaves are

volumetrically absorbed producing an inverse temperature profile (arising from a combination of volumetric heating and surface heat loss).

The temperature rise in porcelain samples during microwave sintering has already been highlighted by Eq. 3.14 in section 3.8.2. However, surface heat loss (Q_L) during microwave sintering produces a temperature gradient in the porcelain body. In general, the surface heat loss is a combination of convection and radiation as presented by Eq. 8.1

$$Q_L = hA(T_s - T_{sur}) + \varepsilon\sigma A(T_s^4 - T_{sur}^4) \tag{8.1}$$

where h is the convection heat transfer coefficient, A is the sample area, T_s is sample surface temperature, T_{sur} is surrounding temperature, ε is sample surface emissivity, and σ is is the Stefan-Boltzmann coefficient.

Thus, the temperature (dT) produced at the sample surface can be calculated from Eq. 8.2.

$$\rho C_p \frac{dT}{dt} = \omega\varepsilon_0\varepsilon''_{eff}E_i^2 - \varepsilon\sigma A(T_s^4 - T_{sur}^4) \tag{8.2}$$

where ρ is sample density, C_p is heat capacity of the sample, ω is angular frequency which is $2\pi f$ (f is frequency of the applied microwave), ε_0 is permittivity of free space (8.85x10^{-12}, V/m^3), ε''_{eff} is the effective dielectric loss, E_i^2 is internal electric field intensity (V/m), ε is sample surface emissivity, and σ is is the Stefan-Boltzmann coefficient, and A is the sample area, T_s is sample surface temperature, T_{sur} is surrounding temperature.

In this case, it is assumed that surface heat loss is due to radiation only because convective heat loss contributes little compared to radiation above red heat.

Fig. 8.1 shows a schematic diagram of the temperature monitoring system used in this study illustrating that temperature measured by the pyrometer is lower than that generated in the interior resulting from the radiation heat loss. The pyrometer measures temperature of the sample at the surface, which is

exposed to the surrounding temperature of 30 °C. The microwaves interact with the porcelain generating heat inside the sample bulk.

Due to the complication of microwave-materials interaction and heat generation by the microwaves, the temperature read by the pyrometer is used as the surface temperature while the interior temperature is calculated using the surface temperature obtained from the pyrometer, the radiative heat loss coefficient (Q_L), and thermal conductivity (k) as described in section 6.8.

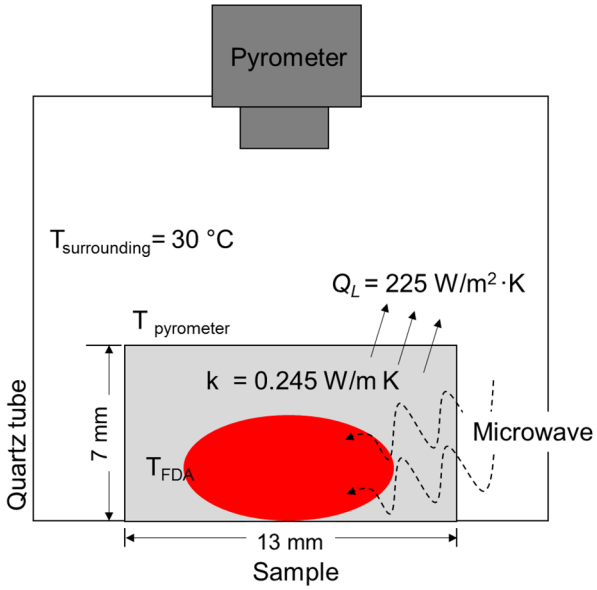

Figure 8.1: Schematic diagram of the temperature monitoring system used during microwave sintering.

Finite difference analysis (FDA), which was used to calculate the temperature distribution of the DS process in section 6.8, is also performed in this section to estimate the interior temperature of the porcelain samples produced by the microwave sintering process. It is assumed that the surface temperature is a function of heat transfer coefficient and thermal conductivity and calculated at steady state.

Fig. 8.2a reveals the sample surface temperature of 850 °C monitored using the pyrometer corresponding to ~950 °C of the interior temperature estimated by FDA (hereafter called FDA temperature). The interior temperature (in the sample centre) is about 100 °C higher than that measured at the sample surfaces. The

microstructure of the sample in Fig. 8.2a is in good agreement with that expected to form at the FDA temperature (Fig. 8.2b) where the surface of the sample has a bisque-characteristic representing an under-fired microstructure with the temperature of 850 °C.

The sample centre in Fig. 8.2b has seen an FDA temperature about 950-1100 °C consistent with the well-sintered microstructure in this region. At the bottom of the sample large pores/bubbles are observed indicating the bloating produced by high temperature (>1175 °C, the optimum firing temperature of this porcelain composition under a conventional firing process, presented in section 6.3), the FDA result indicates that the sample temperature was as high as 1300 °C.

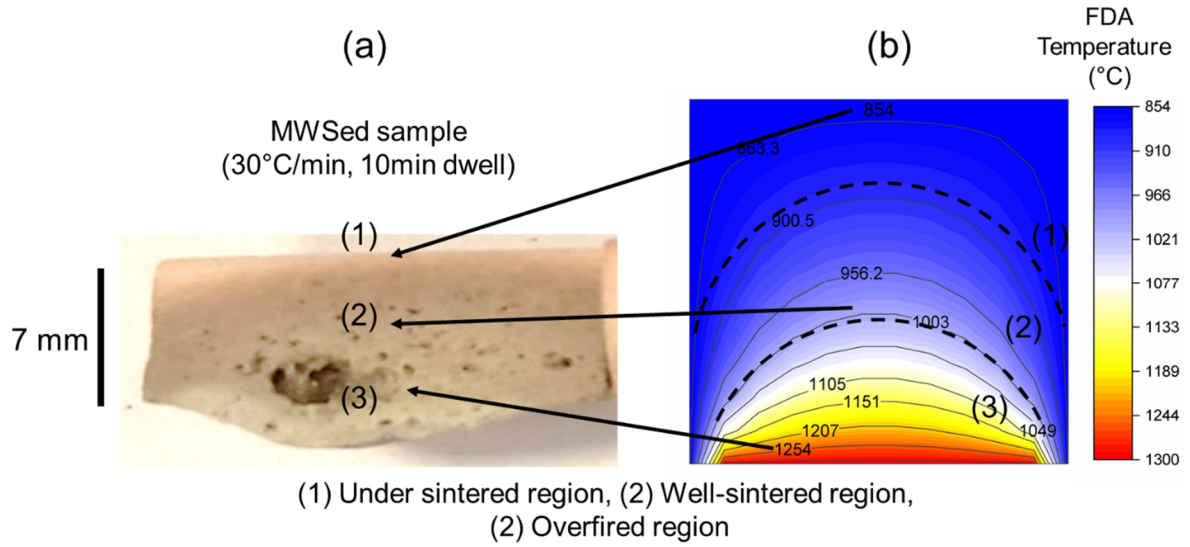

Figure 8.2: (a) Polished microstructure of the MWSed sample using 30 °C/min, 10 min dwell at surface temperature of 850 °C. (b) FDA result shows the temperature profile which agrees with the actual sample microstructure.

The FDA temperatures (Fig. 8.3) were calculated as a function of the surface temperature obtained by the pyrometer to identify the interior temperature of the MWSed samples. For example, the surface temperature of 850 °C corresponds to an FDA temperature of 950 °C, the surface temperature of 1000 °C is comparable to 1115 °C while the surface temperature of 1100 °C indicates 1230 °C interior temperature.

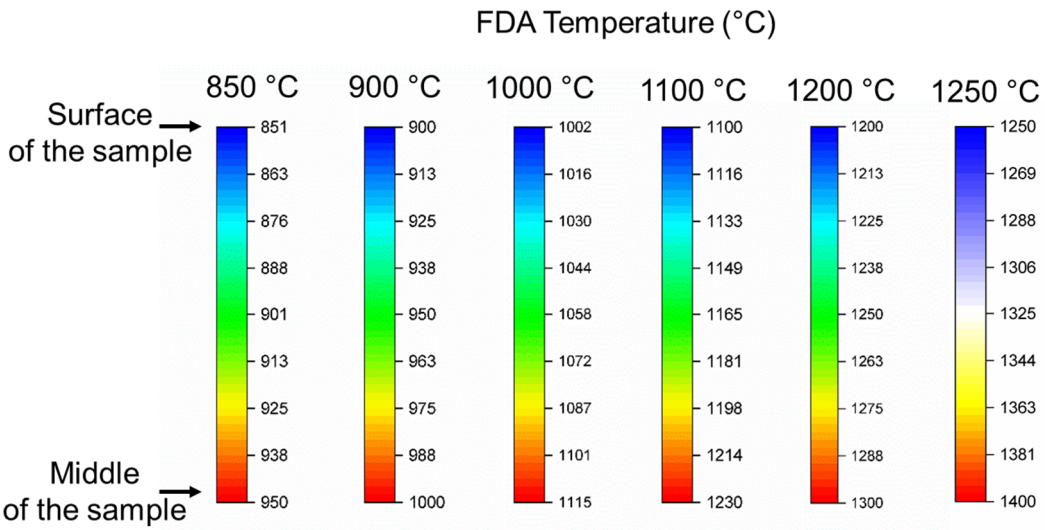

Figure 8.3: The surface temperature of the porcelain samples monitored using a pyrometer and estimated interior temperature calculated using FDA.

8.3 Microwave power absorption by porcelain

The microwave power absorbed by the porcelain samples is measured using the software described in section 4.15.3. The basic idea of the absorbed microwave power measurement is that the software measures the power input, which is produced by the magnetron, to the cavity and measures the power output from the cavity, so the power absorbed by the sample is known.

Fig. 8.4 presents an example of a microwave process showing how the microwave absorption is monitored. It shows temperature profile, power supplied, and power absorbed for MWSed samples using 1100 °C, 50 °C/min, 5 min dwell. 500 W of power is supplied to the cavity from the beginning and throughout the experiment.

At 0-15 s the operation shows a peak of power absorbed (~440 W) which is believed to be due to the presence of physically absorbed water in the sample which absorbs microwave energy well at room temperature. Therefore, surface temperature increases from 30 to 450 °C at 0-15 s. Once the physically bound water completely evaporates the power absorbed drops to a more normal value about 15 W (at t=16 s).

The temperature measured at the sample surface in this range (<600 °C) is close to the interior temperature of the sample because the surface heat loss is

relatively small below the red hot. For example, FDA calculation indicates that the surface temperature of 450 °C is ~500 °C in the sample centre.

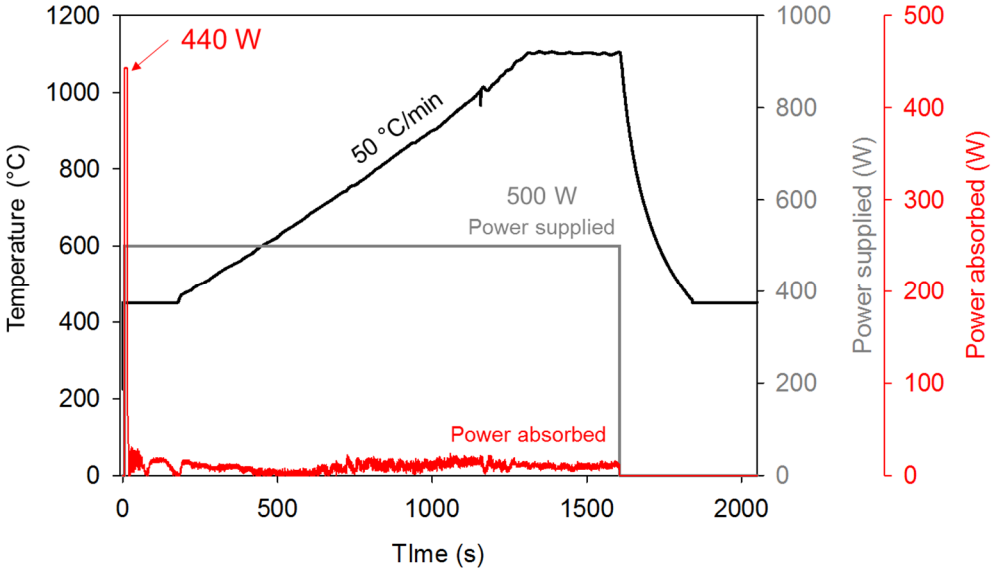

Figure 8.4: Temperature profile, power supplied, and power absorbed for MWSed samples sintered at 1100 °C, 50 °C/min, 5 min dwell.

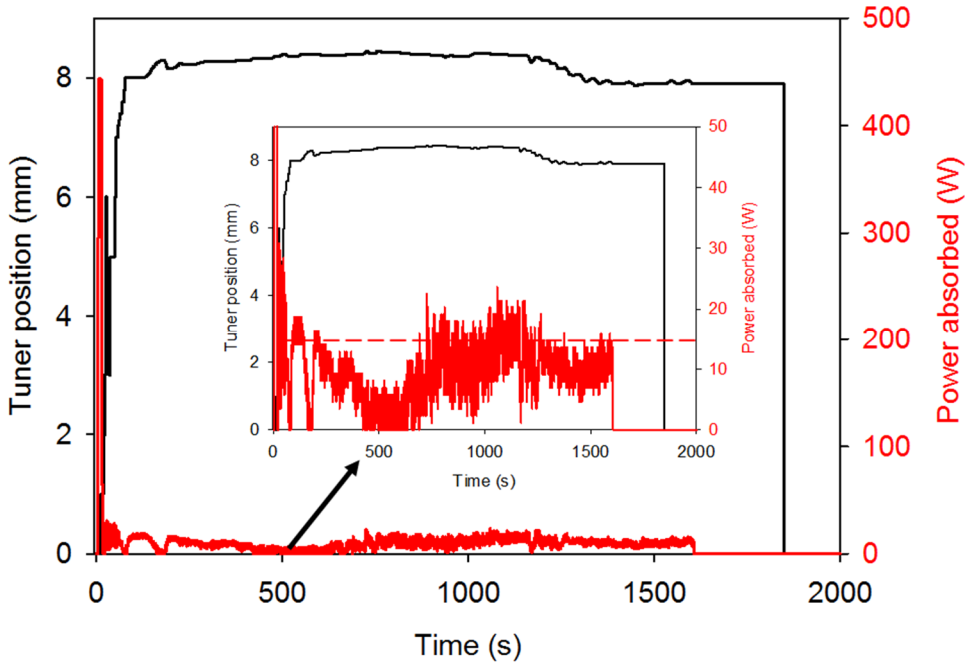

Figure 8.5: Tuner position and power absorbed vs time for a MWSed sample sintered at 1100 °C, 50 °C/min, and 5 min dwell.

The porcelain sample absorbs microwave power again once the tuner position is adjusted (see section 4.19.3), the sample then absorbs microwave energy according to the tuner position Fig. 8.5. However, the power absorbed by

the sample is low compared to the input power (500 W). The average power absorbed to raise temperature from 450 to 1100 °C is ~15 W · s as presented in the inset of Fig. 8.5. Nevertheless, Figs. 8.4 and 8.5 show an example of a well-controlled operation. Several other experiments were unsuccessful because of the difficulty of manual control. For example, Fig. 8.6a reveals an example of a difficult-to-control experiment showing unstable temperature rise caused by changing dielectric properties of the porcelain sample. Three difficult-to-control points are found at (i) <200 °C associated with the loss of physically bound water, (ii) 500-600 °C associated with dehydroxylation of the kaolinite and (iii) ~800 °C from the melting of albite as already mentioned in section 5.3.

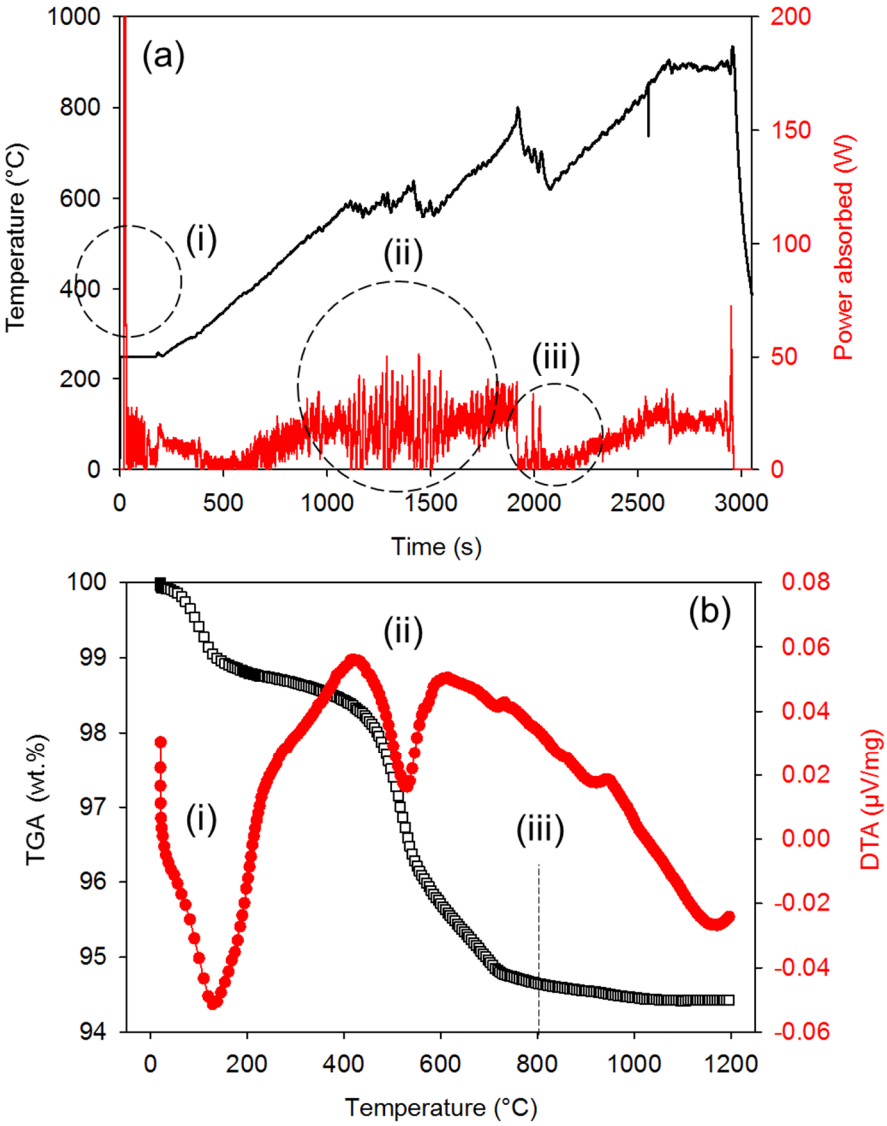

Figure 8.6: (a) An example of difficult-to-control points during microwave processing, (b) thermal events associated with the change of microwave absorption.

Thermal events shown in Fig. 8.6b imply that changing thermal behaviour of the porcelain sample with elevated temperature changed its ability to absorb microwaves.

Fig. 8.7a shows dielectric behaviour of the porcelain sample under an alternating electric field of 1 MHz. The calculated loss tangent of the porcelain powder from room temperature to 900 °C using equation 4.17 ($tan\ \delta = \sigma/2\pi f \varepsilon_0$), described in section 4.8.2.

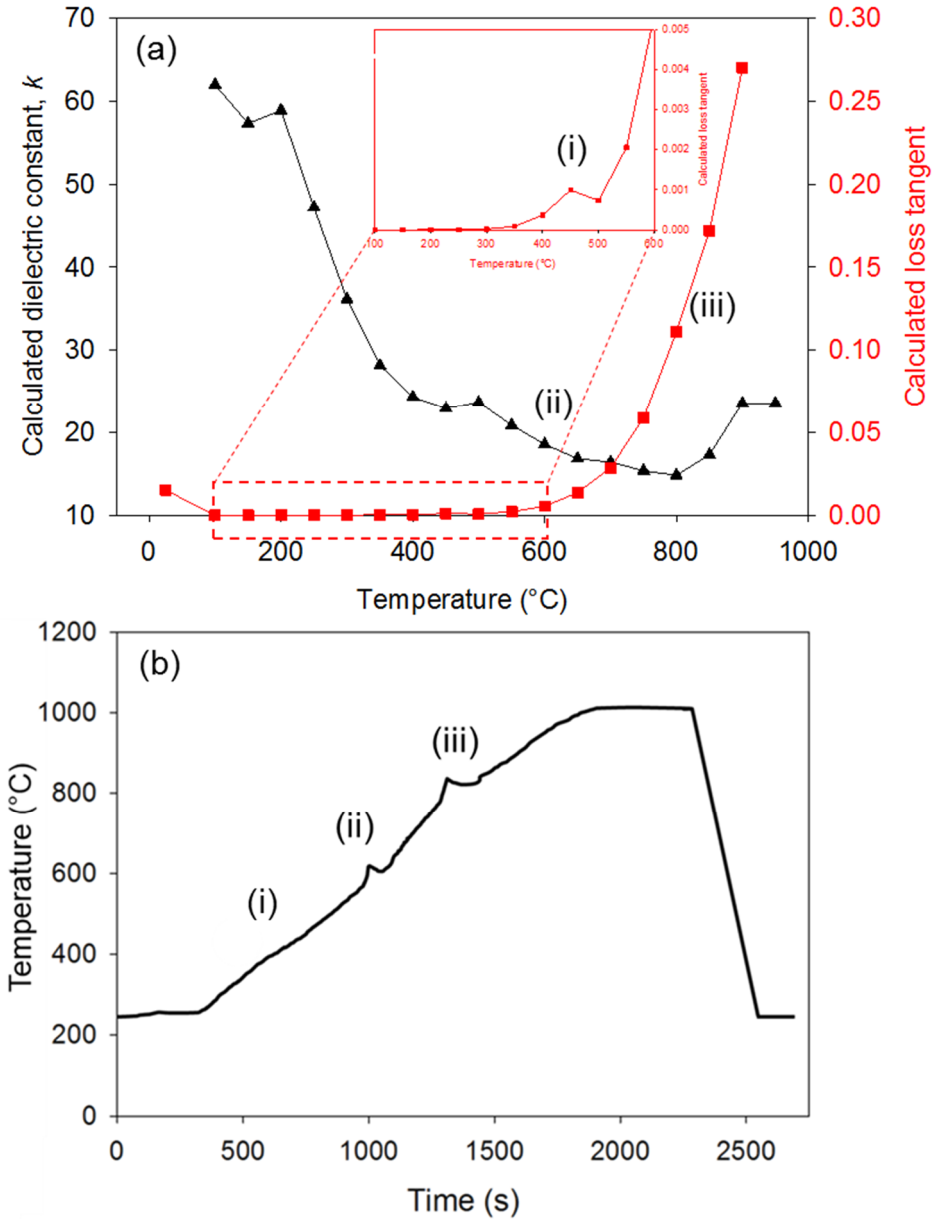

Figure 8.7: (a) Calculated loss tangent ($tan\ \delta$) of porcelain sample as a function temperature, and (b) the temperature profile of microwave sintering (1000 °C, 30 °C/min, 5 min dwell) showing 3 humps at (i) 450 °C, (ii) 600 °C, and (iii) 800 °C (FDA temperature) corresponding to rapid change of $tan\ \delta$.

Fig. 8.7b shows the temperature control of the MWSed 1000 °C, dwell 5 min. It suggests that the change of *tan δ* affects the temperature control showing three peaks (i, ii, and iii). The three peaks are also in good agreement with the loss of physically bound water, chemically bound water of the clay substances, and melting of feldspars, respectively.

8.4 Densification and microstructure

Fig. 8.8a and b show development of ABD and WA of MWSed samples as a function of sintering temperature. At 950 °C (note that the temperature reported in this section is the FDA temperature), ABD of the sample is 2.25±0.02 g/cm^3 and increases with temperature. The MWSed sample reached maximum ABD of 2.36±0.03 g/cm^3 at 1100 °C. WA data, on the other hand, varies between 0-3±2% from 950-1200 °C due to unevenly sintered microstructures but reaches a minimum of 0.5±0.02 % at 1100 °C.

Fig. 8.8 also suggests that the FDA temperature for the densification of the porcelain samples under microwave irradiation is about 100 °C higher than that measured using the pyrometer. Microwave densification of this porcelain composition started at ~950 °C and full density was achieved at ~1100 °C producing promising physical properties. However, the standard deviations of the ABD and WA data are influenced by the heterogeneous sample microstructure (uneven sintered microstructure).

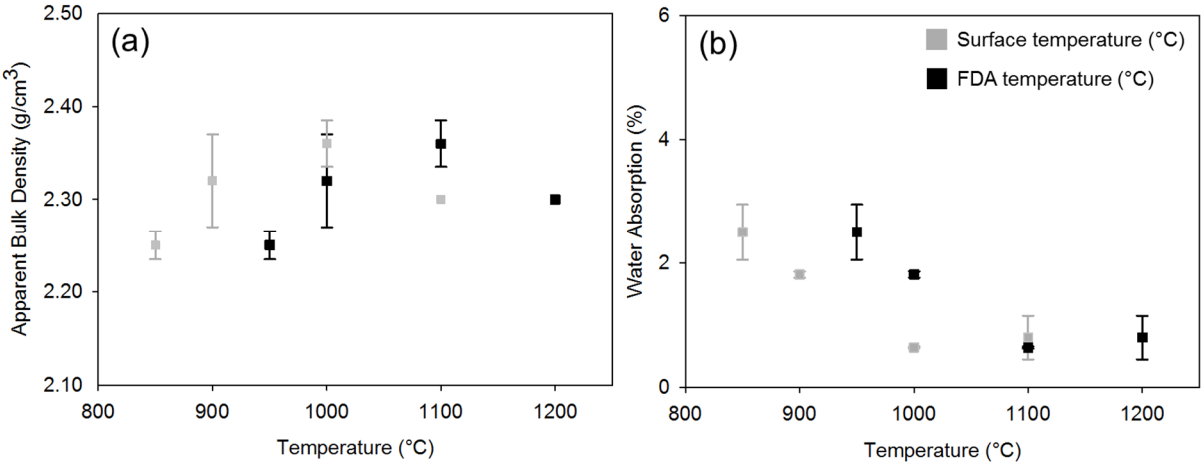

Figure 8.8: (a) ABD and (b) WA of MWSed porcelain sample as a function of temperature. Note that—30 °C/min and 5 min dwell are used in this experiment for comparison.

Fig. 8.9 shows polished microstructures after different sintering temperatures of the MWSed samples. The four samples are not sintered homogeneously since their electrical properties change during the microwave irradiation making the power absorption difficult-to-control, which resulted in an uneven sintered microstructure. However, well-sintered areas of ~3x5 mm^2 were examined in the samples sintered under the four conditions for further investigation.

Fig. 8.9a reveals the MWSed sample sintered at 950 °C shows low degree of densification with low ABD and high WA. The MWSed 1000 °C (Fig. 8.9b) shows better densification compared to the MWSed 950 °C. The MWSed 1100 °C (Fig. 8.9c) has the most dense and promising microstructure with high content of glassy phase produced (85 vol.% of albite melt, which is calculated from albite integrated peaks area in Fig. 8.11) while MWSed 1200 °C (Fig. 8.9d) is bloated (with 100 vol.% albite melt). All of this agrees well with the physical properties data (shown in Fig. 8.8).

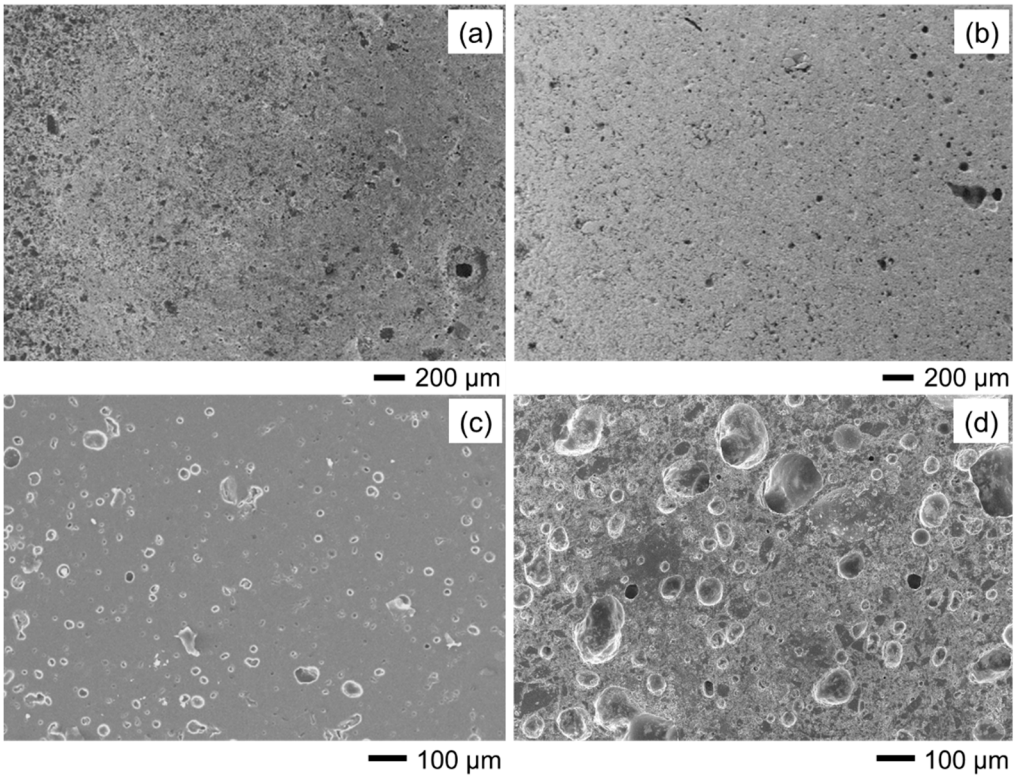

Figure 8.9: Polished microstructures of MWSed samples after (a) 950 °C, (b) 1000 °C, (c) 1100 °C, and (d)1200 °C, all of which are sintered using 30 °C/min and 5 min dwell.

Fig. 8.10 shows HF-etched microstructures of the MWSed samples revealing mullite formation. Between 950-1000 °C, (Fig. 8.10a and b respectively), the MWSed samples show poor densification and just small mullite nuclei of ~70-100 nm (indicated as M) are observed. In contrast, the MWSed samples at 1100 and 1200 °C (Fig. 8.10c and d respectively) shows large amounts of mullite formation (9.8±0.1 vol.% and 9.9±0.1 vol.% respectively) in both kaolinite relicts (M_I) and glassy phase (M_{II}).

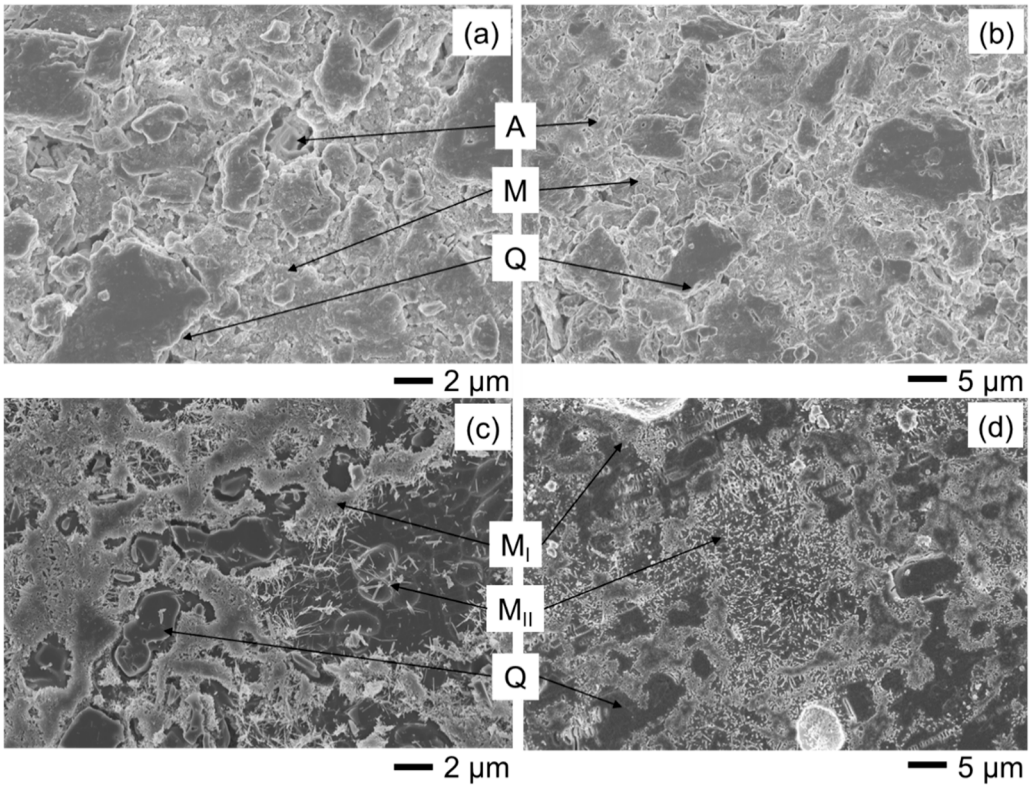

Figure 8.10: HF-etched microstructures of MWSed samples sintered at (a) 950 °C, (b) 1000 °C, (c) 1100 °C, and (d)1200 °C, all of which are sintered using 30 °C/min and 5 min dwell. A is albite, Q is quartz, M is small (100 nm) mullite nuclei, M_I is mullite found in kaolinite relicts, and M_{II} is mullite found in glassy matrix.

8.5 Phase evolution of MWSed porcelain

XRD (Fig. 8.11) reveals the phase changes of MWSed samples as a function of sintering temperature using 30 °C/min heating rate and 5 min dwell. After sintering at 950 °C, residual albite is significant (~27.1 vol.% compared with the green porcelain using the integrated peak area) while a small fraction of mullite

is detected (5.21±0.2 vol.%). Albite peaks are observed in the MWSed samples sintered at 950-1100 °C but disappeared after sintering at 1200 °C indicating complete melting of albite.

Mullite, on the other hand, is found in samples sintered at 950-1200 °C but its peaks are broad and small resulting from the small crystallite size (discussed in section 8.7.1). However, the amount of mullite increases with temperature increase as indicated by the mullite integrated peak area.

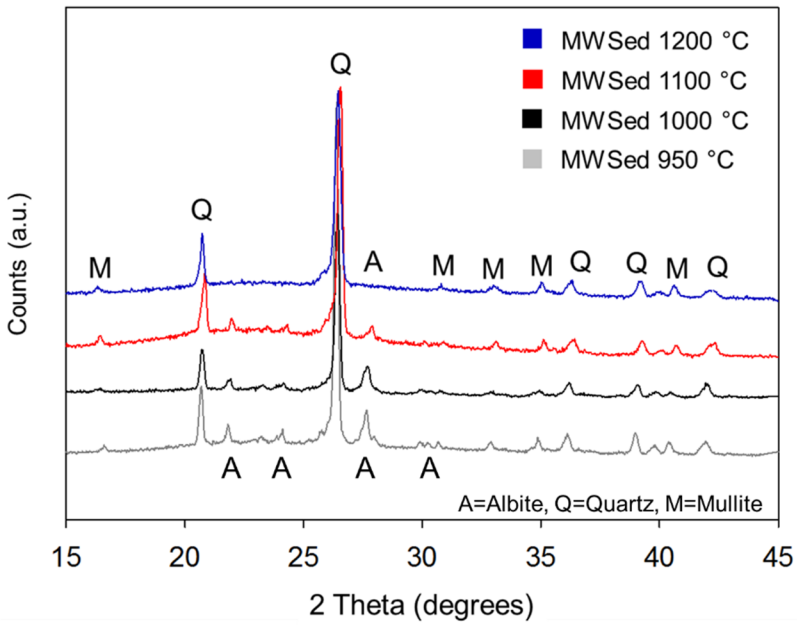

Figure 8.11: XRD of MWSed samples sintered at 950 °C, 1000 °C, 1100 °C, and 1200 °C, using 30 °C/min and 5 min dwell. A is albite, Q is quartz, M is mullite.

8.6 Mechanical properties of porcelain sintered using microwaves

Vickers hardness (H_V) was measured in the well-sintered regions of the MWSed samples. As shown in Fig. 8.12, H_V at 950 °C and 1000 °C could not be determined because of the highly porous microstructure. H_V increases for the MWSed samples sintered at 1100 °C, but little drops for the one sintered at 1200 °C, explained by their dense microstructures. The maximum H_V is 5.6±0.2 GPa at MWSed 1100 °C.

Fracture toughness (K_{IC}) of MWSed samples shows the same trend as observed for Vickers hardness. Cracks could not be observed in samples sintered at 950 and 1000 °C due to their highly porous nature so that it was not possible to determine K_{IC}. However, K_{IC} of MWSed are similar once the sample sintered at

optimal temperature (1100-1200 °C) with 4.8±0.2 MPa · $m^{1/2}$ at 1100 °C and 4.8±0.4 MPa · $m^{1/2}$ at 1200 °C. This similar K_{IC} can be explained by the similar degree of densification of both samples (Fig. 8.8). Even though MWSed 1200 °C sample is bloated but the K_{IC} was measured at microscale (at the dense region) so, they are similar as also described in section 7.6.

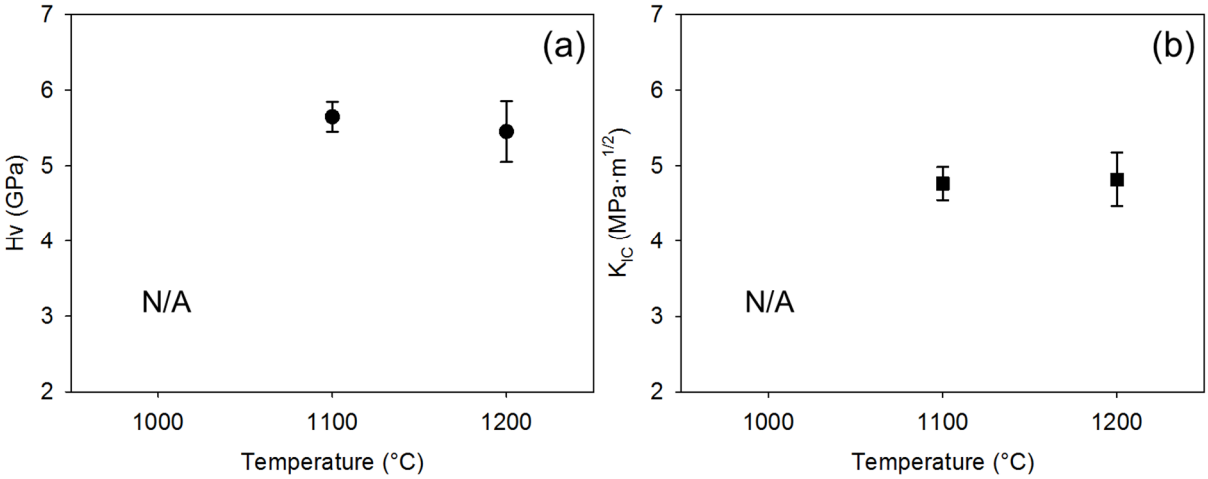

Figure 8.12: (a) Vickers hardness (H_V), and (b) fracture toughness (K_{IC}) of MWSed samples as a function of sintering temperature.

H_V and K_{IC} in Fig. 8.12 represent the mechanical properties measured at the microscale because the indentation was made in highly dense areas, which is also explained by the ABD and mineralogical composition in the particular area. For example, the MWSed sample sintered at 1100 °C has highest H_V because they have highest ABD, but the hardness does not decrease when the sample is bloated as observed in Fig. 8.8. This is because the glassy phase and other constituents (residual albite, mullite and quartz) are responsible of the mechanical property in the microscale, as discussed in section 7.6.

In general, hardness is a surface property of materials. It represents the resistance of a materials surface to abrasion, scratching, and plastic deformation (indentation). Even though hardness is a surface property of material, theoretical attempts have been made to describe hardness in term of bulk properties such as elastic modulus. The concept is based on the elastic modulus being an intrinsic mechanical property of material dominated by strength of chemical bonds between

atoms. Also, hardness represents the deformation of the materials thus the higher hardness assumes higher elastic modulus [326].

A more reliable relationship was proposed by Chen et al., [327]. Chen et al., proposed a ratio referred to as the Pugh's modulus ratio k= G/B which relates the brittleness (G), to the ductility (B) of materials. The higher the value of G/B, the more brittle the materials would be. Thus, brittle materials are bound to possess a larger k value compared to ductile ones. A reliable equation used to predict the hardness of crystalline materials is correlated to the product of the squared Pugh's modulus ratio and the shear modulus.

$$H_v = 2(k^2G)^{0.585} - 3 \qquad 8.3$$

where H_v is Vickers hardness, H_v is Pugh's modulus ratio, and G is shear modulus. In this study, Hv measured in MWSed samples is considered as a surface property, not a bulk property, because the Hv was measured predominantly on the dense (pore-free) areas. The body of the porcelain samples contains pores which may alter the bulk property compared to the surface property.

8.7 Further results and discussion

8.7.1 Mullite formation in porcelain under microwave sintering

In this section, the effect of microwaves on microstructural changes in porcelain is studied in MWSed 1100 °C sample and compared with those in fully dense CSed 1175 °C sample (Fig. 8.13).

The low magnification SEM images in Fig. 8.13a and b reveal etched microstructures of the CSed (Fig. 8.13a) and MWSed samples (Fig. 8.13b) containing mullite, quartz, and glassy phase. The CSed sample is dense containing mainly mullite found in the clay relicts (M_I) and partially dissolved quartz (Q) in the glass matrix while MWSed sample contains mullite in the clay relicts (M_I) and networks of mullite needles grown in the glass matrix (M_{II}).

There are two different aspects of mullite formed in the CSed and MWSed samples that are highlighted from this observation; (1) the amount of mullite formed, and (2) mullite morphology.

In the first case, it is clear that the amount of mullite formed in the MWSed sample is greater than in the CSed sample (discussed in section 8.5). The latter case is explained using the high magnification SEM images in Fig. 8.13b and d. They reveal distinctive mullite morphologies in terms of crystallite size and aspect ratio.

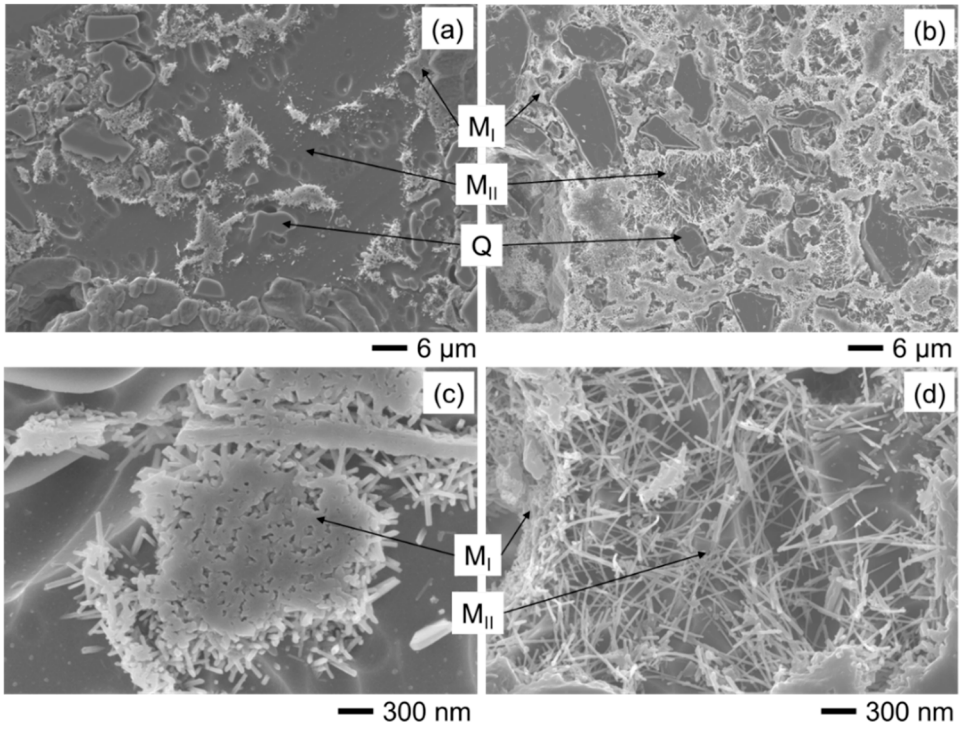

Figure 8.13: SEM images of CSed sample (1175 °C, 10 °C/min, 15 min dwell) and MWSed (1100 °C, 30 °C/min, 5 min dwell). (a) and (c) are the SEM images of CSed sample at low and high magnification respectively, (b) and (d) are the SEM images of MWSed sample at low and high magnification respectively. Q is quartz, M_I is mullite found in the clay relicts, and M_{II} is mullite found in the glassy matrix.

Fig. 8.14 compares mullite crystallite size (Fig. 8.14a) and aspect ratio (Fig. 8.14b) of CSed and MWSed samples determined from the micrographs. The mullite crystallite size in CSed sample is 71±11 nm whereas in MWSed sample is 56±9 nm (Fig. 8.14a). However, the CSed sample contains lower aspect ratio mullite needles (~9±2:1) while MWS produced fibre-like mullite with a high aspect ratio (~32±3:1) (Fig. 8.14b).

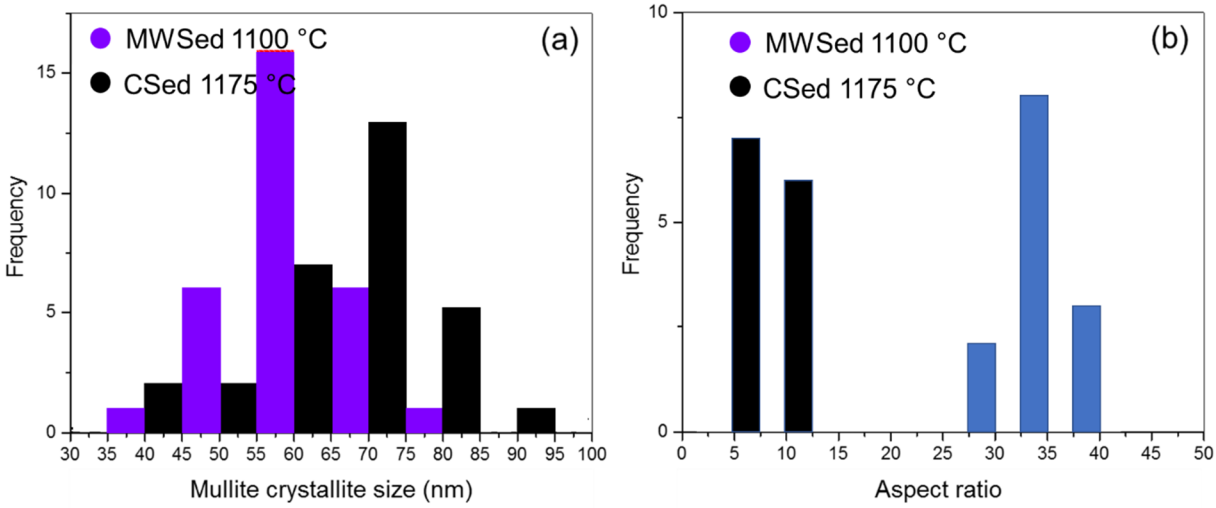

Figure 8.14: Histograms of mullite formed in CSed and MWSed samples (a) crystallite size and (b) aspect ratio.

Types of mullite formed in porcelains can be differentiated by its aspect ratio. Lee and Iqbal [148] proposed a notation considering the aspect ratio in which, type I mullite (primary mullite) exhibits low aspect ratio (1-3:1), type II (secondary mullite) has aspect ratio of 3-10:1, and type III (secondary mullite) possesses very high aspect ratio (>30:1). Therefore, the mullite formed in this porcelain via MWS is likely to be type III while CSed sample is type II.

Mullite crystallite size was also determined from XRD peak broadening using the Scherrer equation on the (110) plane peak. The full width half maximum (FWHM) indicates that the average mullite crystallite size of the CSed sample is ~39±3 nm while in the MWSed sample it is ~28±3 nm. Clearly mullite crystal sizes obtained from SEM and XRD give different values. The difference may arise from the different sampling volumes of each technique. Nonetheless the same trend is observed in both methods.

Mullite formed in porcelains usually has acicular morphology with fibres length aligned along the c-axis [311]; the c-axis has higher free energy than other [hk0] directions. Fig. 8.15a reveals an unusual mullite morphology growing inside a bubble in the MWSed sample sintered at 1100 °C. Mullite formed in the bubbles is believed to grow via a vapour-liquid-solid (VLS) mechanism [328,329]. Mullite then continually grows in [001] direction in the air which has randomly precipitated nuclei on the needles (Fig. 8.15b-c). These nuclei may aid the growth

of high aspect ratio needles. This feature is not observed in CSed samples. Also, the formation of mullite via VLS has been not reported in conventional sintering of porcelains. This observation is discussed further in section 8.7.2.

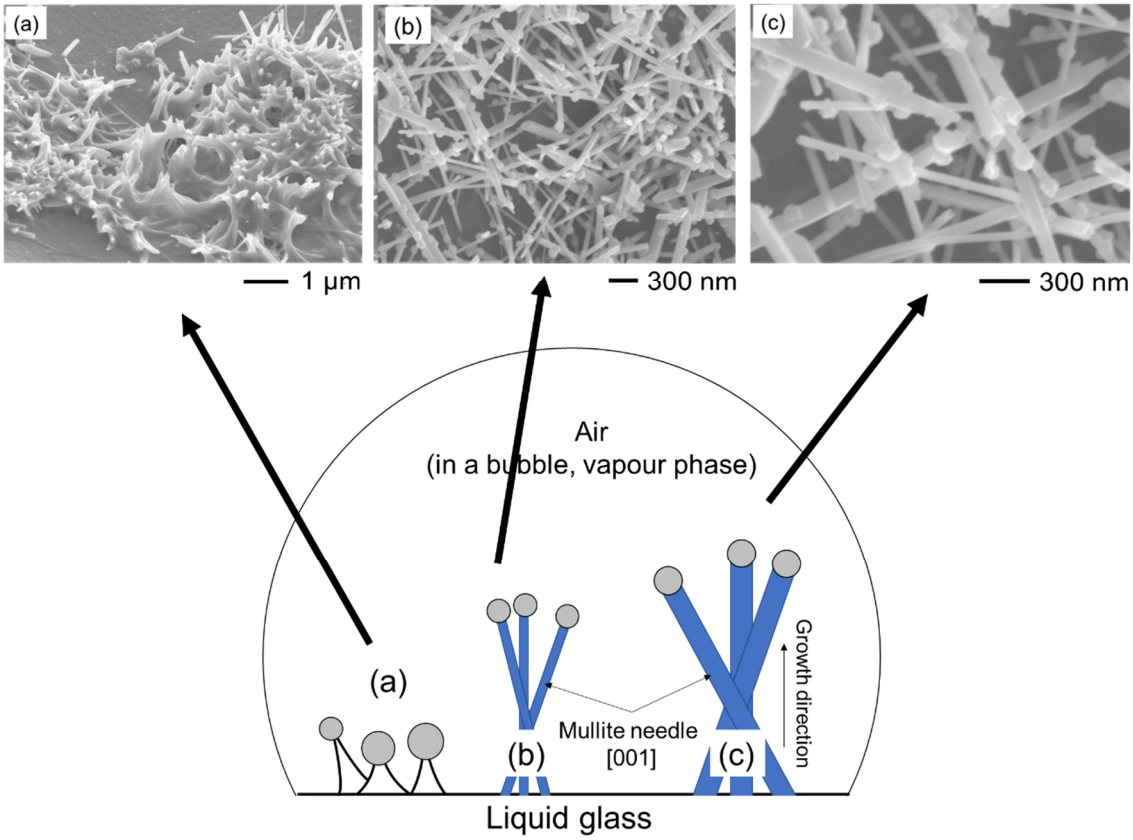

Figure 8.15: Vapour-Liquid-Solid growth mechanisms of mullite needles under microwave radiation: (a) mullite initially formed in a bubble surrounded by liquid glass phase, (b) further mullite needle growth in bubbles/pores, (c) mullite nuclei precipitated on mullite needles, and (d) schematic diagram of the growth mechanism.

XRD (Fig. 8.16a) reveals detail of an MWSed sample sintered at 1100 °C showing greater mullite integrated peak area (~7 %) than in a CSed sample. This suggests that mullite content in MWS sintering is higher than in conventional sintering with agreement to SEM observations (Fig. 8.13). Furthermore, the CSed sample contains greater residual albite (~5 vol.%) than the MWSed sample (Fig. 8.16b-c).

From a microstructural point of view, in the CSed sample mullite formed mainly in the clay relicts, rather than in the glassy matrix. Conversely, the MWSed sample contains mullite in the clay relicts and in the glassy phase, all of

which combined to give greater mullite content (~7 vol.%) than observed in the CSed sample.

Microwave energy can enhance mullite formation in three ways. Firstly, enhanced reaction rate of mullite formation from kaolinite. Zhang et al., [330] reported that microwaves can enhance formation of mullite from kaolinite because of a selective heating, accelerating the nucleation and growth of mullite, which changed the mullite formation route from kaolinite. Secondly, melting of albite providing more alumina for mullite formation in the glassy matrix. Thirdly, additional mullite can form from the VLS mechanism not seen in other sintering routes.

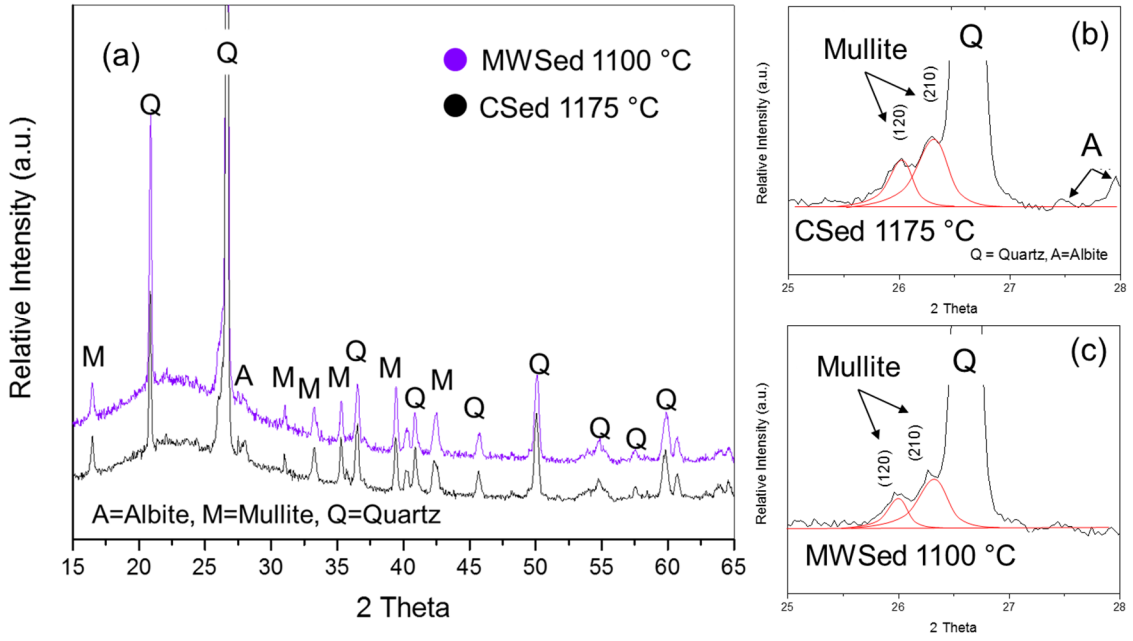

Figure 8.16: (a) XRD of CSed and MWSed samples. Mullite formed under both conditions is identified as orthorhombic by splitting of (120) and (210) peaks revealed in (b) CSed 1175 °C sample, and (c) MWSed 1100 °C samples.

Mullite chemistry was determined using the method of Ban and Okada [135] showing molar percent of alumina in mullite. MWSed mullite contained ~63 mol.% of alumina compared to ~60 mol.% of alumina in CSed mullite. However, the crystal structure of the mullite in both samples is orthorhombic instead of tetragonal as indicated by splitting of (120) and (210) XRD peaks (Fig. 8.16b and c). The reason why mullite has different alumina content is explained by the effect of the microwave radiation as follows.

Formation of mullite in the MWSed sample is accelerated by the reduction of activation energy barriers for diffusion of Al^{+3} ions in the mullite structure, which can also be deduced from its fibrous morphology [330]. Moreover, since the liquid glass formed at lower temperatures (about 950 °C FDA temperature) and so earlier time in MWSed samples the mullite crystals have more time to grow and accommodate alumina into their structures. Thus, MWSed mullite has higher alumina content than stoichiometric.

Another possibility is that the temperature to obtain the stoichiometric mullite (60 mol.% alumina) under microwaves might be lower [331]. However, since the mullite chemistry calculated from the XRD is an average of a large volume (3x5 mm^3) both mullites in the clay relicts and the glassy matrix are included.

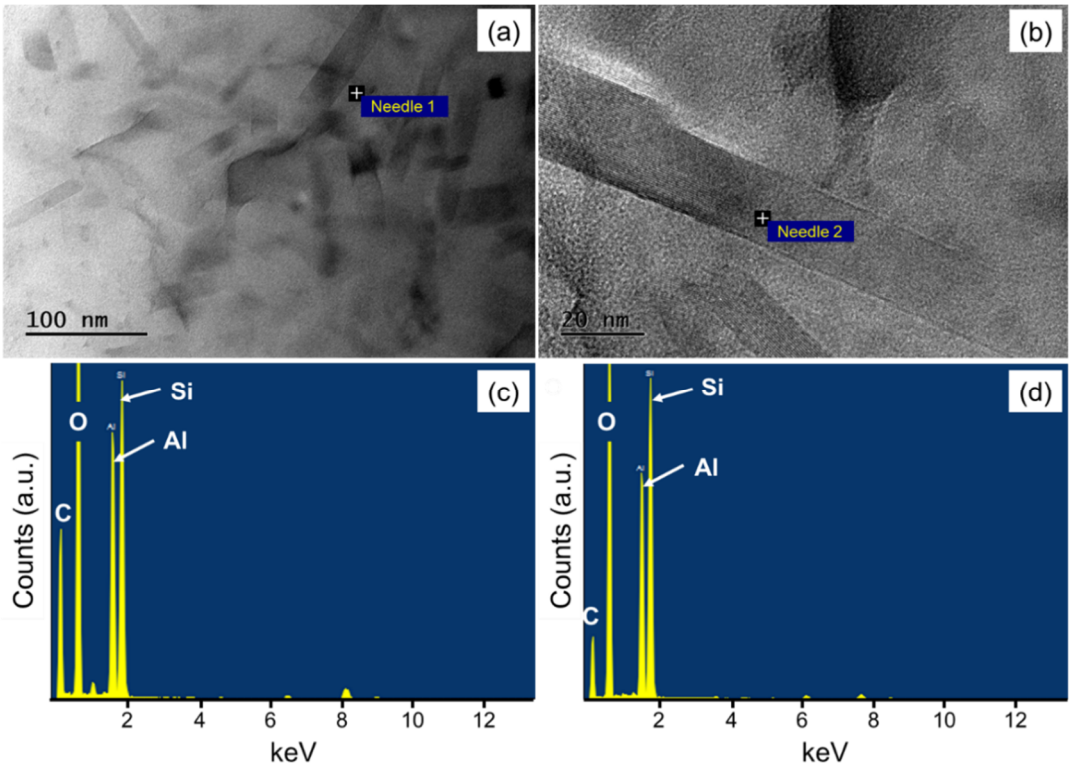

Figure 8.17: (a) TEM of mullite in clay relicts, (b) mullite in glassy phase, EDS of mullite in (c) clay relicts, and (d) glassy matrix from MWSed sample sintered at 1100 °C with 5 min dwell.

Fig. 8.17 shows TEM images of mullite needles and their chemistry located in clay relicts (Fig. 8.17a and c) and glassy matrix (Fig. 8.17b and d) of the MWSed sample sintered at 1100 °C with 5 min dwell. These suggest that mullite in the

clay relicts has greater alumina content than that formed in the glassy matrix because clays provide more alumina for mullite formation. Although, the mullite needles are very small as ~20 nm thick but their chemistries acquired by the TEM are representative the actual chemistry because the interaction volume of TEM in the porcelain sample is much smaller than that in SEM, it provides more accurate chemistry of mullite needles. TEM employs a very small electron beam typically <5 nm and the beam interacts with a thin section (50-100 nm) of the sample. So that the TEM interaction volume is disc shaped (because most electron beam transmits through the thin sample as beam energies are generally great i.e. 100 kV) with approximately 5x100 nm (beam diameter x section thickness). This is unlike the interaction volume of SEM (see section 4.13), which is a hemispherical to jug-shaped because SEM samples are too thick for the electron beam to pass through the sample. Thus the EDS results in Fig. 8.17 fit reasonably the mullite chemistries.

8.7.2 Effect of microwaves on mullite formation mechanism

Mullite formed in MWSed samples has an unusual morphology showing a spherical cap at the end of the needles (Fig. 8.18). The spherical cap indicates that this mullite needle forms via a vapour-liquid-solid mechanism (VLS).

In this MWSed sample, 5 kV accelerating voltage was used to minimize the interaction volume and increase spatial resolution of the image, giving an interaction volume as discussed in section 4.13. As the mullite needle cap is about 0.2 µm thick and the mullite needle itself is about 0.15 µm (Fig. 8.18). It can be deduced that the semi-quantitative EDS analysis at 5 kV to determine the chemical composition of the mullite needle and its cap is indicative because while the interaction volumes included a significant volume of the mullite needle, they did overlap.

The cap has an average diameter of 180±13 nm and the cross-section (thickness) of the needles is 87±5 nm. This morphology is only found in mullite located in the bubbles/pores suggesting that vapour phase must be involved as discussed in section 8.7.1 (see Fig. 8.15). Semi-quantitative EDS analysis shows the chemical composition of the needles (spectra 1 and 3 in Fig. 8.18) which are $0.6Al_2O_3 \cdot SiO_2$ and $3Al_2O_3 \cdot 2SiO_2$ respectively. EDS also reveals that the spherical

cap contains Fe which serves as catalyst in the VLS process (spectrum 2). The porcelain starting powder contains impurities as described in section 5.2 i.e. 0.68±0.01 wt.% TiO_2, 1.24±0.04 wt.% Fe_2O_3, and organic matter which can act as a catalyst for the VLS.

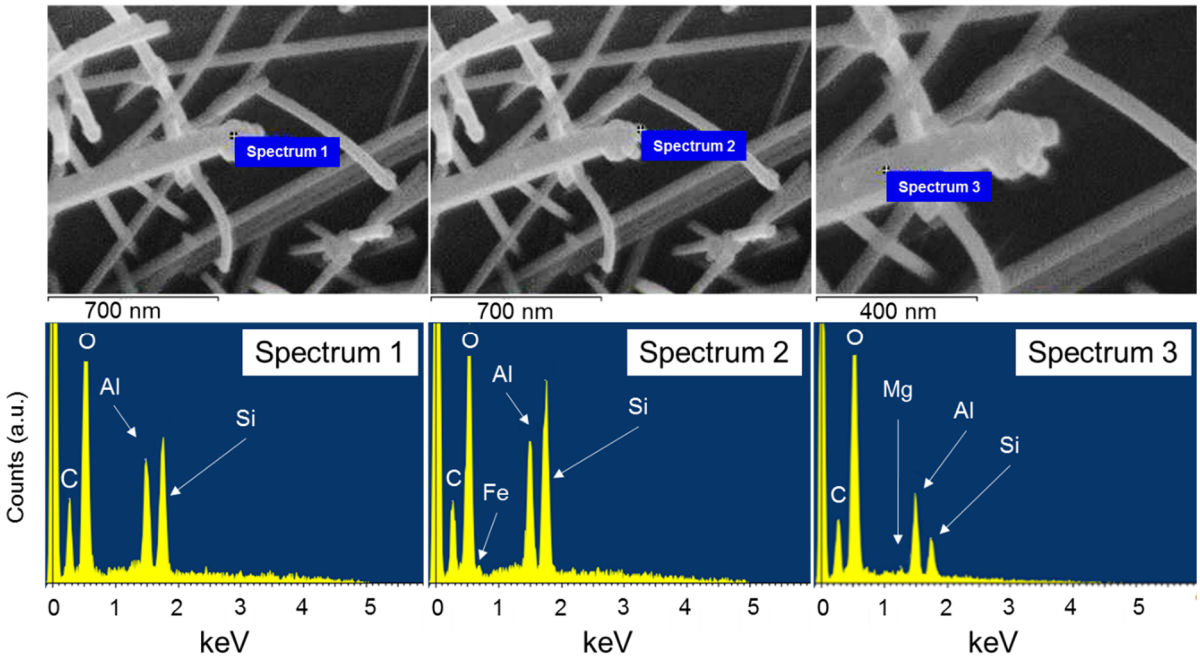

Figure 8.18: EDS analysis of a mullite needle and its spherical cap in MWSed sample sintered at 1100 °C with 5 min dwell.

The VLS mechanism involved in the fibrous mullite formation can be explained using the following reactions. From a thermodynamic point of view, Fe_2O_3 and TiO_2 can react with carbons and form a metallic liquid as presented by the following chemical reactions (Reaction 1-6).

$TiO_2(s) + 2C\ (s) = Ti(s)+2CO(g)$ (Reaction 1)

$Fe_2O_3\ (s) + 3C\ (s) = 2Fe\ (l) + 3CO(g)$ (Reaction 2)

$2Fe_2O_3\ (s) + 3C\ (s) = 4Fe\ (l) + 3CO_2(g)$ (Reaction 3)

$Fe_2O_3\ (s) + 3CO\ (g) = 2Fe\ (l) + 3CO_2\ (g)$ (Reaction 4)

$SiO_2\ (s) + C\ (s) = SiO\ (g) + CO\ (g)$ (Reaction 5)

SiO_2 (s) + CO (g) = SiO (g) + CO_2 (g) (Reaction 6)

Carbons found in this porcelain sample are in solid form (organic compounds) and can react with Fe_2O_3 resulting in Fe(l) and CO(g) or CO_2(g) (Reactions 2 and 3) and these reactions are spontaneous according to the calculated Gibbs free energy (Fig. 8.19). Either CO or CO_2 formed in the porcelain samples during the firing process is sealed in the sample (in the bubbles) because of the high heating rates used (30 °C/min). Generally, CO forms at <500 °C [332,333] and reacts with other oxides. The CO continually reacts with Fe_2O_3 to form Fe(l) and CO_2 (Reaction 4).

The silica component (quartz) reacts either with solid carbon or CO gas, producing SiO gas (Reaction 5 and 6), this reaction is possible at ~1050 °C, according to the calculated Gibbs energy from Fig. 8.19. This SiO gas is then absorbed by Fe(l). At ~1000 °C, albite melts to form liquid aluminosilicate providing alumina and silica for mullite formation. Initially the mullite formed is silica rich because of absorption of SiO and later the alumina component diffuses to grow the mullite needles and increase their alumina content.

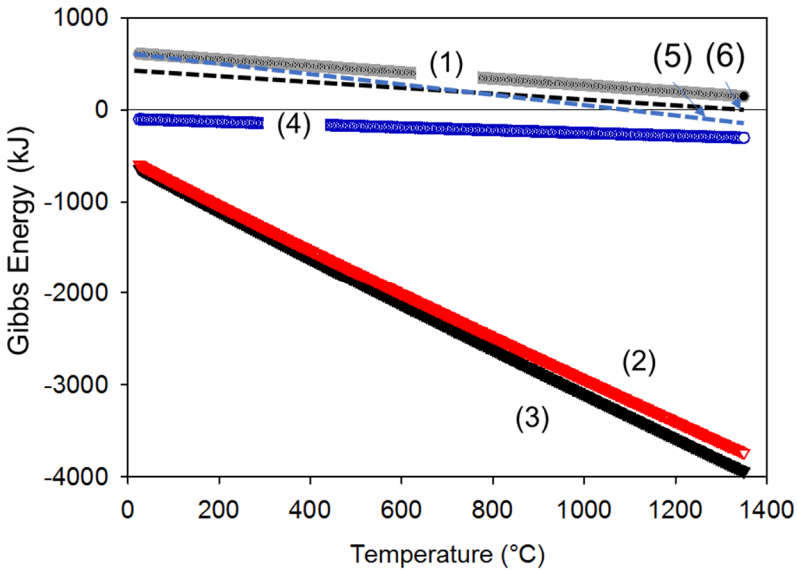

Figure 8.19: Gibbs free energy calculations presented for different possible chemical reactions of the Fe_2O_3, SiO_2 and TiO_2 and carbons, occurring from 25-1350 °C. Reaction 5 and 6 [333]. The total equilibrium gas pressure during the entire formation process was assumed to be constant at 1atm.

In contrast, reaction via TiO_2 (Reaction 1) is not possible since the Gibbs energy calculation shows positive value over the studied temperature range, but it could be feasible above 1700 °C, which is confirmed by the fact that Ti is not observed in the EDS data in Fig. 8.18.

Fig. 8.20 summarises the steps of fibrous mullite formation via the VLS mechanism proposed in this study.

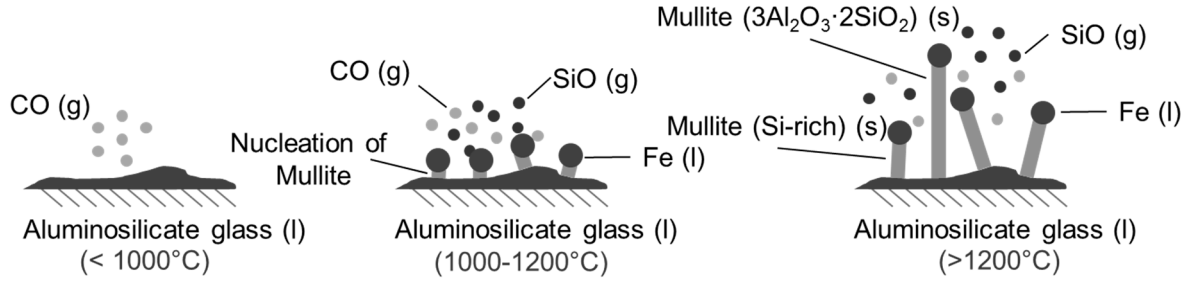

Figure 8.20: Schematic illustration of the VLS formation mechanism of the fibrous mullite.

8.8 Conclusions

Porcelain samples are fully sintered using microwave radiation at 1100 °C, a temperature 75 °C lower than when using a conventional sintering process. Liquid started to form at ~800 °C under microwave radiation while ~950 °C is required using conventional sintering.

MWSed samples have maximum ABD (2.36±0.03 g/cm^3) at 1100 °C, WA varied from 0-3 % from 950-1200 °C. MWSed also have Vickers hardness about 5.6±0.2 GPa, and fracture toughness of 4.8±0.2 MPa·m$^{1/2}$, all of which resulting from a combination of the density and mineralogical composition.

Mullite, moreover, formed under microwave radiation had small crystallite size (~76 nm) but high aspect ratio (>30:1) compared to mullite from the conventional process. Mullite chemistry in both samples was slightly different; the microwave sintered samples had higher alumina content (~63 mol.%) while conventionally sintered samples had stoichiometric mullite (~60 mol.%). Both mullites, however, had orthorhombic crystal structure. Formation of mullite was enhanced by microwave energy and may also arise via a vapour -liquid- solid mechanism.

Porcelains have heterogeneous microstructures because of the complex interplay between their starting raw materials and sintering conditions. This heterogeneity has a positive effect on the mechanical strength of porcelains, through a mechanism of matrix reinforcement [42,272]. However, the porosity plays a role in mechanical strength which must be controlled carefully. Fully dense commercial porcelains generally contain about 5 vol.% residual porosity, but 0% water absorption [42,272].

Hardness and fracture toughness measurements were made in local dense areas of the porcelain samples. They may not exactly describe the bulk property of the porcelain, but they are a reasonable representation of the bulk property.

Chapter 9

Preliminary study of the effect of FS on porcelain

9.1 Chapter review

This chapter examines flash sintering of porcelain. Several experiment conditions, combinations of applied electric field and furnace temperature, were attempted but only two experiments were successful. Nonetheless, these gave a good picture of the effect of flash sintering on densification, and mullite formation in porcelain. Even though, the actual mechanism of flash sintering is still under debate, this study shades light on a possible mechanism occurring during flash sintering of porcelain.

9.2 Flash sintering of porcelains

Fig. 9.1a presents the experimental conditions attempted in this study, highlighting when a flash event occurred. To achieve the flash event, a combination of furnace temperature of 950-1000 °C and applied electric field of 1.5 kV/cm were used. Since optimal conventional firing temperature of this porcelain is 1175 °C, a lower maximum furnace temperature of 1000 °C was used with the electric field. Higher electric fields (>1.5 kV/cm) were not possible because of the voltage limit of the power supply. However, it can be seen from Fig. 9.1a that to achieve flash sintering of this porcelain body, an electric field of at least 1.5 kV/cm and temperatures over 950 °C were required. This is likely because of the low electrical conductivity of this porcelain compact (10^{-4} S·cm^{-1}) in the temperature range 800-950 °C (presented in section 5.7). Therefore, from now on only results from two flash sintered samples will be analysed and discussed.

Fig. 9.1b reveals a sample surface after flash sintering at 950 °C and 1.5 kV/cm. Well-sintered and overfired regions could be observed. The well-sintered area contains mainly glassy phase while the overfired area (containing bubbles) was developed underneath the Pt-wire. This microstructure suggests that there are temperature gradients across the sample which might be associated with heat localization.

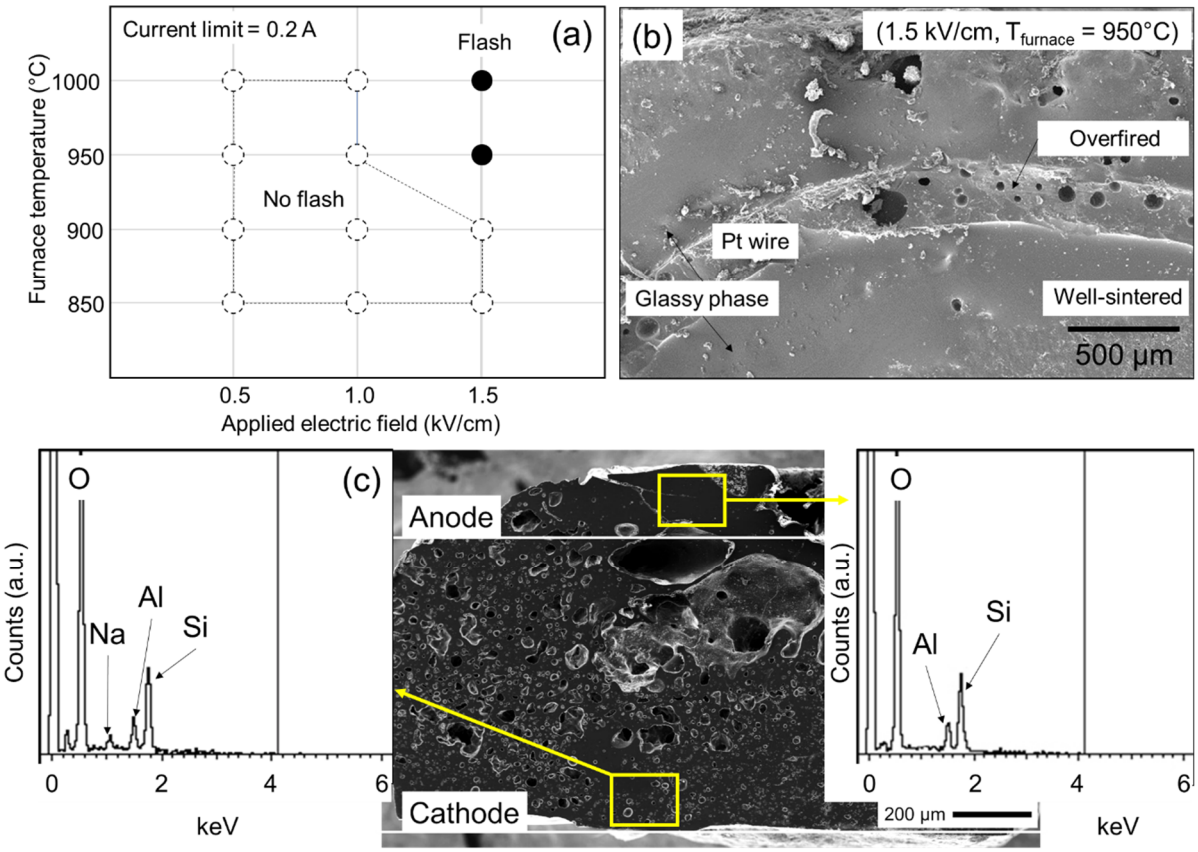

Figure 9.1: (a) Diagram showing experimental conditions explored in this work. (b) SEM microstructure of the flash sintered porcelain at 950 °C using 1.5 kV/cm. (c) SEM cross section microstructure (anode-cathode) with EDS result.

The sample temperature estimated using Eq. 4.31 (addressed in section 4.18.4) was ~1265 °C, which corresponds with the surface temperature. However, temperature in the area surrounding the Pt wire could be higher (it is the region of highest power dissipation), due to the low thermal conductivity of porcelain in this temperature range (2.40 W/m·K at 1150-1200 °C, presented in section 5.6) so that little heat dissipated to the adjacent area, resulting in a temperature

gradient. Calculations by Zapata-Solvas et al., [65] highlight the possible thermal gradients present during flash sintering as a consequence of electric current localization, which have the potential to melt the material. These observations agree with the observed microstructures in Fig. 9.1b. Although there is still debate about the mechanisms responsible for flash sintering, it could be assumed that higher temperatures might be required to produce sintering in shorter times, which agrees well with diffusional theory and results shown by Zapata-Solvas et al., [65]. Nonetheless, the calculated sample temperature for the external surface (~1265 °C) is above optimum porcelain sintering temperature producing an overfired microstructure.

Round pores were found next to the Pt wire, area with the highest temperature in the sample indicating overfiring, suggesting that the amount of local heat was too high to produce a well sintered porcelain microstructure. Moreover, SEM images in Fig. 9.1c shows that the main phase produced near the cathode and anode is the glass phase. The EDS analyses were done to determine the chemical composition near the cathode and anode (not the mullite needles). Fig. 9.1c shows high level of Na^+ ions at the cathode suggesting that cations are mobile in the aluminosilicate glass melt and they move towards the cathode as confirmed by EDS results (since the amount of sodium in the composition of the starting raw material is low, the 20 kV of the accelerating voltage was used to obtain sodium in large interaction area).

9.3 Power dissipation

Fig. 9.2 shows the applied voltage and current signal from the experiment held at 950 °C. It can be seen that the applied electric fields of 0.5-1.0 kV/cm (100-200 V) did not generate current to trigger a flash sintering event (current spikes when changing the voltage could be attributed to signal noise). The flash event occurred when the applied voltage reached 1.5 kV/cm (300 V) at which point the current rose to the current limit of 0.2 A. It should be noted that the interval time of each applied field was 60 s. During the flash event, the voltage was observed to drop while the current still remains on the 0.20 A limit, which gradually decreases with time (Fig. 9.2b). This could be related to the fact that the sample is heterogeneous composed of partially melted albite, metakaolinite, and quartz,

which have different electrical behaviour and could facilitate current localization through a melted phase. In other words, the resistivity of a liquid (molten albite) is relatively low compared to a solid due to higher charge carrier mobility, so ions and electrons could move readily through the liquid glassy phase.

A material which starts as an open circuit (applied voltage with no current flow) followed by a sharp current spike generates dielectric breakdown phenomena [334]. The flash event could be described as a dielectric breakdown followed by a thermal runaway as a consequence of the Joule heat being dissipated in the system. Microstructural mechanisms are under investigation and are still a matter of some debate in the flash sintering community, but they should be compatible with the macroscopic observation of dielectric breakdown and Joule heating.

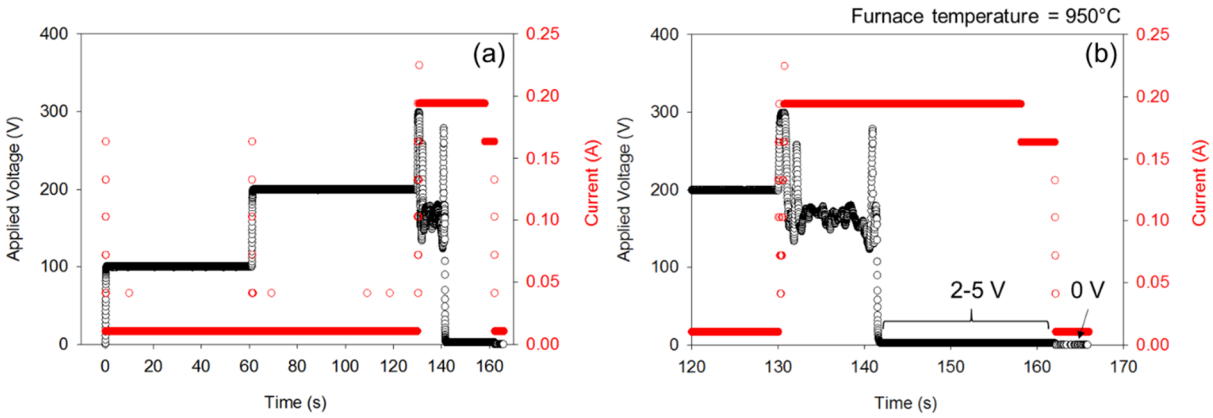

Figure 9.2: Electric field and current during the flash sintering at furnace temperature of 950 °C, (a) 0-165 s, and (b) 120-165 s.

Fig. 9.3 takes a closer look at the voltage and current signal associated with a series of images from the CCD camera showing the flash event as a function of time during current control regime (1.5 kV/cm). At the first current spike (1), it is believed that the increase in current was signal noise as previously observed at 100, 200 V (Fig. 9.2a). At point (2), the current increased abruptly to the current control limit while the applied field was constant. This is commonly observed in a flash sintering event and it is related to the process used to trigger flash sintering (at constant electric field).

During the holding period (131-135 s) (Fig. 9.3), a fluctuation of the applied voltage to maintain the constant current was present indicating the change of sample resistivity, which could be a consequence of temperature increase in the sample during the flash. Since, temperature increases, the resistivity of the sample decreases, which means that for the same current, a lower voltage is exhibited. As discussed in section 5.7, Na^+, K^+, Ca^{2+}, and Fe^{3+} ions are the charge carriers in the porcelain sample at high temperature. Thus, electrical resistivity changes are expected during porcelain microstructure development as it is a multiphase material. In other words, the electrical resistivity of the porcelain decreases as temperature increases because of the presence of liquid phase (melting of feldspars), and mullite. Moreover, there could be a contribution from the electrode polarization, which might alter the output voltage [335].

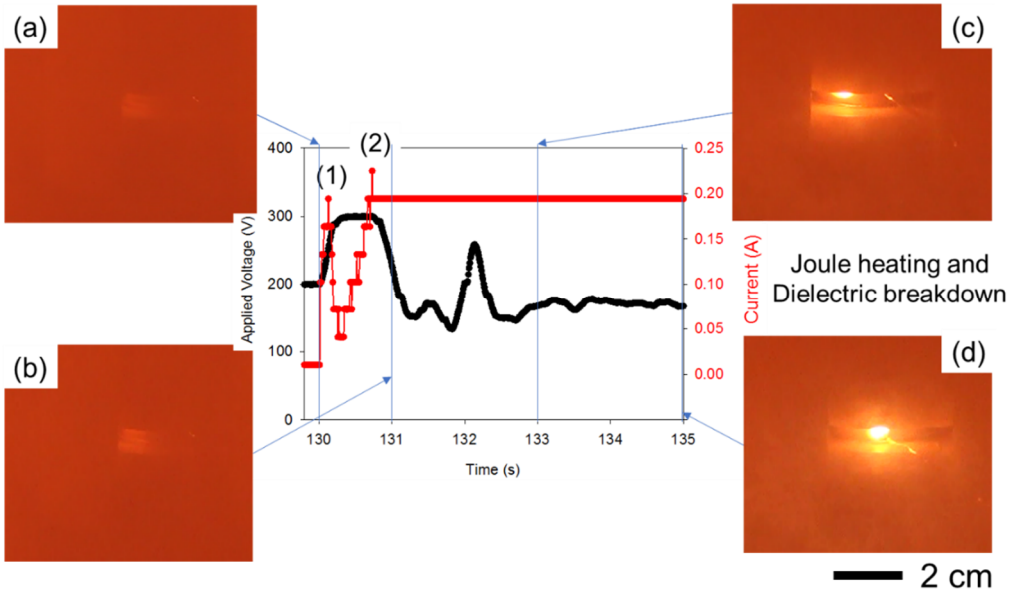

Figure 9.3: A series of images taking during the flash event of the sample flash sintered at 1.5 kV/cm under a constant furnace temperature of 950 °C. (a) indicates initial Joule heating occurred simultaneously when 1.5 kV/cm was applied, while (b-d) indicate the sample continues glowing once the current limit reached 0.2 A.

9.4 Microstructure and mullite formation

Fig. 9.4 shows etched microstructures of a FSed sample at a furnace temperature of 950 °C under 1.5 kV/cm. Distinct regions were observed, which were regarded as 'clay-rich' and 'glass-rich' (Fig. 9.4a and b respectively).

Interestingly, the etched microstructure reveals a large number mullite nuclei in the glass-rich region and they nucleated uniformly (Fig. 9.4b). The mullite nuclei population in the glass-rich region (Fig. 9.4b) was counted as ~120 nuclei/100μm^2, while 210 nuclei/100μm^2 were found in the clay-rich region (Fig. 9.4a). High level of alumina and silica available in the clay-rich region produces a greater mullite population as observed in Fig. 9.4a and b.

However, mullite nuclei formed in the glass-rich region had larger diameter (47±5 nm) than those observed in the clay region (33±4 nm). The faster diffusion of Al^{3+} and Si^{4+} in supersaturated of molten glass is responsible for the larger mullite nuclei in liquid glass.

In addition, Fig. 9.4d-g highlights that mullite nucleated in the liquid glass can grow rapidly and with a higher aspect ratio compared to mullite formed in the clay-rich regions.

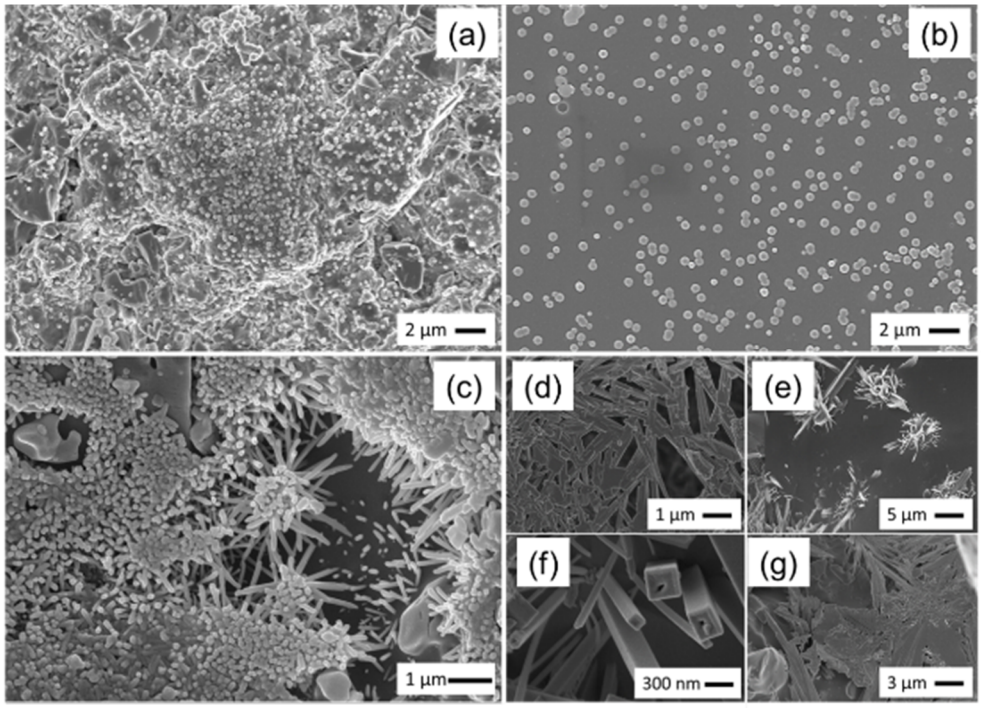

Figure 9.4: SEM images of a sample sintered at 1.5 kV/cm at 950 °C furnace temperature. (a) mullite nuclei formed in clay-rich region, (b) mullite nuclei formed in glass-rich region, (c) mullite needles growing in clay-rich region, (d-g) mullite growing in the glass-rich region having different morphologies. This sample was etched using 5% HF for 10 s.

Several mullite morphologies were observed in Fig. 9.4d-g. This observation suggests that mullite formed in the liquid glass melt is dependent on the degree of the supersaturation of alumina in the liquid glass, while mullite formed in the clay-rich region should be similar to mullite formed in a conventional sintering process because the mullite found in clay relicts forms by decomposition of clays.

Fig. 9.5 presents two distinct mullite morphologies formed in the glass. The two different morphologies were related to the degree of supersaturation of alumina, which alters mullite formation mechanism. The 'elongated crystallite mullite' (Fig. 9.5a) was formed at low level of alumina supersaturation while the 'dendritic mullite' (Fig. 9.5b) was formed at high alumina supersaturation. The transition point of elongated/dendritic mullite is explained by Kossel-Stranski and Burton-Carbrera-Frank's models [336,337].

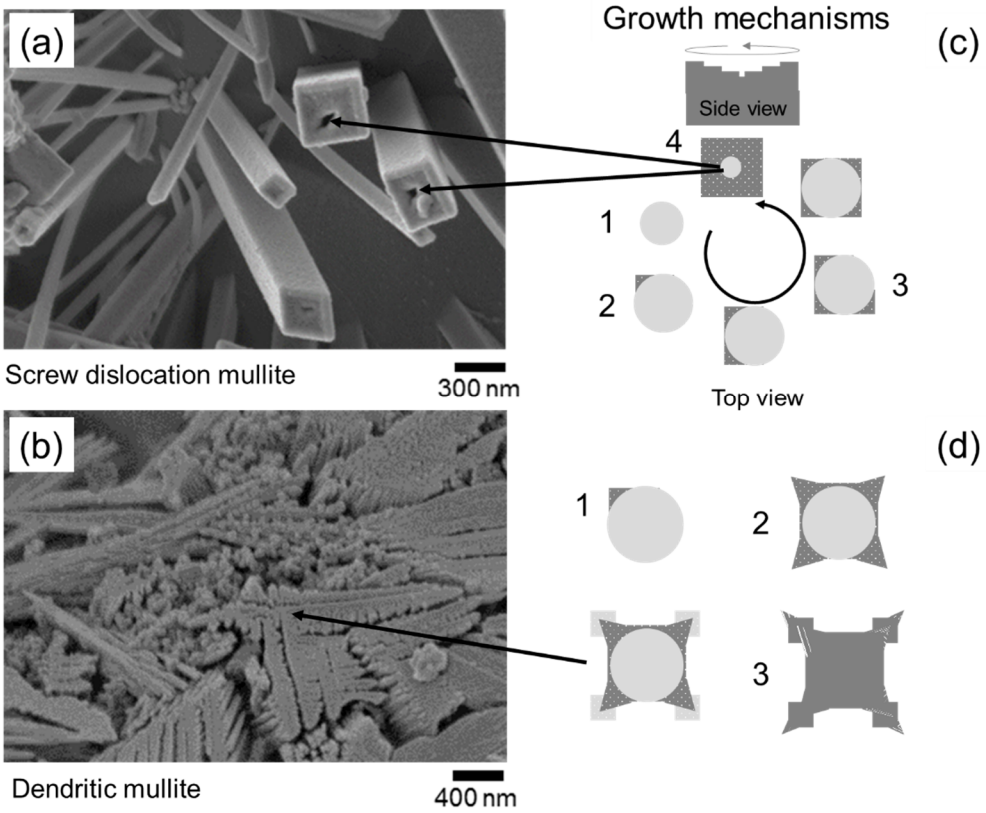

Figure 9.5: SEM images of (a) elongated mullite found at low alumina supersaturation, (b) dendritic mullite found in high alumina supersaturation. Schematic diagram showing mullite formed in the liquid glass via different growth mechanism, (c) screw dislocation mullite, and (d) dendritic mullite. Grey circle represents a mullite nuclei, and dark grey areas are the new layers.

According to the crystal growth theory, the growth morphology of crystals is a function supersaturation. If the supersaturation of the specie of interest (i.e. alumina in mullite) is less or equal to the critical value, the crystals grow via a screw dislocation mechanism (Burton-Carbrera-Frank's model). On the other hand, if the supersaturation of the specie of interest is higher than the critical value, the crystal growth is controlled by the two-dimensional growth (Kossel-Stranski model) [336]. The critical value of supersaturation is the point that nucleation occurs instantaneously.

Above the critical value, Kossel and Stranski explained that crystals grow by incorporating new atoms onto the crystal surface, layer-by-layer in 2-dimensions. The new atoms incorporate onto the crystal surface at one of three sites: ledges, steps or kinks but incorporation at the kink site is the most favourable. This 2-dimensional growth occurs only at relatively high supersaturation when random nuclei are generated on existing flat surfaces [338]. In other words, Kossel and Stranski model suggests that crystal growth is dependent on surface nucleation.

Below the critical value, Burton, Carbrera, and Frank explained that the Kossel and Stranski's model is based on the perfect flat crystal surface [337]. To create a new layer on a flat surface, requires 2-dimensional nucleation and supersaturation approximately 50% (which is rare). However, the presence of dislocations in the crystals has a great influence on crystal growth because they are a source of new steps where atoms can be incorporated. Hence, growth can proceed at lower temperatures and supersaturations. Thus, the supersaturation of alumina plays an important role in the mullite morphologies observed in this study.

Fig. 9.5c reveals that mullite forms via screw dislocations because of the low alumina supersaturation. In other words, screw dislocation growth takes place when the supersaturation is not high enough to allow a new layer to nucleate on a flat mullite surface. The mullite growth starts with small circle nuclei (Fig. 9.5c,1), the mullite grows firstly at the corner because the corners and edges of the mullite contact with a greater volume of liquid phase than the face centres (Fig. 9.5c,2), so the supersaturation of alumina at these regions is higher. The new

layer then start at the edges and corners of a crystal face, and then spreads toward the centre region (Fig. 9.5c,3). However, since the formation of mullite in the FSed sample is fast (3s during the flash event), a residual hole at the centre of the mullite needles is observed (Fig. 9.5c,4).

Fig. 9.5d reveals dendritic mullite at high alumina supersaturation. Because of the high supersaturation, new layers form at the edges and corners of the mullite nuclei (Fig. 9.5d,1) and protrude into the liquid glass (Fig. 9.5d, 2-3), rather than spread across the face.

The EDS result in Fig. 9.6a suggests that the rapid temperature increase in FS produced non-uniform and out of equilibrium chemical distributions in the liquid glass melt resulting in different supersaturation levels of alumina. High alumina supersaturation (dendritic mullite) with 7.19±0.36 wt.% alumina (point 004 in Fig. 9.6a) is found in the well-sintered area which at temperature is liquid (albite melts so that all alumina from albite is in the liquid phase) producing high levels of supersaturation of alumina.

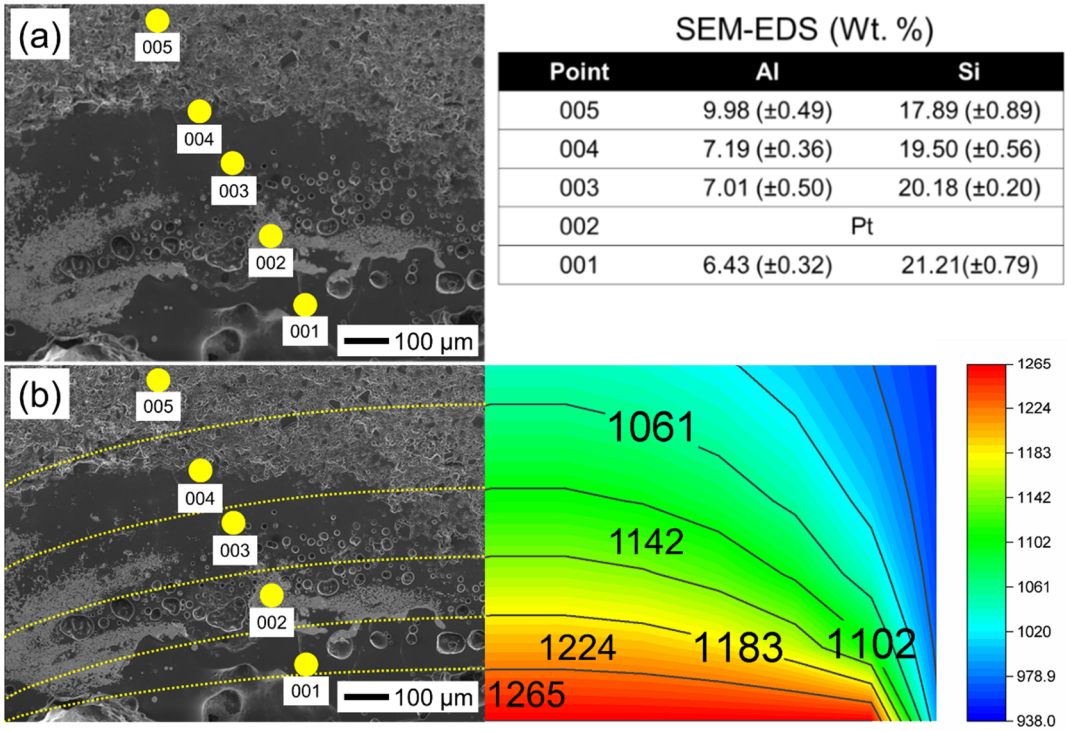

SEM-EDS (Wt. %)

Point	Al	Si
005	9.98 (±0.49)	17.89 (±0.89)
004	7.19 (±0.36)	19.50 (±0.56)
003	7.01 (±0.50)	20.18 (±0.20)
002	Pt	
001	6.43 (±0.32)	21.21(±0.79)

Figure 9.6: SEM with (a) EDS shows the level of supersaturation in different areas of the sample, and (b) FDA temperature shows temperature gradient in the FSed sample.

The temperature at point 004 is lower (~1110 °C) compared to well-sintered-point 001 in Fig. 9.6a. The elongated mullite found in point 001 with 6.43±0.32 wt.% alumina is at the low alumina supersaturation because the temperature is high (~1265 °C in Fig. 9.6b) resulting in increasing of silica level from quartz dissolution. The FDA is also employed to determine temperature gradient in the FSed sample showing different alumina supersaturation.

However, since the electric field was high (1.5 kV/cm), it might be reasonable to postulate that different supersaturation levels could be induced by high mobility under an electric field of different species present in the system. In addition, Fig. 9.5a shows a hollow mullite morphology, which suggests that a screw dislocation mechanism was responsible for the formation of hollow shapes [338].

The heterogeneity (non-uniform microstructure) in Fig.9.6 is due to the temperature variation in different parts of the sample. The different mullite morphologies in Fig. 9.4-9.5 and variation of microstructure in Fig. 9.6 suggest that this porcelain sample did not reach thermodynamic equilibrium because they were sintered very rapidly, so that most reactions during sintering were not completed. However, most of the porcelain products from fast firing processes (i.e. 60-90 min cold-to-cold) are non-equilibrium because thermodynamic equilibrium is not achievable [42,271]. Further work is needed to show how these microstructures and different mullite morphologies produced by FS process affect the final property of the finished products.

9.5 Further results and discussion

9.5.1 Electric field enhances mullite formation in porcelain

A CSed sample with identical chemistry (temperature of 1175 °C, heating rate of 5 °C/m, and 15 min dwell) was produced to compare the effect of electric field on mullite formation (Fig. 9.7). It is clear that the electric field accelerated mullite nucleation in the liquid glass melt because a small number of mullite nuclei (<10 nuclei/100μm^2) was observed in the CSed sample while ~120 nuclei/100μm^2 in FSed sample. Thus, mullite formation in porcelain under flash sintering is worthy of further investigation and highlights the effect of an electric field on the mobility of charge carriers in a liquid phase.

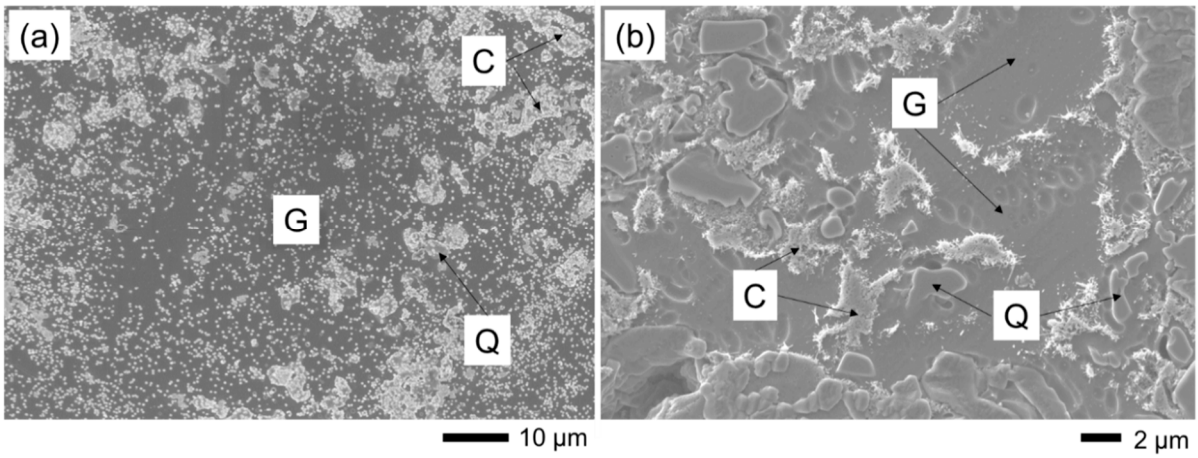

Figure 9.7: Comparison of porcelain microstructures sintered using different process. (a) FSed sample was fabricated at 950 °C under 1.5 kV/cm, (b) CSed was fabricated at 1175 °C, 5 °C/min, 15 min dwell, (C is clay, G is glass, and Q is quartz).

9.5.2 Alkali ions migration under electric field

According to Fig. 9.1b, the round pores were found only underneath the Pt wire, which might suggest that they may not result from the overfiring. Another possibility could be that the round pores may be produced via an electrolytic reaction of free oxygen ions, produced during the melting of albite. At the anode, in which gaseous oxygen was produced as presented in Eq.9.1 [339].

$$O^{2-} \rightarrow \frac{1}{2}O_2 + 2e^- \tag{9.1}$$

Fig. 9.8a shows the elemental mapping across the sample in the area between the anode and cathode. The two distinct microstructures, well-sintered (L1:left) and under-sintered (L2:right), result from the non-uniform sintering as previously mentioned in section 9.2.

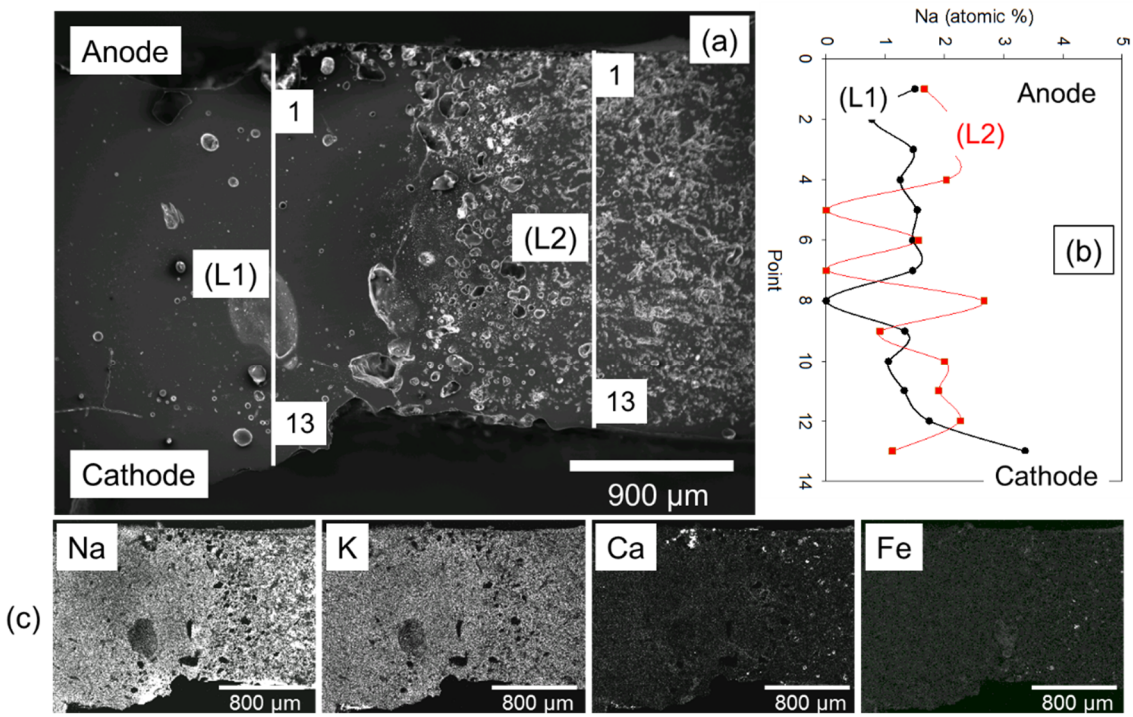

Figure 9.8: SEM with EDS presents the level of supersaturation as a function of temperature gradient in the sample. (a) the cross section of the FSed sample at the furnace temperature of 950 °C showing EDS lines at well-sintered (L1) and under-sintered (L2), (b) the move of Na^+ ions to the cathode (black line), and (c) EDS mapping of cations.

In the well-sintered area, elemental analysis was conducted labelled as L1, from which 13 points were collected along line L1. L1 reveals the Na^+ ions move towards the cathode, which is evident in Fig. 9.8b and c. The L2 line, on the other hand, presents elemental analysis of the un-sintered area. It suggests that there is no difference in Na^+ ion concentration across the porcelain sample. The movement of the Na^+ ions found in the well-sintered area is evidence that the Na^+ ions are more mobile in the liquid glass and easily move towards the cathode under the applied electric field and this movement produces ionic current inducing Joule heating and sintering the porcelain sample.

A similar observation was made by MacKenzie and Brown [340] who concluded that by applying an electric field of 10^3 V/cm, alkali metal ions (i.e. Na^+ and K^+) in aluminosilicate glass (solid glass) migrated to the cathode resulting in an electrolytic mechanism, but migration of Al^{3+} and Si^{4+} was not found. They also proposed that the overall electrolytic mechanism involved the movement of

vacancies, alkali ions and protons to the cathode, and free oxygen towards the anode [340].

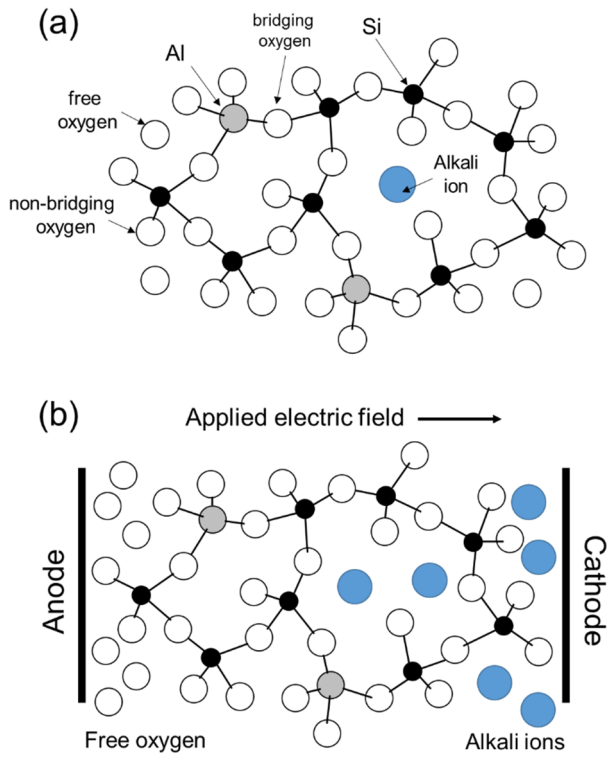

Figure 9.9: (a) Structure of the albite melt producing non-bridging oxygen and free oxygen, (b) movement of free oxygen towards anode and alkali ions towards cathode [adapted from Ref. 340].

Fig. 9.9 schematically represents the structure of the melt which is in a disordered 3D network having network formers (Si), intermediates (Al), network modifiers (Na^+, K^+, and Ca^{2+}), bridging oxygens (O) and non-bridging oxygens (O^-) making up the tetrahedra network, and free oxygens (O^{2-}), which are not part of tetrahedra (Fig. 9.9a). The melt is flexible and can rearrange itself through the random motions of atoms and molecules.

Under an applied electric field condition (Fig. 9.9b), alkali ions (or other cations) move towards the cathode while free oxygens (O^{2-}) move as an interstitial toward the anode [309]. Moreover, the bubbles found underneath the Pt-electrode (anode) are likely to have resulted from the electrolytic mechanism as suggested by Eq.9.1. Varshneya [339] also suggested during the migration of alkali ions, the glass structure is modified, and free oxygen is produced by combination of two non-bridging oxygen forming free oxygen then moving towards the anode. This

suggests strongly that the bubble formed near the anode arise from migration of the free oxygen and produce gaseous oxygen via an electrolytic reaction.

9.5.3 Proposed flash sintering mechanism in porcelains

The flash event in porcelain may be caused by either Joule heating or dielectric breakdown or both. With the present experimental setup, it was observed that the abrupt increase of current (<1 s, see Fig. 9.3) should result from dielectric breakdown rather than Joule heating because the electric current increased abruptly which is the result of a disruptive discharge (breakdown) of the minerals in the porcelain.

In general, a gradual increase in the electrical conductivity is usually observed before a flash sintering event [90,341,342], which makes Joule heating controllable. In this work, in contrast, the abrupt increase of electric current caused by electrical breakdown made control of Joule heating difficult.

In addition, at 950 °C, partial melting of albite was observed, and it was assumed that a thin layer of this liquid glass covered most of the solid particles throughout the porcelain sample (see section 5.4 and 5.7). The liquid glass film should act as a conductive path generating a flow of current [63]. At this point, Na^+, K^+, and Fe^{3+} should contribute to electrical conduction but the current was not detected when the applied electric potential was lower than 1.5 kV/cm. At the higher furnace temperature of 1000 °C when more liquid glass expected, the ions should move more freely producing flow of current. However, there was still no sign of conduction once the electric potential was applied.

Even dielectric breakdown of these minerals (quartz, feldspar, and kaolinite) is in a high range of 10^5-10^7 MV/cm at room temperature. Thus, at the relatively high temperature of 950 °C, the breakdown voltage must be lower than that. Biesuz et al., [343] explained that the presence of pores and their shape can enhance local electric field strength of solid/air interface, which is expressed by Eq. 9.2.

$$E_c \sim e^{-bP} \qquad 9.2$$

where E_c is critical electric field strength, b is a constant depending on pore size and shape, and P is fraction of porosity. From Eq. 9.2, E_c decreases as porosity increases, and pore shape becomes more complex.

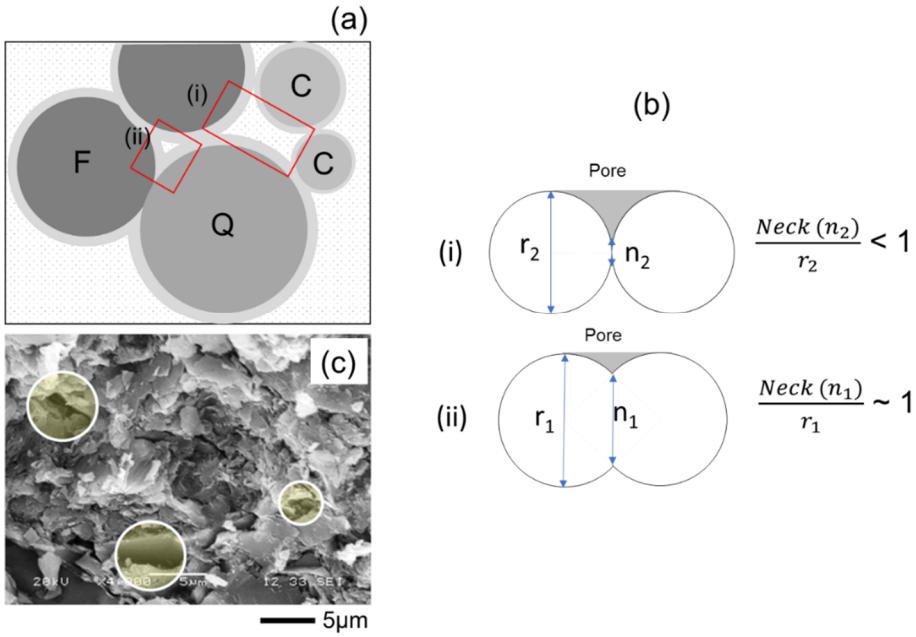

Figure 9.10: Schematic diagram explaining the local field enhancement by pores, (a) contacts between particles producing different triangular pores (Q is quartz, F is feldspar, C is clay), (b) pore size and shapes influencing E_c, (c) SEM of green porcelain heated at 950 °C showing complex pore shapes (circled).

Fig. 9.10a is a schematic illustration of the green porcelain compact composed of feldspar (F), quartz (Q), and clay (C) particles. When the particles contact each other, they form pores with different shapes i.e. small triangular pores (Fig. 9.10a, ii) and large irregular pores (Fig. 9.10a, i). Enhancement of E_c can be explained by the ratio of the particle size and the neck [343]. The ratio between neck (n) and particle (r), which is less than 1 (Fig. 9.10b, i) can enhance the local electric field, decreasing E_c and vice versa. In addition, Fig. 9.10b, ii suggests that in the case of sintered samples (large neck formation, n_1), the local field is not intensified, so E_c is not decreased.

In the case of the porcelain pellet used in this experiment, the pore shapes were complex, and the volume fraction of the pore was about 25±1 vol.% at 950 °C (Fig. 9.10c), the breakdown voltage of the porcelain sample should be lower than

that at room temperature, so the high voltage of 1.5 kV/cm applied to the porcelain may be large enough to trigger dielectric breakdown. Thus, it can be deduced from the abruptly increasing electrical current and reducing E_c due to porosity that flash sintering of porcelains was likely due to dielectric breakdown.

9.6 Conclusions

Flash sintering in porcelains is complex as they are is a multicomponent material containing i.e. quartz, feldspar, and clays. Microstructures developed during flash sintering of porcelain are a consequence of the formed liquid glass phase, which provides a conductive path producing a non-uniformly sintered sample. During a flash event, the electric field increases mullite nucleation and altered the mullite formation mechanism by producing different supersaturation levels of alumina in the liquid glass phase.

The different supersaturations produce different mullite morphologies. Insights into the flash sintering process for examination of porcelains highlights the need for further investigation of viscous flow sintering under applied electric field of composite materials and its effects on microstructure development.

Chapter 10

Further results and discussion

10.1 Chapter review

This chapter compares in greater depth densification, microstructure, mullite formation, mechanical property, and energy consumption of all the sintering techniques studied. Porcelain densification behaviour for the three processes (DS, SPS, and MWS) was compared to that from CS. Flash sintering was not included since the density of the sample could not be obtained because the well-sintered area was too small (<2x2 mm^2) to measure the density. Polished surfaces as well as etched surfaces were examined to compare mullite formation. The amount of mullite formed by the different sintering techniques is also discussed. The mechanical properties (Vickers hardness and fracture toughness) of the sintered samples are discussed. Finally, the energy consumption of the different densification processes is compared based on the actual energy measured and reported as the specific energy consumption (SEC). Limitations of applying the rapid sintering techniques on the industrial scale are also addressed.

10.2 Comparison of densification behaviour

Densification behaviour, density and densification rate, of the porcelains sintered under the different sintering techniques are shown in Fig. 10.1. Fig. 10.1a shows density of the porcelains as a function of temperature revealing different onset temperatures while all peak temperatures (which produce maximum density by each process) are between 1100-1200 °C. SPS produced the highest ABD (2.46±0.01 g/cm^3) resulting from the applied pressure, MWS process produced

similar density to the CS process (2.36±0.03 g/cm^3 and 2.38±0.01 g/cm^3 respectively) but densification of MWS starts at lower temperature (~950 °C). DS produced similar density (2.36±0.01 g/cm^3) compared to CS. Interestingly, once maximum densities are achieved, they all decrease as a result of bloating.

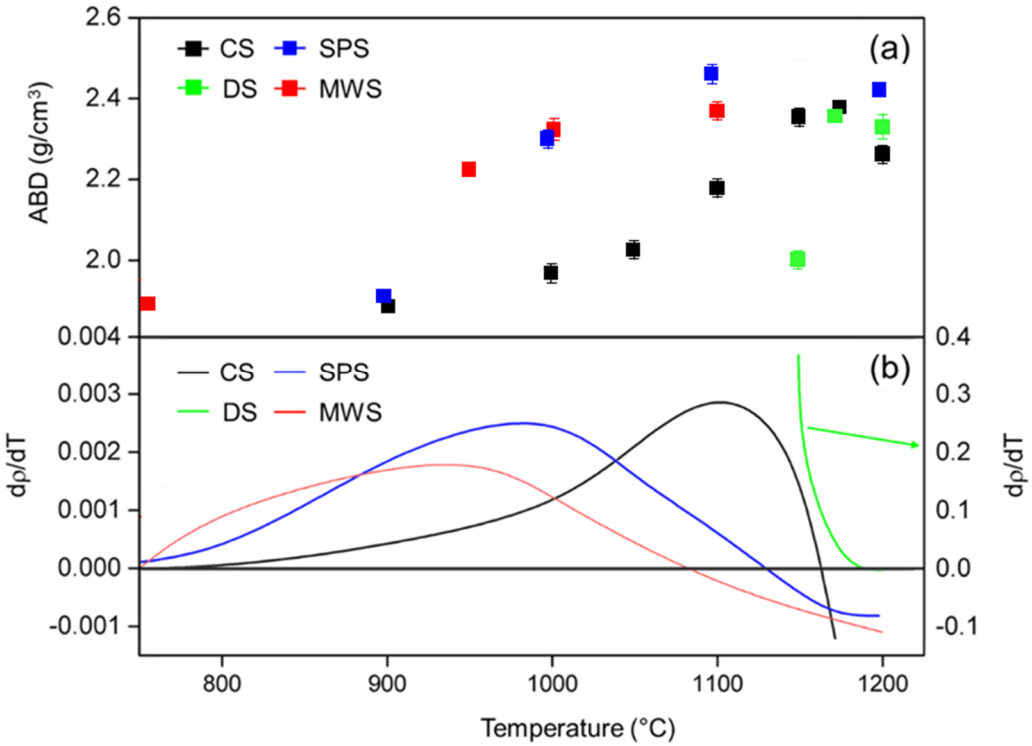

Figure 10.1: (a) Comparison of densification behaviour of porcelains sintered using different techniques, (b) densification rate (dρ/dT) of each process.

The densification rates in Fig. 10.1b are different. The onset temperature of the sintering processes, when densification starts, also varies. For example, the onset temperature of the densification in SPS is 900-1000 °C while it is 1000-1100 °C for CS and the onset temperature of MWS is 900-950 °C. Interestingly, densification rate of the DS process (green line) is the greatest among these processes starting at 1150 °C and finishing at 1200 °C. Note that densification rate during CS and DS is higher than during SPS because the rate is accelerated over the SPS cycle with an initial densification below 600 °C (as discussed in section 7.7.1).

Densification of the porcelain in the SPS process is enhanced by the applied pressure and requires little amount of the liquid glass, which is compared to the

CS process, to obtain maximum density (as discussed in section 6.4 and 7.2). Once the liquid glass is produced, it rapidly fills the voids between the solid particles resulted from the applied pressure so producing rapid densification.

MWS produced dense porcelain at lower temperature starting from ~900 °C, believed associated with lower temperature feldspar melting due to the microwave effect. However, it is important to note that the energy required to melt feldspars is thermodynamically limited regardless of the energy input routes. Thus, the temperature of feldspar melting cannot be lower than their melting points. Watanabe et al., [344] observed that on microwave sintering of a porcelain, liquid started to appear at 900 °C, which is approximately 220 to 250 °C lower than the melting point of feldspars. Their experiment showed that the temperature of feldspars was higher than 900 °C, which was explained by selective heating in a microwave. In other words, the temperature of the porcelain sample was measured over a large scale, which represents the average temperature of the sample, not locally at feldspar grains, where feldspars absorbed microwaves and reached higher temperature than the other constituents. The heat then dissipated to the surroundings producing an average sample temperature of ~900 °C.

Even though the melting temperature of feldspars does not change, the microwave energy can potentially enhance densification by a mechanism involving increased diffusivity. This is suggested by the high densification rate in MWS compared to e.g. CS (Fig. 10.1b). Microwaves could enhance the melting of feldspars because the major factor of porcelain densification is the production of liquid from feldspar melting. As mentioned in section 8.3, the loss tangent of the porcelain sample changes rapidly around 600 °C due to melting of albite thus, suggesting that microwaves enhance feldspar decomposition.

A study of microwave-assisted potassium feldspar decomposition confirmed that microwaves increase the dissolution of potassium ions from the feldspar structure [345]. The increasing in potassium ion dissolution can be explained by the caged molecule concept [346]. The caged molecule concept may enhance the decomposition of feldspars by rotation of the dipoles ($(Si,Al)O_4$ tetrahedra) leaving space allowing potassium ions to escape from the feldspar structure as illustrated schematically in Fig. 10.2.

Fig. 10.2 presents the concept of diffusivity enhancement by microwave energy proposed by Antonio and Dream [346]. They proposed a model of a molecule (the white oval), which is called a caged molecule, surrounded by a group of molecules (the grey ovals), which constitute the cage. The cage creates an inter-atomic potential around the caged molecule represented by the solid circle (Fig. 10.2b). In the model, the caged molecule has certain probability of jumping out of the cage as shown by the arrow going from left to right in Fig. 10.2b and c. Under normal conditions, molecules orient randomly (Fig. 10.2b) but under an applied microwave field, the molecules are all responding to the microwave field as shown in Fig. 10.2c. The alignment of the cage with the microwaves leads to decrease the average potential of the cage opening through which the caged molecule is more likely to pass, thus resulting in enhanced diffusion [346].

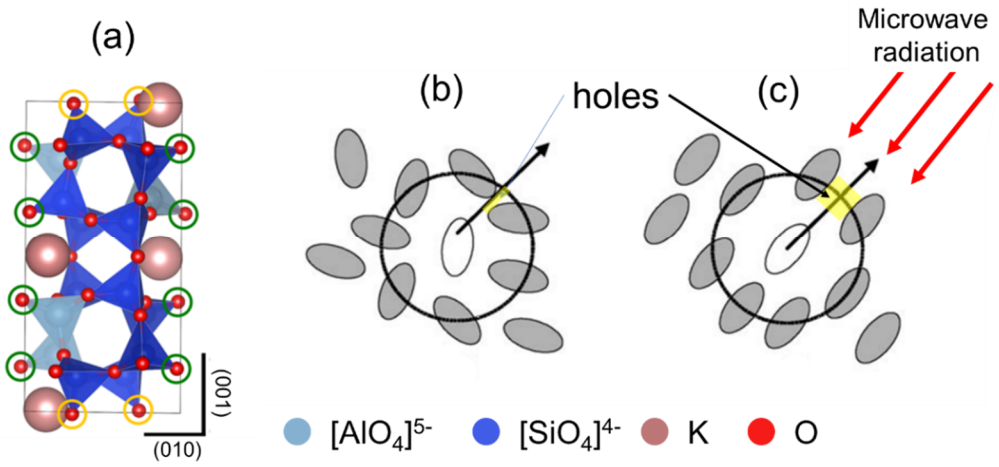

Figure 10.2: The cage model arrangement under (a) normal conditions and no microwaves and (b) under a microwave field. K^+ (pink) and Oxygen (red) arrange in $[AlO_4]^{5-}$ (light blue), $[SiO_4]^{4-}$ (dark blue) tetrahedra of microcline. A primitive unit cell contains $4AlO_4$ tetrahedra, $4K^+$ ions (to balance the charge), and $12SiO_4$ tetrahedra. Oxygens in the green circle are bridged to oxygens atoms at the (001) surface while oxygens in the yellow circle are bridged to the oxygen atoms at the (010) surface [adapted from Ref. 346 and 347].

The caged molecule model can be applied to feldspars, Fig. 10.2a represents the crystal structure of potassium feldspar. At the normal condition with no microwave radiation (Fig. 10.2b), the molecules ($[SiO_4]^{4-}$ and $[AlO_4]^{5-}$) in feldspars may orient randomly producing an internal electric field (the black circle) and

having small atomic space, so that sodium or potassium ions (the white oval in Fig. 10.2b) have little chance of escaping from the cage. As microwaves are applied the molecules response to the oscillating wave, producing sufficient atomic holes, allowing the ions to escape from the feldspar structure. Once sodium and potassium ions escape into the porcelain bulk, they behave like an ionic conductor in the porcelain under the microwave radiation producing excess heating of the porcelain bulk under microwave irradiation [344].

This model suggests that densification of the porcelain starts at lower temperature due to the microwave energy, which increases decomposition of feldspars, because they strongly absorb microwave energy. Densification starts early because the liquid phase (molten feldspar) fills the pores between solid particles pulling them together inducing densification.

10.3 Microstructures

Comparing the polished surfaces of porcelain samples sintered using different sintering processes is shown in Fig. 10.3. The polished surface of the DSed sample (Fig. 10.3a) is dense resulting from the glassy phase but there are significant numbers of residual pores (25±3 pores/100x100 μm^2, of size >20 μm) embedded in the glassy matrix producing 12.8±1 vol.% porosity. The SPSed sample (Fig. 10.3b) has similar polished surface to that produced by the DS process but there are fewer residual pores (10±2 pores/100x100 μm^2, of size >20 μm) having 1.5±0.5 vol.% porosity. Large craters (>100μm diameter) and pores (37±7 pores/100x100 μm^2, of size >20 μm) are found in the MWSed sample arising from overfiring (bloating). As mentioned in section 10.2, the temperature of the feldspars is higher than the average temperature of the sample which, along with an increase of sample loss tangent, leads to overfiring. However, considering the dense area of the MWSed sample (Fig. 10.3c), there are more pores (37±7 pores/100x100 μm^2, of size >20 μm) compared to the DSed and SPSed samples. The FSed sample (Fig. 10.3d) shows a different and heterogeneous microstructure with un-sintered and well-sintered regions. This resulted from the preferred sintering pathway, arising from the different electrical conductivity paths.

At high magnification SEM images (Fig. 10.3, bottom row) of the polished surfaces of all samples reveal similar features. All samples are dense due to

vitrification, and the only difference is in the numbers of residual pores (pore size >20 μm) including DS=25±3 pores/100x100μm^2, SPS=10±2 pores/100x100μm^2, MWS=37±7 pores/100x100μm^2, and FS=20±2 pores/100x100μm^2.

Although, porcelain has different densification behaviour when made through different sintering techniques, once it is fully densified regardless of the processing route, the polished surfaces are similar because the major phase, which dominates the densification of porcelains, is glassy phase (arising from vitrification). If sufficient glassy phase is produced a dense polished surface is obtained.

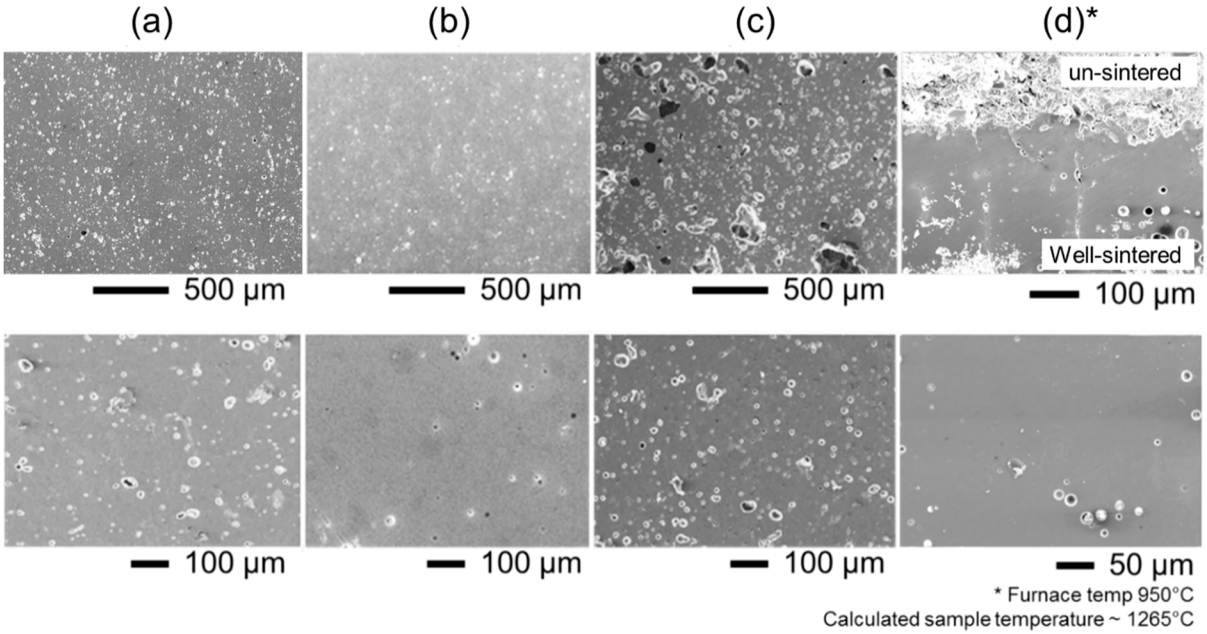

Figure 10.3: Polished surface of (a) DSed sample (1175 °C, 15 min dwell), (b) SPSed sample (1100 °C, 100 °C/min, 5 min dwell), (c) MWSed sample (1100 °C, 30 °C/min,5 min dwell), and (d) FSed sample (furnace temperature of 950 °C, calculated sample temperature of 1265 °C). Top row is low magnification, bottom row is high magnification.

10.4 Mullite formation from the different sintering techniques

Although polished surfaces of porcelain samples sintered by different sintering techniques are similar, the etched microstructures are different. Fig. 10.4 shows the etched microstructure of CSed and DSed samples, which illustrates two types of mullite formation. Type I (M_I) is the mullite formed from the clay relicts while type II (M_{II}) is the elongated mullite formed in the clay relicts

resulted from the interaction with the liquid glass during sintering. Type III (M_{III}) is found in the SPSed sample (Fig. 10.5) and formed in the liquid glass during sintering and occurs in the glassy matrix with elongated morphology.

In addition, the mullites needles in the SPSed sample orient perpendicular to the compressive plane as shown in the inset of Fig. 10.5 and previously discussed in section 7.7.3.1. in relation to the micrographs. M_{III} mullite is also found in the MWSed sample but with different morphology to that found in the SPSed sample. M_{III} in MWSed sample (Fig. 10.6) is believed to form via the VLS mechanism discussed in section 8.7.2. M_{III} in MWSed sample have the highest aspect ratio (>30:1) observed (see section 8.7.1) compared to that in the SPSed sample (15-22:1). The FSed sample (Fig. 10.7) contains all three types of mullite. FSed sample contains large amounts of mullite (discussed in section 10.5) in the clay relicts (M_I), large amounts of the elongated mullite (M_{II}) as well as mullite formed in the liquid phase during sintering (M_{III}). The schematic representations on the right-hand side in Fig. 10.4-10.7 illustrate the various mullite types found in the different samples.

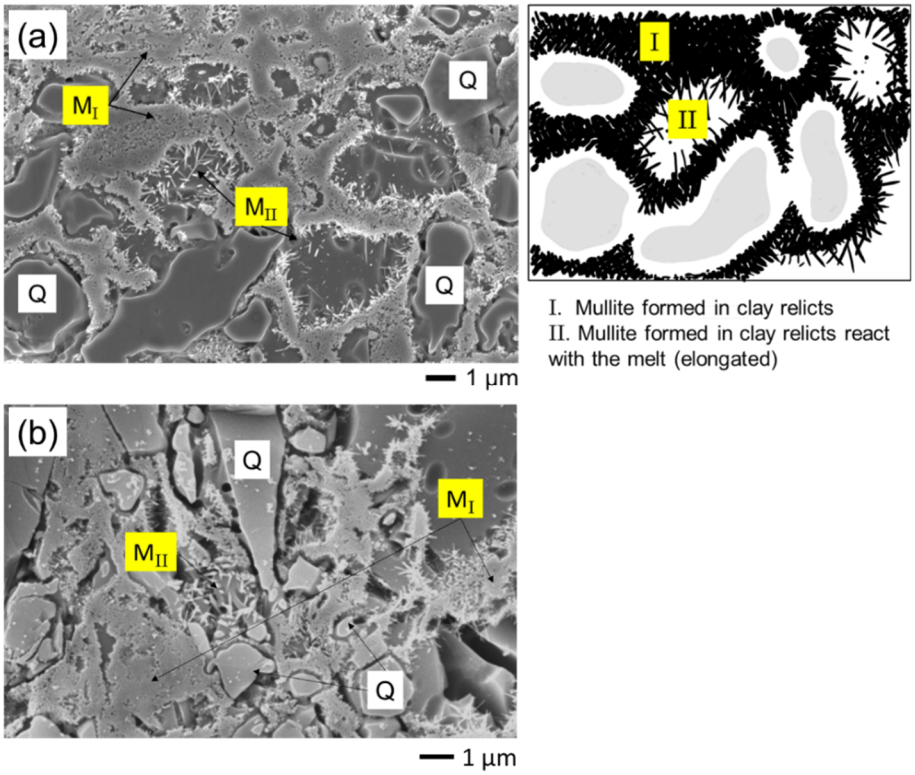

Figure 10.4: SEM image and schematic illustration of mullite formation in (a) CSed 1175 °C (5 °C/min,15 min dwell, and (b) DSed 1175 °C (15 min dwell) samples. M_I is mullite type I, M_{II} is mullite type II, and Q is quartz.

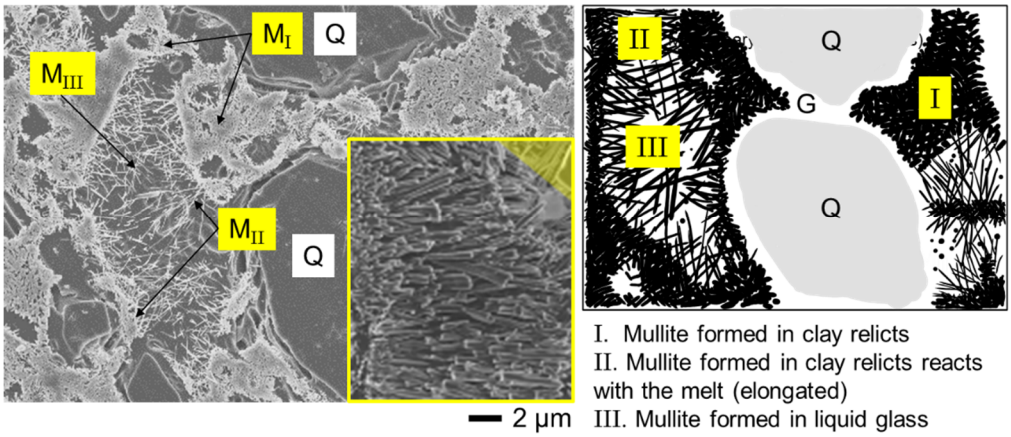

Figure 10.5: SEM image and schematic illustration of mullite formed in the SPSed 1100 °C sample (100 °C/min, 5 min dwell). M_I is mullite type I, M_{II} is mullite type II, M_{III} is mullite type III, and Q is quartz. Inset shows mullite orientation perpendicular to the SPS compressive plane.

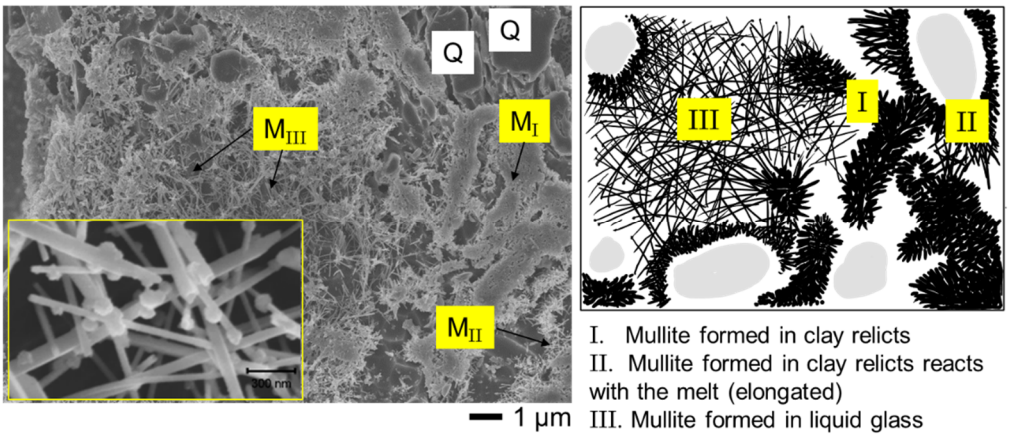

Figure 10.6: SEM image and schematic illustration of mullite formed in the MWSed 1100 °C sample (30 °C/min,5 min dwell). M_I is mullite type I, M_{II} is mullite type II, M_{III} is mullite type III, and Q is quartz.

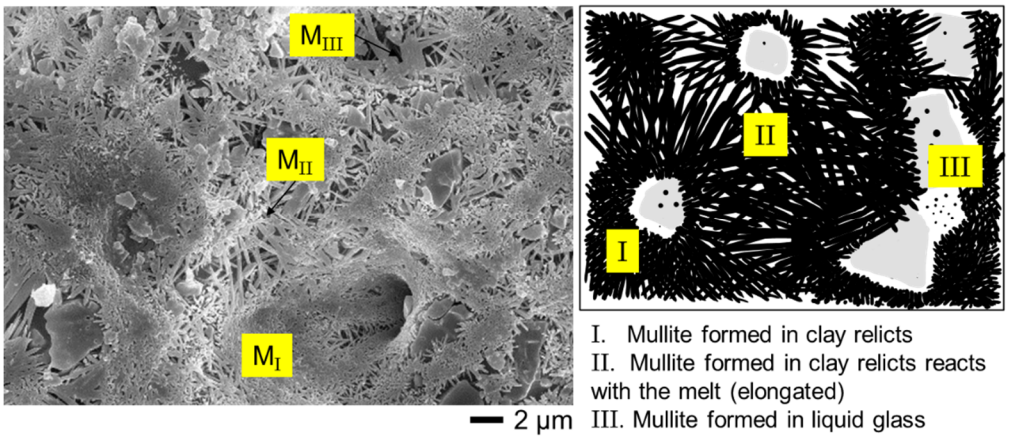

Figure 10.7: SEM image and schematic illustration of mullite formed in the FSed sample (furnace temperature of 950 °C and sample temperature of 1265 °C). M_I is mullite type I, M_{II} is mullite type II, and M_{III} is mullite type III.

The mechanism of mullite formation in each sintering process has already been discussed in the individual chapters. In short, mullite type I and II, in CSed, DSed, SPSed, MWSed and FSed samples, all form in a similar manner. Type I mullite (M_I) is produced by the decomposition of the clay component (kaolinite) while elongated mullite (M_{II}) originates from the clay but with interaction with the liquid glass melt (molten albite) during sintering producing a more elongated morphology arising from the more fluid alkali-rich liquid.

Interestingly, the formation of type III mullite, which is found in SPS, MWS and FS, is different to the type I and II mullites. Considering the type III mullite in SPS and MWS, they are different in terms of their sizes (SPSed sample has shorter aspect ratio mullite than MWSed sample) which is likely to result from the different process conditions leading to different growth mechanisms.

The porcelain contains Fe_2O_3 impurity (1.24±0.04 wt.%, see section 4.2) which affects the viscosity of the liquid phase under different sintering atmospheres (oxidation and reduction). This variable viscosity of the liquid phase leads to different mullite growth mechanisms locally in the porcelain.

Lee et al., [165] suggested that the mechanism of mullite growth may be associated with atmosphere. They explained that larger mullite crystals formed in oxidising than in reducing atmosphere because of the presence of iron oxide (Fe_2O_3), which causes lower viscosity of the silicate liquid (mullite grows faster). Fe metal, on the other hand, was detected in reducing atmosphere because the fluidising iron oxide was converted to FeO then Fe metal from the silicate liquid.

In contrast, Dingwell and Virgo [348] reported that the atmosphere changes the viscosity of the silicate melt during heating; reducing atmosphere decreases the viscosity of the silicate melt while oxidation atmosphere produces more viscous silicate melt. They explained that Fe_2O_3 is reduced to Fe^{2+} in the reducing atmosphere and Fe^{2+} ions behave as network modifiers resulting in depolymerization of the silicate melts so decreasing silicate melt viscosity [348].

SPS employs an applied pressure which increases viscosity of the liquid glass. Increasing pressure causes polymerisation of the glass network because the liquid glass structure is compressed (ring structure collapses), and new bonds can be formed. In other words, increasing pressure causes reduction of the volume of

liquid glass (increasing density), thus viscosity increases. Vacuum, on the other hand, is also employed by SPS and is likely to decrease the melt viscosity in the same way that reducing atmosphere does. Thus, mullite produced in SPS has low aspect ratio compare to that produced in MWS; likely affected by the applied pressure because the pressure increases liquid phase viscosity making mullite growth more difficult. Although mullite grows faster in reducing atmosphere (low viscosity of liquid phase) the short aspect ratio mullite in the SPSed may also result from the large amount of mullite found in liquid phase leaving less alumina-silica for growth.

In the FSed sample, it is evident that mullite nuclei are found in the liquid phase as presented in Fig. 10.8. The light grey circles are mullite nuclei, confirmed by the EDS showing alumina and silica while the glassy phase additionally contains sodium. The result shows that there are differences between the two spectra. Spectrum 2 contains Na, Ca and Fe representing composition of glass while spectrum 1 contains only Al and Si indicating mullite. However, this is still the beginning of mullite formation so the mullite is silica-rich

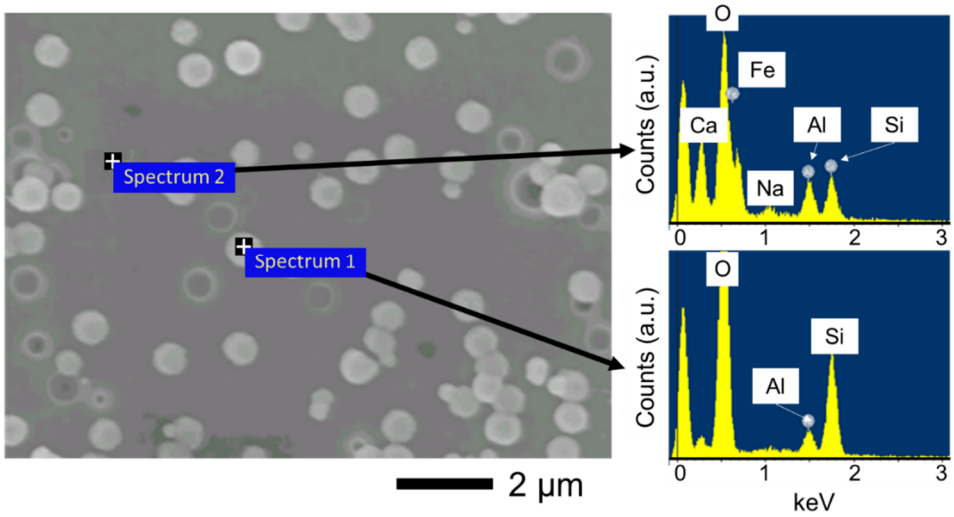

Figure 10.8: Mullite nuclei formed in liquid glass during flash sintering (FSed 1265 °C).

Takei et al., [349] explained the growth mechanism of mullite in liquid glass. They stated that mullite crystallization in liquid glass occurs in three stages, depending on the temperature as presented in Fig. 10.9b. The first stage, mullite nucleation occurred at <1000 °C as suggested by phase separation. The

second stage, nuclei growth, occurred at higher temperature of 1000-1200 °C but there is no appreciable grain growth in mullite. The third stage, above 1200 °C, shows mullite grain growth via coalescence.

It is believed that the SPS, MWS and FS initially produce type III mullite in the liquid glass (Fig. 10.9a) as suggested by Takei et al., but type III mullite found in this study (Fig. 10.5-10.7) was elongated since the SPS, MWS and FS have typical growth atmosphere which enhanced the mullite growth mechanism.

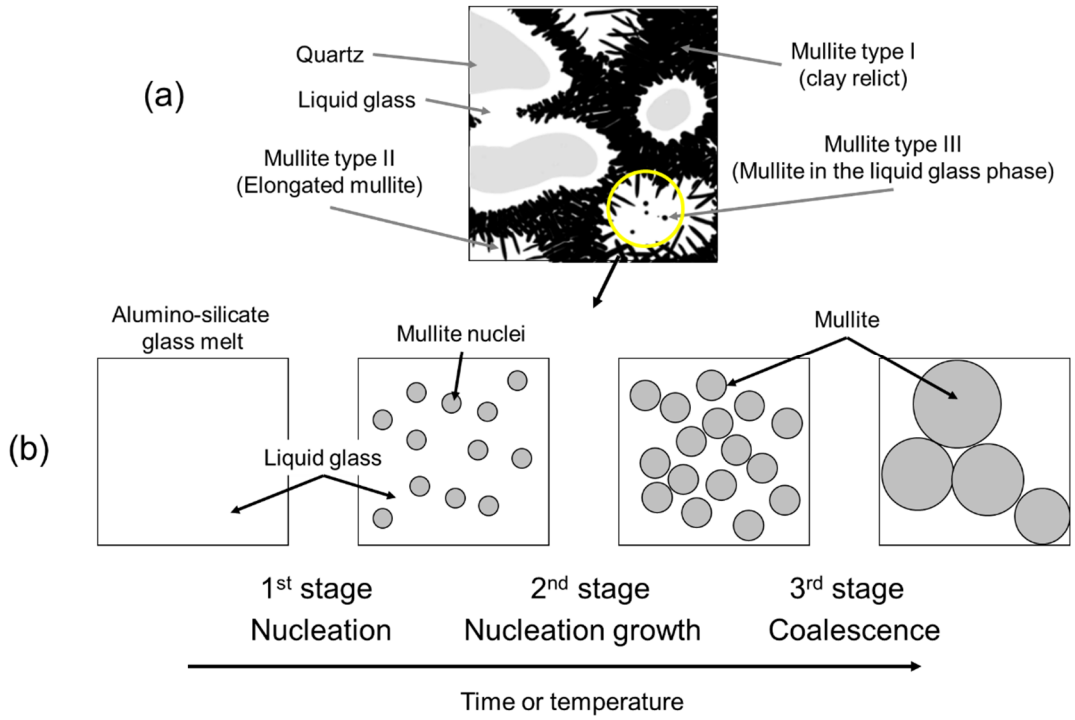

Figure 10.9: Schematic illustration of mullite formation, (a) different mullite types (author's image), and (b) mullite crystallization stages [adapted from Ref. 349].

10.5 Amount of mullite in the different rapid firing techniques

The amount of mullite formed in the studied sintering processes was determined using the internal standard method (described in section 4.11) shown in Fig. 10.10.

The amount of mullite formed in the CSed sample increased as temperature increases but remained constant from 1175-1200 °C. The amount of mullite formed in the CSed sample is 4.1±0.5 wt.% at 1000 °C, and reached its maximum of 9.2±0.2 wt.% at 1175-1200 °C. A similar trend is observed in the DSed samples in

which mullite formation increased from 7.7±0.3 wt.% at 1150 °C to ~9.1±0.4 wt.% at 1175-1200 °C.

It is also clear that the amount of mullite found in MWSed samples increased as temperature increased and reached a plateau once the temperature reached 1100-1200 °C at 9.9±0.4 wt.%. The MWSed sample has slightly higher levels of mullite than seen in the CSed and DSed samples because MWS enhances mullite formation (as described in section 8.7.1), as also seen from the microstructure (Fig. 10.4 and 10.6).

In the case of SPSed samples, the amount of mullite formed at 1100 °C is altered by the dwell time. Fig. 10.10 shows that the amount of mullite formed at 0 min dwell was 13.8±0.1 wt.% but as dwell time increased, the amount of mullite decreased to the similar level of other samples sintered under different sintering techniques (~9-10 wt.%). As mentioned in section 7.7.3.1, the effect of vacuum enhances the decomposition of kaolinite and albite, resulting in enhancing Al^{3+} diffusion for mullitisation.

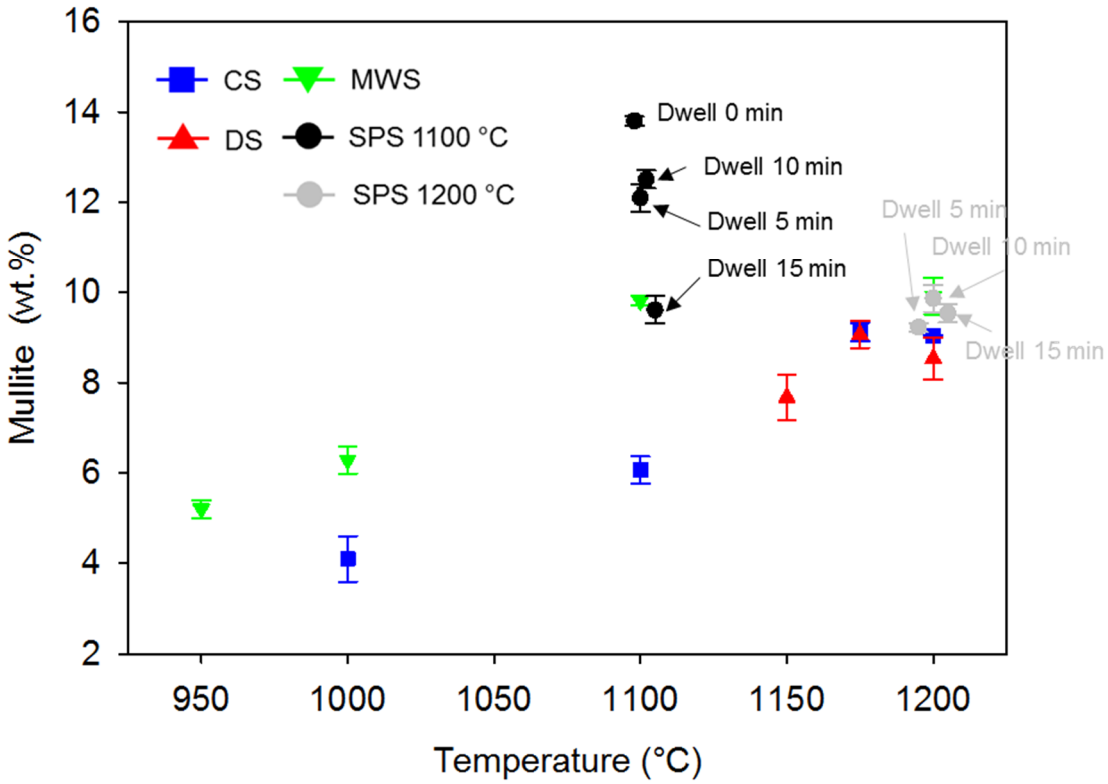

Figure 10.10: Amount mullite as a function of temperature formed in the sintering processes. Note that dwell time of CS, DS, and MWS are 15 min, 5 min and 5 min respectively.

The decreasing amount of mullite in the SPSed 1100 °C sample with increasing dwell time resulted from an adverse effect of pressure on the dissolution of mullite as previously explained in section 7.7.3.3. The SPSed 1200 °C samples sintered with different dwell times show similar amounts of mullite at ~9.8±0.3 wt.% because the dissolution of mullite may be stopped.

It is interesting that the amount of mullite formed in the fully dense porcelain samples is in a similar range (9.5±0.5 wt.%) regardless of the processing routes, this is because the chemistry of the porcelain is identical so the mullite formed is similar. It has been experimentally reported that mullite formation in porcelains is constant and independent of heating rate and dwell time over the temperature range of industrial firing schedules (1200-1400 °C) [110,160,206].

In addition, even though mullite in the FSed sample cannot be quantified examination of SEM images (Fig. 10.7) reveals that large amounts of mullite forms in the FSed sample. Mullite is found everywhere in the FSed sample, in the clay relict, and in the glass, resulting from the applied electric field.

10.6 Mullite crystallite growth via different sintering processes

The calculated mullite crystal sizes using the Scherrer equation were found to increase with increasing temperature in all sintering techniques as presented in Fig. 10.11. For example, mullite crystallite size of the CSed samples varies from 32-40 nm from 1000-1175 °C. The mullite crystallite sizes in the DSed sample (32-37 nm) and MWSed sample (24-27 nm) show a similar trend to those in the CSed sample.

Mullite growth in the SPSed samples is much faster than that in the CSed, DSed and MWSed sample (mullite crystallite size varies from 17 to 55 nm) because the applied pressure of 25 MPa in this SPS condition is significant for mullite formation as well as the plastic deformation combined with a heating rate of 100 °C/min that triggers the transformation of kaolinite in porcelain at lower temperature; thus mullite has more time to grow (as discussed in section 7.7.3). However, mullite dissolution is observed in the SPSed sample sintered at 1200 °C and 10 min dwell by decreasing of mullite crystallite size.

It also can be seen in Fig. 10.11 that increase mullite size in CSed, DSed, and MWSed samples is similar (similar slopes) but MWSed sample has smaller

mullite size compared to CSed, and DSed because it shows fibre-like mullite formed via VLS mechanism as addressed in section 8.7.1. DSed samples have smaller mullite size compared to CSed samples e.g. at 1200 °C because it has less time to grow (DSed sample have faster heating rates).

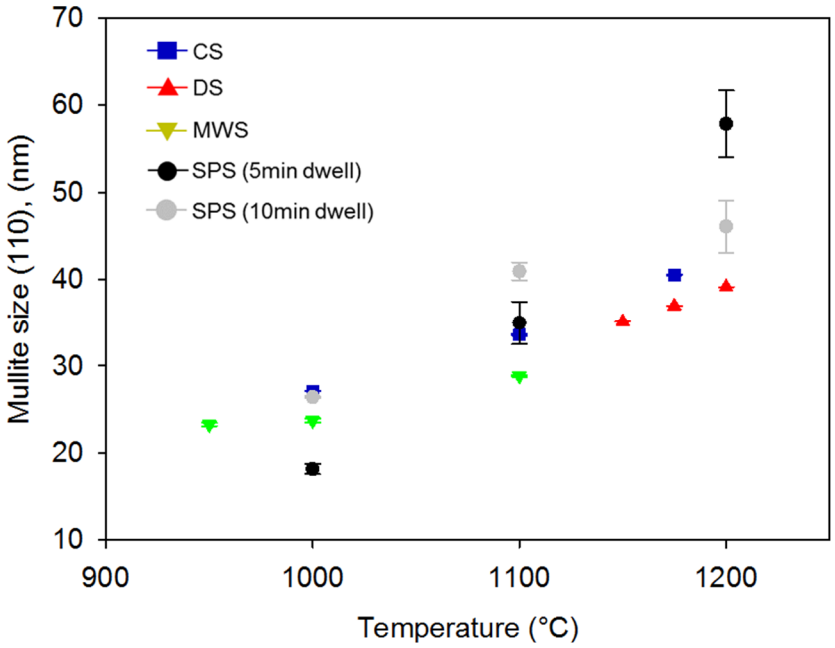

Figure 10.11: Calculated mullite crystallite size (001) growth in different sintering techniques using the Scherrer equation.

10.7 Mechanical behaviour

10.7.1 Vickers hardness

A comparison of Vickers hardness (H_V) in the dense areas of the porcelain samples sintered using different sintering techniques (Fig. 10.12a) shows that DSed 1200 °C samples have greatest H_V (7.6±0.3 GPa), while SPSed 1200 °C samples have H_V of 6.8±0.03 GPa. MWSed 1200 °C samples have similar H_V to the CSed 1200 °C sample ranging ~5.5±0.4 GPa.

It is clear that H_V increased in the dense areas with increased sintering temperature resulting from higher ABD; the greater the density the greater the H_V. For example, the CSed samples have low H_V (~2±0.2 GPa) after firing at 1100 °C due to incomplete sintering but H_V reaches a maximum value of 5.2±0.4 GPa in a fully sintered sample at 1200 °C. In the case of MWSed and SPSed samples, they reach their maximum H_V after sintering at 1100 °C when they are fully dense and the H_V remains constant after sintering at 1200 °C; MWSed

samples have 5.6±0.2 GPa and SPSed samples have 6.7±0.2 GPa. SPSed samples sintered at 1100 °C have greater H_V than the CSed and MWSed samples because they have denser microstructures (greater ABD) and less porosity (Fig. 10.13b, and c).

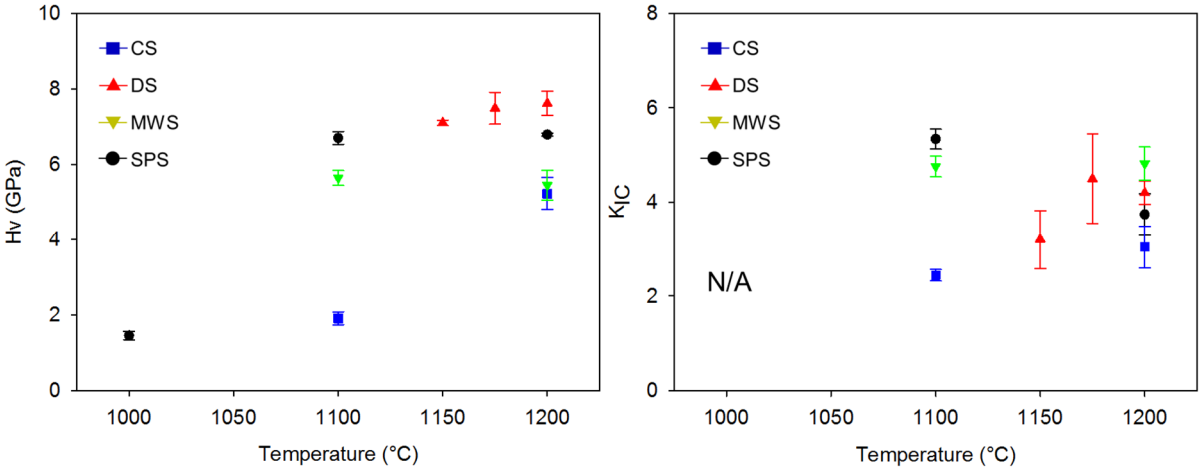

Figure 10.12: (a) Vickers hardness and (b) fracture toughness of CSed, DSed, SPSed and MWSed samples as a function of temperature.

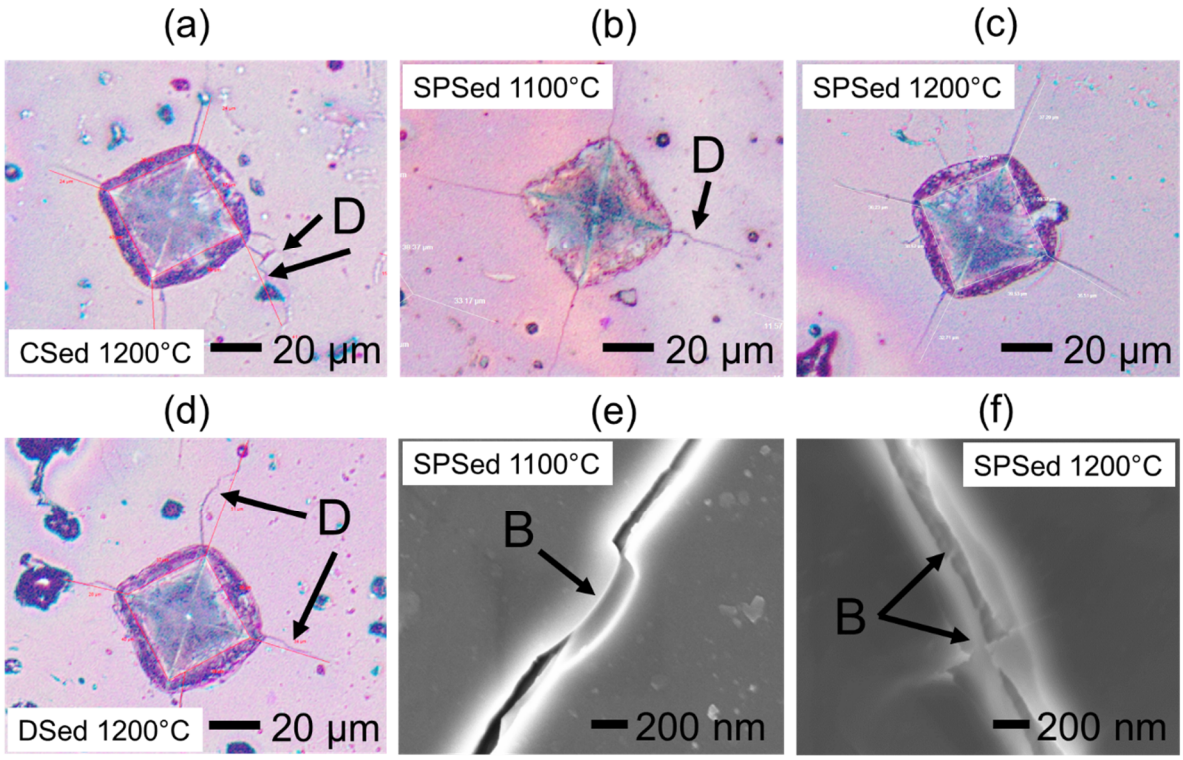

Figure 10.13: Microstructures of porcelain samples, indents and cracks generated from indentation corners. (a) CSed 1200 °C, (b) SPSed 1100 °C, (c) SPSed 1200 °C and (d) DSed 1200 °C samples, and the toughening mechanisms, crack bridging (B), and crack deflection (D).

The DSed samples, on the other hand, have the greatest H_V among these samples, which is likely due to the local density, phase composition and pore structure which is associated with the selected indentation area, as presented in section 6.7. Fig. 10.13d reveals that the indentation area was selected from the dense area, but residual pores are still observed.

SPSed samples exhibit higher H_V compared to CSed and MWSed samples resulting from their high density, and the pore-free and dense selected area. In addition, from the microstructure point of view, it was previously mentioned (section 7.6) that SPS produced mullite with preferred orientation to the compressive direction, which should increase H_V although the cracks reveal no evidence of any texture effect. A texture effect would be indicated by the cracks generated from the indentation corners having different lengths [349] but in this study the crack lengths are similar indicating random orientation of the mullite needles. Nonetheless, the SEM images (e.g. Fig. 10.5) show evidence of mullite having preferred orientation but not revealed by the indentation cracks.

However, the H_V of samples sintered to 1200 °C vary over a narrow range between 5-8 GPa because the samples have similar degree of densification (density range between 2.3-2.46 g/cm^3) and similar phase composition; similar glassy phase (no albite), and similar mullite (~9.8±0.3 wt.%). Please note that that H_V results in Fig. 10.12a may have uncertainty from the measurements resulted from the porcelain inhomogeneity and the crack length, which some are not satisfied >2a, however, the standard deviations of the H_V results are relatively small suggesting that the H_V values spread in a narrow range.

10.7.2 Fracture toughness

Fig. 10.12b shows that fracture toughness (K_{IC}) varies over a narrow range between 3-6 MPa · m$^{1/2}$ for samples sintered at 1200 °C. The SPSed 1200 °C samples have lower K_{IC} compared to DSed and MWSed samples likely due to two aspects; local density and phase composition. The local density of the SPSed samples is greater than that in DSed and MWSed samples because of the effect of the applied pressure (Fig. 10.1) and should produce greater K_{IC}. However, it is not the case because the local phase composition, which is composed of mainly glass

and mullite, plays an important role producing long and straight cracks in SPSed samples.

Straight cracks are observed in the dense and pore-free regions of the SPSed samples (Fig. 10.13b and c). Highly magnified SEM images (Fig. 10.13e and f) show crack bridging (denoted as "B") suggesting that SPSed samples have crack bridging as a toughening mechanism while the DSed, and CSed (Fig.10.14a and d) samples have crack deflection (denoted as "D") as toughening mechanisms.

Fig. 10.14 shows schematically the toughening mechanisms in ceramics due to dispersed particles in the matrix. The toughness of ceramics is enhanced by crack bridging (B), and crack deflection (D) [351-354], and these toughening mechanisms were observed to be present in this study (Fig. 10.13).

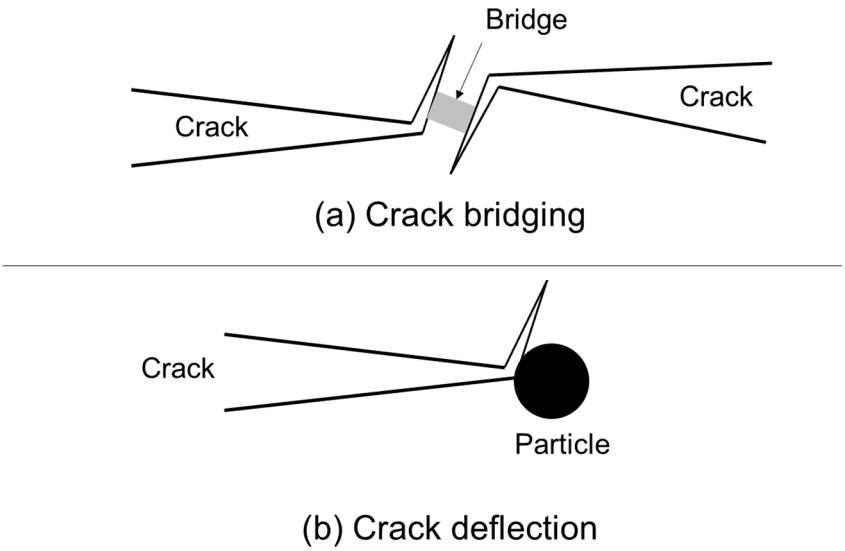

Figure 10.14: Schematics of principal toughening mechanisms in cementitious composites. (a) crack bridging, and (b) crack deflection, [adapted from Ref. 351].

Fig. 10.13a and d (the CSed and DSed samples) also suggests that the cracks are deflected (denoted as "D") by the dispersed particles (mullite, quartz, and residual albite) while these mechanisms were not observed in the SPSed sample i.e. SPSed 1200 °C. This crack deflection mechanisms in CSed and DSed samples may lead to the greater K_{IC} compared to the SPSed samples.

Crack lengths (c parameter used to calculate K_{IC}) in SPSed samples were longer (28.21±5 μm) than those found in DSed (25.66±2 μm) and MWSed

(21.47±1 μm) samples (see Table 10.1) because the SPSed samples contain fewer pores to pin the cracks, and less evidence of crack deflection; so producing lower K_{IC}.

It is worth noting that the drop of K_{IC} (Fig. 10.12b) in DSed, MWSed and SPSed samples sintered at 1200 °C is due to the increasing crack length (c parameter in Table 10.1) while the *a* parameter is similar (see Table 10.1). Please also note that some parts of the uncertainty of the K_{IC} measurement resulted from the porcelain inhomogeneity and the crack length (as previously mentioned), for example, the standard deviation of the K_{IC} of DSed samples is relatively large resulting from the measurement uncertainty.

Table 10.1: a and c parameter used to calculate K_{IC} in the porcelain samples.

Process	a-parameter (μm)			c-parameter (μm)		
	1000 °C	1100 °C	1200 °C	1000 °C	1100 °C	1200 °C
CS	n.d.*	22.50±6	18.48±1	n.d.	22.03±5	26.54±6
DS	n.d.	n.d.	18.77±1	n.d.	n.d	25.66±2
MWS	n.d.	19.63±1	20.81±1	n.d.	20.50±1	21.47±1
SPS	25.05±7	19.83±1	18.98±1	n.d.	22.11±5	28.21±5

* n.d. is not determined.

Fig. 10.15 shows SEM images illustrating crack bridging (B), and crack deflection (D) in the porcelain samples. H_V and K_{IC} of the porous samples i.e. CSed 1000 °C cannot be determined because the a and c parameters were not identified. As mentioned earlier, cracks in SPSed samples are straight (no deflection) and longer compared to those in other samples (Table 10.1).

Even though, toughness and strength of the materials are different, attempts have been made to correlate the toughness to the bulk property as discussed in section 8.6. In short, the hardness of a material can affect the fracture toughness. In general, the harder the material the lower the fracture toughness. In this study, the fracture toughness value may not represent the bulk property because the measurement was done in the dense area of the samples so porosity may have less effect on the toughness. On the other hand, porosity plays an important role in bulk properties. Thus, it would be better to experimentally determine the bulk properties of the porcelain rather than predicting from the toughness values.

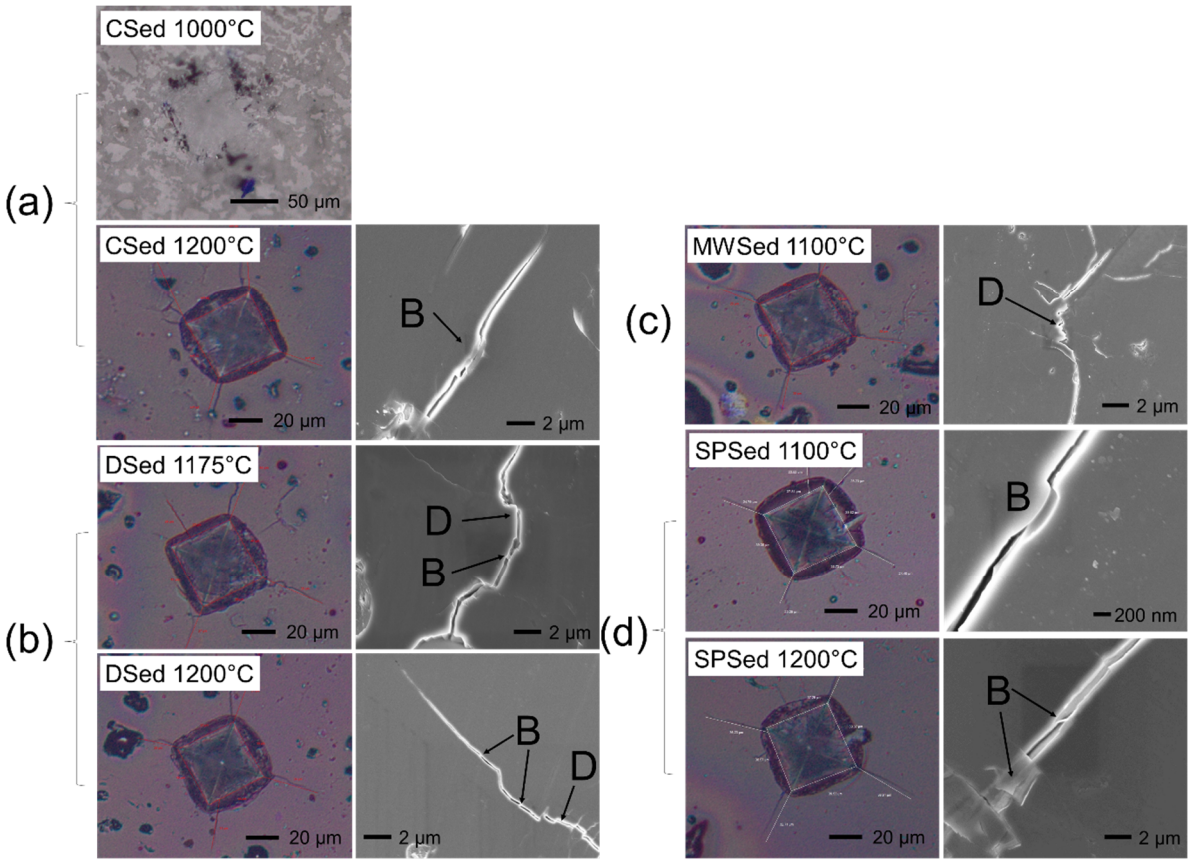

Figure 10.15: SEM images of indentations and cracks in (a) CSed, (b) DSed, (c) MWSed and (d) SPSed samples showing crack bridging (B), and crack deflection (D), which control the toughness.

10.8 Evaluation of energy consumption in the rapid sintering techniques

Fig. 10.16 presents the measured power (watt) of the studied sintering processes as a function of processing time (second). The energy used in each process was calculated from the integrated area under the graph (W · s = Joule).

For example, the porcelain sintered using CS with conditions of 1175 °C, 5 °C/min and 15 min dwell in the 4.5 litres chamber consumed energy ~11.7 MJ (Fig. 10.16a) while the DS process, which used only dwelling step in the same furnace used in CS (marked as red box in Fig. 10.16b), consumed ~1.1 MJ of energy. Fig. 10.16c shows 3.2 GJ of energy obtained from the integrated software of the SPS. Fig. 10.16d presents the energy consumed in the microwave sintering of ~0.04 MJ.

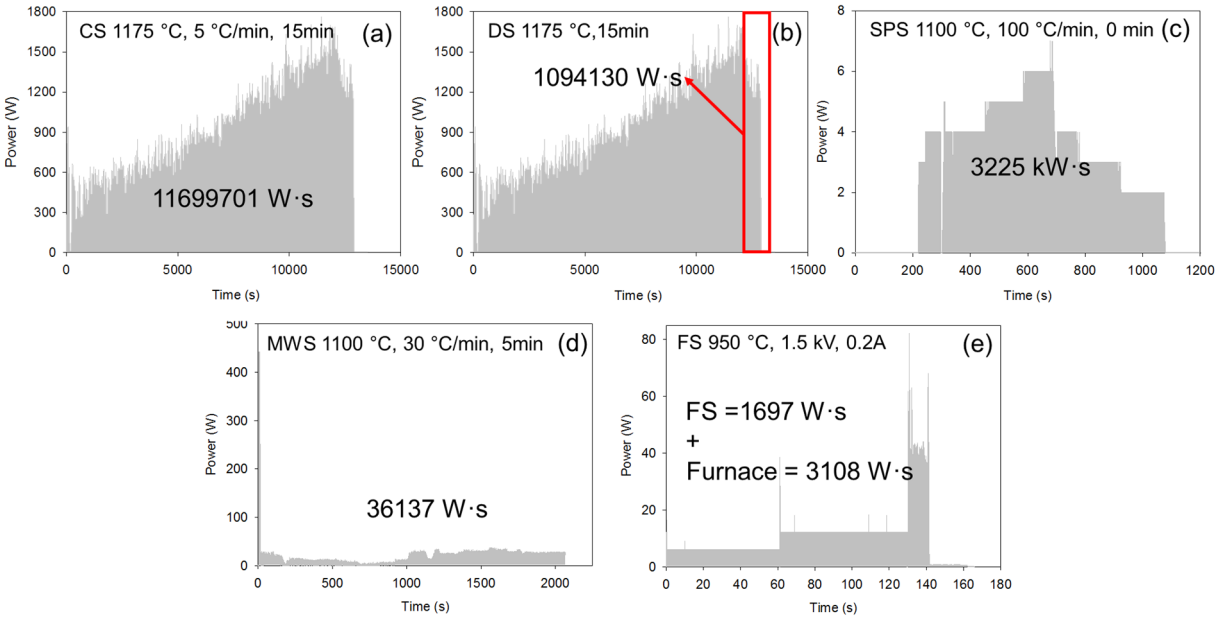

Figure 10.16: The power value measured by the power meter, and calculate energy (Joule, (W · s)), (a) CS, (b) DS, (c) SPS, (d) MWS, and (e) FS.

The energy consumed by the FSed sample was ~1.6x10^{-3} MJ (only energy supplied to the sample to produce Joule heating), which was low compared to the other processes. However, once the energy from the furnace, which used to heat up the sample to the flash event was included (3108 J) the FS process needed energy ~4.8x10^{-3} MJ. Thus, from the energy consumption point of view, SPS consumed a lot more energy that other processes and FS consumed less energy

than other processes. Fig. 10.16 suggests that the SPS process is the most energy consuming process (3225 MJ) followed by CS (11.70 MJ), DS (1.10 MJ), MWS (0.0036 MJ) and FS (4.8×10^{-3} MJ), respectively (to be discussed in detail in section 10.8.2-10.8.4). However, to make a better comparison, the sample mass is used to calculate the specific energy consumption (SEC) as presented in Tables 10.3-10.6.

Briefly, the specific energy consumption (SEC) in CS process (Table 10.2) is 117 MJ/kg, which was calculated by the measured power divided by the porcelain weight. The SEC of DS is 10.8 MJ/kg (Table 10.3), the SEC of FS is 4.79 MJ/kg (Table 10.4), the SEC of SPS is 1612 MJ/kg (Table 10.5), and the SEC of MWS is 18 MJ/kg (Table 10.6).

10.8.1 Energy losses in CS, DS, and FS

Table 10.2 presents calculations of (1) energy supplied to the furnace, (2) energy required by the sample at 1175 °C, (3) energy required by the alumina setter at 1175 °C, (4) energy losses at 1175 °C and (5) SEC of CS.

The SEC of CS (without considering losses) is 117 MJ/kg calculated for a 100 g sample. However, only 0.13 MJ of energy was required by the sample and only 0.12 MJ was consumed by the alumina setter, the rest of the energy is consumed by the furnace structure and lost.

In the case of CS, a laboratory furnace was used to heat the sample and it is assumed that there are energy losses via the furnace walls (Q_W) and opening gaps (Q_G). The heat loss via the furnace walls was calculated based on the convection (Q_C) and radiation (Q_R) as presented in Eq. 10.7-10.9 and Fig. 10.17.

$$Q_W = Q_C + Q_R \tag{10.7}$$

$$Q_C = h_c \int_0^A A \, dT \tag{10.8}$$

$$Q_R = \varepsilon \sigma A (T_w^4 - T_a^4) \tag{10.9}$$

where h_c is the convective heat transfer coefficient, A is the area of the furnace walls (5 sides excluding the bottom side of the furnace). T_w is the temperature of

the furnace wall, T_a is the ambient temperature, σ is the Stefan-Boltzmann coefficient, and ε is the emissivity of the furnace walls.

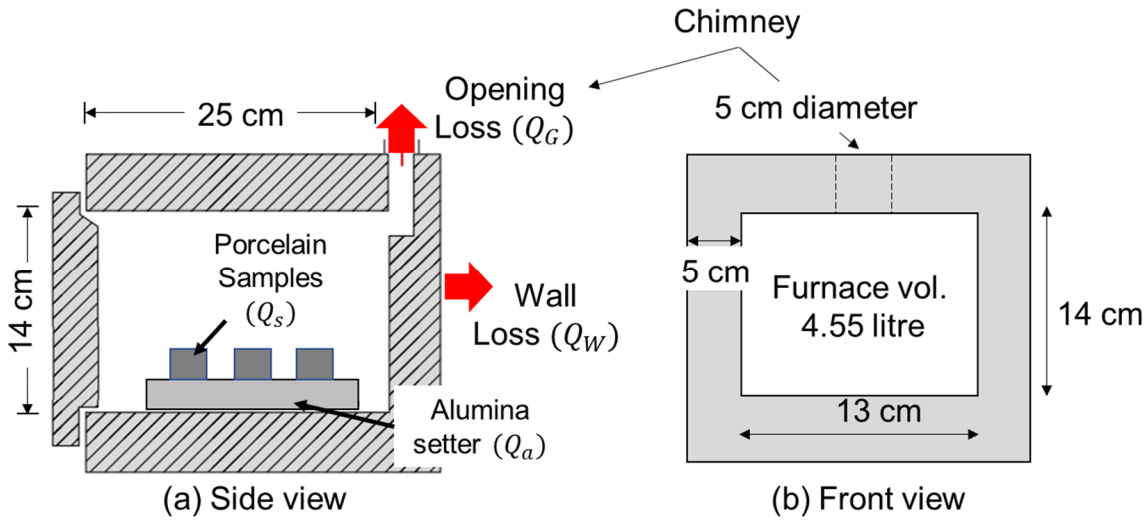

Figure 10.17: Schematic diagram of the laboratory furnace used in the CS and DS, (a) side view, and (b) front view.

In this study, the convective heat transfer by air was calculated using Eq. 10.10, which is valid for air velocity from 2 to 20 m/s [355]. It is assumed that the velocity of the air (v) surrounding the furnace was 5 m/s. Thus, the h_c was 27.8 W/ m^2·K.

$$h_c = 10.45 - v - 10(v^{1/2}) \tag{10.10}$$

Heat losses from the opening gaps (Q_G) can be calculated using the concept of radiation, Eq. 10.11, in which T_f is 1175 °C. From this assumption, the heat losses from the laboratory furnace in the CS were as shown in Table 10.3.

$$Q_G = \varepsilon\sigma A(T_f^4 - T_a^4) \tag{10.11}$$

Table 10.3 shows that the energy losses via the furnace wall (Q_W) are ~5.75 MJ (5.73 MJ from Q_C and 0.024 MJ from Q_R) while the loss from opening gap (Q_G) is about 2.82 MJ. From Table 10.3, the majority of energy used is due to the losses, just a small amount of energy is acquired by the sample.

Table 10.2: Energy measured by the power meter, energy losses and SEC in CS.

Energy	Equation	Energy (MJ)	Parameter
1. Energy measured by the power meter		11.70	Processing time (t)=14010 sec.
2. Energy required by porcelain sample (Q_s) *	$Q_s = m\int_{T_1}^{T_2} C_P dT$	0.13	m= 100 g, T_1=30 °C, T_2=1175 °C
3. Energy required by alumina setter (Q_a) **	$Q_a = m\int_{T_1}^{T_2} C_P dT$	0.12	m = 80 g, T_1=30 °C T_2=1175 °C
4. Energy losses			
4.1 Wall loss via convection (Q_C)	$Q_C = h_c\int_0^A A\,dT$	5.73	A=0.163 m^2 $h_c = 10.45 - v - 10v^{1/2}$ $v = 5\ m/s$
4.2 Wall loss via radiation (Q_R)	$Q_R = \varepsilon\sigma A(T_w^4 - T_a^4)$	0.024	ε= 0.9 σ=5.67x10^{-8} W/ (m^2 · K) T_w=120 °C, T_a= 30 °C T_f= 1175 °C Opening gaps (A) = 0.0019 m^2
4.3 Opening gaps loss (Q_G)	$Q_G = \varepsilon\sigma A(T_f^4 - T_a^4)$	2.82	
5. Specific Energy Consumption (SEC)		**117 MJ/kg**	

* Heat capacity of the porcelain is obtained from section 5.5.
** Heat capacity of alumina setter is retrieved from Ref. 356.

Table 10.3 and 10.4 present the estimation of energy losses and SEC of DS and FS processes using the same calculation concept to the CS because these three processes (CS, DS, and FS) employ a laboratory furnace which has the same loss parameters. The only two differences are sample size and furnace processing time. The SEC of DS is 10.8 MJ/kg calculated from 10 g of sample. Again, only 0.013 MJ of energy was consumed by the sample and only 0.12 MJ was consumed by the alumina setter, the rest of energy is lost as presented in Table 10.3.

The SEC of FS is 4.79 MJ/kg (excluding the furnace heating, which is the power used to heat the furnace and sample from 30 to 950 °C) but 3060 MJ/kg when the furnace heating is included. The energy consumed by the sample is low (4.79x10^{-3} MJ/kg) because the sample weight used in the FS was only ~1 g (the sample was in a small pellet with 13 mm diameter and 1 mm thick, the rest of the furnace energy is lost (Table 10.4).

Table 10.3: Energy measured by the power meter, energy losses and SEC in DS.

Energy	Equation	Energy (MJ)	Parameter
1. Energy measured by the power meter		0.11	Processing time (t)=900 sec.
2. Energy required by porcelain sample (Q_s) *	$Q_s = m\int_{T_1}^{T_2} C_P dT$	0.013	m= 10 g, T_1=30 °C, T_2=1175 °C
3. Energy required by alumina setter (Q_a) **	$Q_a = m\int_{T_1}^{T_2} C_P dT$	0.12	m = 80 g, T_1=30 °C T_2=1175 °C
4. Energy losses			
4.1 Wall loss via convection (Q_C)	$Q_C = h_c\int_0^A A\,dT$	0.72	A=0.163 m^2 h_c $= 10.45 - v - 10v^{1/2}$ $v = 5\,m/s$
4.2 Wall loss via radiation (Q_R)	$Q_R = \varepsilon\sigma A(T_w^4 - T_a^4)$	0.08	ε= 0.9 σ=5.67x10^{-8} W/(m$^2\cdot$K) T_w=120 °C, T_a= 30 °C T_f= 1175 °C Opening gaps (A) = 0.0019 m^2
4.3 Opening gaps loss (Q_G)	$Q_G = \varepsilon\sigma A(T_f^4 - T_a^4)$	0.18	
5. Specific Energy Consumption (SEC)		**10.8 MJ/kg**	

* Heat capacity of the porcelain is obtained from section 5.5.

** Heat capacity of alumina setter is retrieved from Ref. 356.

Table 10.4: Energy measured by the power meter, energy losses and SEC in FS.

Energy		Energy (MJ)	Parameter
1. Furnace heating excluded			
1.1 Energy measured by the power meter (electric power to produce Joule heating)		1.68×10^{-3}	Processing time (t)=3 sec.
1.2 Energy required by porcelain at 950 °C (furnace energy)		3.11×10^{-3}	m= 1 g, T_1=30 °C, T_2=950 °C, Processing time (t)=3 sec.
1.3 Energy required at flash event (1.1) + (1.2)		4.79×10^{-3}	
1.4 Specific Energy Consumption (SEC)		**4.79 MJ/kg**	
2. Furnace heating included			
2.1 Energy measured by the power meter (heating)		3.06	Processing time (t) =5520 sec (30-950 °C) heating rate 10 °C/min m=1 g
2.2 Energy required at flash event (1.3) + (2.1)		3.06	
2.2 Energy loss			
2.2.1 Wall loss via convection (Q_c)	$Q_C = h_c \int_0^A A\, dT$	2.01	A=0.163 m² $h_c = 10.45 - v - 10v^{1/2}$ $v = 5m/s$
2.2.2 Wall loss via radiation (Q_R)	$Q_R = \varepsilon\sigma A(T_w^4 - T_a^4)$	0.008	ε= 0.9 σ=5.67x10^{-8} W/ (m² K) T_w=120 °C, T_a= 30 °C T_f= 950 °C Opening gaps (A) = 0.0019 m²
2.2.3 Opening gaps loss (Q_G)	$Q_G = \varepsilon\sigma A(T_f^4 - T_a^4)$	0.40	
2.3 Specific Energy Consumption (SEC)		**3060 MJ/kg**	

* Heat capacity of the porcelain is obtained from section 5.5.

10.8.2 Energy losses in SPS

The energy input (Fig. 10.16c) was used to heat porcelain sample, graphite components, and the rest power are lost via conduction and radiation. The energy required to heat the porcelain sample was 0.003 MJ (Table 10.5). The energy used to heat the graphite components was calculated using graphite properties (such as density and heat capacity) and geometrical parameters as given in Table 10.5 and Fig. 10.18b. For example, energy required by the graphite components is 3.36 MJ (including energy for punch, die, and spacer in Table 10.5, 3.1-3.3). The energy loss via radiation is 9.53 MJ while the loss via conduction is not determined because it is too large, but it may be assumed that the conduction loss is equal to energy input subtracted by the energy required by porcelain sample, graphite components and radiative heat loss. The measured energy in the SPS was 3225 kW to

consolidate 2 g (because just a small mass of porcelain powder can be sintered in the 20 mm diameter graphite die) of porcelain thus the SEC of SPS is 1612 MJ/kg.

Table 10.5: Energy measured by the power meter, energy losses and SEC in SPS.

Energy	Equation	Energy (MJ)	Parameter
1. Energy measured by the power meter		**3225**	Processing time (t) = 960 sec.
2. Energy required by porcelain sample (Q_s) *	$Q_s = m\int_{T_1}^{T_2} C_P dT$	0.003	m= 2 g, T_1=30 °C, T_2=1100 °C
3. Energy required by graphite components**			$C_P = 310 + 1.09T$
3.1 Die	$Q = m\int_{T_1}^{T_2} C_P dT$	0.66	m= 340 g
3.2 Punch		0.22	m= 114 g
3.3 Spacer		2.48	m=1534 g
4. Losses			
4.1 Radiative loss by graphite (Q_R)	$Q_R = \varepsilon\sigma\int_0^A A\,(T^4)$	9.53	ε is 0.9 A = see geometrical parameter in Fig. 10.19b.
4.2 Conduction loss to water cooling via steel ram	n/a	n/a	
4. Specific Energy Consumption (SEC)		**1612 MJ/kg**	

* Heat capacity of the porcelain is obtained from section 5.5.

** Heat capacity of graphite is $310 + 1.09T$ J/kg-K, density (ρ) of graphite is 1.90 g/cm^3 [357].

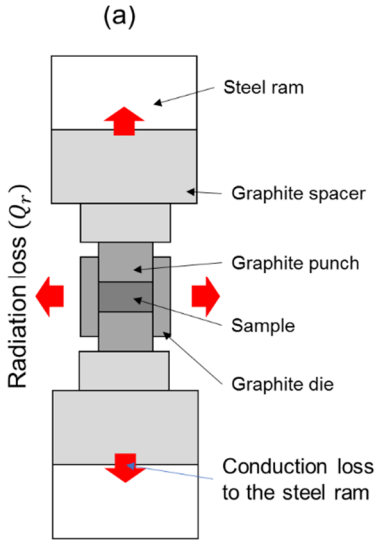

(b)

Geometrical parameters of parts of the SPS used in this study

Components	Diam./Height (mm)
Graphite spacer	60/30
Graphite punch	20/20
Graphite die	20 (inside),40(outside)/40

Figure 10.18: (a) Schematic diagram of energy losses in SPS process, and (b) geometrical parameters of parts of the SPS used in this study.

Fig. 10.18a shows that the energy input was used to heat the graphite components while the energy losses are conduction from the graphite dies to the steel ram, where the steel ram was cooled by water, and heat loss by radiation from the graphite die to the chambers, graphite felt was used to reduce the surface radiative heat loss from the die during sintering. It has been suggested that the energy loss of the SPS process is dominated by conduction from the graphite components to the steel ram as presented in Fig. 10.19a and Table 10.5. Because the steel ram is water cooled the heat generated in the graphite components flows irresistibly away to the cooling water [357].

10.8.3 Energy consumption in MWS

In the case of MWS, the microwave energy was solely absorbed by the porcelain sample and heat internally generated, giving some energy loss via sample surface radiation (see Fig. 8.1 in section 8.2). The SEC of the MWS was calculated as 18 MJ/kg, which is presented in Table 10.6.

Table 10.6: Energy measured by the power meter, energy losses and SEC in MWS.

Energy	Energy (MJ)	Parameter
1. Energy measured by the power meter	0.036	m = 2 g
2. Specific Energy Consumption (SEC)	18 MJ/kg	

10.9 Comparison of the energy consumption

Fig. 10.19 presents plots of processing time (Fig. 10.19a) and SEC (Fig. 10.19b) to obtain fully sintered porcelains by each sintering technique. Fig. 10.19 reveals that the CS process is the most energy and time-consuming process using time in hours compared to minutes and seconds for the other techniques. The DS can reduce both processing time (hours to minutes) and energy consumption (about 10 times lower because rapid heating rate (780 °C/min) is used). The MWS, on the other hand, reduces the total energy consumption by about half compared to the DS but used longer processing time. This is due to the slower heating rate used in MWS which is 30 °C/min while for DS it was 780 °C/min. FS appears to be the least energy and time-consuming process among those techniques. However, if the furnace energy is taken into account it becomes

the most energy consuming process with 3060 MJ/kg because FS can only produce a small sample but requires large energy to heat up the furnace and sample. The SPS has SEC with 1612 MJ/kg, while the processing time is comparable to the DS and MWS (~1000-2000 s) because most energy is used to heat the graphite die and is lost through the water-cooling system, not used directly to heat the sample.

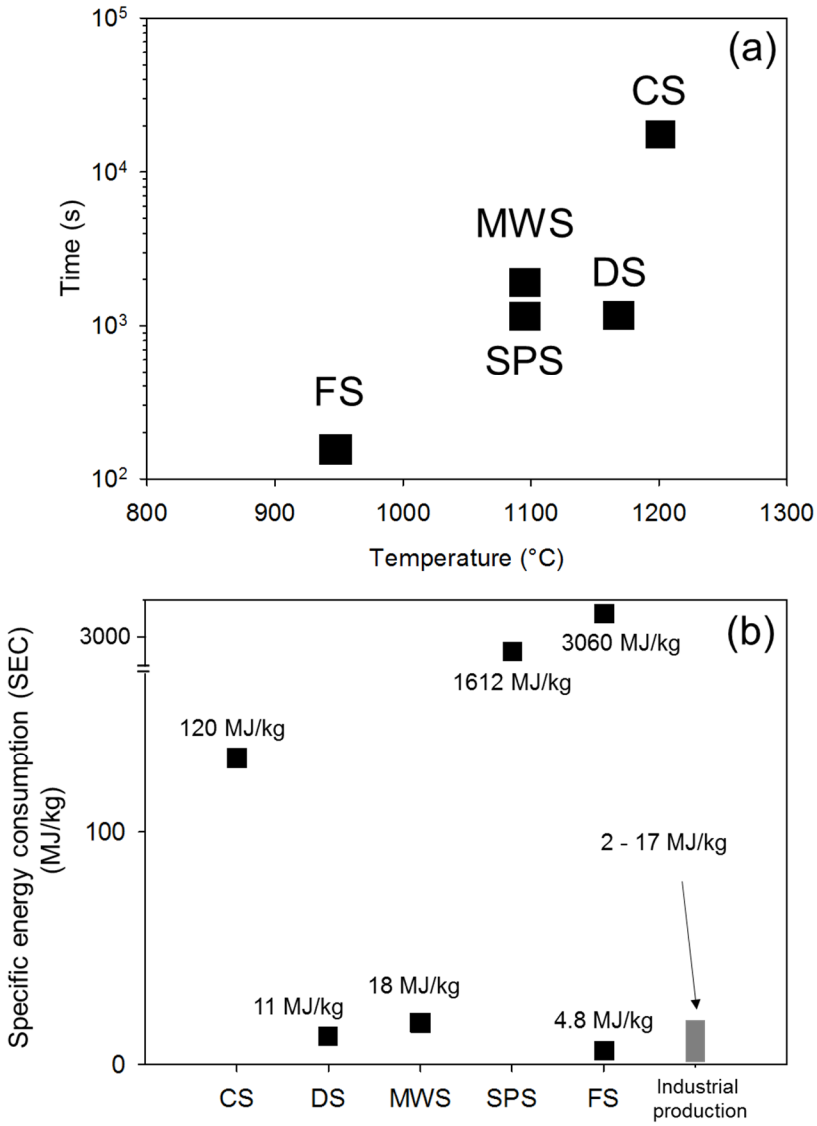

Figure 10.19: (a) Processing time, (b) specific energy consumption (SEC) used to consolidate the porcelain sample by different techniques. SEC in industrial production varies with products and firing temperatures.

Fig. 10.19b presents the SEC in each sintering technique obtained as well as the energy consumption by the industrial sector [358]. The energy used to produce ceramics on the industrial scale is presented on the right-hand side in

Fig. 10.19b suggesting that the energy required (only in the firing process) to produce masonry bricks and roof tiles is 2-4 MJ/kg, wall and floor tiles is 5-10 MJ/kg, sanitaryware is 7-10 MJ/kg, and tableware 15-17 MJ/kg.

The CS process presented in this study (which has comparable heating rate to those used commercially) consumes large amounts of energy compared to the industrial sector because of only one sample is produced, which is different from the actual industrial process in terms of the sample size, shape, continuity of the process, source of energy used, and losses.

Although, DS, MWS and FS can potentially reduce energy compared to the CS process even though the comparison made here is on a laboratory scale. This comparison can give an idea that the DS, MWS and FS are potential techniques aiming to challenge the current sintering techniques.

10.10 Limitations of applying rapid firing processes to porcelains

Even though the rapid sintering techniques in this study show potential to reduce processing time and energy consumption of porcelain production there are still some aspects to be considered including porcelain characteristics and furnace technology.

10.10.1 Porcelain characteristics

a. Porcelains usually are composed of natural raw materials (clays, feldspar, and quartz), which contain impurities such as organic matter and volatile substances. The volatile substances need to be burned out before densification complete. By employing rapid heating rates, the volatile matter would be trapped producing undesirable bubbles embedded in the porcelains reducing the technological properties. However, the applied pressure and vacuum conditions in the SPS help to minimize porosity even though the volatile matter is not fully burnt out.
b. The actual porcelain products are large and complex in shape such as tableware and sanitaryware. The rapid heating rates may not be possible because the heat transfer would be limited producing different shrinkage rates, which cause internal strains.

c. Some of porcelains are glazed to obtain desired properties. It is difficult to sinter porcelains together with the glaze by using the rapid sintering techniques because the glaze would melt and adhere to the die (in SPS) or electrode (in FS). The thermal expansion mismatch is another problem which would possible limit the heating rates because the mismatch induces stress in the glaze and porcelain body when the glazed porcelain is cooled, crack in the glaze occurs. Instead of glazed porcelain, a surface polishing (in the case of tiles) is required to flatten the surface and/or get rid of the defects from processing.

d. Large amounts of liquid phase produced makes porcelain difficult to sinter by FS because of the non-uniform electrical current distribution.

10.10.2 Furnace technology

e. In the case of DS process, as shown in sections 10.8 and 10.9, the energy is mainly consumed by the furnace, not the samples. The large furnace chamber requires large amounts of energy to heat the furnace and sample to the desired temperature. Moreover, the large amount of heat lost through the furnace wall and opening gaps must be considered.

f. The energy spent in the SPS is for heating the die components not the sample, the energy loss is large from the discussion in section 10.8-10.9. Even though the radiation loss can be reduced by employing graphite felt wrapped around the die, the energy loss due to conduction via water cooling of steel structure is unavoidable. Cooling the graphite die is also an energy consuming process. Larger samples require larger graphite dies resulting in higher power being needed to heat the die. The larger graphite die means greater energy losses through radiation. Moreover, it is difficult to engineer the applied pressure and electric current homogeneously as both play an important role in controlling microstructure [359].

g. Complication of the sample shape is the major drawback of the rapid sintering process. SPS can produce only simple geometry such as discs. FS can produce small dog-bone sample or small pellets.
h. The FS process aims to apply the energy directly to the sample, hoping to reduce the energy consumed by the furnace and loss via the furnace wall. However, as porcelain is poorly conductive at low temperature a preliminary hearing process is still required (furnace temperature is 950 °C) which means that the energy to heat the furnace and losses cannot be reduced.
i. High power is required to sinter porcelain which is associated with high cost electric equipment in FS.
j. Surface heat loss is crucial because the temperature generated within the sample bulk is as high as >1200 °C so the radiative heat loss between the sample and its surroundings, which produces a temperature gradient, is unavoidable.
k. In the case of MWS, it is possible to sinter porcelain homogeneously by employing a turntable cavity (to homogenize the microwave radiation in the cavity) and susceptor (to reduce sample surface heat loss). However, controlling the microwave distribution in the furnace cavity is a challenge because the loss tangent of porcelain changes rapidly.
l. It is possible to waste the power because the magnetron, where the microwave is produced, would fully run but partially be absorbed by the samples, the rest of the power is wasted to the circulator. The circulator redirects the microwave power, which is not consumed by the material, towards a water load. This water load consumes the microwave preventing the reflected power travels back causing damages to the microwave source.

10.11 Conclusions

In this chapter it has been shown that the rapid sintering techniques have potential to produce porcelains with lower energy consumption when considering

the densification, microstructure, and mechanical properties. It is interesting that once the porcelain is fully sintered regardless of the processing routes, in the fully dense areas the microstructure, phase evolution and mechanical properties are similar.

However, the specific energy consumption suggest that reduction of heat losses and microstructural homogeneity is the key to making the rapid sintering process more competitive. Even though the studied rapid sintering techniques have a potential to be commercialised, there are several restrictions which need to be considered.

Chapter 11

Conclusions and future perspective

11.1 Conclusions

An industrially processed porcelain powder was sintered using different rapid sintering techniques including direct sintering (DS), spark plasma sintering (SPS), microwave sintering (MWS), and flash sintering (FS). Densification, phase evolution and physicomechanical properties of the sintered samples were investigated in order to improve understanding of the role of particular process parameters.

Study of the thermal properties at 50-1200 °C with 10 °C/min was primarily performed using DTA-TGA, DSC, dilatometer, laser flash apparatus, and impedance spectroscopy, aimed to understand the porcelain sample behaviour during heat treatment and help to interpret sintering behaviour. DTA-TGA revealed that the porcelain powder experienced four major thermal events including the loss of physically bound water (<200 °C), loss of the chemically bound water (400-600 °C), mullite formation (~942 °C), and liquid phase formation (>950 °C). Dilatometry revealed the porcelain started to shrink at ~950 °C at the eutectic point of the porcelain (in kaolinite-felspar-quartz system) and the porcelain sample was fully sintered at 1200 °C with total contraction ~7%.

Laser flash apparatus determined thermal conductivity of samples as a function of temperature up to 1300 °C, revealing that thermal conductivity of the porcelain decreases to 0.37 W/m·K at 900 °C from room temperature (0.45 W/m·K) before melting of albite, once albite melts at ~950 °C, thermal conductivity

increases substantially (becoming 3.12 W/m·K at 1200 °C) due to increasing density of the porcelain.

AC conductivity was determined from 100-950 °C and during heating, conductivity increased from 100-200 °C mainly arising from H^+ and OH^- generated from the physically bound water. At >200 °C, a combination of H^+, OH^-, Na^+ and K^+ dominated the conductivity by ionic conduction. Upon cooling, the change of phases in the sample produced higher values of electrical conductivity over the same temperature range because change in the phase composition and elimination of porosity.

DS at 1150-1200 °C revealed that it had great potential to reduce processing time due to the high heating rate used (780 °C/min). The physicomechanical properties of the DSed samples were comparable to the porcelain conventionally sintered, the apparent bulk density and water absorption of the DSed samples sintered at 1175 °C were 2.36±0.01 g/cm^3 and 0 % respectively. Vickers hardness (H_V) was ~7.4±0.5 GPa. DS reduced total processing time by ~50 % and also lowered the sintering temperature from 1200 °C to 1175 °C. The microstructural characterisation of the DSed samples suggested that the phase evolution, such as mullite formation in the porcelain, was heating rate independent while glass formation was heating rate dependent.

The porcelain was consolidated using SPS from 1000 to 1200 °C with a heating rate of 100 °C/min. The porcelain started to densify at ~920 °C observed from the punch displacement. SPS produced about 10 times faster densification rate than the conventional sintering and the dwelling step was negligible due to rapid flow of the molten glass assisted by applied pressure. The SPSed samples exhibited denser microstructures resulting in improved physicomechanical properties compared with conventionally sintered samples. For example, apparent bulk density improved from 2.38 to 2.46 g/cm^3, Vickers hardness from 6-7 GPa, and fracture toughness from 4-6 MPa·m$^{1/2}$. SPS affected the kinetics and morphology of mullite formed in the porcelain samples. SPS promoted the formation of mullite above 1100 °C due to a combination of vacuum and applied pressure. The effect of vacuum enhances the decomposition of kaolinite and albite, resulting in enhancing Al^{3+} diffusion for mullitisation while the applied pressure

induced plastic deformation that triggers the transformation of kaolin at low temperature. Mullite growth was altered by the atmosphere (vacuum), dwell time, and temperature. The atmosphere changes the viscosity of the silicate melt during heating; reducing atmosphere decreases the viscosity of the liquid glass while oxidation atmosphere produces more viscous silicate melt.

The applied pressure caused mullite needles to orient perpendicular to the direction of the applied load. Depending on SPS dwell time, the mullite formed after sintering at 1100 °C also had different crystal structure (tetragonal for short dwell time of 0-5 min and orthorhombic for a long dwell time of 10-15 min). Dissolution of mullite was observed at 1100 °C by extending the dwell time by up to 15 minutes and the dissolved mullite reprecipitated on the small needles (~40 nm in (110) reflection) and coarsened via Oswald ripening resulting in larger mullite needles (~60 nm at (110) reflection).

By using microwave energy, sintering temperature of the porcelain powder was reduced by ~75 °C and dwell time from 15 min to 5 min while retaining comparable physicomechanical properties to conventionally sintered porcelain i.e. apparent bulk density (2.36±0.03 g/cm^3), water absorption (~0 %), Vickers hardness was 5-6 GPa, fracture toughness was 4-5 MPa·m$^{1/2}$. Porcelain absorbed microwave energy significantly above 600 °C due to a rapid increase in its dielectric loss tangent. Mullite in the porcelain samples produced by microwave sintering had a nanofibre morphology with high aspect ratio (~32±3:1) believed to be associated with a vapour-liquid-solid (VLS) formation mechanism, in which Fe acted as the catalyst. Microwaves also produced mullite with different chemistry having ~63 mol.% alumina content compared to ~60 mol.% alumina in conventional sintered porcelain. This was likely due to accelerated Al^{+3} diffusion in mullite under microwave radiation. Liquid phase was observed to form at relatively low temperature (~900-1000 °C) using microwaves when compared to conventional sintering. This liquid phase promoted the microwave absorption ability of porcelains.

Porcelain powder compacts were flash sintered using a two-electrode setup, an electric field of 1.5 kV/cm and furnace temperatures of 950 and 1000 °C. The liquid phase produced during the flash event acted as a conductive path, producing

localised melting and non-uniformly sintered microstructure. During flash events, the applied electric field increased mullite nucleation and altered mullite formation mechanisms by producing different supersaturation of alumina levels in the liquid glass phase such that 'elongated' mullite was formed at low level of alumina supersaturation while 'dendritic' mullite was found at high alumina supersaturation. Under an applied electric field, alkali ions (or other cations) move towards the cathode while free oxygens (O^{2-}) move towards the anode (producing bubbles at the anode). In this study, it is proposed that the flash event might be occurring by a combination of Joule heating and dielectric breakdown because the pore shapes in the porcelain were complex, and the volume fraction of the pore was about 25±1 vol.% at 950 °C, which can lower the breakdown voltage.

The polished surface in CSed, DSed, SPSed, MWSed, and FSed samples are similar showing dense surface, only the number and size of residual pores is different. Most pores observed in CSed, DSed, SPSed, MWSed, and FSed samples are round. A few interconnected pores were only found in the CSed, DSed and MWSed samples, not SPSed and FSed. The H_V in fully dense areas of CSed, DSed, SPSed, and MWSed samples are between 4-7 GPa, and K_{IC} is between 3-6 $MPa \cdot m^{1/2}$. The amount of mullite in CSed, DSed, SPSed and MWSed samples are similar, ~9.5±0.5 wt.%. However, the formation of type III mullite, which is found in SPS, MWS and FS, is different to the type I and II mullites. Considering the type III mullite in SPS and MWS, they are different in terms of their sizes (SPSed samples have shorter aspect ratio mullite than MWSed samples) which is likely to result from the different process conditions leading to different growth mechanisms.

The comparison of specific energy consumption showed that the CS consumed 117 MJ/kg, DS consumed 10.8 MJ/kg, MWS 18 MJ/kg, FS consumed 4.79 MJ/kg (but 3060 MJ/Kg when the furnace heating is included), and SPS consumed 1612 MJ/kg. The DS, MWS and FS can potentially reduce energy in commercial systems compared to CS process even though the comparison made here is on a laboratory scale. This comparison suggests that DS, MWS and FS could potentially challenge the current sintering techniques. However, all of them consumed large amounts of energy compared to the current industrial processes

because they are different in terms of sample size, shape, continuity of the process, source of energy used, and losses. The specific energy consumption also suggests that reduction of heat losses is the key to making the rapid sintering process more competitive. Even though the studied rapid sintering techniques have a potential to be commercialised, they also have limitations such as the volatile matter would be trapped producing undesirable bubbles embedded in the porcelains reducing the technological properties. The actual porcelain products are large and complex in shape such as tableware and sanitaryware. The rapid heating rates may not be possible because the heat transfer would be limited producing different shrinkage rates, which cause internal strains. Some of porcelains are glazed to obtain desired properties. It is difficult to sinter porcelains together with the glaze by using the rapid sintering techniques because the glaze would melt and adhere to the die (in SPS) or electrode (in FS).

11.2 Future perspectives

11.2.1 Porcelains

It is interesting that regardless of the processing routes for porcelain with identical chemistry, mullite amounts formed are in a similar range and produce a similar hardness. It is believed that the dispersed particles and the glassy phase control the hardness of porcelain thus, it is interesting to know the chemistry of the glassy phase in porcelain produced under different processing routes.

The amount of mullite determined via X-ray diffraction is a combination of the primary mullite and secondary mullite. It would be interesting to see if the primary and secondary mullite can be distinguished by more advanced characterisation techniques.

The hardness of porcelain is a function of the combination of the dispersed particles and the glass matrix. It would be useful to determine the hardness at the nanoscale using nanoindentation. The hardness might suggest which area dominates the overall hardness, whether it be the glassy matrix, primary mullite, secondary mullite, quartz or other residual particles. The result might be useful in order to tailor the porcelain microstructure to obtain better mechanical properties.

11.2.2 Processing

11.2.2.1 DS process

The study of DS process suggests that an optimal glassy phase, which is required to produce fully dense porcelain, can be calculated. Thus, it is possible that the optimal glassy phase might be different for different processing methods. The effect of rapid heating rate on the internal residual stress generation requires further investigation, because porcelain is composed of mullite, residual albite, quartz and glass, all of which have different coefficients of thermal expansion. Thus, a useful study would be to determine the residual stress produced by different processing routes. In addition, it is important to sinter larger porcelain samples because the effect of heating rate may be different.

11.2.2.2 SPS process

Special properties of porcelain might be produced by the SPS process, for example, mullite oriented perpendicular to the compressive plane might have different properties (electrical and/or dielectric) in different directions.

Dissolution of mullite under SPS conditions is not fully understood. It would be useful to further investigate the effect of dwell time, pressure and temperature on mullite dissolution.

11.2.2.3 MWS process

A more accurate sample temperature measurement system is important for the MWS process which would help to better control the heating rate. A simulation of microwave distribution in the microwave furnace cavity and in the sample needs to be done to enable a more uniform temperature distribution to be obtained. A hybrid furnace, electric-microwave heating, infrared-microwave heating, gas-microwave heating for porcelain production can be potentially developed.

11.2.2.4 FS process

The densification mechanisms of flash sintering in porcelain should be further investigated. Since the liquid phase produced during the flash sintering causes localised melting, it would be worth to reduce or reformulate the liquid phase chemistry. The effect of electric current direction might affect the mullite orientation which could produce some interesting properties.

In addition, the technological properties of the flash sintered porcelain must be investigated, as to the best of the authors knowledge, no literature reports any comparison of porcelain properties between flash sintering and conventional sintering.

Reference

1. Chanthapan, S., Rape, A., Gephart, S., Kulkarni, A. K., and Singh, J., *Industrial Scale Field Assisted Sintering*. Advanced materials & processes, 2011. 169(8): p. 25-28.

2. Tokita, M., *Large-size WC/Co functionally graded materials fabricated by spark plasma sintering (SPS) method*. Materials Science Forum, 2003. 423 (-): p. 39-44.

3. Grasso, S., Sakka, Y., abd Maizza, G., *Electric current activated/assisted sintering (ECAS): a review of patents 1906–2008*. Science and Technology of Advanced Materials, 2009.10(5): p. 053001.

4. Rajeswari, K., Hareesh, U. S., Subasri, R., Chakravarty, D., and Johnson, R., *Comparative evaluation of spark plasma (SPS), microwave (MWS), two stage sintering (TSS) and conventional sintering (CRH) on the densification and micro structural evolution of fully stabilized zirconia ceramics.* Science of Sintering, 2010.42(3): p.259-267.

5. The European Ceramic Industry Association. *Europe's ceramic industry in 2015*. Cerame-Unie 2015 Annual Report, 2016. p. 4

6. Barald, L., *World production and consumption of ceramic tiles*. Ceramic World Review—Technology, News, Market, 2017. (127): p. 56-70.

7. MECS—Acimac Research Department, *World sanitaryware production and exports*. Tile International, 2017. (1): p. 70-75.

8. Huson, D., and Hoskins, S., *3D printed ceramics for tableware, artists/designers and specialist applications*. Key Engineering Materials, 2014. 608 :p. 351-357.

9. Niederhãusern, S., Bondi, M., and Bondioli, F., *Self-cleaning and antibacteric ceramic tile surface*. International Journal of Applied Ceramic Technology, 2013. 10(6): p. 949-956.

10. Machida, M., Norimoto, K., and Kimura, T., *Antibacterial activity of photocatalytic titanium dioxide thin films with photodeposited silver on the surface of sanitary ware*. Journal of the American Ceramic society, 2005. 88(1): p. 95-100.

11. Bondioli, F., Taurino, R., and Ferrari, A., *Functionalization of ceramic tile surface by sol–gel technique*. Journal of Colloid and Interface Science, 2009. 334(2): p. 195-201.

12. Jung, D., Kim, U., and Cho, W., *Study on the growth of monoclinic VO_2 phase applicable for thermochromic ceramic tile*. Journal of Korean Ceramics Society, 2015. 52(5): p. 361-365.

13. Pini, M., Ferrari, A. M., Gamberini, R., Neri, P., and Rimini, B., *Life cycle assessment of a large, thin ceramic tile with advantageous technological properties.* The International Journal of Life Cycle Assessment, 2014. 19(9): p. 1567-1580.

14. Balistreri, J., and Dion, S., *Creating ceramic art using rapid prototyping*, Proceeding Association for Computing Machinery (ACM) Siggraph 2008, posters Article No. 18, ACM New York, NY, USA.

15. McDermott, A., *Ceramic Industry: Current / Future Energy Efficiency Solutions*. Presentation at PLEEC Energy Efficiency Forum, 2013. Stoke-on-Trent, UK.

16. Monfort, E., Mezquita, A., Granel, R., Vaquer, E., Escrig, A., Miralles, A., and Zaera, V., *Analysis of energy consumption and carbon dioxide emissions in ceramic tile manufacture*. Boletin De La Sociedad Espanola De Ceramica Y Vidrio, 2010. 49(4): p.303-310.

17. Mezquita, A., Boix, J., Monfort, E., and Mallol, G., *Energy saving in ceramic tile kilns: Cooling gas heat recovery*. Applied Thermal Engineering, 2014. 65(1): p.102-110.

18. Le, A., *Optimisation of Energy Usage in Ceramic Kiln Using Pinch Technique*. Chemical Engineering Transactions, (2018). 63(-): p. 313-318.

19. Lucideon, *Flash Sintering: Manufacturing cost reduction and energy efficiency are key priorities for many industries.* Available from: https://www.lucideon.com/materials-technologies/flash-sintering. [Accessed 15 August 2017].

20. Rahaman M.N., *Sintering of Ceramics*. 2008, FL, CRC Press.

21. Specht E., *Process Engineering of Metals and Ceramics*. Available from: http://www.ltv.ovgu.de/ltv_media/Downloads/Lehre/Vorlesungen/Process+Engineering+of+Metals+and+Ceramics/Ceramics+Production.pdf. [Accessed 15 August 2017].

22. Lee, W.E., and Rainforth, M., *Ceramic Microstructures: property control by processing*. 1994, London, Chapman-Hall.

23. Kang, S. J. L., *Sintering: densification, grain growth and microstructure*. 2004, Oxford, Elsevier Butterworth-Heinemann.

24. German, R.M., *Sintering: from empirical observations to scientific principles*. 2014, MA, Butterworth-Heinemann.

25. Kingery, W.D., Bowen, H. K., and Uhlmann, D. R., *Introduction to ceramics*.1976, NY, Wiley.

26. Anselmi-Tamburini, U., Garay, J. E., Munir, Z. A., Tacca, A., Maglia, F., and Spinolo, G., *Spark plasma sintering and characterization of bulk nanostructured fully stabilized zirconia: part I. densification studies*. Journal of materials research, 2004. 19(11): p. 3255-3262.

27. Olevsky, E., and Dudina, D., *Field-Assisted Sintering Science and Applications.* 2018, Cham, Switzerland, Springer International Publishing.

28. Sladek, R., *The fast firing process in the ceramic industry*. Interceram, 1986. 35(4): p. 5.

29. Olevsky, E.A., Kandukuri, S., and Froyen, L., *Consolidation enhancement in spark-plasma sintering: Impact of high heating rates*. Journal of Applied Physics, 2007. 102(11): p. 114913.

30. Obare, J., Griffin, W.D., and Conrad, H., *Effects of heating rate and DC electric field during sintering on the grain size distribution in fully sintered tetragonal zirconia polycrystals stabilized with 3% molar yttria (3Y-TZP)*. Journal of Materials Science, 2012. 47(13): p. 5141-5147.

31. Guire, E.D., *Ceram building first commercial-scale flash sintering kiln.* Available from: http://ceramics.org/ceramic-tech-today/ceram-building-first-commercialscale-flash-sintering-kiln. [Accessed 12 December 2017].

32. Baumgartner, C.E., *Fast firing and conventional sintering of lead zirconate titanate ceramic*. Journal of the American Ceramic Society, 1988. 71(7): p. C-350-C-353.

33. Seal, A., Mazumder, R., Sen, A., and Maiti, H. S, *Fast firing of lead zirconate titanate ceramics at low temperature*. Materials Chemistry and Physics, 2006. 97(1): p. 14-18.

34. Miclea, C., Tanasoiu, C., Miclea, C. F., Amarande, L., Iorgulescu, R., Tanasoiu, V., and Moscu, S., *Advanced technology for making PZT type ceramics by fast firing*. Journal of Optoelectronics and Advanced Materials, 2001. 3(1): p. 83-88.

35. Garcia, D. E., Seidel, J., Janssen, R., and Claussen, N., *Fast firing of alumina.* Journal of the European Ceramic Society, 1995. 15(10): p. 935-938.

36. Possamai, T.S., Oba, R., Nicolau, V. P., Hotza, D., and García, D. E., *Numerical simulation of the fast firing of alumina in a box furnace*. Journal of the American Ceramic Society, 2012. 95(12): p. 3750-3757.

37. Dondi, M., Marsigli, M., and Venturi, I., *Microstructure and mechanical properties of clay bricks: comparison between fast firing and traditional firing.* British Ceramic Transactions, 1999. 98(1): p. 12-18.

38. Sanchez, E., García-Ten, J., Sanz, V., and Moreno, A., *Porcelain tile: Almost 30 years of steady scientific-technological evolution.* Ceramics International, 2010. 36(3): p. 831-845.

39. Saleiro, G.T., and Holanda, J.F., *Processing of red ceramic using a fast-firing cycle*. Cerâmica, 2012. 58(347): p. 393-399.

40. Manfredini, T., and Pennisi, L*., Recent innovations in fast firing process*, in Science of Whitewares, Henkes, V., Onoda, G., Carty, W., Editors. 1996, Westerville, OH, The American Ceramic Society.

41. Schulle, W., *Trends and problems in the development of the porcelain firing process*. Interceram, 2003. 52(4): p. 192-196.

42. Carty, W.M., and Senapati, U., *Porcelain—Raw materials, processing, phase evolution, and mechanical behaviour*. Journal of the American Ceramic Society, 1998. 81(1): p. 3-20.

43. Omori, M., *Sintering, consolidation, reaction and crystal growth by the spark plasma system (SPS)*. Materials Science and Engineering: A, 2000. 287(2): p. 183-188.

44. Hungría, T., Galy, J., and Castro, A., *Spark plasma sintering as a useful technique to the nanostructuration of piezo-ferroelectric materials*. Advanced Engineering Materials, 2009. 11(8): p. 615-631.

45. Grasso, S., Sakka, Y., and Maizza, G., *Electric current activated/assisted sintering (ECAS): a review of patents 1906–2008*. Science and Technology of Advanced Materials, 2009. 10(5): p. 053001.

46. Munir, Z.A., Anselmi-Tamburini, U., and Ohyanagi, M., *The effect of electric field and pressure on the synthesis and consolidation of materials: A review of the spark plasma sintering method*. Journal of Materials Science, 2006. 41(3): p. 763-777.

47. Nightingale, R. E. (Ed.). *Nuclear Graphite*: Prepared under the Auspices of the Division of Technical Information United States Atomic Energy Commission. (2013). Academic press.

48. Rahaman, M. N. Ceramic processing and sintering. 2003, FL, CRC press.

49. Mackie, A. J., Hatton, G. D., Hamilton, H. G., Dean, J. S., and Goodall, R. *Carbon uptake and distribution in spark plasma sintering (SPS) processed Sm (Co, Fe, Cu, Zr)*. Materials Letters, 2016. 171: p. 14-17.

50. Solodkyi, I., Xie, S. S., Zhao, T., Borodianska, H., Sakka, Y., and Vasylkiv, O., *Synthesis of B_6O powder and spark plasma sintering of B_6O and B_6O–B_4C ceramics*. Journal of the Ceramic Society of Japan,2013. 121(1419): p. 950-955.

51. Grasso, S., Sakka, Y., and Maizza, G., *Pressure effects on temperature distribution during spark plasma sintering with graphite sample*. Materials Transactions, 2009. 50(8): p. 2111-2114.

52. Raj, R., Cologna, M., and Francis, J.C., *Influence of externally imposed and internally generated electrical fields on grain growth, diffusional creep, sintering and related phenomena in ceramics*. Journal of the American Ceramic Society, 2011. 94(7): p. 1941-1965.

53. Antolovich, S.D., and Conrad, H., *The effects of electric currents and fields on deformation in metals, ceramics, and ionic materials: An interpretive survey.* Materials and Manufacturing Processes, 2004. 19(4): p. 587-610.

54. Holland, T.B., Anselmi-Tamburini, U., Quach, D.V., Tran, T.B., and Mukherjee, A. K., *Local field strengths during early stage field assisted sintering (FAST) of dielectric materials*. Journal of the European Ceramic Society, 2012. 32(14): p. 3659-3666.

55. Zhang, Z. H., Liu, Z. F., Lu, J. F., Shen, X. B., Wang, F. C., and Wang, Y. D., *The sintering mechanism in spark plasma sintering–proof of the occurrence of spark discharge*. Scripta materialia, 2014. 81(-): p. 56-59.

56. Groza, J. R., and Zavaliangos, A. *Sintering activation by external electrical field*. Materials Science and Engineering: A, 2000. 287(2): p. 171-177.

57. Chakraborty, S., Mallick, A. R., Debnath, D., and Das, P. K., *Densification, mechanical and tribological properties of ZrB_2 by SPS: Effect of pulsed current.* International Journal of Refractory Metals and Hard Materials, 2015. 48(0): p. 150-156.

58. Santanach, J.G., Estournès, C., Weibel, A., Chevallier, G., Bley, V., Laurent, C., and Peigney, A., *Influence of pulse current during spark plasma sintering evidenced on reactive alumina–hematite powders*. Journal of the European Ceramic Society, 2011. 31(13): p. 2247-2254.

59. Chen, W., Anselmi-Tamburini, U., Garay, J.E., Groza, J.R., and Munir, Z.A., *Fundamental investigations on the spark plasma sintering/synthesis process: I. Effect of dc pulsing on reactivity*. Materials Science and Engineering: A, 2005. 394(1): p. 132-138.

60. Xie, G., Ohashi, O., Chiba, K., Yamaguchi, N., Song, M., Furuya, K., and Noda, T., *Frequency effect on pulse electric current sintering process of pure aluminum powder.* Materials Science and Engineering: A, 2003. 359(1–2): p. 384-390.

61. Cologna, M., Rashkova, B., and Raj, R., *Flash sintering of nanograin zirconia in < 5s at 850 °C*. Journal of the American Ceramic Society, 2010. 93(11): p. 3556-3559.

62. Yu, M., Grasso, S., Mckinnon, R., Saunders, T., and Reece, M.J., *Review of flash sintering: materials, mechanisms and modelling*. Advances in Applied Ceramics, 2017. 116(1): p. 24-60.

63. Gonzalez-Julian, J., and Guillon, O., *Effect of electric field/current on liquid phase sintering*. Journal of the American Ceramic Society, 2015. 98(7): p. 2018-2027.

64. Zapata-Solvas, E., Gómez-García, D., Domínguez-Rodríguez, A., and Todd, R.I., *Ultra-fast and energy-efficient sintering of ceramics by electric current concentration*. Scientific Reports, 2015. 5. 8513.

65. Zapata-Solvas, E., Bonilla, S., Wilshaw, P.R., and Todd, R.I., *Preliminary investigation of flash sintering of SiC*. Journal of the European Ceramic Society, 2013. 33(13): p. 2811-2816.

66. Cologna, M., Francis, J.S., and Raj, R., *Field assisted and flash sintering of alumina and its relationship to conductivity and MgO-doping*. Journal of the European Ceramic Society, 2011. 31(15): p. 2827-2837.

67. Baraki, R., Schwarz, S., and Guillon, O., *Effect of electrical field/current on sintering of fully stabilized zirconia*. Journal of the American Ceramic Society, 2012. 95(1): p. 75-78.

68. Hewitt, I., Lacey, A., and Todd, R.I., *A mathematical model for flash sintering.* Mathematical Modelling of Natural Phenomena, 2015. 10(6): p. 77-89.

69. Narayan, J., *A new mechanism for field-assisted processing and flash sintering of materials*. Scripta Materialia, 2013. 69(2): p. 107-111.

70. Kim, S.W., Kang, S.L., and Chen, I.W., *Electro-sintering of yttria-stabilized cubic zirconia*. Journal of the American Ceramic Society, 2013. 96(5): p. 1398-1406.

71. Kim, S.W., Kim, S.G., Jung, J.I., Kang, S.J.L., and Chen, I.W., *Enhanced grain boundary mobility in yttria-stabilized cubic zirconia under an electric current.* Journal of the American Ceramic Society, 2011. 94(12): p. 4231-4238.

72. Naik, K., Jha, S. K., and Raj, R., *Correlations between conductivity, electroluminescence and flash sintering.* Scripta Materialia, 2016. 118: p. 1-4.

73. Lebrun, J. M., and Raj, R., *A First report of photoemission in experiments related to flash sintering*. Journal of the American Ceramic Society, 2014. 97(8): p. 2427-2430.

74. Muccillo, R., and Muccillo, E.S., *Light emission during electric field-assisted sintering of electroceramics*. Journal of the European Ceramic Society, 2015. 35(5): p. 1653-1656.

75. Raj, R., *Joule heating during flash-sintering*. Journal of the European Ceramic Society, 2012. 32(10): p. 2293-2301.

76. Todd, R., Zapata-Solvas, E., Bonilla, R.S., Sneddon, T., and Wilshaw, P.R., *Electrical characteristics of flash sintering: thermal runaway of Joule heating*. Journal of the European Ceramic Society, 2015. 35(6): p. 1865-1877.

77. Jha, S., Lebrun, J., and R. Raj, *Phase transformation in the alumina–titania system during flash sintering experiments*. Journal of the European Ceramic Society, 2016. 36(3): p. 733-739.

78. Raj, R., *Analysis of the power density at the onset of flash sintering.* Journal of the American Ceramic Society, 2016. 99(10): p. 3226-3232.

79. Cologna, M., Prette, A.L., and Raj, R*., Flash-sintering of cubic yttria-stabilized zirconia at 750 °C for possible use in SOFC manufacturing*. Journal of the American Ceramic Society, 2011. 94(2): p. 316-319.

80. Muccillo, R., and Muccillo, E., *Shrinkage control of yttria-stabilized zirconia during ac electric field-assisted sintering*. Journal of the European Ceramic Society, 2014. 34(15): p. 3871-3877.

81. Lebrun, J.M., Morrissey, T.G., Francis, J.S., Seymour, K.C., Kriven, W.M., and Raj, R., *Emergence and extinction of a new phase during on–off experiments related to flash sintering of 3YSZ*. Journal of the American Ceramic Society, 2015. 98(5): p. 1493-1497.

82. Prette, A.L., Cologna, M., Sglavo, V., and Raj, R*., Flash-sintering of Co_2MnO_4 spinel for solid oxide fuel cell applications*. Journal of Power Sources, 2011. 196(4): p. 2061-2065.

83. M'Peko, J.C., Francis, J.S., and Raj, R., *Field-assisted sintering of undoped $BaTiO_3$: microstructure evolution and dielectric permittivity*. Journal of the European Ceramic Society, 2014. 34(15): p. 3655-3660.

84. Lemke, F., Rheinheimer, W., and Hoffmann, M.J., *A comparison of power-controlled flash sintering and conventional sintering of strontium titanate*. Scripta Materialia, 2017. 130: p. 187-190.

85. Zhang, Y., Jiuyuan, N., and Jian, L., *Effects of phase and doping on flash sintering of TiO_2*. Journal of the Ceramic Society of Japan, 2016. 124(4): p. 296-300.

86. Zhang, Y., and Luo, J., *Promoting the flash sintering of ZnO in reduced atmospheres to achieve nearly full densities at furnace temperatures of <120 °C.* Scripta Materialia, 2015. 106: p. 26-29.

87. Bichaud, E., Chaix, J.M., Carry, C., Kleitz, M., and Steil, M.C., *Flash sintering incubation in Al_2O_3/TZP composites*. Journal of the European Ceramic Society, 2015. 35(9): p. 2587-2592.

88. Liu, D., Gao, Y., Liu, J., Li, K., Liu, F., Wang, Y., and An, L., *SiC whisker reinforced ZrO_2 composites prepared by flash-sintering*. Journal of the European Ceramic Society, 2016. 36(8): p. 2051-2055.

89. Liu, D., Gao, Y., Liu, J., Liu, F., Li, K., Su, H., Wang, Y., and An, L., *Preparation of Al_2O_3–$Y_3Al_5O_{12}$–ZrO_2 eutectic ceramic by flash sintering*. Scripta Materialia, 2016. 114: p. 108-111.

90. Biesuz, M., and Sglavo, V.M., *Liquid phase flash sintering in magnesia silicate glass-containing alumina*. Journal of the European Ceramic Society, 2017. 37(2): p. 705-713.

91. Trombin, F., and Raj, R., *Developing processing maps for implementing flash sintering into manufacture of whiteware ceramics*. American Ceramic Society Bulletin, 2014. 93(6): p. 4.

92. Jha, S.K., and Raj, R., *The effect of electric field on sintering and electrical conductivity of titania*. Journal of the American Ceramic Society, 2014. 97(2): p. 527-534.

93. Zhang, Y., Jung, J.I., and Luo, J., *Thermal runaway, flash sintering and asymmetrical microstructural development of ZnO and ZnO–Bi_2O_3 under direct currents*. Acta Materialia, 2015. 94: p. 87-100.

94. Haque, K.E., *Microwave energy for mineral treatment processes—a brief review*. International Journal of Mineral Processing, 1999. 57(1): p. 1-24.

95. Oghbaei, M., and Mirzaee, O., *Microwave versus conventional sintering: A review of fundamentals, advantages and applications*. Journal of Alloys and Compounds, 2010. 494(1–2): p. 175-189.

96. Katz, J.D., *Microwave sintering of ceramics*. Annual Review of Materials Science, 1992. 22(1): p. 153-170.

97. Mishra, R. R., and Sharma, A. K., *Microwave–material interaction phenomena: heating mechanisms, challenges and opportunities in material processing*. Composites Part A: Applied Science and Manufacturing, 2016. 81: p. 78-97.

98. Clark, D. E., and Sutton, W. H.. *Microwave processing of materials.* Annual Review of Materials Science, 1996. 26(1):p. 299-331..

99. Clark, D. E., and Folz D.C., *What is microwave processing? in microwave solutions for ceramic engineers*. Clark, D. E., Folz, D.C., Folgar, C.E., Mahmoud, M.M., Editors. 2005, MA, Wiley. p.494.

100. Menezes, R.R., Souto, P.M., and Kiminami, R.H., *Microwave fast sintering of ceramic materials*. 2012. Intech Open Access Publisher.

101. Kenkre, V., Skala, L., Weiser, M.W., and Katz, J.D., *Theory of microwave interactions in ceramic materials: the phenomenon of thermal runaway*. Journal of materials science, 1991. 26(9): p. 2483-2489.

102. Wang, J., Binner, J., Vaidhyanathan, B., Joomun, N., Kilner, J., Dimitrakis, G., and Cross, T.E., *Evidence for the microwave effect during hybrid sintering.* Journal of the American Ceramic Society, 2006. 89(6): p. 1977-1984.

103. Gaustad, G., Metcalfe, J., Shulman, H., and Allan. S., *Susceptor investigation for microwave heating applications.* in Innovative Processing and Synthesis of Ceramics, Glasses and Composites VIII: Proceedings of the 106th Annual Meeting of The American Ceramic Society, Indianapolis, Indiana, USA 2004, Ceramic Transactions. 2005. Wiley-American Ceramic Society.

104. Shulman, H., Fall, M., and Allan. S., *Microwave assist technology for product improvement and energy efficiency*. in 4th Korea/Japan International Symposium on Material Science and Resources Recycling. 2007.

105. Norton, F.H., *Fine ceramics: technology and applications*. 1978, Huntington, NY, R.E.Krieger Pub.Co. p.507.

106. Iqbal, Y., and Lee, W.E., *Microstructural evolution in triaxial porcelain*. Journal of the American Ceramic Society, 2000. 83(12): p. 3121-3127.

107. Zanelli, C., Raimondo, M., Guarini, G., and Dondi, M., *The vitreous phase of porcelain stoneware: composition, evolution during sintering and physical properties*. Journal of Non-Crystalline Solids, 2011. 357(16-17): p. 3251-3260.

108. Amigó, J.M., Serrano, F.J., Kojdecki, M.A., Bastida, J., Esteve, V., Reventós, M.M., and Martí, F., *X-ray diffraction microstructure analysis of mullite, quartz and corundum in porcelain insulators*. Journal of the European Ceramic Society, 2005. 25(9): p. 1479-1486.

109. Ece, O.I., and Nakagawa, Z., *Bending strength of porcelains.* Ceramics International, 2002. 28(2): p. 131-140.

110. Carty, W.M., *Observations on the Glass Phase Composition in Porcelains.* Materials & Equipment/Whitewares: Ceramic Engineering and Science Proceedings. 2008, OH, The American Ceramic Society. 23(2): p. 79-94.

111. Carty, W.M., and Pinto, B.M., *Effect of filler size on the strength of porcelain bodies.* Materials & Equipment/Whitewares: Ceramic Engineering and Science Proceedings, 2008. OH, The American Ceramic Society. 23(2): p. 95-105.

112. Schroeder, P.A., and Erickson, G., *Kaolin: From ancient porcelains to nanocomposites.* Elements, 2014. 10(3): p. 177-182.

113. Maynard, R., Millman, N., Iannicelli, J., and Huber, J.M., *A method for removing titanium dioxide impurities from kaolin.* Clays and Clay Minerals, 1969. 17(2): p. 59-62.

114. Kyonka, J.C., and Cook, R.V., *The properties of feldspars and their use in whitewares.* University of Illinois Bulletin, 1954. 51 (38): p. 5-34.

115. Amigo, J.M., Clausell, J.V., Esteve, V., Delgado, J.M., Reventos, M.M., Ochando, L.E., Debaerdemaeker, T., and Marti, F., *X-ray powder diffraction phase analysis and thermomechanical properties of silica and alumina porcelains.* Journal of the European Ceramic Society, 2004. 24(1): p. 75-81.

116. Bragança, S., and Bergmann, C*., A view of whitewares mechanical strength and microstructure.* Ceramics International, 2003. 29(7): p. 801-806.

117. Richerson, D.W., *Modern ceramic engineering: properties, processing, and use in design*. 2005, NW, CRC press, p.860.

118. Lundin, S.T., *Studies on triaxial whiteware bodies.* 1959, Stockholm, Almqvist & Wiksell, p. 197.

119. Okada, K., Ōtsuka, N., and Ossaka, J., *Characterization of spinel phase formed in the kaolin-mullite thermal sequence.* Journal of the American Ceramic Society, 1986. 69(10): p. C-251-C-253.

120. Sonuparlak, B., Sarikaya, M., and Aksay, I.A., *Spinel phase formation during the 980 °C exothermic reaction in the kaolinite-to-mullite reaction series.* Journal of the American Ceramic Society, 1987. 70(11): p. 837-842.

121. Iqbal, Y., *On the glassy phase in tri-axial porcelain bodies.* Journal of Pakistan Materials Society, 2008. 2(2): p. 62-71.

122. Iqbal, Y., and Lee, W.E., *Fired porcelain microstructures revisited.* Journal of the American Ceramic Society, 1999. 82(12): p. 3584-3590.

123. Duval, D.J., Risbud, S.H., and Shackelford, J.F., *Mullite*, in Ceramic and Glass Materials, Shackelford, J.F., and Doremus, R.H., Editors. 2008, Boston, MA, Springer. p. 27-39.

124. Schneider, H., Fischer, R.X., and Schreuer, J., *Mullite: crystal structure and related properties.* Journal of the American Ceramic Society, 2015. 98(10): p. 2948-2967.

125. Schneider, H., and Eberhard, E., *Thermal expansion of mullite.* Journal of the American Ceramic Society, 1990. 73(7): p. 2073-2076.

126. Osendi, M., and Baudin, C., *Mechanical properties of mullite materials.* Journal of the European Ceramic society, 1996. 16(2): p. 217-224.

127. Lessing, P., Gordon, R., and Mazdiyasni, K., *Creep of polycrystalline mullite.* Journal of the American Ceramic Society, 1975. 58(3-4): p. 149-149.

128. Ohira, H., Ismail, M. U., Yamamoto, Y., Akiba, T., and Sōrniya, S., *Mechanical properties of high purity mullite at elevated temperatures.* Journal of the European Ceramic Society, 1996. 16(2): p. 225-229.

129. Hoffman, D.W., Roy, R., and Komarneni, S., *Diphasic xerogels, a new class of materials: phases in the system Al_2O_3-SiO_2.* Journal of the American Ceramic Society, 1984. 67(7): p. 468-471.

130. Aramaki, S., and Roy, R., *Revised phase diagram for the system Al_2O_3-SiO_2.* Journal of the American Ceramic Society, 1962. 45(5): p. 229-242.

131. Schneider, H., and Rymon-Lipinski, T., *Occurrence of pseudotetragonal mullite.* Journal of the American Ceramic Society, 1988. 71(3): p. C-162-164.

132. Cameron, W. E., *Composition and cell dimension of mullite.* American Ceramic Society Bulletin, 1977. 56(11): p.1003-1007.

133. Fischer, R.X., Gaede-Köhler, A., Birkenstock, J., and Schneider, H., *Mullite and mullite-type crystal structures.* International Journal of Materials Research, 2012. 103(4): p. 402-407.

134. Frscnnn, R.X., *Crystal structure of Al-rich mullite.* American Mineralogist, 1994. 79(9-10): p. 983-990.

135. Ban, T., and Okada, K., *Structure refinement of mullite by the Rietveld method and a new method for estimation of chemical composition.* Journal of the American Ceramic Society, 1992. 75(1): p. 227-230.

136. Chen, C., Lan, G., and Tuan, W., *Preparation of mullite by the reaction sintering of kaolinite and alumina.* Journal of the European Ceramic Society, 2000. 20(14-15): p. 2519-2525.

137. Pask, J.A., and Tomsia, A.P., *Formation of mullite from sol-gel mixtures and kaolinite.* Journal of the American Ceramic Society, 1991. 74(10): p. 2367-2373.

138. Panneerselvam, M., and Rao, K., *Novel microwave method for the synthesis and sintering of mullite from kaolinite.* Chemistry of Materials, 2003. 15(11): p. 2247-2252.

139. Al-Jarsha, Y., Emblem, H.G., Jones, K., Rahman, M.A., Davies, T.J., Wakefield, R., and Sargeant, G.K., *Preparation, characterization and uses of mullite grain.* Journal of Materials Science, 1990. 25(6): p. 2873-2880.

140. Schneider, H., Okada K., and Pask. J., *Mullite and mullite ceramics*. 1994, Chichester, Wiley. p. 266.

141. Tripathi, H.S., and Banerjee, G., *Synthesis and mechanical properties of mullite from beach sand sillimanite: effect of TiO_2.* Journal of the European Ceramic Society, 1998. 18(14): p. 2081-2087.

142. Tripathi, H.S., Das, S.K., and Banerjee, G., *Thermal shock behaviour of high alumina aggregates derived from sillimanite beach sand with and without Fe_2O_3 doping*. Ceramics International, 2000. 26(1): p. 1-6.

143. Bhattacharyya, S., Das, S.K., and Mitra, N.K., *Effect of titania on fired characteristics of triaxial porcelain.* Bulletin of Materials Science, 2005. 28(5): p. 445-452.

144. Piva, R.H., Vilarinho, P., Morelli, M.R., Fiori, M.A., and Montedo, O. K., *Influence of Fe_2O_3 content on the dielectric behaviour of aluminous porcelain insulators.* Ceramics International, 2013. 39(7): p. 7323-7330.

145. Skinner, K.G., Cook, W.H., Potter, R.A., and Palmour, H., *Effect of TiO_2, Fe_2O_3, and alkali on mineralogical and physical properties of mullite-type and mullite-forming Al_2O_3-SiO_2 mixtures: I.* Journal of the American Ceramic Society, 1953. 36(11): p. 349-356.

146. Tripathi, H.S., Ghosh, A., Halder, M.K., Mukherjee, B., and Maiti, H.S., *Microstructure and properties of sintered mullite developed from Indian bauxite.* Bulletin of Materials Science, 2012. 35(4): p. 639-643.

147. Percival, H., Duncan, J., and Foster, P., *Interpretation of the kaolinite-mullite reaction sequence from infrared absorption spectra*. Journal of the American Ceramic Society, 1974. 57(2): p. 57-61.

148. Brown, I.W., MacKenzie, K.J., Bowden, M.E., and Meinhold, R.H., *Outstanding problems in the kaolinite-mullite reaction sequence investigated by ^{29}Si and ^{27}Al solid-state nuclear magnetic resonance: 11, high-temperature*

transformations of metakaolinite. Journal of the American Ceramic Society, 1985. 68(6): p. 298-301.

149. McConville, C., Lee, W.E., and Sharp, J.H., *Microstructural evolution in fired kaolinite*. British Ceramic Transactions, 1998. 97(4): p. 162-168.

150. Brindley, G., and Nakahira, M., *The kaolinite-mullite reaction series: I, a survey of outstanding problems.* Journal of the American Ceramic Society, 1959. 42(7): p. 311-314.

151. Chen, Y.F., Wang, M.C., and Hon, M.H., *Phase transformation and growth of mullite in kaolin ceramics.* Journal of the European Ceramic Society, 2004. 24(8): p. 2389-2397.

152. Chakraborty, A., and Ghosh, D., *Reexamination of the kaolinite-to-mullite reaction series.* Journal of the American Ceramic Society, 1978. 61(3-4): p. 170-173.

153. Srikrishna, K., Thomas, G., Martinez, R., Corral, M.P., De Aza, S., and Moya, J.S., *Kaolinite-mullite reaction series: a TEM study*. Journal of Materials Science, 1990. 25(1): p. 607-612.

154. Chakraborty, A.K., *DTA study of preheated kaolinite in the mullite formation region.* Thermochimica Acta, 2003. 398(1-2): p. 203-209.

155. Comeforo, J., Fischer, R., and Bradley, W., *Mullitization of kaolinite.* Journal of the American Ceramic Society, 1948. 31(9): p. 254-259.

156. Martín-Márquez, J., Rincón, J.M., and Romero, M., *Mullite development on firing in porcelain stoneware bodies.* Journal of the European Ceramic Society, 2010. 30(7): p. 1599-1607.

157. Romero, M., Martín-Márquez, J., and Rincón, J.M., *Kinetic of mullite formation from a porcelain stoneware body for tiles production.* Journal of the European Ceramic Society, 2006. 26(9): p. 1647-1652.

158. Seymour, D.I., Misture, S.T., and Carty, W.M., *Development of fast firing schedules for porcelains from the study of mullite formations in porcelains.* Materials & Equipment/Whitewares: Ceramic Engineering and Science Proceedings, 2009. OH, The American Ceramic Society. 22(2): p. 161.

159. Zanelli, C., Raimondo, M., Dondi, M., Guarini, G., and Tenorio, P.M., *Sintering mechanisms of porcelain stoneware tiles.* In Qualicer 2004, Proc. VIII World Cong. Ceramic Tile Quality, Cámara Official de Comercio, Industria y Navegación, Castellón, Spain. papers C (2004) 247-259.

160. Lerdprom, W. *Firing of porcelain,* [MS. Thesis]. New York State College of Ceramics at Alfred University. 2014, Alfred, NY.

161. Lee, W.E., and Iqbal, Y., *Influence of mixing on mullite formation in porcelain.* Journal of the European Ceramic Society, 2001. 21(14): p. 2583-2586.

162. Dannert, C., Durschang, B., Raether, F., and Becker, F., *Optimisation of sintering processes for porcelain using in-situ measuring methods.* Glass Science Technology, 2003. 76(-): p. 71.

163. Martín-Márquez, J., De la Torre, A.G., Aranda, M.A., Rincon, J.M., and Romero, M., *Evolution with temperature of crystalline and amorphous phases in porcelain stoneware.* Journal of the American Ceramic Society, 2009. 92(1): p. 229-234.

164. Martín-Márquez, J., Rincón, J.M., and Romero, M., *Effect of firing temperature on sintering of porcelain stoneware tiles.* Ceramics International, 2008. 34(8): p. 1867-1873.

165. Lee, W.E., Souza, G.P., McConville, C.J., Tarvornpanich, T., and Iqbal, Y., *Mullite formation in clays and clay-derived vitreous ceramics.* Journal of the European Ceramic Society, 2008. 28(2): p. 465-471.

166. Sacks, M.D., *Sintering Behavior of Mullite-Containing Materials,* [PhD Thesis]. 1979, University of California. Berkeley, CA.

167. Johnson, S.M., *Mullitization of kaolinite and Al_2O_3-SiO_2 mixtures*, [MS. Thesis]. 1979, University of California. Berkeley, CA.

168. Serrano, F.J., Bastida, J., Amigó, J.M., and Sanz, A., *XRD line broadening studies on mullite.* Crystal Research and Technology, 1996. 31(8): p. 1085-1093.

169. Seymour, D.I., *Phase evolution of electrical porcelains during firing*, [MS. Thesis]. 2000, New York State College of Ceramics at Alfred University.Alfred, NY.

170. Pinto, B., Carty, W. M., and Misture, S., *Measurement of Residual Strain in Quartz Particles in Porcelain.* presented at Science of Whitewares III, Alfred University, 12-14 June 2000.

171. Rambaldi, E., Carty, W.M., Tucci, A., and Esposito, L., *Using waste glass as a partial flux substitution and pyroplastic deformation of a porcelain stoneware tile body.* Ceramics International, 2007. 33(5): p. 727-733.

172. Jander, W., *Reaktionen im festen Zustande bei höheren Temperaturen. Reaktionsgeschwindigkeiten endotherm verlaufender Umsetzungen*. Zeitschrift für Anorganische und Allgemeine Chemie, 1927. 163(1): p. 1-30.

173. Krause, P., and Keetman, E., *Zur kenntnis der keramischen brennvorgange (On combustion processes in ceramics)*. Sprechsaal, 1936. 69: p. 45-47.

174. Lee, H., and Carty, W.M., *Glass phase composition in porcelains and correlation with firing temperature*. in Proceedings of the 106th Annual Meeting and Exposition of the American Ceramic Society. 2004, American Ceramic Society. Indianapolis, IN. p. 108-132.

175. Carty, W.M., Katz, M., and Gill, J., *The unity molecular formula approach to glaze development*, Materials & Equipment/Whitewares: Ceramic Engineering and Science Proceedings. 2008, OH, The American Ceramic Society. p. 95-107.

176. Hermansson, L., and Carlsson, R., *Crystallization of the glassy phase in whitewares.* Transactions and Journal of the British Ceramic Society, 1978. 77(2): p. 32-35.

177. Chaudhuri, S., *Influence of mineralizers on the constitution of hard porcelain: II, Microstructures.* American Ceramic Society Bulletin, 1974. 53(3): p. 251-254.

178. Moroz, I.K., and Mironova, A.F., *Establishing the composition of glass phase in an electrical-engineering porcelain.* Glass and Ceramics, 1986. 43(5): p. 209-212.

179. Amorós, J.L., Orts, M.J., Garcia-Ten, J., Gozalbo, A., and Sánchez, E*., Effect of the green porous texture on porcelain tile properties.* Journal of the European Ceramic Society, 2007. 27(5): p. 2295-2301.

180. Sanchez, E., Orts, M.J., García-Ten, J., García-Ten, J., and Cantavella, V., *Porcelain tile composition effect on phase formation and end products.* American Ceramic Society Bulletin, 2001. 80(6): p. 43-49.

181. Biasini, V., Dondi, M., Guarini, G., Raimondo, M., Argnani, A., and Di Primio, S., *Effect of talc and chlorite on sintering and technological behaviour of porcelain stoneware tiles.* Silicates Industrials, 2003(5-6): p. 67-73.

182. Zanelli, C., Raimondo, M., Dondi, M., Guarin, G., and Tenorio, P.M., *Sintering mechanisms of porcelain stoneware tiles.* In Qualicer 2004, Proc. VIII World Cong. Ceramic Tile Quality, Cámara Official de Comercio, Industria y Navegación, Castellón, Spain. papers C (2004) 247-259.

183. Salem, S., and Salem, A., *Mechanisms of Momentum Transport in Viscous Flow Sintering*. 2013. Intech Open Access Publisher.

184. Matteucci, F., Dondi, M., and Guarini, G., *Effect of soda-lime glass on sintering and technological properties of porcelain stoneware tiles.* Ceramics International, 2002. 28(8): p. 873-880.

185. Salem, A., Jazayeri, S.H., Rastelli, E., and Timellini, G., *Effect of nepheline syenite on the colorant behavior of porcelain stoneware body.* Journal of Ceramic Processing Research, 2009. 10(5): p. 621-627.

186. Tsukada, G., Sueyoshi, H., Kamibayashi, H., Tokuda, M., and Torii, M., *Bending strength of zirconia/porcelain functionally graded materials prepared using spark plasma sintering*. Journal of Dentistry, 2014. 42(12): p. 1569-1576.

187. Spotz, M.S., Skamser, D.J., and Johnson, D.L., *Thermal stability of ceramic materials in microwave heating*. Journal of the American Ceramic Society, 1995. 78(4): p. 1041-1048.

188. Menezes, R.R., Souto, P.M., and Kiminami, R.A., *Microwave hybrid fast sintering of porcelain bodies.* Journal of Materials Processing Technology, 2007. 190(1–3): p. 223-229.

189. Satapathy, L.N., *Microwave assisted sintering of high voltage porcelain material and its characterization.* Journal of Ceramic Processing Research, 2009. 10(5): p. 5.

190. Santos, T., Costa, L.C., Hennetier, L., Valente, M.A., Monteiro, J., and Sousa, J., *Microwave processing of porcelain tableware using a multiple generator configuration.* Applied Thermal Engineering, 2013. 50(1): p. 677-682.

191. Allan, S., Fall, M., Shulman, H., and Carnahan, G., *Microwave assist sintering of porcelain insulators with large cross section,* paper presented at the 33rd International Conference and Exposition on Advanced Ceramics and Composites, FL, 2009. Retrieved from http://www.ceralink.com/sites/default/files/MicrowaveAssistSintering ofPorcelainInsulatorswithLargeCross-section.pdf

192. Monteiro, J., Valente, M. A., Santos, T., Costa, L.C., and Sousa, J., *Microwave radiation: An alternative method to sinter utilitarian porcelain,* in Microwave & Optoelectronics Conference (IMOC), 2011 SBMO/IEEE MTT-S International, Natal, 2011, p. 561-564.

193. Hou, X., Amais, R.S., Jones, B.T., and Donati, G.L., *Inductively coupled plasma optical emission spectrometry*, in Encyclopedia of Analytical Chemistry, R.A. Meyers. Editor.2000, John Wiley & Sons Ltd, Chichester. p.1-17.

194. Manning, T.J., and Grow, W.R., *Inductively coupled plasma-atomic emission spectrometry.* The Chemical Educator, 1997. 2(1): p. 1-19.

195. Mie, G., *Contributions on the optics of turbid media, particularly colloidal metal solutions*. Annals of Physics, 1976. 25(3): p. 377-445.

196. Rawle, A., *Basic principles of particle size analysis*. 2014, Worcestershire, UK, Malvern Instruments. p. 8.

197. Leng, Y., *Introduction to Microscopic and Spectroscopic Methods*, 2008, Singapore, John Wiley & Sons (Asia).

198. Daw, J., *Measurement of specific heat capacity using differential scanning calorimeter*. In Report of US Department of Energy National Laboratory (INL/EXT-08-15056). 2008, Idaho, Idaho National Laboratory.

199. ASTM International, *E1296-11 Standard test method for determining specific heat capacity by differential scanning calorimetry*. 2011, ASTM International: West Conshohocken, PA, USA.

200. Yanagida, H., Koumoto, K., and Miyayama, M., *The chemistry of ceramics*. 1996, Chichester, Wiley. p. 97.

201. Callister, W.D., and Rethwisch, D.G., *Materials science and engineering: an introduction*. 2007, New York, Wiley. p. 720.

202. Parker, W., Jenkins, R.J., Butler, C.P., and Abbott, G.L., *Flash method of determining thermal diffusivity, heat capacity, and thermal conductivity*. Journal of Applied Physics, 1961. 32(9): p. 1679-1684.

203. ASTM International, *E1461 Standard Test Method for Thermal Diffusivity by the Flash Method.* 2013, ASTM International: West Conshohocken, PA, USA.

204. Min, S., Blumm, J., and Lindemann, A., *A new laser flash system for measurement of the thermophysical properties*. Thermochimica Acta, 2007. 455 (1-2): p. 46–49.

205. ASTM International, *E228 Standard Test Method for Linear Thermal Expansion of Solid Materials with a Push-Rod Dilatometer.* 2011, ASTM International: West Conshohocken, PA, USA.

206. Brantervik, K., and Niklasson, G., *Circuit models for cement based materials obtained from impedance spectroscopy.* Cement and Concrete Research, 1991. 21(4): p. 496-508.

207. Zia, A.I., and Mukhopadhyay S.C., *Impedance Spectroscopy and Experimental Setup.* In Electrochemical Sensing: Carcinogens in Beverages. Smart Sensors, Measurement and Instrumentation. 2016, Cham, Springer. p. 21-37.

208. Barsoukov, E., and Macdonald, J.R., (Eds). *Impedance spectroscopy: theory, experiment, and applications*. 2018, Hoboken, New Jersey, John Wiley & Sons.

209. Öijerholm, J., *Ionic transport of α-alumina below 1000 °C: an in-situ impedance spectroscopy study*, [PhD thesis]. KTH Royal Institute of Technology. 2004, Stockholm, Sweden.

210. Hiraga, T., Anderson, I.M., and Kohlstedt, D.L., *Grain boundaries as reservoirs of incompatible elements in the Earth's mantle.* Nature, 2004. 427(6976): p. 699.

211. Roberts, J.J., and Tyburczy, J.A., *Frequency dependent electrical properties of polycrystalline olivine compacts.* Journal of Geophysical Research: Solid Earth, 1991. 96(B10): p. 16205-16222.

212. Roberts, J., and Tyburczy, J., *Impedance spectroscopy of single and polycrystalline olivine: evidence for grain boundary transport.* Physics and Chemistry of Minerals, 1993. 20(1): p. 19-26.

213. Yoshino, T., Manthilake, G., Matsuzaki, T., and Katsura, T., *Dry mantle transition zone inferred from the conductivity of wadsleyite and ringwoodite.* Nature, 2008. 451(7176): p. 326.

214. Sethi, G., Bontempo, B., Furman, E., Horn, M.W., Lanagan, M.T., Bharadwaja, S.S.N., and Li, J., 2011. *Impedance analysis of amorphous and polycrystalline tantalum oxide sputtered films.* Journal of Materials Research, 26(6), pp.745-753.

215. Macdonald, J.R., *Impedance spectroscopy.* Annals of Biomedical Engineering, 1992. 20(3): p. 289-305.

216. Krupka, J., Breeze, J., Centeno, A., Alford, N., Claussen, T., and Jensen, L., *Measurements of permittivity, dielectric loss tangent, and resistivity of float-zone silicon at microwave frequencies*. IEEE Transactions on microwave theory and techniques, 2006. 54(11): p. 3995-4001.

217. Cullity, B.D., and Stock, S.R., *Elements of X-ray Diffraction*. 3rd Ed. 2001, NY, Prentice-Hall.

218. Chung, F.H., *Quantitative interpretation of X-ray diffraction patterns of mixtures. I. Matrix-flushing method for quantitative multicomponent analysis.* Journal of Applied Crystallography, 1974. 7(6): p. 519-525.

219. Hillier, S., *Accurate quantitative analysis of clay and other minerals in sandstones by XRD: comparison of a Rietveld and a reference intensity ratio (RIR) method and the importance of sample preparation.* Clay Minerals, 2000. 35(1): p. 291-302.

220. Jenkins, R., and Snyder, R. L., *Diffraction Theory, in Introduction to X-ray Powder Diffractometry.* 1996, Hoboken, NJ, John Wiley & Sons, Inc.

221. Goldstein, J.I., Newbury, D.E., Michael, J.R., Ritchie, N.W., Scott, J.J., and Joy, D.C., *Scanning electron microscopy and X-ray microanalysis*. 4th Ed. 2016, New York, Springer. p.689.

222. Wassilkowska, A., Czaplicka-Kotas, A., Bielski, A., and Zielina, M., 2015. *An analysis of the elemental composition of micro-samples using EDS technique.* Czasopismo Techniczne, 2014. (-): p. 133-148.

223. Potts, P.J., *A Handbook of Silicate Rock Analysis*. 1987, Dordrecht, Springer.

224. Shindo, D., and Oikawa, T., *Analytical electron microscopy for materials science*. 2013, Berlin, Springer Science & Business Media.

225. Williams, D.B., and Carter, C.B., *Transmission Electron Microscopy.* 2nd Ed. 2009, New York, New York, Springer. p 760.

226. ASTM International, *C20-00 Standard Test Methods for Apparent Porosity, Water Absorption, Apparent Specific Gravity, and Bulk Density of Burned Refractory Brick and Shapes by Boiling Water*. 2015, ASTM International: West Conshohocken, PA, USA.

227. El-Sheikh, M., and Powers, J., *Tensile bond strength of four denture resins to porcelain teeth with different surface treatment.* The Journal of Advanced Prosthodontics, 2013. 5(4):p. 423-427.

228. Spriestersbach, A., Röhrig, B., du Prel, J. B., Gerhold-Ay, A., and Blettner, M., *Descriptive statistics: The specification of statistical measures and their presentation in tables and graphs. Part 7 of a series on evaluation of scientific publications*. Deutsches Ärzteblatt International, 2009. 106(36):p. 578-583.

229. Stathis, G., Ekonomakou, A., Stournaras, C. J., and Ftikos, C., *Effect of firing conditions, filler grain size and quartz content on bending strength and physical properties of sanitaryware porcelain.* Journal of the European Ceramic Society, 2004. 24(8):p. 2357-2366.

230. Kurama, S., and Eren, E. *Characterization of mechanical properties of porcelain tile using ultrasonics.* Gazi University Journal of Science, 2012. 25(3):p. 761-768.

231. Cannillo, V., Esposito, L., Rambaldi, E., Sola, A., and Tucci, A., *Effect of porosity on the elastic properties of porcelainized stoneware tiles by a multi-layered model.* Ceramics International, 2009. 35(1):p. 205-211.

232. Maity, S., and Sarkar, B., K., *Development of high-strength whiteware bodies.* Journal of the European Ceramic Society, 1996. 16(10):p. 1083-1088.

233. Pérez, J. M., and Romero, M., *Microstructure and technological properties of porcelain stoneware tiles moulded at different pressures and thicknesses*. Ceramics International, 2014. 40(1):p.1365-1377.

234. Batista, S., F., Messer, P, F., and Hand, R. J., *Fracture toughness of bone china and hard porcelain*. British ceramic transactions, 2001. 100(6):p. 256-259.

235. Nyongesa, F. W., Rahbar, N., Obwoya, S. K., Zimba, J., Aduda, B. O., and Soboyejo, W. O., *An investigation of thermal shock in porous clay ceramics*. ISRN Mechanical Engineering, 2011. 2011 (-): p. 1-9.

236. Martín-Márquez, J., Rincón, J. M., and Romero, M., *Effect of microstructure on mechanical properties of porcelain stoneware.* Journal of the European Ceramic Society, 2010. 30(15): p. 3063-3069.

237. Ridler, T. W., and Calvard, S., *Picture thresholding using an iterative selection method.* IEEE Transaction on System, Man, and Cybernetics, 1978. 8(8): P. 630-632.

238. Shetty, D., Rosenfield, A., and Duckworth, W., *Mixed-mode fracture of ceramics in diametral compression.* Journal of the American Ceramic Society, 1986. 69(6): p. 437-443.

239. Jaeger, J., and Hoskins, E., *Stresses and failure in rings of rock loaded in diametral tension or compression.* British Journal of Applied Physics, 1966. 17(5): p. 685.

240. De With, G., *Note on the use of the diametral compression test for the strength measurement of ceramics.* Journal of Materials Science Letters, 1984. 3: p. 1000-1002.

241. Mostafa, N.Y., Shaltout, A.A., Abdel-Aal, M.S., and El-Maghraby, A., *Sintering mechanism of blast furnace slag–kaolin ceramics.* Materials & Design, 2010. 31(8): p. 3677-3682.

242. Barde, M. P., and Barde, P. J., *What to use to express the variability of data: Standard deviation or standard error of mean?.* Perspectives in Clinical Research, 2012. 3(3):p. 113-116.

243. Quinn, G.D., and Morrell, R., *Design data for engineering ceramics: a review of the flexure test*. Journal of the American Ceramic society, 1991. 74(9): p. 2037-2066.

244. Fairhurst, C.W., Lockwood, P.E., Ringle, R.D. and Twiggs, S.W., *Dynamic fatigue of feldspathic porcelain*. Dental Materials, 1993. 9(4): p. 269-273.

245. Thompson, G.A., *Determining the slow crack growth parameter and Weibull two-parameter estimates of bilaminate disks by constant displacement-rate flexural testing*. Dental Materials, 2004. 20(1): p.51-62.

246. Kim, H., and Kim, T., *Measurement of hardness on traditional ceramics.* Journal of the European Ceramic Society, 2002. 22(9-10): p. 1437-1445.

247. ASTM International, ASTM E384-17 Standard Test Method for Microindentation Hardness of Materials. 2017, ASTM International: West Conshohocken, PA, USA.

248. Batista, S., Messer, P., and Hand, R., *Fracture toughness of bone china and hard porcelain.* British Ceramic Transactions, 2001. 100(6): p. 256-259.

249. Evans, A.G., and Charles, E.A., *Fracture toughness determinations by indentation.* Journal of the American Ceramic society, 1976. 59(7-8): p. 371-372.

250. Kedir, N., Faucett, D. C., Choi, S. R., and Bansal, N. P., *Slow-crack-growth and indentation damage in calcium magnesium aluminosilicate (CMAS) glass from desert sand.* Ceramics International, 2018. 44(3):p. 2676-2682.

251. Chen, L.F., Ong, C.K., Neo, C.P., Varadan, V.V., and Varadan, V.K., *Microwave electronics: measurement and materials characterization.* 2004, Chichester, West Sussex, John Wiley & Sons.

252. Benavente, R., Salvador, M.D., Peñaranda-Foix, F.L., García-Moreno, O., and Borrell, A., *High thermal stability of microwave sintered low-ε_r ß-eucryptite materials.* Ceramics International, 2015. 41(10): p. 13817-13822.

253. Benavente, R., Borrell, A., Salvador, M.D., Garcia-Moreno, O., Peñaranda-Foix, F.L., and Catala-Civera, J.M., *Fabrication of near-zero thermal expansion of fully dense ß-eucryptite ceramics by microwave sintering.* Ceramics International, 2014. 40(1): p. 935-941.

254. Raj, R., *Joule heating during flash-sintering*. Journal of the European Ceramic Society, 2012. 32(10): p. 2293-2301.

255. Brown, M.E., and Gallagher, P.K., *Handbook of Thermal Analysis and Calorimetry Applications to Inorganic and Miscellaneous Vol. 2*. 1998, Amsterdam, Elsevier.

256. Ghiorso, M.S., Carmichael, I. E., and Moret, L.K., *Inverted high-temperature quartz.* Contributions to Mineralogy and Petrology, 1979. 68(3): p.307-323.

257. Hirono, T., and Hamada, Y., *Specific heat capacity and thermal diffusivity and their temperature dependencies in a rock sample from adjacent to the Taiwan Chelungpu fault.* Journal of Geophysical Research: Solid Earth, 2010. 115(B5): p. 1-13.

258. Richet, P., and Neuville, D.R., *Thermodynamics of silicate melts: configurational properties.* In Saxena S.K. (Eds). Thermodynamic Data. Advances in Physical Geochemistry, vol. 10. 1992, NY, Springer.

259. Holland, T. B., and Powell, R., *An internally consistent thermodynamic data set for phases of petrological interest.* Journal of Metamorphic Geology, 1998. 16(3): p.309-343.

260. Helgeson, H. C., Delany, J. M., Nesbitt, H. W., and Bird D. W., *Summary and critique of the thermodynamic properties of rock-forming minerals.* American Journal of Science, 1978. 278-A: p: 1–229.

261. Callister, W. D., and Rethwisch, D.G., *Fundamentals of materials science and engineering: An integrated approach.* 2008, Hoboken, NJ, John Wiley & Sons.

262. Shibata, H., Suzuki, A., and Ohta, H., *Measurement of thermal transport properties for molten silicate glasses at high temperatures by means of a novel laser flash technique.* Materials Transactions, 2005. 46(8): p. 1877-1881.

263. Podoba, R., Štubňa, I., Trnovcová, V., and Trník, A., *Temperature dependence of DC electrical conductivity of kaolin.* Journal of Thermal Analysis and Calorimetry, 2014. 118(2): p. 597-601.

264. Noritomi, K., *Studies on the change of electrical conductivity with temperature of a few silicate minerals*. Science Reports of the Tohoku University. Ser. 5, Geophysics, 1954. 6(2): p. 119.

265. Njiokep, T., Imre, E. M., Mehrer, A. W., and Mehrer, H., *Tracer diffusion of ^{22}Na and ^{45}Ca, ionic conduction and viscosity of two standard soda-lime glasses and their undercooled melts.* Physics of Non-Crystalline Solids, 2008. 11, 354 (2-9): p.355-59.

266. Yoshino, T., *Laboratory electrical conductivity measurement of mantle minerals.* Surveys in Geophysics, 2010. 31(2): p. 163-206.

267. Mott, N. F., *Metal-Insulator Transition.* 1990, London, Taylor & Francis.

268. Jones, R., Thrall, M., and Henderson, C., *Complex impedance spectroscopy and ionic transport properties of natural leucite, $K_{0.90}Na_{0.08}$ $[Al_{0.98}Si_{2.02}]$ O_6, as a Function of Temperature and Pressure.* Mineralogical Magazine, 2010. 74(3): p. 507-19.

269. Sperinck, S., Raiteri, P., Marks, N., and Wright, K., *Dehydroxylation of kaolinite to metakaolin—a molecular dynamics study.* Journal of Materials Chemistry, 2011. 21(7): p. 2118-25

270. Trnovcova, V., Podoba, R., and Štubna, I., *DC conductivity of kaolin-based ceramics in the temperature range 20–600 °C.* Epitoanyag, 2012. 64: p. 46-9.

271. McConville, C. J., Lee, W. E., and Sharp, J. H., *Microstructural evolution in dense kaolinite, illite, and smectite clay bodies*, In Carty, W.M., and Sinton, C.W., (Eds). Science of Whiteware II. 2006, Westerville, OH, Wiley-American Ceramic Society.

272. Romero, M., and Pérez, J. M., *Relation between the microstructure and technological properties of porcelain* stoneware. A review. Materiales de Construcción, 2015. 65(320):p. 065.

273. Messler, Jr., and Robert, W., *The essence of materials for engineers*. 2010, MA, Jones & Bartlett Publishers.

274. Manouchehri, H.R., Hanumantha, Rao, K., and Forssberg, K.S.E., *Triboelectric charge, electrophysical properties and electrical beneficiation potential of chemically treated feldspar, quartz and wollastonite.* Physical Separation in Science and Engineering, 2002. 11(1-2): p.9-32.

275. Leluk, K., Orzechowski, K., Jerie, K., Baranowski, A., SŁonka, T., and GŁowiński, J., *Dielectric permittivity of kaolinite heated to high temperatures.* Journal of Physics and Chemistry of Solids, 2010. 71(5): p:827-831.

276. Morton, J., *Electrical and optical properties of materials.* [Lecture notes]. 2014. Retrieved from https://www.ucl.ac.uk/qsd/people/teaching/EOPM-Part2.pdf. [Accessed 6 February 2018].

277. Sharma, A., and Mehta, N., *Study of dielectric relaxation and thermally activated ac conduction in lead containing topological glassy semiconductors.* Royal Society of Chemistry Advances, 2017. 7(31): p.19085-19097.

278. Heidary, D. B., Lanagan, M., and Randall, C. A., *Contrasting energy efficiency in various ceramic sintering processes*. Journal of the European Ceramic Society, 2018. 38(4):p. 1018-1029.

279. Chinnam, R., Francis, A., Will, J., Bernardo, E., and Boccaccini, A.R., *Functional glasses and glass-ceramics derived from iron rich waste and combination of industrial residues.* Journal of Non-Crystalline Solids, 2013. 365: p. 63-74.

280. International Standard Organisation, Ceramic tiles–definitions, classification, characteristics and marking (ISO 13006):1998. Available from: https://www.iso.org/obp/ui/#iso:std:iso:13006:ed-2:v1:en [Accessed 1 October 2017].

281. Siegesmund, S., and Dürrast, H., *Physical and mechanical properties of rocks*. In Siegesmund, S., and Snethlage, R., (Eds). Stone in Architecture. 2011, Heidelberg, Springer. p.97-225.

282. Chinnam, R.K., Boccaccini, A.R., Bernardo, E., and Epstein, H., *Glass-ceramic composites from borosilicate glass and alumina-rich residues.* International Journal of Applied Ceramic Technology, 2013. 12 (S2): p. E19–E27.

283. Roether, J.A., Daniel, D.J., Rani, D.A., Deegan, D. E., Cheeseman, C.R., and Boccaccini, A.R., *Properties of sintered glass-ceramics prepared from plasma*

vitrified air pollution control residues. Journal of Hazardous Materials, 2010. 173 (1-3): p. 563-569.

284. Stubna, I., Sin, P., Viljus, M., and Trnik, A., *The effect of the firing temperature on hardness of alumina porcelain.* Materials and Technology, 2014.48 (3): p. 331–336.

285. Aguilar-García, O., Bribiesca-Vazquez, S., and Zárate-Medina. J., *Evaluation of hardness and fracture toughness in a porcelain stoneware with pseudoboehmite additions.* Journal of Ceramic Processing Research, 2009. 10 (1): p. 37-42.

286. Della, B., Álvaro P., Márcia, B., and Dileta, C., *Flexural and diametral tensile strength of composite resins.* Brazilian Oral Research, 2008. 22(1): p. 84-89.

287. Bresciani, E., Barata, T., Fagundes T.C., Adachi, A., Terrin, M. M., and Navarro, M. F., *Compressive and diametral tensile strength of glass ionomer cements.* Journal of Applied Oral Science, 2004. 12(4): p. 344-348.

288. Kobayashi, Y., Ohira, O., and Kato, E., *Effect of firing temperature on bending strength of porcelains for tableware.* Journal of the American Ceramic society, 1992. 75 (7):p. 1801–1806.

289. Ece, O.I., and Nakagawa, Z., *Bending strength of porcelains*. Ceramics International, 2002. 28(2):p. 131–140.

290. Stathis, G., Ekonomakou, A., Stournaras, C.J., and Ftikos, C., *Effect of firing conditions, filler grain size and quartz content on bending strength and physical properties of sanitaryware porcelain.* Journal of the European Ceramic Society, 2004. 24(8):p. 2357–2366.

291. Fredericci, C., Yoshimura, H.N., Molisani, A.L., Pinto, M.M., and Cesar, P.F., *Effect of temperature and heating rate on the sintering of leucite-based dental porcelains.* Ceramics International, 2011. 37(3): p. 1073-1078.

292. Coulson, J.M., Richardson, J.F., and Coulson, J.M., *Chemical Engineering, Vol.1: Heat Flow and Mass Transfer*, 6th Edn. 2000, Oxford, Butterworth Heinemann. p.928.

293. Edwards, R., and Lobaugh., M., *Using excel to implement the finite difference method for 2-D heat transfer in a mechanical engineering technology Course*. in 2014 ASEE Annual Conference & Exposition. 2014, Indiana, USA.

294. Stevenson, C.M., and Gurnick, M., *Structural collapse in kaolinite, montmorillonite and illite clay and its role in the ceramic rehydroxylation dating of low-fired earthenware.* Journal of Archaeological Science, 2016. 69(-): p. 54-63.

295. Sperinck, S., Raiteri, P., Marks, N., and Wright, K., Dehydroxylation of kaolinite to metakaolin—a molecular dynamics study. Journal of Materials Chemistry, 2011. 21(7): p. 2118-2125.

296. Grasso, S., Hu, C., Maizza, G., Kim, B.N., and Sakka, Y., *Effects of pressure application method on transparency of spark plasma sintered alumina.* Journal of the American Ceramic Society, 2011. 94(5): p. 1405-1409.

297. Sousa, F.J., Dal Bó, M., Guglielmi, P.O., Janssen, R., and Hotza, D., *Characterization of Young's modulus and fracture toughness of albite glass by different techniques.* Ceramics International, 2014. 40(7): p. 10893-10899.

298. Kanzaki, S., Tabata, H., Kumazawa, T., and Ohta, S., *Sintering and mechanical properties of stoichiometric mullite.* Journal of the American Ceramic Society, 2006. 68(1): p.C6–C7.

299. Bradt, R.C., Hasselman, D.P.H., Munz, D., Sakai, M., Shevchenko, V.Y., (Eds.)., *Fracture mechanics of ceramics: Fracture fundamentals, high-temperature deformation, damage, and design.* Vol. 10, 2013, NY, Springer Science & Business Media.

300. Akono, A.T., Randall, N.X., and Ulm, F.J., *Experimental determination of the fracture toughness via microscratch tests: application to polymers, ceramics, and metals.* Journal of Materials Research, 2012. 27(02): p. 485-493.

301. Spray, J.G., *Frictional melting processes in planetary materials: from hypervelocity impact to earthquakes.* Annual Review of Earth and Planetary Sciences, 2010. 38: p.221–254.

302. Ruh, R., Mazdiyasni, K.S., Mendiratta, M.G., *Mechanical and microstructural characterization of mullite and mullite-SiC-Whisker and ZrO_2-toughened-mullite-SiC-whisker composites.* Journal of the American Ceramic Society, 1988. 71(6): p.503–512.

303. Kingery, W., Woulbroun, J., and Charvat, F., *Effects of applied pressure on densification during sintering in the presence of a liquid phase.* Journal of the American Ceramic Society, 1963. 46(8): p. 391-395.

304. Wolf, G., and McMillan, P., *Pressure effects on silicate melt structure and properties.* Reviews in Mineralogy and Geochemistry, 1995. 32(1): p. 505-561.

305. Boettcher, A., Guo, Q., Bohlen, S. and Hanson, B., *Melting in feldspar-bearing systems to high pressures and the structures of aluminosilicate liquids.* Geology, 1984. 12(4): p.202-204.

306. Barth, T.W., *Feldspar equilibria and their implication I.* Norwegian Journal of Geology, 1938. 17(-), p.177.

307. Goldsmith, J.R., and Peterson, J.W., *Hydrothermal melting behaviour of $KAlSi_3O_8$ as microcline and sanidine.* American Mineralogist, 1990. 75(11-12): p.1362-1369.

308. Blair, G., and Chaklader, A., *Kaolinite-mullite series: firing vs. reactive hot-pressing*. Journal of Thermal Analysis and Calorimetry, 1972. 4(3): p.311-322.

309. Weiss, A., Range K.J., and Russow, J., *The Al, Si-Spinel phase from kaolinite (Isolation, chemical analysis, orientation, and relations to its low temperature precursors).* In Proceeding of International Clay Conference, 1970. Tokyo: Israel University Press.

310. Lerdprom, W., Grasso, S., Jayaseelan, D.D., Reece, M.J., and Lee, W.E, *Densification behaviour and physicomechanical properties of porcelains prepared using spark plasma sintering*. Advances in Applied Ceramics, 2017. 116(6): p.1-9.

311. Hartman, P., and Perdok, W., *On the relations between structure and morphology of crystals. I.* Acta Crystallographica, 1955. 8(1): p. 49-52.

312. Shinoda, Y., Suzuki, Y., and Yoshida, K., *Electric field effect on texture formation of mullite in spark plasma sintered SiC with Al_2O_3–SiO_2 additive.* Scripta Materialia, 2015. 100: p. 51-54.

313. Plascencia, G. and Jaramillo, D., *Basic Thermochemistry in Materials Processing*. 2017, Mexico City, Mexico, Springer International Publishing.

314. Adamson W.A., *Liquid and their simple phase equilibria*. In A Textbook of Physical Chemistry, 2nd Ed. 1979, NY, Academic Press, p. 251-299.

315. WWW-MINCRYST (2018), KAOLINITE-2291, Crystallographic and crystallochemical database for minerals and their Structural Analogues. http://database.iem.ac.ru/mincryst/

316. WWW-MINCRYST (2018), MULLITE-7222, Crystallographic and crystallochemical database for minerals and their Structural Analogues. http://database.iem.ac.ru/mincryst/

317. Schieltz, N., and Soliman, M., *Thermodynamics of the various high temperature transformations of kaolinite*. In Proceedings of the 13th National Conference on Clays and Clay Minerals. 1966, Pergamon Press, NY. p. 419-428.

318. Ptáček, P., Šoukal, F., Opravil, T., Havlica, J., and Brandštetr J., *Crystallization of spinel phase from metakaolin: the nonisothermal thermodilatometric CRH study.* Powder Technology, 2013. 243: p. 40-45.

319. Gebremariam, A.T., *CFD modelling and experimental testing of thermal calcination of kaolinite rich clay particles - an effort towards green concrete,* [PhD thesis]. Aalborg University. 2015, Aalborg, Denmark.

320. MacKenzie, K.J.D., Meinhold, R.H., Brown, I. M., and White, G.V., *The formation of mullite from kaolinite under various reaction atmospheres.* Journal of the European Ceramic Society, 1996. 16(2): p. 115-119.

321. Li, D.X., and Thomson, W.J., *Tetragonal to orthorhombic transformation during mullite formation.* Journal of Materials Research, 1991. 6(04): p. 819-824.

322. Aksaf, I., and Pask, J., *Stable and metastable equilibria in the system SiO_2-Al_2O_3.* Journal of the American Ceramic Society, 1975. 58(11-12): p. 507-512.

323. Klug, F.J., Prochazka, S., and Doremus, R.H., *Alumina-silica phase diagram in the mullite region.* Journal of the American Ceramic Society, 1987. 70(10): p. 750-759.

324. Baudín, C., and Villar, M.P., *Influence of thermal aging on microstructural development of mullite containing alkalis.* Journal of the American Ceramic Society, 1998. 81(10): p. 2741-2745.

325. Ribeiro, M.J., Tulyagavov, D.U., Ferreira, J.M., and Labrincha, J.A., *High temperature mullite dissolution in ceramic bodies derived from Al-rich sludge.* Journal of the European Ceramic Society, 2005. 25(5): p. 703-710.

326. Kanyanta, V., *Microstructure-Property Correlations for Hard, Superhard, and Ultrahard Materials*. 2016, Switzerland, Springer.

327. Chen, X. Q., Niu, H., Li, D., and Li, Y., *Modeling hardness of polycrystalline materials and bulk metallic glasses*. Intermetallics, 2011. 19(9): p. 1275-1281.

328. Cerecedo, C., Valcárcel, V., Gómez, M., Drubi, I., and Guitián, F., *New massive vapor-liquid-solid deposition of α-Al_2O_3 fibres.* Advanced Engineering Materials, 2007. 9(7): p.600–603.

329. Dan, L., Xiumin, Y., Jian, C., Fang, J., Yong, Y., Zhengren, H., and Xuejian, L., *Microstructure and reaction mechanism of SiC ceramic with mullite-zircon as a new liquid-phase sintering additives system.* Materials Science and Engineering: A, 2013. 559: p. 510–514.

330. Zhang, Z., Qiao, X., and Yu, J., *Microwave selective heating-enhanced reaction rates for mullite preparation from kaolinite.* RSC Advances, 2014. 4(6): p.2640–2647.

331. Panneerselvam, M., and Rao, K.J., *Novel microwave method for the synthesis and sintering of mullite from kaolinite.* Chemistry of Materials, 2003. 15(11): p. 2247–2252.

332. Bergeron, C.G., and Risbud, S.H., *Introduction to phase equilibria in ceramics*. 1986, OH, Wiley-American Ceramic Society.

333. Li, D., de Moraes, E.G., Guo, P., Zou, J., Zhang, J., Colombo, P., and Shen, Z., *Rapid sintering of silicon nitride foams decorated with one-dimensional nanostructures by intense thermal radiation.* Science and Technology of Advanced Materials, 2014. 15(4): p.045003.

334. O'Dwyer, J.J., *The theory of electrical conduction and breakdown in solid dielectrics*. 1973, Oxford, Clarendon Press.

335. Jaitly, N. C., Sudarshan, T. S., Dougal, R. A., and Miller, H., C., *Degradation due to wet hydrogen firing on the high-voltage performance of alumina insulators in vacuum applications.* Electrical Insulation IEEE Transactions, 1987, (EI-22): p. 447-452.

336. Nakae, H., Nakano, S., and Yoshida, M., *Influence of melting temperature on morphology of primary mullite in SiO_2–Al_2O_3 system.* Materials Transactions, JIM, 1995. 36(9): p. 1163-1169.

337. Burton, W.K., Cabrera, N., and Frank, F., *The growth of crystals and the equilibrium structure of their surfaces.* Philosophical Transactions of the Royal Society of London A: Mathematical, Physical and Engineering Sciences, 1951. 243(866): p. 299-358.

338. Venugopal, S., Jayaseelan, D. D., Paul, A., Vaidhyanathan, B., Binner, J. G., and Brown, P. M., *Screw dislocation assisted spontaneous growth of HfB_2 tubes and rods*. Journal of the American Ceramic Society, 2015. 98(7): p. 2060-2064.

339. Varshneya, A.K., *Fundamentals of inorganic glasses*. 1994, CA, Academic Press, Inc.

340. MacKenzie, K., and Brown, I., *Devitrification of aluminosilicate glasses under applied electric fields: I. The system $Al_2O_3 \cdot 2SiO_2$.* Journal of Thermal Analysis and Calorimetry, 1975. 7(3): p. 619-633.

341. Caliman, L. B., Bouchet, R., Gouvea, D., Soudant, P., and Steil, M., *Flash sintering of ionic conductors: the need of a reversible electrochemical reaction.* Journal of the European Ceramic Society, 2016. 36(5): p. 1253-1260.

342. McLaren, C., Heffner, W., Tessarollo, R., Raj, R., and Jain, H., *Electric field-induced softening of alkali silicate glasses.* Applied Physics Letters, 2015. 107(18): p. 184101.

343. Biesuz, M., Luchi, P., Quaranta, A., and Sglavo, V.M., *Theoretical and phenomenological analogies between flash sintering and dielectric breakdown in α-alumina*. Journal of Applied Physics, 2016. 120(14): p. 145107.

344. Watanabe, T., Sato, M., Takayama, S., and Matsubara, A., *Observation of diffusive flows during liquid phase microwave sintering.* Plasma and Fusion Research, 2009. 4(9): p. 1-5.

345. Zhao, J., Meng, J., Xu, C., and Zhao, J., *Microwave-assisted decomposition of K-feldspar at low temperature in acids system.* International Journal of Geophysics and Geochemistry. 2017, 4(2): p. 18-22.

346. Antonio, C., and Dream, R.T., *Can "microwave effect" be explained by enhanced diffusion.* Physical Chemistry Chemical Physics, 2007. 9(23): p. 2976–2982.

347. Pedevilla, P., Cox, S. J., Slater, B., and Michaelides, A., (2016). *Can ice-like structures form on non-ice-like substrates? The example of the K-feldspar microcline.* The Journal of Physical Chemistry C, 2016. 120(12): p. 6704-6713.

348. Dingwell, D.B., and Virgo, D., *The effect of oxidation state on the viscosity of melts in the system Na_2O-FeO-Fe_2O_3-SiO_2.* Geochimica et Cosmochimica Acta, 1987. 51(2): p. 195-205.

349. Takei, T., Kameshima, Y., Yasumori, A., and Okada, K., *Crystallization kinetics of mullite in alumina–silica glass fibres.* Journal of the American Ceramic Society, 1999. 82(10): p. 2876-2880.

350. Albakry, M., Guazzato, M., and Swain, M.V., *Influence of hot pressing on the microstructure and fracture toughness of two pressable dental glass–ceramics.* Journal of Biomedical Materials Research Part B: Applied Biomaterials, 2004. 71(1): p. 99-107.

351. Momber, A.W., *An SEM-study of high-speed hydrodynamic erosion of cementitious composites.* Composites Part B: Engineering, 2003. 34(2): p. 135-142.

352. Kon, M., Ishikawa, K., and Kuwayama, N., *Effects of zirconia addition on fracture toughness and bending strength of dental porcelains*. Dental Materials Journal, 1990. 9(2): p. 181-192.

353. Kon, M., Kawano, F., Tada, Y., Inoue, S., Asaoka, K., and Matsumoto, N., *Effect of crystallization on fracture strength of castable glass-ceramics containing two crystals*. Dental Materials Journal, 1994. 13(1): p. 47-54.

354. Seghi, R.R., Daher, T., and Caputo, A., *Relative flexural strength of dental restorative ceramics.* Dental Materials, 1990. 6(3): p. 181-181.

355. Khabari, A., Zenouzi, M., O'Connor, T., and Rodas, A., *Natural and forced convective heat transfer analysis of nanostructured surface.* In Proceedings of the World Congress on Engineering (Vol. 1). 2014, London, UK.

356. Furukawa, G. T., Douglas, T. B., McCoskey, R. E., and Ginnings, D. C., *Thermal properties of aluminum oxide from 0 to 1200 K.* Journal of Research of the National Bureau of Standards. 1956, 57(2): p. 67-82.

357. Huang, L., Qian, M., Lu, H., Sun, Y., Wang, L., and Zou, J., *Reducing electric current and energy consumption of spark plasma sintering via punch configuration design.* Ceramics International, 2017. 43(18): p. 17225-17228.

358. Bartusch, R., *Potential for saving energy in the Ceramic Industry.* Keramische Zeitschrift, 2002. 54(1): p. 6-10.

359. Heidary, D. B., Lanagan, M., and Randall, C.A., *Contrasting energy efficiency in various ceramic sintering processes.* Journal of the European Ceramic Society, 2018. 38(4): p. 1018-1029.